

Semi-Rigid Moment-Resisting Behavior of Multiple Tab-and-Slot Joint for Freeform Timber Plate Structures

THÈSE N° 8236 (2017)

PRÉSENTÉE LE 18 DÉCEMBRE 2017

À LA FACULTÉ DE L'ENVIRONNEMENT NATUREL, ARCHITECTURAL ET CONSTRUIT

LABORATOIRE DE CONSTRUCTION EN BOIS

PROGRAMME DOCTORAL EN GÉNIE CIVIL ET ENVIRONNEMENT

ÉCOLE POLYTECHNIQUE FÉDÉRALE DE LAUSANNE

POUR L'OBTENTION DU GRADE DE DOCTEUR ÈS SCIENCES

PAR

Stéphane ROCHE

acceptée sur proposition du jury:

Prof. A. Nussbaumer, président du jury

Prof. Y. Weinand, directeur de thèse

Prof. T. Descamps, rapporteur

Dr J.-F. Bocquet, rapporteur

Prof. A. Frangi, rapporteur



ÉCOLE POLYTECHNIQUE
FÉDÉRALE DE LAUSANNE

Suisse
2017

Acknowledgements

After many years in industry, I reconverted myself to a job that allied my engineering background with my passion for Wood. In the initiatory journey that led me into the world of wood, it was full of curiosity at first that I crossed the Lemman's lake to push the IBOIS's door. This is where my supervisor Prof. Yves Weinand proposed me to invest myself in a doctoral thesis. I thank him for this opportunity he offered me to deepen my knowledge of wood. The road ahead was long and could have been full of obstacles without all those who shared my way :

The members of the thesis jury, the President Prof. Alain Nussbaumer, the experts, Prof. Andrea Frangi, Prof. Thierry Descamps and Dr. Jean-François Bocquet, who accepted these roles and with whom I discussed in depth to finalize this document.

The pool of technicians and in particular François, Frédérique, Armin, Sylvain and Gilles without whom all these samples and test rigs could never have seen the light of day. The assistants of the laboratory, Hildegard who past away too early, Tamina and Francine which greatly facilitated the office's life.

My former colleagues, Laurent, Benjamin, Christopher and Sina, with whom I exchanged a lot "to advance research" as we say.

My current colleagues Andrea, Ahn-Chi, Aryan, Julien and Petras with whom I shared the questions of the researcher but also slice of unique life.

The master students, Geoffroy M., Julien, Daniel, Gabriel, Anouk, Geoffroy G, Camille and Saskya who directly collaborated with me.

Our group of architects, Fred, Marielle, Céline, Sacha and Didier who make IBOIS an unusual place where the collaboration between architects and engineers is not just a sweet dream.

Professor Hideaki Tanahashi who has always responded with great promptness and clarity to my inquiries on all these interesting publications ... obviously in Japanese.

And a special tenderness for my wife Sandrine and my daughter Evana who wait patiently for a husband and father more available to finish the family home in straw and ... wood, of course.

Lausanne, 1st November 2017

S. R.

Abstract

Historically based on the transfer of ancestral know-how, the art of carpentry changed considerably at the beginning of the 21st century with the arrival on the market of engineered wood products (EWP) and computer numerically controlled machines (CNC). The development of these wood products was initially started for the needs of aeronautics : lightweight panels but with high structural capacity. It is also in this field that automated multi-axis milling machines and the accompanying computing tool, computer-aided design and manufacturing (CAD / CAM), have begun to be developed to produce more complex mechanical parts.

It was also in the early 2000s that several teams of researchers in the field of computer graphics but also in architecture were interested in complex free forms. One of the many challenges is still the discretization with planar elements of doubly curved surfaces oriented freely in space. The encounter of these “ algorithms ” with the high-performant wood panels was ineluctable. However, the assembly of polygonal panels in space to form a structure is not trivial. Optimization efforts are made so that the topology in itself favors the distribution of forces to tend towards a behavior of shells. But the problem is sometimes insoluble for very irregular shapes alternating negative, zero and positive Gaussian curvatures. To ensure the transmission of the axial, shear and bending internal forces induced by vertical or horizontal external loads, whether symmetrical or not, the performance of the assemblies used to connect these panels by their edges becomes paramount.

In wood construction, this is a topic currently being studied by a few research laboratories including EPFL for innovative wood-to-wood joints with multiple tab and slots (MTSJ). The main difficulty lies in how to connect thin wood panels with the best stiffness and strength. In the recent past, the assembly of wood parts between them, often with metal fasteners to provide a certain ductility, was assimilated to a hinge. With the new standards like the Eurocodes, the notion of semi-rigidity is now essential to obtain a realistic response of structures to both ultimate and service limit states. The solution proposed at IBOIS enters into this new context. It allows, without glue or metallic connectors, to interconnect thin engineered wood panels, ensuring both locator and connector features and the transfer of multidirectional forces.

This thesis focuses on the semi-rigid moment resisting behavior of the through tenon variant (TT) with closed slots. The numerous experiments conducted during this study demonstrated the ability of this variant to compete with screws to resist a moment around the angularly connected edges. The joint is directly generated during the multiaxial cutting of laminated veneer lumber(LVL) panels which include a certain percentage of cross-layers. From a structural point of view, the local mechanical study under a bending moment was inspired by a

Abstract

wood-to-wood joint in service in the ancestral Japanese shrines, the "Nuki" joint. Analyzed by Japanese researchers as it historically participates in the resilience of their ancestral constructions to typhoons and earthquakes, it activates embedment mechanisms of wood in rotational partial compression (RPC) to resist the moment resulting from the external loads. It is these mechanisms that are taken into account for through tenon variant.

The local forces at the compression zones perpendicular to the panel plane are calculated from embedded elastic and plastic volumes, in single contact (SC) and double contact (DC). These volumes consist of a part with a triangular section beneath the directly loaded area and a part with an exponential profile, beyond. This additional deformation was characterized by preliminary tests and from a simplified analytical model of the two components (single and double contacts) involved in the whole joint. The model was then extrapolated by assembling these local components with the lever arms which allow them to counterbalance the applied moment. A series of tests on seventeen configurations of the through tenon variant then allowed to qualify the model. The influences of the initial rotational slip and of the dihedral angle on the rotational stiffness were highlighted. The identified modes of joint failures were mainly due to an exceeding of the bending strength limits in the weakened area where tabs and slots were cut.

The non-linear moment-resisting model of the through tenon variant of the multiple tab-and-slot wood-to-wood joint showed promising results. However, its application in practice requires refining the data already obtained for the mechanical characterization of laminated veneer lumber with cross layer (X-LVL), in partial rotational compression perpendicular to the plane of the panels.

Key words: Wood-to-Wood Connection, Multiple Tab-and-Slot Joint, Through Tenon, Laminated Veneer Lumber (LVL), Semi-rigidity, Rotational Stiffness, Rotational Partial Compression Perpendicular to Grain, Analytical model, Non-linear moment-rotation relationship.

Résumé

Historiquement basé sur la transmission de savoir-faire ancestraux, l'art de la charpenterie s'est considérablement transformé au début du XXI^e siècle avec l'arrivée sur le marché des produits de bois transformés et des machines à commande numérique. Le développement de ces produits d'ingénierie a tout d'abord démarré pour les besoins de l'aéronautique : des panneaux légers mais à grande capacité structurelle. C'est aussi dans ce domaine que les machines d'usinage à plusieurs axes automatisés et l'outil informatique qui les accompagne, la conception et fabrication assistées par ordinateur (CFAO), ont commencé à voir le jour pour la réalisation de pièces mécaniques de plus en plus complexes.

C'est aussi au début de ces années 2000 que plusieurs équipes de chercheurs dans le domaine de l'informatique graphique mais aussi en architecture se sont intéressées aux formes libres et complexes. Un des nombreux challenges est encore actuellement la facettisation de surfaces doublement courbées, développées librement dans l'espace. La rencontre de ces "algorithmes" avec les panneaux de bois plat à haute capacité structurelles était inéluctable. Cependant, l'assemblage de panneaux polygonaux dans l'espace pour former une structure n'est pas triviale. Des efforts d'optimisation sont faits pour que la topologie en elle-même favorise la distribution des efforts pour tendre vers un comportement de coques. Mais le problème est parfois insoluble pour des formes très irrégulières alternant courbures gaussiennes négatives, nulles et positives. Pour assurer la transmission des efforts internes axiaux, de cisaillement et de flexion, induits par des charges extérieures verticales ou horizontales, symétriques ou non, la performance des assemblages servant à relier ces panneaux par leurs arêtes devient primordiale.

En construction bois, c'est un thème étudié actuellement par quelques laboratoires de recherche dont celui de l'EPFL pour des assemblages bois-bois innovants, à rainures-languettes multiples (MTSJ). La difficulté principale réside en comment connecter des panneaux de bois de faible épaisseur avec les meilleures rigidités et résistances possibles. En effet l'assemblage de pièces de bois entre elles, le plus souvent avec des connecteurs métalliques pour apporter de la ductilité, était assimilé à une articulation. Avec les nouvelles normes comme les euro-codes, la notion de semi-rigidité est maintenant essentielle pour obtenir une réponse réaliste des structures aux états limites ultimes et de service. La solution proposée à l'IBOIS entre dans ce nouveau contexte. Elle permet, sans colle ni connecteurs métalliques, de réaliser l'interconnexion de panneaux de bois de faible épaisseur en assurant à la fois le positionnement spatial, la fixation des éléments entre eux et le transfert d'efforts multidirectionnels.

L'étude proposée dans cette thèse s'intéresse au comportement semi-rigide en rotation de

Abstract

la variante avec tenons traversant et rainures à contour fermé. Les nombreuses expériences menées durant cette étude ont en effet démontré sa faculté à concurrencer les vis dans cet axe de sollicitation. Cet assemblage a directement été généré lors de la découpe multiaxiale de panneaux en lamibois à couches croisées. D'un point de vue structurel, son étude mécanique locale sous l'application d'un couple s'est inspirée d'un assemblage bois-bois, lui aussi traversant, utilisé dans les temples japonais, le « Nuki ». Analysé par les chercheurs japonais car il participe historiquement à la résilience de leurs constructions ancestrales aux typhons et tremblements de terre, il actionne des mécanismes de compression locale partielle en rotation pour résister au moment résultant des charges extérieures. Ce sont ces mécanismes qui ont été pris en compte pour notre variante à tenon traversant.

Dans ces travaux, les forces locales au niveau des zones de compression perpendiculaire au plan des panneaux ont été calculées à partir des volumes déformés, élastiques et plastiques, en simple contact (SC) et en double contact (DC). Ces volumes sont constitués d'une partie à section triangulaire sous la surface directement chargée et d'une partie à profil exponentiel, au-delà. Cette déformation additionnelle a été caractérisée par des essais préliminaires et un modèle analytique simplifié des deux composantes (simple et double contacts) en jeu dans le comportement de la variante à tenon traversant. Le modèle a ensuite été extrapolé en assemblant ces composantes locales aux bras de levier qui leur permettent de s'opposer au couple qui les sollicite. Une série de tests sur dix-sept configurations de l'assemblage étudié a ensuite permis de qualifier le modèle. Les influences du glissement rotationnel initial et de l'angle entre panneaux sur la rigidité rotationnelle ont été soulignées. La limite de résistance en flexion au niveau de l'inertie réduite à l'endroit de l'assemblage s'est avérée la source principale de rupture.

Le modèle non-linéaire moment-rotation de la variante à tenon traversant de l'assemblage bois-bois à rainures-languettes multiples a montré des résultats prometteurs. Son application pratique nécessite toutefois d'affiner les données déjà obtenues dans le cadre de la caractérisation mécanique du lamibois à couches croisées en compression rotationnelle partielle perpendiculaire au plan du panneau.

Mots clefs : Assemblage Bois-Bois à Rainures-Languettes Multiples, Tenon Traversant, Lami-bois(LVL), Semi-rigidité Rotationnelle, Compression Perpendiculaire Rotationnelle Partielle, Modèle Analytique, Relation Non-linéaire Moment Rotation.

Contents

Acknowledgements	i
Abstract (English/Français)	iii
Introduction and State-of-the-Art	1
1 Introduction	3
1.1 Overview	3
1.2 From handicraft to digital fabrication in timber construction	3
1.3 Freeform faceted plate structures	4
1.4 Pure plate structures	6
1.5 Edge connections for thin timber panels	7
References	9
2 State-of-the-Art	11
2.1 Angular Connections for Thin Structural Wood Panels	11
2.1.1 Angular connections review for engineered wood panels	11
2.1.2 Folded plate structures: Research projects	14
2.1.3 Folded plate structures : Actual building	23
2.1.4 Free-form timber plate structures: Research projects	26
2.1.5 Free-form timber plate structures: Actual projects	32
2.1.6 Conclusion on the review	38
2.2 Moment-resisting Models of Timber Connections	39
2.2.1 Semi-rigid Joints	39
2.2.2 Component Method	43
2.2.3 Component method : Application to traditional timber joints	45
2.2.4 Stiffness models for the components	57
2.3 Laminated veneer lumber for timber plate structures	85
2.4 Research motivation	87
2.5 Scope of research	90
References	92

Investigations and Publications	103
3 On the semi-rigidity of dovetail joint for the joinery of LVL panels	105
Objective ①	105
3.1 Introduction	106
3.2 Numerical Model	106
3.3 Experimental study	110
3.3.1 Introduction to the MTSJ geometry	110
3.3.2 Description of the samples	112
3.3.3 Method	113
3.3.4 Experimental results	113
3.4 Conclusion	117
Outcomes ①	119
References	121
4 Rotational Stiffness at Ridges of Timber Folded-plate Structures	123
Objective ②	123
4.1 Introduction	124
4.2 The Multiple Tab-and-Slot Joint as a Structural Panel Connection	126
4.2.1 Forces at ridges and valleys	126
4.2.2 Description of the MTSJ	126
4.3 Experimental study	129
4.3.1 Description of the samples	129
4.3.2 Method	130
4.4 Numerical model	130
4.4.1 Material model	130
4.4.2 Elastic behaviour	130
4.4.3 Damage approach	132
4.4.4 User Defined Field (USDFLD) in Abaqus	134
4.5 Results and discussion	135
4.5.1 Experimental results	135
4.5.2 Numerical model versus experiments	139
4.6 Conclusions	142
Outcomes ②	143
References	146
5 Improvement of the Rotational Stiffness for the Connection of Thin Structural Wood Panels	149
Objective ③	149
5.1 Introduction	150
5.2 MTSJ design for improved rotational stiffness	151
5.3 Bending experiments	153
5.3.1 Method	153

5.3.2 Results	153
5.4 Embedment Effect on MTSJ with TT	157
5.4.1 Contact surfaces	157
5.4.2 Embedment by rotational partial compression	157
5.5 Conclusions	167
Outcomes ③	168
References	171
6 Material characterization of spruce LVL in rotational partial compression	173
Objective ④	173
6.1 Introduction	174
6.1.1 Objectives	174
6.1.2 Additional length in partial compression	174
6.1.3 Yield point	176
6.2 Material characterization in rotational partial compression	176
6.3 Method	176
6.3.1 Single contact component	177
6.3.2 Double contact component	179
6.3.3 Non-linear Measurements	182
6.4 Simplified analytical model	182
6.5 Results for single contact	186
6.5.1 Adjustment of the analytical model	186
6.5.2 Additional length profile	187
6.6 Results for double contact	194
6.6.1 Adjustment of the analytical model	194
6.6.2 Additional length profile	194
6.7 Conclusion	198
Outcomes ④	199
References	201
7 Semi-rigid Moment-resisting Model of the Through Tenon variant of Multiple Tab-and-Slot Joint for LVL panels	205
Objective ⑤	205
7.1 Introduction	206
7.2 Geometry of the multiple tab-and-slot joint with through tenon	207
7.3 Analytical moment-resisting model	209
7.3.1 Assumptions	209
7.3.2 Flowchart	210
7.3.3 Kinematics of the MTSJ-TT in bending	212
7.3.4 Characteristic lengths	215
7.3.5 Embedded volumes	219
7.3.6 Elasto-plastic moment-rotation relationship	222
7.4 Experimental study	224

Contents

7.4.1	Series of samples	224
7.4.2	Description of the bending test	224
7.4.3	Embedment parameters for the model	226
7.5	Results and discussion	227
7.5.1	Moment-rotation curves of MTSJ-TT	227
7.5.2	Failure modes	235
7.6	Conclusions	236
	Outcomes ⑤	237
	References	239
Conclusion		243
8 Conclusion		245
Appendices		249
A Simplified methodology for the calculation of MTSJ-TT in pure bending		251
A.1	Parameters	252
A.1.1	Geometry	252
A.1.2	Material properties	255
A.2	Semi-rigid moment-resisting behavior of MTSJ-TT	256
A.2.1	Kinematics in pure bending	256
A.2.2	Assumptions for simplification	257
A.2.3	Characteristic moment-rotation curve	257
A.2.4	Simplified formulas	258
A.3	Serviceability Limit States (SLS)	261
A.3.1	Limitation of the rotation angle	261
A.3.2	Elementary rotational stiffnesses (in N·m/°)	261
A.4	Ultimate Limit States (ULS)	262
A.5	Examples	262
A.5.1	Geometrical parameters	262
A.5.2	Material properties	263
A.5.3	Simplified formulas	263
B MTSJ Geometry Script		265
List of figures		269
List of tables		275
Curriculum Vitae		277

Introduction and State-of-the-Art



1 Introduction

1.1 Overview

Over the ages Carpentry required hand tool workers with high skills even in trigonometry and geometry. During the past period, CNC machines and Computer aided design brought semi-industrialization in the workshop. Initially dedicated to joinery for framing, timber CNC routers became available for machining panels. First step was computer integrated manufacturing of shear walls, roofs and floor elements. Then association of qualified carpenters and flexible systems contributed to the development of non standards architecture in Timber construction. To compete with others building materials, Timber producers developed new products as engineered wood panels. The main idea was to optimize wood delivery from logs and lighten the structures. Hence very efficient multi-layered systems appeared. Starting in their most simple forms as I-beams and box elements, thin panels can be imagined now as components of shells and spatial structures. A comfortable solution for connecting such panels remains unresolved. Usual fasteners where strength and slip model are well known are unfortunately non conform to European standard when thickness of panels is too small. In a other hand, adhesive bonding is really restrictive and achievement must be done in the workshop. Integral mechanical attachment when connection is directly integrated during the cutting could be a real improvement. It opens the field of applications and industrial equipment like polymorphic robots can join the challenge to go further. Obviously, the mechanical modeling of the behaviour of these wood-to-wood joints shall append their digital fabrication.

1.2 From handicraft to digital fabrication in timber construction

The first tools for carpenters appeared at the earliest known in the second millennium BC. But this was only in the 19th century with the Industrial Revolution that men have improved methods and work tools. Hand-tool-technology has been overlapped with machine-tool technology when the first modern-era power tools became possible [Sch07]. With the industrialization and the advent of powered machine, standardization and then mechanization led to a breakthrough in timber building technology. In the same period, consumer demand became more versatile. The combination of automation and customization replaced step by step the era of Mass production in many industrial domains. In order to improve conjointly productivity and adaptability, Information-tool-technology overlapped the two previous waves of hand-tool

and machine-tool technology. In this new environment starting after Second war, Numerical Control was developed in the late 1940s and early 1950s by John T. Parsons in collaboration with MIT (Massachusetts Institute of Technology). Accuracy and repeatability that Human operator could not achieve were now reached [Alb11]. In the early 1950s aeronautical companies could not simply automate machines without associating them with advanced design tools. In 1957 Dr Patrick Hanratty the father of Computer Aided Design and Manufacturing (CAD/CAM) commercialized for General Electric the first PROgram for Numerical Tooling Operations (PRONTO) [unk04]. In 1975, the first 2D CAD software CADAM was industrially used by Dassault. Two years later the same company put into service the first version of CATIA 3D CAD. The development of such software was possible because of a great technological leap in complex 3D surface modelling and curve (research works at Syracuse University, K.Vesprille, R.F. Risenfeld) [unk04].

Only in end of the 1970s, 5 axis CNC appeared in woodworking. Initially designed for engineering manufacturing, CNC machines were adapted to soft materials like wood which require higher machine speeds. In 1984 Hans Hundegger demonstrated facility for performing carpentry joints driven by a computer. He delivered the first joinery machine in 1985. Four years later CAD data was directly transfer to the machine controller. These joinery machines and their latest developments with several axis have favoured the revival of wood-to-wood joints mainly in the timber-frame construction. For better optimization of these High-Tech equipments, a direct link with CAD/CAM computer is strongly recommended. Although developed on the same basis than CAD/CAD software for Mechanical engineering Timber solutions were most often all-in-one solutions. Every operation from design to CNC instructions generation was managed by modules in one package. The major players of the domain are CADWORK, DDS, Dietrich's, hsbCAD, SEMA, Bocad [NN07]. The standard timber design software have shown their limits for solving complex geometries. Until 2013 none of these tools were able to deal with NURBS-surface and import it in their environment. Rhinoceros whose implementation started in the late 1990s was really helpful to join the digital chain within the projects. The challenge of simplifying NURBS-based geometry into files readable by CNC machines has been raised by few companies and research laboratories. They placed their expertise in parametric design and digital process into non-standard architecture. High technology as described above is now a reality for traditional carpenters. Initially multi-function bridges have been developed to automatize basic and repetitive tasks as cutting/nailing of shear walls. However, many producers currently offer advanced panel processing centres with 5 axis tooling path, multiple-fold tool changer and even automated turning tables for double-side cutting. Nowadays structural panels and CNC machines are available for panel-based structures in non-standard Timber Architecture. These new possibilities encouraged university's research groups to develop algorithm and methodology to discretize free-form structures into planar elements.

1.3 Freeform faceted plate structures

For less than fifteen years, many researchers work to simplify the construction of dual-curved complex geometry by planarization and digital fabrication. In order to subdivide doubly

curved surfaces with planar mesh, they proposed different forms of tessellation *.

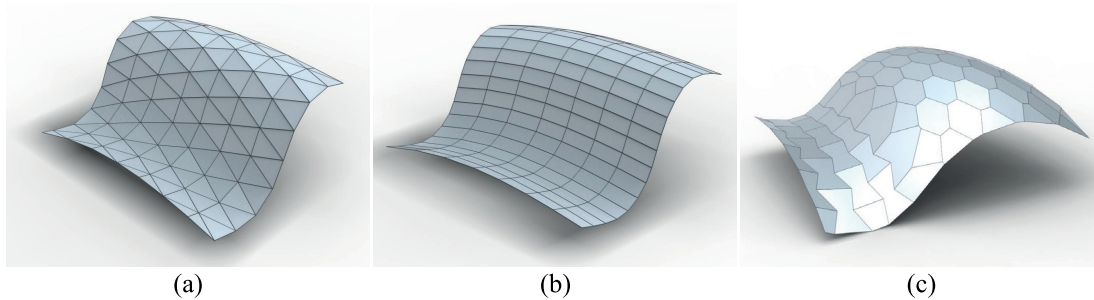


Figure 1.1 – Planar subdivision mesh : (a) triangular, (b) quadrangular, (c) polygonal [SWF10].

The first and most commonly adopted is the triangular mesh (Fig.1.1a). Any free-form shape can be quite easily achieved as the vertices can be freely moved without disturbing the mesh planarity. From a structural point of view, the triangular pattern when built from bars and articulated nodes is intrinsically stable. However, this leads to more complexity for design and assembly as a vertex (a node) is incident with six edges. When cutting triangle into flat panels, more waste are generated from rectangular commercial products [PEVW15, GSC⁺04]. It also needs more parts and weight to achieve a global structure. Hence the solution is economically less advantageous than other type of ornaments (quadrangular, hexagonal).

To overcome the aforementioned disadvantages, the quadrangular mesh is an alternative (Fig.1.1b). It is not really a free-form approach as it is generated from translational surface. A translational surface consists on a surface generated by translating any spatial curve along another random spatial curve. On the other hand, the quasi-rectangular plates makes it possible to optimize the use of the raw material during the cutting [PEVW15]. As mentioned by Glymph [GSC⁺04], the quadrangular tessellation is practical for glass structure. Plane elements similar in shape and size can be efficiently cut and the weight of the final structure is minimized compared with triangles. By using quadrangular pattern and conical mesh which allow offset, double-layered structures of developable surfaces can be built [LPW⁺06]. Quadrangular-patterned structure are commonly built from lattices frame with plate or diagonal element to make stable the movable elementary rectangular mesh. Structurally speaking, it then behaves as a triangulated structure. If the construction of the free-form structure is performed with flat panels, the connection at the edges must ensured the stability and the continuity of the shells. It becomes very challenging and expensive to achieve with standard product of the markets.

Inspired by Nature, discretizing a doubly curved surface into 3-valent ** plates has been the topics of many researchers in the last ten years. The resulting planar hexagonal mesh is very challenging in design (Fig.1.1c). The small number of incident edges requires to tessellate the surface with non convex elements, different in shape. The hexagonal pattern offers structural inherent performance but the meshes are more rigid and less eligible to

* A tessellation of a flat surface is the tiling of a plane using one or more geometric shapes, called tiles, with no overlaps and no gaps [SKM14].

** n -valency means that n -edges are incident per vertex or n -edges meet at the vertices.

planarization method as quad meshes. Among the planarization algorithm, adaption of Variational Shape Approximation (AVSA) [CSAD04], Tangent Plane Intersection (TPI) [Tro08] and Variational Tangent Plane Intersection (VTPI) [ZCHK13] can be cited. The most frequently

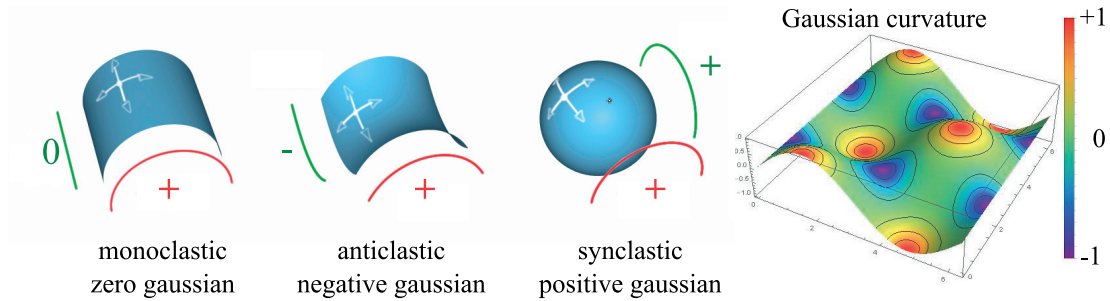


Figure 1.2 – Gaussian curvatures

implemented method is TPI as it is robust for both synclastic (positive Gaussian curvature) and anticlastic(negative Gaussian curvature) surfaces (see fig.??). However, when the Gaussian curvature approaches zero in the transition zones, the method produce invalid results and “manual” adjustments have to be done. As soon as the number of elements and manipulations increase, the setting of the planarization becomes impractical to adapt to the curvature changes. In the transition zone, the shape of the element deviates from the hexagonal pattern and its mesh of vertex valence three is disturbed. The advantage of the “pure plate” behavior is partially lost and bending-resisting connection are highly recommended.

1.4 Pure plate structures

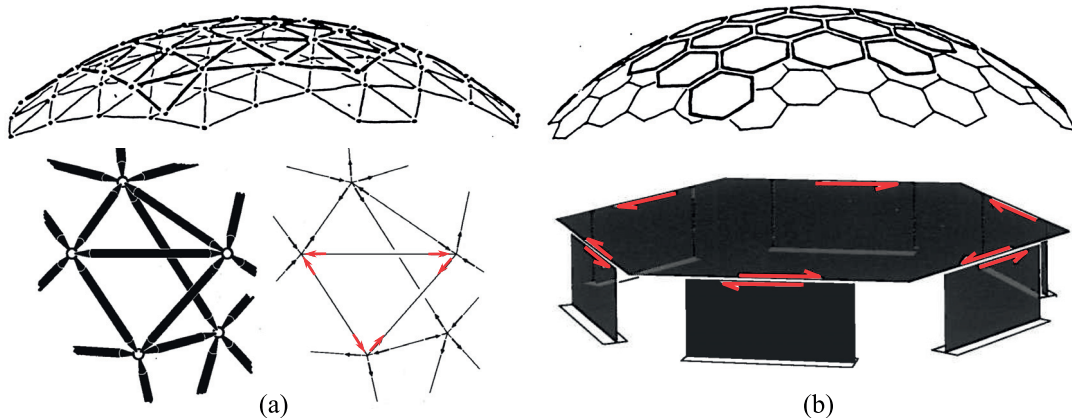


Figure 1.3 – Dual stable faceted structures : (a) triangular mesh with bars and nodes to carry load by tension and compression forces in the edges and the vertices of the geometry, (b) hexagonal mesh with plates to carry load by distributing in-plane forces in the plates and then transferring by shear along the plate edges [Wes84, Wes93].

The simplest planar discretizations with triangular(6-valent) or quad (4-valent) flat panels imply structural concerns. These topologies reveal alignment of edges which allows the freeform shell to largely deform under both dead and live loads. When using plates, if the

1.5. Edge connections for thin timber panels

connected edges are hinged, the structures are not kinematically stable anymore. It is even worst with quad mesh as the line of edges are along the principal curvature of the surface. Both tessellations require rigid connections to resist to the bending action.

Through its works on the plate-lattice dualism, Wester demonstrated that a trivalent polygonal mesh is, in general, a statically efficient solution to ensure the stability of a shell with only hinged connections at the plate edges [Wes84, Wes93]. The out of plane loads which create bending are taken via torsional restraint along each edge. Dually to a triangulated lattice structure which transfer tension and compression loads through bars and nodes, a pure plate system carries loads via in-plane stresses distributed in the plates and then transferred by shear along the plate edges. By this way, the discretized structures behave similarly to a continuous shell. Complementary information about pure plate structures can be found in the following references [Alm08, Bag10, MWK12].

As explained in the previous section, the trivalent mesh has also some limitations when applied to free-form structures with a really random shape in terms of Gaussian curvatures. The tested pure-plate structures proposed by the literature are usually of small size, close to a half sphere or not really submitted to live loads. Larger and more complex shells cannot be performed with only theoretically hinged connections. As concluded by Tannert [TMNM15], “Importantly, all previous studies conclude that for free-form geometries, fully rigid connections between panels are necessary to provide the required performance. Rigid connections at panel edges redistribute bending and load demands, minimize deflections and allow for greater spans and thinner panel sections. The ability to devise fully rigid panel edge connections or assemblies has therefore been given thorough consideration...”.

1.5 Edge connections for thin timber panels

Freeform timber plate structure is a rather new topic that emerged with the combined advent of engineered wood panels, digital fabrication and planarization algorithm. Connecting edge-to-edge timber plates in such structures is a big challenge when loads have to be transferred through the connection. Rigid or at least semi-rigid joints have to be achieved according to the regulation and the economic constraints. In timber, only gluing is considered as rigid but the implementation of curing is really sensitive to moisture and temperature conditions and can be only performed indoor in a climate controlled workshop. It is irreversible without damaging bonded parts and big structures need complementary mechanical joining on site. Mechanical joining is the most widely applied technology for joining timber elements into structures. It removes selected degrees of freedom (from 1 to 6) and allows load transfer in the corresponding directions. The transfer of stresses from parts to parts can be assumed by the geometry features (Integral Mechanical Attachment, IMA) or by additional parts (Mechanical Fastenings). But as soon as the panel thickness is below 8 times the diameter of the fastener (or 10 times for LVL), screwing or nailing directly in the edge ends are not conceivable [fSC08, VESL16]. So screwed connections without additional parts are extremely limited for thin panels.

An all-in-one joining with generating integral attachment during the cutting of panels is a very smart and efficient solution [RSMW14, Rob15]. The concept has been developed at IBOIS

Chapter 1. Introduction

for timber panels. It concerns 1-degree-of-freedom wood-to-wood connection without glue. This connection is a potential solution for joining thin wood panels into structures without bearing fasteners. CNC joining machines play a major role for developing this load-bearing and interlocking connector. 5-axis milling machines and 6/7-axis robotic systems have been already operated for developing this so-called shape-generator connection. Any kind of surfaces (plane, curved and/or ruled) can be intersected to form a curve on which the geometry of a Multiple Tab-and-Slot Joint (MTSJ) is automatically defined. It was applied for the first time on an actual building : Vidy theater in Lausanne Switzerland.

Automation of geometry and machining were experimented with success but resistance and stiffness still have to be predicted. Standards over the world are not proposing any suitable method for traditional wood-to-wood joinery. As shown in section 2.1 of the State-of-the Art, from a review of timber plate structures, very little research works emphasized models (mainly for strength, harder for stiffness). Based on an unique stable material (LVL Kerto-Q), the present work proposes an analytical model which from initial experimental investigation on semi-rigidity allows to predict the non-linear moment-resisting behavior of the through tenon (TT) variant of MTSJ.

References

- [Alb11] A. Albert. *Understanding CNC Routers - First Edition*. FPInnovations - Forintek Division, 2011.
- [Alm08] H. Almgaard. *Plate shell structures - statics and stability*. International Association for Shell and Spatial Structures, 2008.
- [Bag10] A. Bagger. *Plate shell structures of glass: Studies leading to guidelines for structural design*. PhD thesis, 2010.
- [CSAD04] D. Cohen-Steiner, P. Alliez, and M. Desbrun. Variational shape approximation. In *ACM SIGGRAPH 2004 Papers*, SIGGRAPH '04, pages 905–914, New York, NY, USA, 2004. ACM.
- [fSC08] European Committee for Standardization (CEN). *CEN-EN1995-1-1:2005+A1 - Eurocode 5: Design of timber structures - Part 1-1: General - Common rules and rules for buildings*. (CEN), Brussels, 2008.
- [GSC⁺04] J. Glymph, D. Shelden, C. Ceccato, J. Mussel, and H. Schober. A parametric strategy for free-form glass structures using quadrilateral planar facets. *Automation in Construction*, 13(2):187–202, 2004. Conference of the Association for Computer Aided Design in Architecture.
- [LPW⁺06] Y. Liu, H. Pottmann, J. Wallner, Y.-L. Yang, and W. Wang. Geometric modeling with conical meshes and developable surfaces. In *ACM SIGGRAPH 2006 Papers*, SIGGRAPH '06, pages 681–689, New York, NY, USA, 2006. ACM.
- [MWK12] R. La Magna, F. Waimer, and J. Knippers. Nature-inspired generation scheme for shell structures. *Proceedings of the International Symposium of the IASS-APCS Symposium, Seoul, South Korea, 2012*, 2012.
- [NN07] DesignToProduction NTNU and Innovasjon Norge. *Ten Timber Software Solutions*. www.ntnu.no/1-2-tre, www.designtoproduction.com, www.innovasjonorge, 2007.
- [PEVW15] H. Pottmann, M. Eigensatzl, A. Vaxman, and J. Wallner. Architectural geometry. *Computers and Graphics*, 47(C):145–164, apr 2015.
- [Rob15] C. Robeller. *Integral Mechanical Attachment for Timber Folded Plate Structures*. PhD thesis, Ecole Polytechnique Fédérale de Lausanne, 2015.
- [RSMW14] C. Robeller, A. Stitic, P. Mayencourt, and Y. Weinand. Interlocking folded plate - integrated mechanical attachment for structural wood panels. In *Advances in Architectural Geometry 2014*. Springer - submitted may 2014, 2014. <http://www.architecturalgeometry.org/aag14/>.
- [Sch07] C. Schindler. Information-tool-technology: Contemporary digital fabrication as part of a continuous development of process technology as illustrated

- with the example of timber construction. In *ACADIA Conference Expanding Bodies. Proceedings of the International Conference. Halifax Nova Scotia. (<http://www.designtoproduction.com/>)*, 2007.
- [SKM14] T. Schwinn, O. D. Krieg, and A. Menges. Behavioral strategies: Synthesizing design computation and robotic fabrication of lightweight timber plate structures. In *ACADIA 14: Design Agency, Proceedings of the 34th Annual Conference of the Association for Computer Aided Design in Architecture (ACADIA), Los Angeles, October 23-25, 2014*, pages 177–188, 2014.
- [SWF10] M. Stavric, A. Wiltsche, and C. Freißling. Geometric and aesthetic discretization of freeform surfaces. *25th national and 2nd International Scientific Conference, Conference Proceedings, monGeometrija2010, Beograd, Serbia*, 2010.
- [TMNM15] T. Tannert, A. Meyboom, O. Neumann, and I. Macdonald. Shell structures in wood, technical research & testing final report. Technical report, Centre for Advanced Wood Processing, Department of Wood Science, Department of Civil Engineering, and the School of Architecture and Landscape Architecture (SALA), 2015.
- [Tro08] C. Troche. Planar hexagonal meshes by tangent plane intersection. *Advances in Architectural Geometry*, 1(2):57–60, 2008.
- [unk04] unknown. CAD software - history of CAD/CAM. (<http://www.cadazz.com/cad-software-history.htm>), 2004.
- [VESL16] Finland VTT Expert Services Ltd. *Kerto-VTT-C-184-03-Certificate:2016 Kerto-S and Kerto-Q Structural Laminated Veneer Lumber, Certificate NO.184/03*. 2004, Updated 17.5.2016.
- [Wes84] T. Wester. *Structural Order in Space: The Plate-Lattice Dualism*. Plate Laboratory, Royal Academy of Arts, School of Architecture, 1984.
- [Wes93] T. Wester. *Efficient faceted surface structures*. Number vol.1. Thomas Telford, 1993.
- [ZCHK13] H. Zimmer, M. Campen, R. Herkrath, and L. Kobbelt. *Variational Tangent Plane Intersection for Planar Polygonal Meshing*, pages 319–332. Springer Vienna, Vienna, 2013.

2 State-of-the-Art

2.1 Angular Connections for Thin Structural Wood Panels

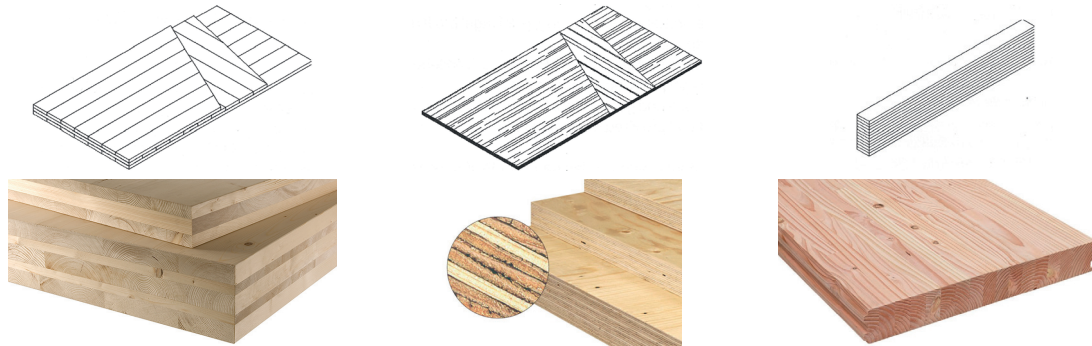
Freeform timber plate structures are essentially an arrangement, in space, of a vast array of flat panels, different in shape and size that interface with their respective neighbors through edge-to-edge angular connections.

In order to better understand the relationship between form, topology and connections in the field, a set of research projects and the few public buildings already constructed are presented in this thesis. The list is intended to be as exhaustive as possible to show the connections already explored and the gap that remains to be ready for solutions applicable in real buildings.

Before going further into innovative solutions, a catalog of more commonly encountered solutions based on additional parts with fasteners is provided in the next section. Some of them are used in the proposed inventory of pavilions, prototypes and buildings which meet the definition of “Timber plate structures”. The integral mechanical attachments (IMAs) developed at IBOIS are also part of the review, including the trough tenon variant (TT) of the multiple tab-and-slot joint (MTSJ), object of this thesis.

2.1.1 Angular connections review for engineered wood panels

The literature about wood-to-wood angular connections for plate structures is relatively poor while joints with metal fasteners are quite well documented. But, to follow the standard and be efficient, the thin panels are connected via one or more intermediate parts, made in wood or steel, and then fastened. In some situations, the panels must even be doubled. For thicker panels as Cross Laminated Timber (CLT), self-taping screws can sometimes be used. These various “conventional” connections are gathered in Fig.2.1 & 2.2.



CLT, LVL and GLULAM Panels

Angular connection review from Katharina Leitner

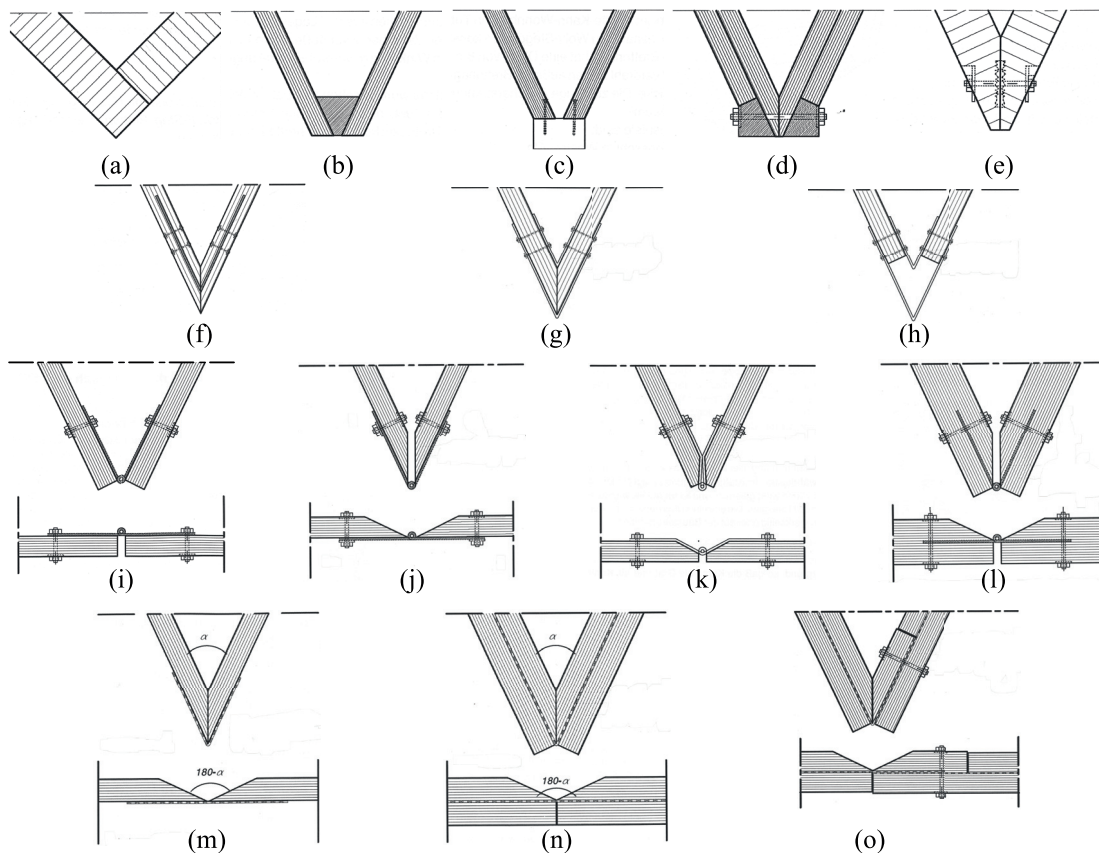


Figure 2.1 – Angular connections for CLT,LVL and Glulam panels [Lei04b]: (a) Glued butt joint, (b) Glued on a spacer, (c) Screwed on a cleat, (d) Two-layered, glued and bolted (acute corner from inside), (e) Miter joint with toothed plate connector, (f) Miter joint with internal metal sheet, (g) bolted to steel or Makrolon plates (one or two-sided arranged possible), (h) Square cut, bolted to Makrolon plates, (i) Square cut, connected by piano hinge, (j) Miter cut, connected by piano hinge, (k) Angled hinge with pivot point at the mid-plane of the panels, (l) Miter cut, connected by in-slot piano hinge, (m) Connected by one-sided diagonal textile as a fold, (n) Textile junction made of two wood-based materials with interleaved textile layer, (o) Textile junction made of two wood-based materials with interleaved textile layer, for on-site assembly.

2.1. Angular Connections for Thin Structural Wood Panels

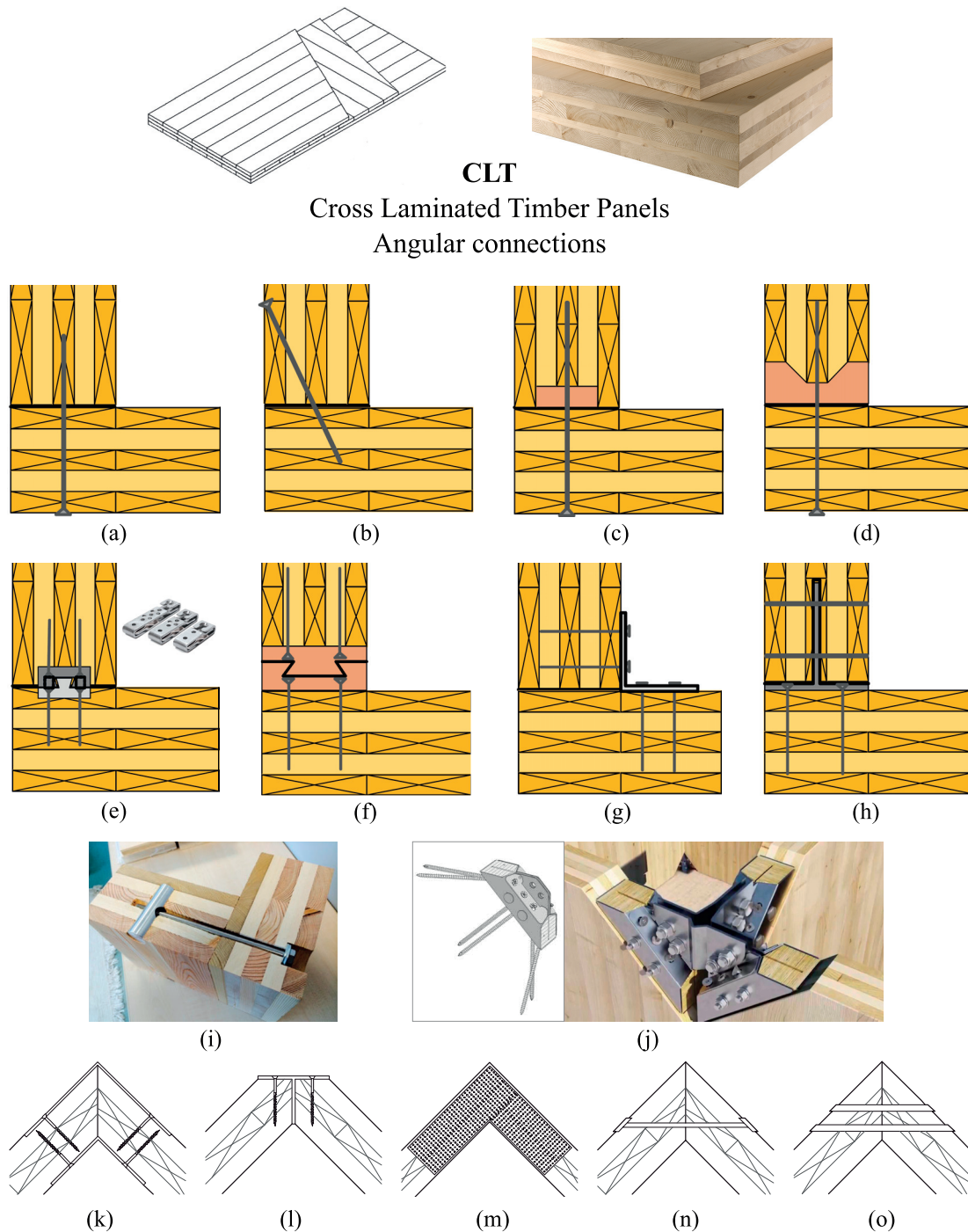


Figure 2.2 – Angular connections for CLT : **FP Innovations** [MM11] – (a) Self-tapping screws from the exterior , (b) Self-tapping screws driven at an angle (toe screwing), (c) Concealed wooden profile, (d) Edge protecting wooden profile, (e) KNAPP ® Gigant system, (f) Dovetail joint with wooden or steel profiles, (g) Interior metal bracket, (h) Concealed metal plate with self-drilling dowel, (i) **TEKNOWOOD** ® Fix fitting attachment, (j) **ROTHOBLOSS** ® X-RAD, **Tannert et al, for folded plates**[TMNM15] – (k) Miter joint with interior and exterior metal brackets, (l) Miter joints with steel T-bars, (m) toothed plates, (n) Bolted miter joint, (o) Miter joint with double glued-in rods.

2.1.2 Folded plate structures: Research projects

2004 - Textile junction, RWTH Aachen University, Germany [Lei04a, Lei04b]

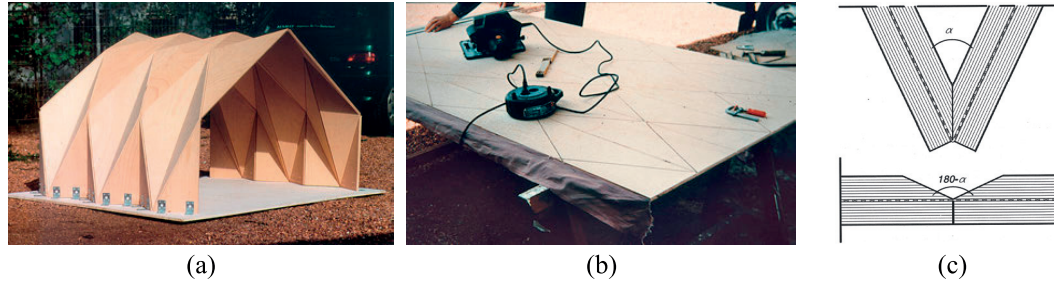


Figure 2.3 – Textile junction [Lei04a, Lei04b] : (a) 2m-span folded plate structure, (b) Three-layered material (6mm beech plywood/linen textile/6mm beech plywood), (c) Textile junction.

In 2004, in the context of her PhD thesis [Lei04b], Katharina Leitner experimented a innovative connection for timber folded plate structures. After a review on angular connections dedicated to CLT, LVL and Glulam panels (see section 2.1.1), she concluded that miter and but joint cannot be used for too thin engineered wood panels as LVL. Moreover, with additional connecting parts, the rendering of the fold was not up to the clear and sharp edges expected for this type of architecture. Instead, she proposed a textile junction in Fig.2.3c, acting as edge-to-edge hinge at the mid plane of laminated timber plates [Lei04a]. In fact, the solution was applied on a folded plate prototype with a yoshimura-type pattern made of triangular plates (see Fig.2.3a). This pseudo-cylindrical concave polyhedral shell was built with a span of 2m from a triple layered material of two 6mm-thick beech plywood panels with a linen textile limed in between (see Fig.2.3b). The deflection of the model at mid-span was 3mm (1/600 span) for a load of 2 kN/m². For full-scale projects, it was foreseen to use Kerto-Q LVL panels and polyester fabric.

Axial, shear and bending tests of the textile junction were performed considering the last mentioned materials. Here is just presented an overview of the bending results for an angular connection composed of two layers of 27mm-thick Kerto-Q LVL panels with a polyester fabric in between, glued all together with a Resorcinol glue Dynosol L-204 and a hardener H-627. Both LVL panel edges of the inner fold were milled at an oblique angle. It allowed the folding at the junction reinforced by the textile and the transfer of compression. Different samples were investigated, without or with (in Fig.2.4a) initial contact between the two internal panels of the folds (convex side). Bending forces were applied parallel or perpendicular to the grain of the outside panel veneers (in Fig.2.4b). Without initial contact in Fig.2.4c(left), a low stiffness is recorded when only polyester fabric and glue resist by tension to the closing of the fold. However, both in-parallel loaded configurations shown quite the same behavior when the wood-to-wood contact is established with an maximum load around 3000 N. The junction subjected to a transverse bending in Fig.2.4d demonstrated a lower stiffness and maximum load about 2000 N.

Fig.2.4e-h gathered the step by step failure modes. Just after the start of loading, the convex wood layer began to peel off (in Fig.2.4e). A plastic deformation in the closed edge created a

2.1. Angular Connections for Thin Structural Wood Panels

compressed surface, which took up the moment counterbalanced by the stretched textile. The tensile-stressed textile led to a plastic deformation of the adjoining corners (in Fig.2.4f). At this stage, the load bearing remained almost constant. The surface of pressure was thus reduced to a pressure point, the textile remained tensioned, creating a gap between the concave and convex LVL layers. The textile continued to fray at the fold between the two layers (in Fig.2.4g). For most of the tested glues, it was the end of the tests. By using PUR glue exclusively, the interior angle was completely close, approaching 0° between the two internal panels (in Fig.2.4h).

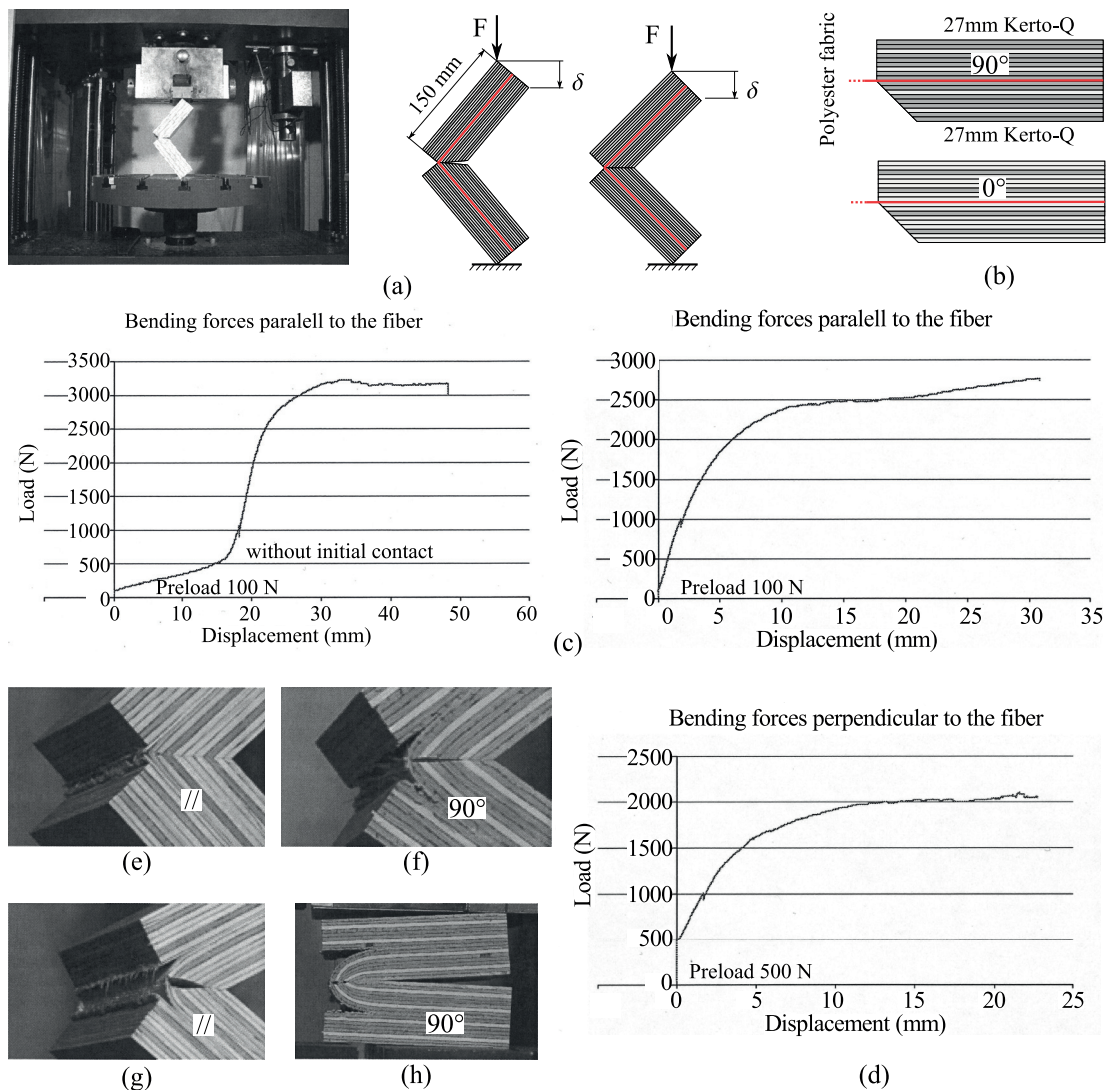


Figure 2.4 – Bending tests on textile junction [Lei04b] : (a) Test setup without(middle) or with(right) initial contact, (b) perpendicular to the grain(90° , top), parallel to the grain(0° , bottom), (c) 0° – Load-displacement curves without(left) or with(right) initial contact, (d) 90° – Load-displacement curves with initial contact, (e) Start of loading, (f) Surface pressure, (g) Almost point pressure, (h) Full closing with PUR glue.

2011 - Vacuumatics for rigid origami structure, University of Tokyo, Japan [TMI12]

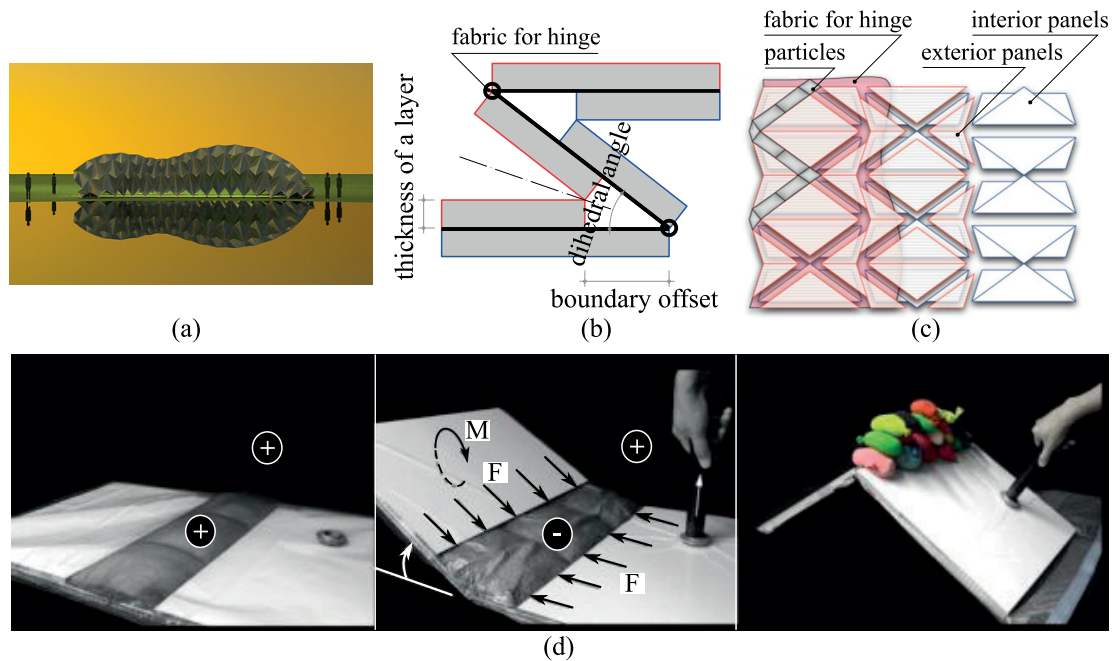


Figure 2.5 – (a) Example design of rigid origami structure, (b) Details of a fabric hinge [Tac10], (c) Vacuumatics arrangement of a waterbomb-patterned rigid origami, (d) Vacuum sequence : initial passive stage (left), folding by negative pressure at the valley(middle), load test at the ridge(right) [TMI12].

Tachi developed mathematical model and software to design rigid origami [Tac10]. A rigid origami is composed of polyhedral rigid and planar facets. From an initial pattern, by changing the boundary conditions, different configurations can be obtained and built with timber panels, for instance. This kind of structures can be temporary as they are foldable and developable at will. Fig.2.5a shows a such structure with a waterbomb pattern. This pattern suits for free-form structures composed with positive and negative curvatures. At the erection, the hinge connections, a fabric interleaved between two panels, ease the unfolding of the structure at any shape. The shape is however constrained by the fixed boundary points and the edge offset which set the maximal dihedral angle (see Fig.2.5). Once the structure is in place, the fold must be stiffened to maintain the shape and the stability [TMI12].

The edge stiffening was proposed here by using vacuum. The whole structures (external and internal layers, particles, and fabric hinge) was encompassed in a vacuum-tight membrane. The gap due to the offset was filled with particles packed in a porous material (see Fig.2.5c). The aggregate particles were placed at the concave side of the fold. By vacuum effect the air pressure in the enclosed particles space was below outside atmospheric pressure. The compressed particles at the concave side of the fold were counterbalanced by the taut membrane at the convex side. The densification of the aggregate particles by compression procured sufficient strength to resist self-weight and a certain level of loads on the whole structure. By setting the amount of vacuum, an initial small moment was applied at the concave side to

2.1. Angular Connections for Thin Structural Wood Panels

start the fold in the right direction, not easily achieved when the elements are at the flat state. When the final form was reached, vacuum was kept all along of the building life. The structure was thus dependent on the reliability of the vacuum system. An other drawback was the lack of data from a concept which was only tested empirically on two panels and never applied and a full-scale timber plate prototype until now.

2008 - Plywood Prototype 01, a regular herringbone pattern, EPFL-IBOIS, Switzerland [Bur10]

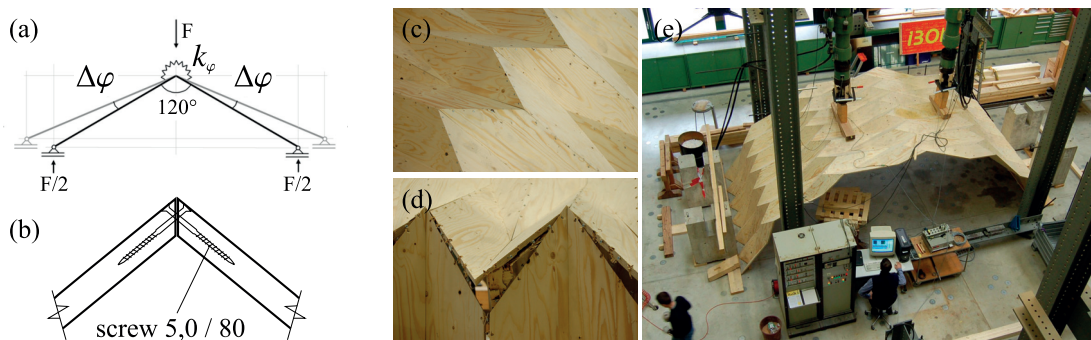


Figure 2.6 – Plywood Prototype 01 [Bur10] : (a) Stiffness model of connections, (b) self drilling screws, every 50mm in staggered rows, (c) Screwing pattern, (d) Failure of the connection, (e) Top view of the loading setup.

At the EPFL's laboratory of wood construction, Buri applied the principles of Origami fold art to architecture [BW08a, Bur10]. Among many studies of different patterns, a folded plate structure with a regular herringbone pattern was analyzed by experiments. This pattern offered the advantages of folded plate structures, plate and slab effect as well as good inertia with thin panels. The model was a complete barrel vault with 6.5m span x 2.4m high x 2.8m wide. As No CNC milling machine was available at this time, hand cut was achieved, using fabrication and assembly rigs. The vault was composed of 144 faces arranged in 12 arches of 12 trapezoids plates. The employed material was a 21mm-thick spruce plywood. The trapezoidal panels were connected by miter joints and self drilling screws $\phi 5\text{mm} \times 80\text{mm}$, arranged every 50mm in staggered rows at the mid-plane of the panels. The equivalent rotational spring stiffness ($K_{\varphi,ser} = 3.953 \cdot 10^6 \text{ N} \cdot \text{mm}/\text{rad}$) was defined by dedicated tests whose the setup is summarized in Fig.2.6a. For this local test, the joint length was 500mm for a total of 10 toe-screws. On the full model, the load was applied on two main-folds and three main-folds at the north side and south side, respectively. The failure of the structure started at 27 kN and came at the knee by tearing of the screws which did not respect the necessary edge distance. The bending stiffness determined experimentally was incorporated at the boundary nodes of the plate elements in the FEM calculation [HW08]. The numerical results showed a stiffer structure than the actual tested prototype. Both structural understanding of folded plate structures and jointing techniques have to be improved for further constructions.

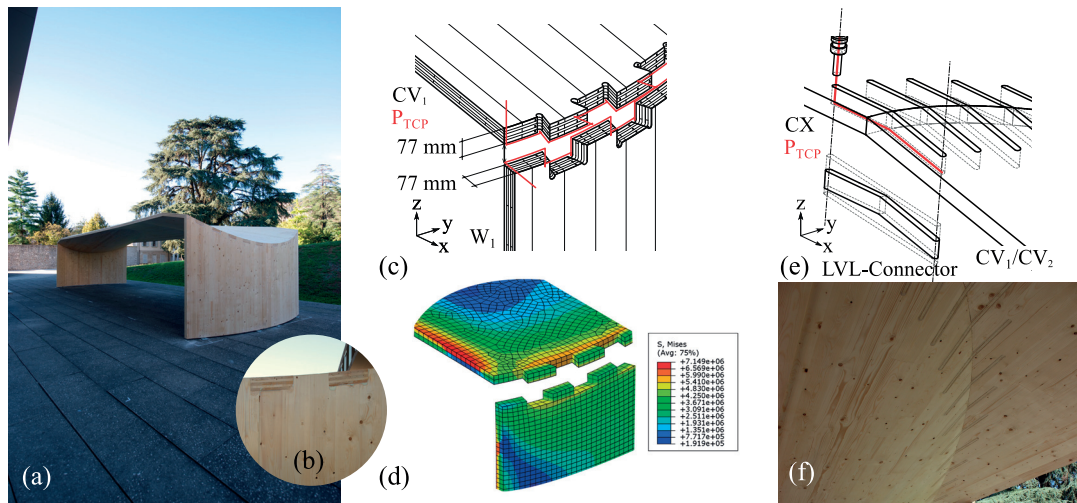


Figure 2.7 – 2013 - Curved-folded thin shell structure [RNW14] : (a) Exhibited at the Academy of Architecture in Mendrisio, Switzerland, (b) Details of glued dovetail, (c) CNC-cutting of dovetailed edge contour, (d) Local Von-Mises stress distribution of dovetail connection, (e) CNC-cutting of sewing connection, (f) Details of sewing connection.

2014 - Curved-folded thin shell structure, EPFL-IBOIS, Switzerland [RNW14]

At the occasion of an exhibition at the Academy of Architecture in Mendrisio (Switzerland), IBOIS, with the partnership of Merck, built a shell-shaped structure composed of CLT curved panels. The design was based on the curved-folding techniques described by Buri in his dissertation [Bur10]. The lightweight construction spanned over 13.5 m with an uniform thickness of only 77mm. The curvature of the panels increased the inertia of the structure despite the thinness of the panels. As wood is unfoldable at this thickness, the structural behavior of such structure depends on the performance of the edge-to-edge panel connections. The origami-inspired structure from Buri was combined with the re-interpretation of integral mechanical attachment (IMA, [Mes11]) developed by Robeller [RNW14]. Usually, IMAs provide both locator and connector features without adhesive or parts other than the wood panels themselves. But for this project, the knee connection between the curved feet and roof were achieved by gluing a series of single degree of freedom dovetail joints (1-DOF). The concave and convex curved elements of the roof were first assembled in the workshop by cross-layered spruce LVL connectors inserted in 30 open slots. The 30mm-wide rounded connectors were cut with a Hundegger K1 joinery machine and bond in position with a 1K-PUR adhesive. 7 axis CNC cutting robots were used to mill the integrated joints (dovetail and open slots) during the outline cutting of the curved panels. In that project, the 1-DOF joint gave advantages to align the feet with the roof and to increase the gluing surface. Stiff connections were secured where it should be.

2014 - Interlocking shell prototype, EPFL-IBOIS, Switzerland [RSMW14]

To extend and test the IMA without adhesive bonding, Robeller [RSMW14] declined the dovetail and Nejiri Arigate (Japanese) variants to doubly-curved timber folded plate shell

2.1. Angular Connections for Thin Structural Wood Panels

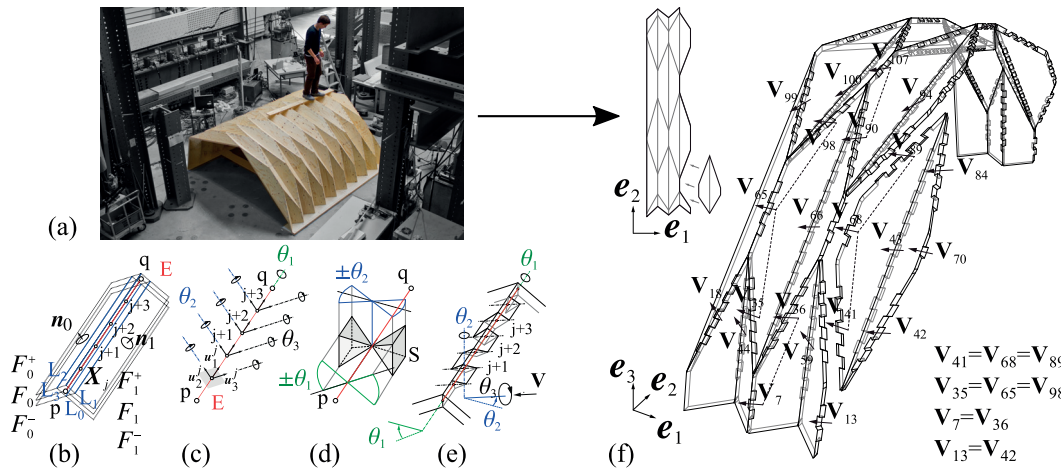


Figure 2.8 – 2014 - Interlocking shell prototype [RSMW14] : (a) Folded plate structure with double curvature, (b) Planes, lines and face centers of the joint, (c) Three Rotation angles of the initial frame ($\mathbf{u}_1, \mathbf{u}_2, \mathbf{u}_3$), (d) Insertion vector subset “S”, (e) Joint from Japanese techniques with $\theta_1 = \theta_2 = 20^\circ$, (f) Different subsets of insertion vectors for simultaneous assembly of multiple edges.

prototype in Fig.2.8a, digitally designed and fabricated in the EPFL’s workshop. The diamond-inspired hexagon pattern, derived from the Yoshimura origami technique, was chosen for a 3m span x 1.32m high x 2.8m wide barrel vault. As timber cannot be naturally fold at such thickness, integrated edgewise connections for thin timber panels with sufficient strength and stiffness were required.

This kind of joints offers a 1-DOF connection and blocks five over six of the usual DOF. The remaining degree of freedom is the translation along the direction of plate insertion. The connection can resist quite efficiently to shear forces parallel to the connected edges and to bending and traction by compressive contacts between the tab and the open slots.

In the present prototype, the assembly sequence and the geometry of the plates blocked their relative movement. It led to an interlocking effect on the plates. The joint geometry enabled the simultaneous assembly between panels consisting of multiple non-parallel edges (see Fig.2.8f). This assembly is possible only if all the assembly direction \mathbf{V} of each edges of a plate are parallel. The adjustment of \mathbf{V} was obtained by two successive rotations θ_1 and θ_2 (see Fig.2.8b-e). The last rotation θ_3 in Fig.2.8e enhanced the contact surface but did not influence the insertion direction. The chosen rotations defined a subset S of insertion vectors for each edge (see Fig.2.8d). By intersecting the different subsets, a common rotation window which fit with all edges was defined. The direction of \mathbf{V} was selected within this window. The choice of the insertion direction is obviously better if not aligned to the main direction of local forces.

Both FEM simulation and experimental tests were conducted. Shell elements were used for the FEM simulation. Transverse shear strain were neglected and completely rigid connections gave a deflection of 2.6mm in the elastic range for a top edge load of a 25kN. By testing, for the same load, 23mm of vertical deflection were measured at the center point and failure came at 45kN. Like conclude by Buri and Haasis [BW08b, HW08], the rigid assumption is

not appropriated to reflect the actual behavior of the structure. Some other benefits can be noticed. No adhesive bonding means rapid and easy assembly on site without any stringent permission as no specific conditions are required. The connection is more aesthetic and not more expensive than cold-formed steel plate and mechanical fasteners. The thickness of the panels can be reduced to a minimum (e.g. 21 mm) while direct screwing at the edges imposes by regulation a thickness of 60 mm for $\phi 5$ mm screws.

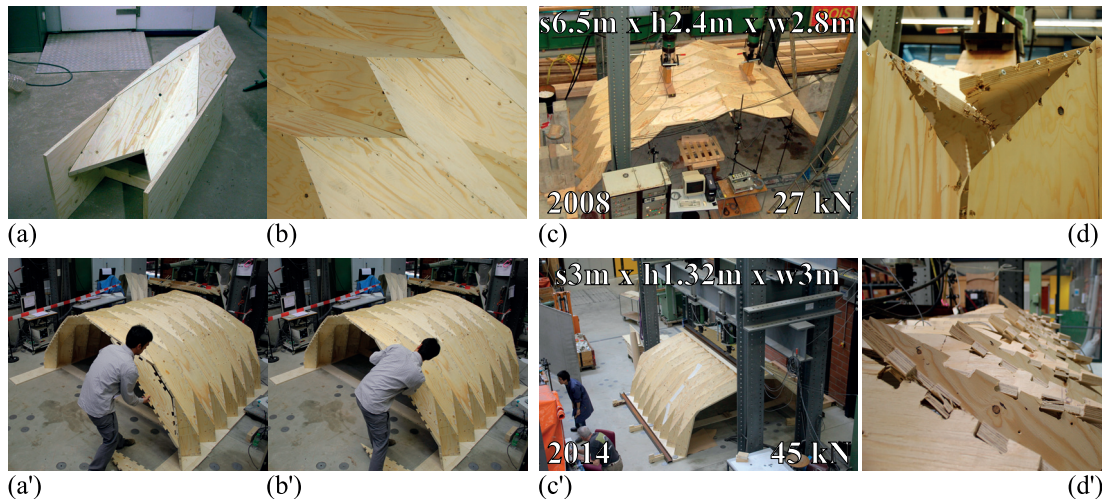


Figure 2.9 – IBOIS FPS evolution : (a) Assembly rig for screwing, (b) Connections by $\phi 5 \times 80$ mm self drilling screw, (c) Load test on herringbone patterned shell, (d) Failure by tearing of screws, (a'-b') Direct 3D insertion of 3 non-parallel-edged panel, (c') Load test on Yoshimura patterned shell and (d') Multiaxial failure of dovetail connections.

By comparison with the shell built by Buri in Fig.2.9a-d, Robeller proposed with his all-in-one joint (positioning, connecting and load-bearing) a possible in-space manual assembly without false-work, rigs and additional fasteners (see Fig.2.9a'-b'). The failure mode was influenced by the asymmetry of the double-curved shell, the connection were damaged and unlocked mainly on one side (see Fig.2.9c'-d').

2014 - Snap-fit joint and double layer, EPFL-IBOIS, Switzerland [RMW14]

At the ACADIA 14, Robeller [RMW14] demonstrated the possibility of assembly of folded plate structure with double layer. The double interlocked layers increased inertia by an offset of 110mm between the two thin panels. It is worth noting that the assembly sequence could be complex for folded plate structure including reverse fold. At the occasion, he introduced the closed slots and the trough snap-fit variant of the 1-DOF joint. A small-scale prototype served as a test platform of a direct interlocking of knee joints without any additional part (see Fig.2.10a-c). The clip function of the snap-fit removed the last degree of freedom after insertion and the connection can still be disassembled for recycling (see Fig.2.10d). The Kerto-Q 21mm panels were cut by 5-axis CNC milling. The prototype was not structurally tested.

2.1. Angular Connections for Thin Structural Wood Panels

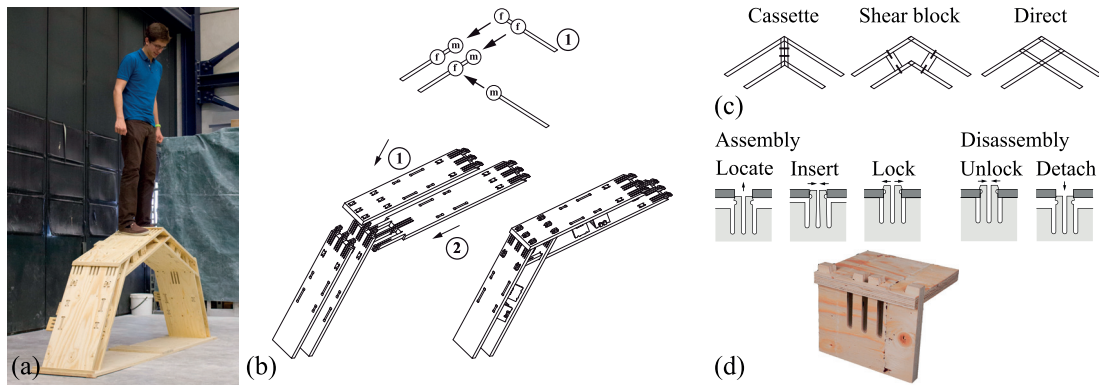


Figure 2.10 – 2014 - Snap-fit joint and double layer [RMW14] : (a) Double-layered folded plate prototype, (b) Assembly sequence of the two layers (f: female, m: male), (c) Direct assembly versus connections with additional parts, (d) Details of the timber snap-fit joint with assembly/disassembly steps

2016 - Bi-layered shell with a Miura-Ori pattern, EPFL-IBOIS, Switzerland [RW16]

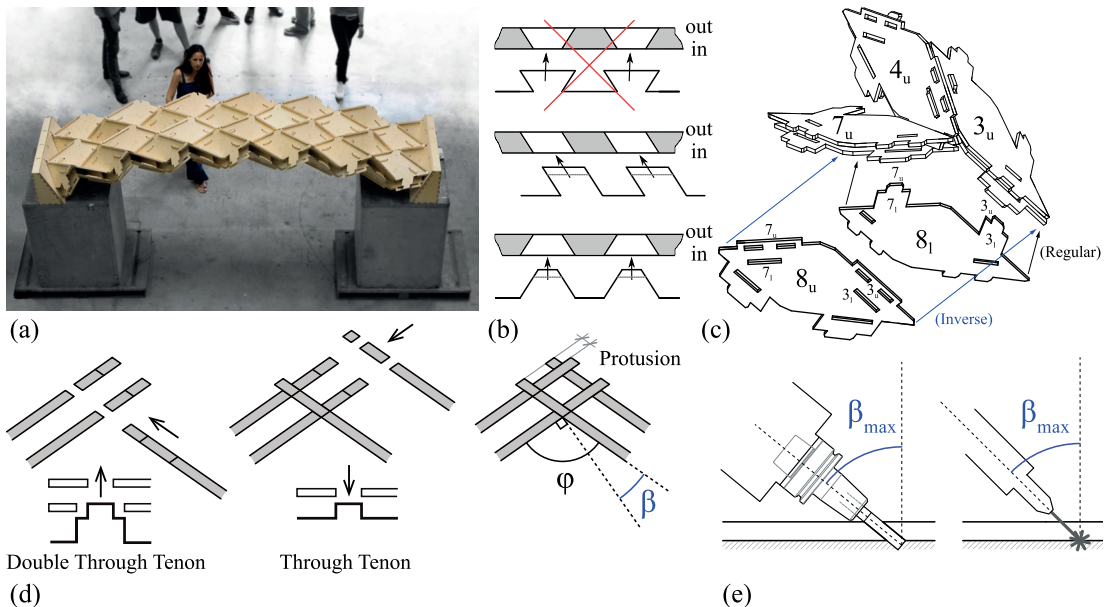


Figure 2.11 – 2016 - Doubly-curved shell with two layers and Miura-Ori pattern [RW16] : (a) Double-layered folded plate structure, (b) Assembly of the upper and the lower plates of a mountain fold, (c) 2-layer assembly, (d) Fabrication constraints : tool inclination angle β_{max}

Based on the previous attempt on double interlocked-layer structure, a single-low-curved prototype with 3.25m span for a total weight of 90 kg was developed 2 years later [RW16] (see Fig.2.11a). The distance between the layer plates was this time set at 48mm (4×panel thickness). 9-veneer birch plywood panels with 12mm-thickness were employed for the fabrication. It would correspond to a full-scale structure with 21mm-thick panels and layer spacing of 84mm.

The selected Miura-Ori pattern in contrast to Yoshimura type is suitable for roof of low cur-

vature. Before building this simplified prototype the design method was applied on a more complex small-scale model with doubly-curved freeform surfaces (Non-standard geometry). Different Methods are available for planarization of such smooth segmented plate shell : TPI, Triangulation, Origami inspired techniques using reflection planes and cross-section profiles or even mathematical models. Here, starting with a quad grid, the initial double-curved surface was deformed to get a Miura Ori pattern with curved element. The ShapeOp (optimizer under constraints [Dox15]) was used to flatten the individual elements and homogenize the dihedral angles. It allowed the milling of plywood by a CNC 5-axis machine.

As described earlier, the joint between plates has to transfer shear, traction and bending forces. A better performance, both in strength and stiffness was found with through tenon joints and closed slot at the cost of short protrusions beyond the jointed corners (in Fig.2.11c-d). The 1-DOF through tenon variant (TT) is composed of a tab and a closed slot. The section of the slot can be a parallelogram, a rectangle or a trapezoid. The section of the cut at the insertion face (in, Fig.2.11b) of the slotted plate is always equal or bigger than the one at the opposite face (out, Fig.2.11b). The height of the slot is equal or bigger than the thickness of the inserted panel. The assembly direction for a closed slot is constrained both by the internal upper, lower, left and right planes of the cut while the open one is constrained only by the lateral faces (left and right). The design of folded timber plate structures and their plate assembly is always compatible with such constraints. A dihedral angle φ of 90° is the best compromise for structural performance and fabrication constraint dependent on the maximal tool inclination β as shown in Fig.2.11d-e. The tool inclination β is the angle from the tool axis to the normal to the panels. Usually, the milling tools for head cutting are designed to work efficiently with their rotation axis perpendicular to the plate to be cut. For faceted free-form shell, curved and irregular, the dihedral angles of the plates will mostly be all different and not orthogonal. On a ridge, the lower plate (8_l , Fig.2.11c) intersect both counterparts (7 and 3, Fig.2.11c) with a double through tenon joint. The upper plate (8_u , Fig.2.11c) is inserted onto the tenons of its neighbors (7 and 3, Fig.2.11c) like a splice plate, which we call inverse assembly. On a valley, the upper plate is inserted with a double-tenon and the lower plate is inserted inversely. A direct connection of four plates which forms a fold with two layers has big advantages. It sets the desired spacing within the layers. Every new inserted plates block the previous ones and only the last pairs can be removed easily. This interlocking assembly process make useless additional connectors or adhesives.

The joints in a timber structures should be considered as semi-rigid. They influence the strength and the rigidity of the structures. Reducing gap and increasing a too low stiffness of joints are very challenging but essential to reduce possible larger deflection. Here each plate is interconnected with 8 plates instead of 4 for a single-layered structure with quadrilateral pattern. The stiffness of the overall structure is improved by a geometric and kinematic arrangement of the plates. The disassembly is only possible piecewise, in a reverse order. The TT joints act as toe-screws (or skew screws) installed opposite each other.

Two cycles of loading/unloading were repeated with maximum load of 0.84 kN corresponding to the self-weight of the structures. In both case, the maximum deflection was monitored just beyond 12mm.

2.1. Angular Connections for Thin Structural Wood Panels

2.1.3 Folded plate structures : Actual building

At the moment, very few buildings with FPS have been erected using the particular technology of timber folded plate structures.

2004 - Thannhausen Rehearsal Room - Germany (Regina Schineis, architect)

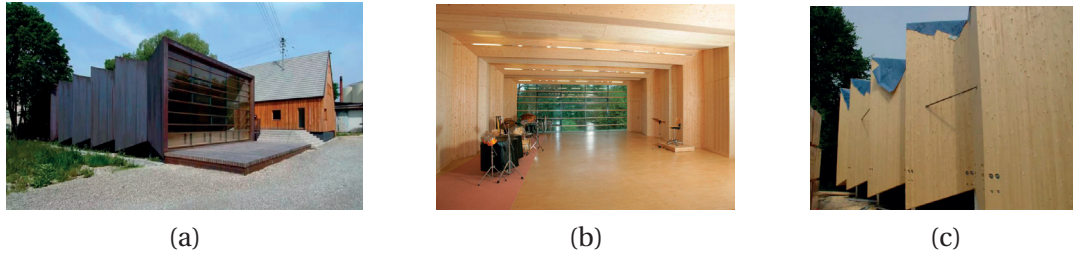


Figure 2.12 – Thannhausen Rehearsal Room [Sch04] : (a) External view, (b) Internal view (glued miter joint) and (c) Prefabricated V-walls, glued and screwed from outside

The Thannhausen Rehearsal Room presented in Fig.2.12a-b is probably one of the first timber folded plate structure built in Europe [Sch04, Rob15]. The use of glued-laminated wood panels made possible a span of 10m for a panel thickness of 100mm. The quadrilateral through-type structure is composed of prefabricated V-shape modules glued side-grain to side-grain at the miter junctions of the interior folds (visible from inside). The widths and dihedral angles were different between the plates (115° to 145° , for the dihedral angles) given a smooth irregular appearance. The final on-site jointing along the V-module free edges formed the exterior folds thanks to the glued and screwed miter cut (See Fig.2.12c). The connections between the V-modules of walls and roof were not glued but just mechanically fastened at the place of horizontal butt joints.

2008 - Chapel Saint Loup - Switzerland (Shell (Yves Weinand and Hani Buri) in association with Localarchitecture)

Approaching in size and shape the Thannhausen Rehearsal Room, the chapel in Fig.2.13a offered even more random folds [BW08c]. Foreseen as a temporary structure in 2008, the folded plate structure, which spans 9m, is still in operation. It was built from cross laminated timber panels (CLT) of 40mm thickness for the 28 wall elements and 60mm for the 14 roof elements (Fig.2.13b). The irregular shape was designed with different dihedral angles between the plates (104° to 130°). The variable angles were set by assembling simple miter joints with 2mm-thick splice steel-plate connectors. The steel-plates were connected by self-taping screws at the exterior side of the building (see Fig.2.13c).

2017 - Vidy theater, Lausanne - Switzerland (Yves Weinand architect)

To replace its obsolete marquee, the Theater of Vidy in Lausanne decided to build a new wooden auditorium with 250 seats (see Fig.2.14a-d). A removable and innovative structure was ecologically designed by the architect Yves Weinand. The parametric geometry and the joint generation were issued from a technology transfer with the EPFL's laboratory of wood construction. The project was also supported by the Wooden Action Plan of the Federal Office

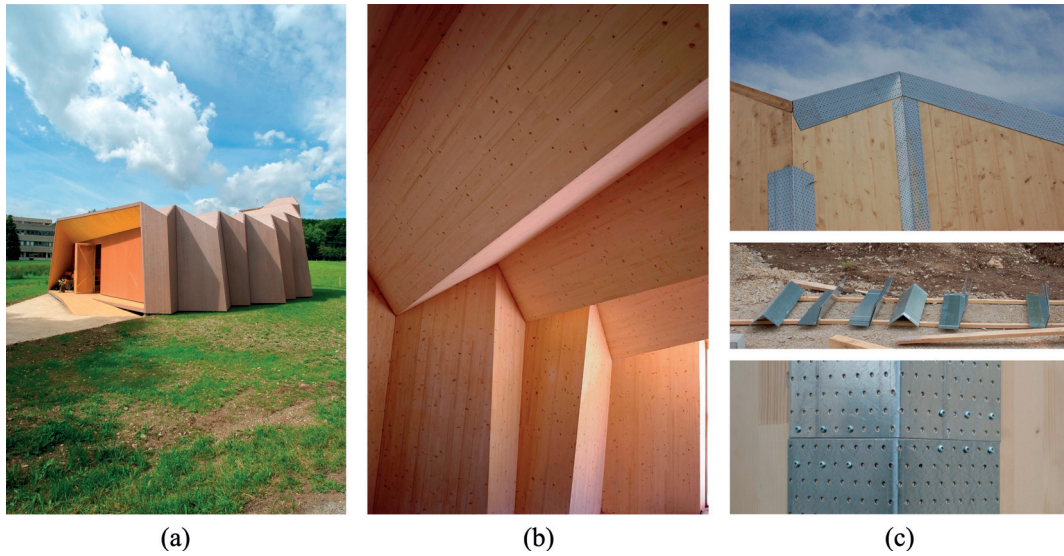


Figure 2.13 – Saint Loup Chapel [BW08b] : (a) External view, (b) Internal view and (c) Splice steel-plate connectors for interior and exterior folds

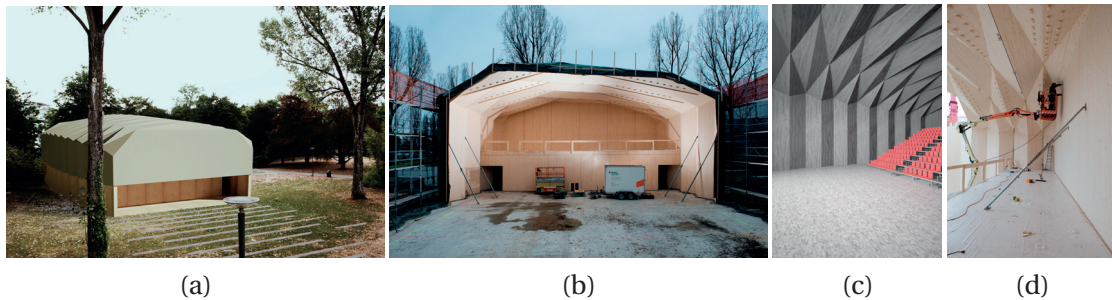


Figure 2.14 – Vidy theater [RGCW16] : (a) External view (render), (b) External view (actual), (c) Internal view (render) and (d) Internal view (actual)

for the Environment. This pavilion is 28m long by 20m wide with a scene of 14m opening by 11m depth. The height at the higher point is 10.5 m. This is the first large-scale double-layer folded plate timber structure currently in construction. It is an application of a research line at IBOIS which started with the Origami-inspired structures and continue now with the integral mechanical attachments and the double-layered segmental plate systems. 304 different panels and 456 edge-to-edge TT connections compose the structure. The CLT used for the fabrication was manufactured in Switzerland from 5 cross layers glued together, for a total thickness of 45mm. The irregular folded shape implied different dihedral angles with an average of 125° and a maximum of 138° .

The geometry of the structure was first represented by a single-layer surface which defined the wall and roof elements by identified and mapped rectangular and triangular polygons, respectively. A CAD plugins for Rhinoceros 5.0 was developed by Robeller [RGCW16] for this project. These software application gave opportunities to customize in real-time the following parameters : the thickness of the layer plates, the spacing between the two layers, the type of

2.1. Angular Connections for Thin Structural Wood Panels

edge connections, the insertion direction of panels and so on.

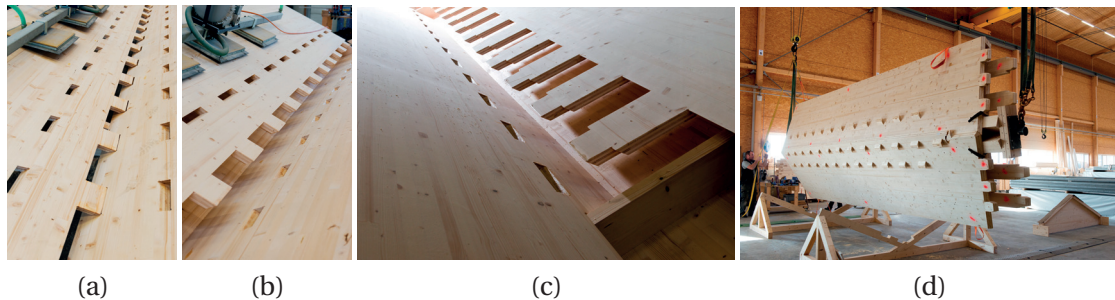


Figure 2.15 – Vidy theater prefab [RGCW16] : (a) External wall layers, (b) Internal wall layer 1, (c) Internal wall layer 2 and (d) Prefab wall

The CNC-code was generated automatically to produce each plate with the exact geometry of the connection at the contour, for the tabs, and inside the panels, for the slots. The walls, including the external cladding were preassembled layer by layer in the workshop. The sequence of tab-to-slot insertions is shown in Fig.2.15a-d. A similar prefab was done for the roof elements.



Figure 2.16 – Vidy theater erection [RGCW16] : (a) External wall with cladding, (b) pre-assembled roof element on a trailer, (c) Roof element lifting and (d) Insertion of wall tab into roof slots

The on-site assembly of the building was done bays by bays. The prefab walls were first put in place (in a). Then the 20m-long preassembled roofs came directly on a trailer (in b) and were, in one operation, lifted (in c) and inserted into the tabs of the wall (in d).

The TT variant was selected for its ability to sustain axial, shear and bending forces at the edges. Particularly at the junction between walls and roofs, the contact between the tab and the closed slots should make it possible to prevent as much as possible a possible rotation. The semi-rigidity complied to the requirements in the combination with the V-shape shaped walls. The top edges of these walls are significantly oblique with respect to the rotation axis at the knee, thus increasing by topological arrangement the bending stiffness.

The TT solution used for the theater was tested in bending by Gambero and Coanon [RGCW16, GRW17]. A first series of tests evaluated single layer samples with dihedral angle of 90° . Three materials were compared, 40mm-thick spruce CLT with three layers, 45mm-thick spruce CLT with five layers and 39mm-thick spruce Kerto-Q with thirteen layers. For all sample, both

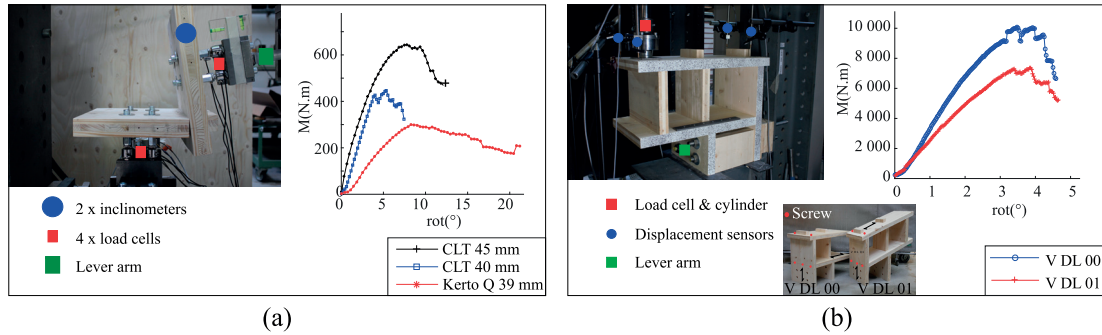


Figure 2.17 – Vidy theater joint tests [GRW17] : (a) Single layer folding test, (b) double-layer bending tests

tab and slot lengths were 150 mm with a start and an end length of 75 mm. The tab flank inclinations were set to 0° or 15° . One screw was added (or not) at each side of the tab. The measured elastic stiffness for CLT did not differ so much between the different configuration. An average value of $125 \text{ N}\cdot\text{m}/^\circ$ was obtained. But for 39mm-thick Kerto-Q, the stiffness was much lower as the value was $51 \text{ N}\cdot\text{m}/^\circ$.

A second series evaluated the double layer sample with dihedral angles of 90° or 110° between the 40mm-thick spruce CLT panels. The double layer was connected by an interlocked TT with additional screws on both sides of the tab. The elastic stiffness of $4004 \text{ N}\cdot\text{m}/^\circ$ for 90° decreased to $2520 \text{ N}\cdot\text{m}/^\circ$ for 110° . It shown that the dihedral angle values had a big influence on the stiffness. The double-layer connection offered a really higher stiffness than the single layer connection. A large part of the improvement came from the number of tab-slot contacts in action and the larger inertia of the bi-layered structure.

2.1.4 Free-form timber plate structures: Research projects

2010–2012 - Non-Standard architecture using planar ornaments and sewed joints, Institute of Architecture and Media, Faculty of Architecture, TU Graz, Austria [SMB10, SDWM12, Wil12]

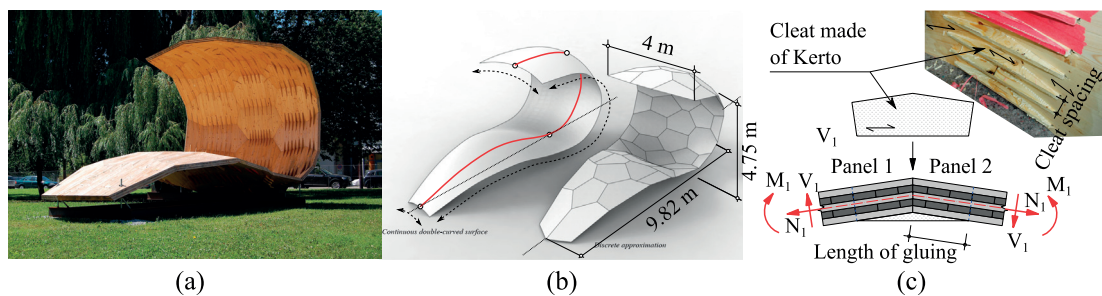


Figure 2.18 – 2010–2012 - Kobra structure [SMB10, SDWM12, Wil12] : (a) Self-supported timber plate structure, (b) Continuous double-curved surface and discrete approximation with planar ornaments, (c) Detail of the sewing joint and load transfer.

A free-form timber plate prototype, whose nickname “Kobra” evokes the shape of the snake, was built at the TU Graz Faculty of Architecture. It was the first self-supporting structure built

2.1. Angular Connections for Thin Structural Wood Panels

with wood-to-wood joint which also resists tensile forces. The overall size was 9.82 m long x 4 m wide x 4.75 m high. It was constituted of fifty-one 95mm-spruce-CLT panels between 1.0 and 2.5 m long. The double-curved surface of the structure mixed positive and negative curvature which influences drastically the ornament pattern. The discrete approximation by TPI techniques finally resulted in planar pentagons, hexagons, heptagons and octagons for the topology of the panels. The constraints for the full scale prototype pattern were the size for transportation and fabrication issues, the number, the topology and the thickness of the panels. The ornament pattern was also governed by the grain direction of the engineered wood panels and the geometry of the sewing connections. The main objective was to combine polygonal panels and joint orientation in order to maintain a certain continuity of the fibers over a structure made of discrete elements. The load path was adjusted to reduce transverse tension to grain which are really problematic for wood material.

The sewing joint connects the panels by wood stitches made of wedge-cut Kerto-S cleat. The cleats are inserted and glued into slots with inclined flanks numerically cut at the edges of the neighboring panels. The inclined flanks contribute to a tight contact (maximum clearance of 0.3 mm) that requires the one component polyurethane glue. A two component cast resin would have procured larger clearance tolerance, up to 4 mm, but its fluidity made unpractical the implementation. For the same reason, the plates were cut with a five axis router, more accurate and less sensitive to spindle vibrations than robots when their arm are extended, at the work space limits, to mill the largest plates. This innovative glued connection offered a rigid solution to bear axial, shear forces and bending moments. It was tested in different configurations to check the shear and bending strength. The following parameters of the connectors were considered for shear : geometry, used bonding adhesive, position and insertion direction. For bending, the main concerns were the load bearing capacity both of the miter joint and the cleats located off-axis of the grain and the influence of insertion direction (top-down or bottom-up). Both directions of insertion gave similar results. The cleats dimensioning were also successfully qualified, as single element, by bending and tensile tests. The sewing connection tests shown promising capacity (65% to 70% of that can be absorbed by the panel itself).

This multiple-constraint optimization problem was addressed by using a parametric CAD system with its algorithm modeling and scripting tools (Rhinoceros + Grasshopper). The parametric model allowed, in addition to a dynamic modification of the form and the ornamental pattern, the integration of the numerical structural data. These data, collected from an external finite element modeling software, summarized principally how to orient the grain of the outer layers of the panels with respect to each other, the thickness of the panels and the configuration of the sewed joints. The number of joint cleats, their spacings and their maximum deviation from the load path were defined according to the stress calculations at the connected edges. This project adopted the principles of concurrent and reverse engineering where information can go dynamically in both direction, CAD to FEM or FEM to CAD.

One other big challenge was the assembly of such self-supported structure. As long as the constructive system, composed of polygonal CLT-plates and glued joints, was not fully assembled, a very accurate falsework was necessary to fulfill the geometric and jointing requirements (see

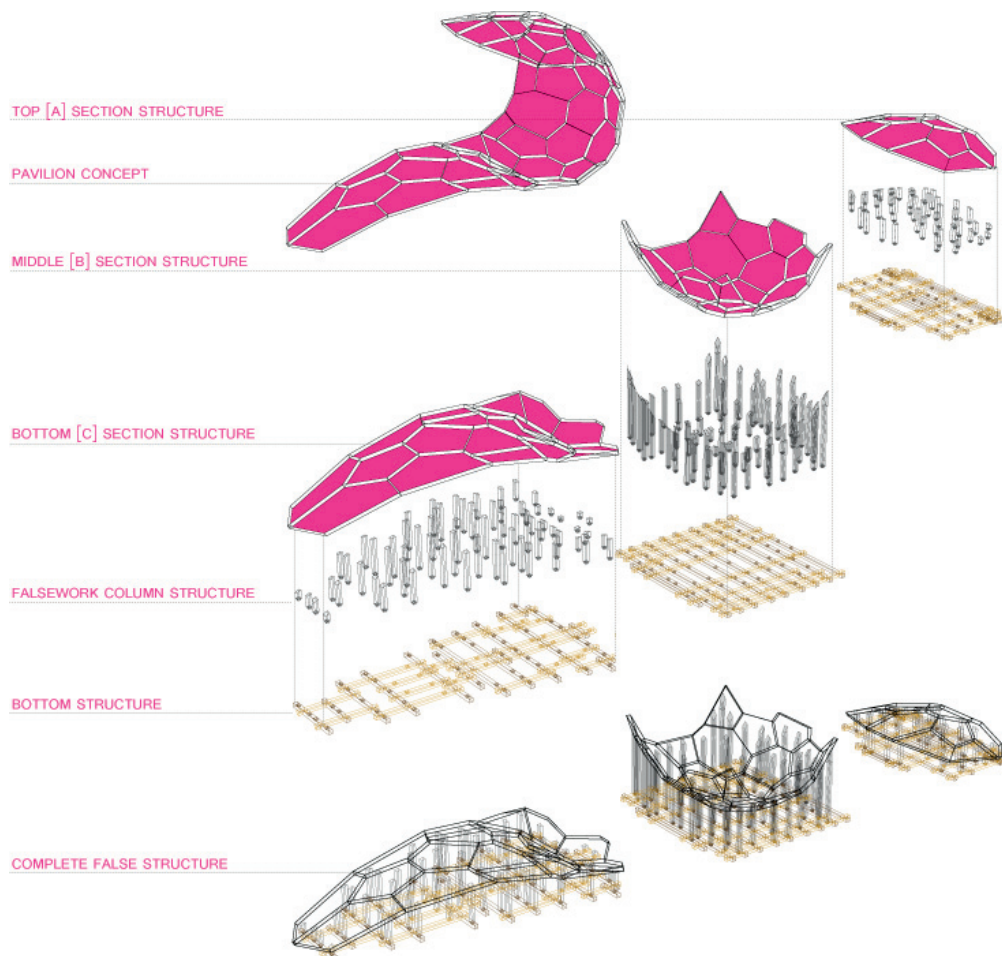


Figure 2.19 – Falsework for the Kobra structure (copyright IAM - TUGraz 2010).

Fig.2.19). The falsework was designed with the same parametric tool than the structure itself. At each step of the assembly process, the as-built spatial positions of the plates were checked by a 3D coordinate measuring system and compared with the virtual model.

2011 - The ICD/ITKE Research Pavilion, University of Stuttgart, Germany [MWK12, SKM12]

In 2011, in the context of a collaborative project between the Institute for Computational Design (ICD) and the Institute of Building Structures and Structural Design (ITKE) at the University of Stuttgart, a pavilion was built and erected (see Fig.2.20a). The design was inspired by Nature and especially by the biological principles of the sea urchin's protective shell. The different plated elements which composed this envelope have scalable calcite protrusions at the outline. The geometry of these protrusions are similar to finger joints and it can evolve with the growth of the echinoderm.

More than 850 geometrically different components and 100 000 finger joints were fabricated by a robotic cell whose the CNC code was automatically generated from the digital parametric model. It represents 2m^3 of wood, only 1% of the living space of the pavilion itself. It is also one of the big advantages of lightweight structures made with timber. The employed material

2.1. Angular Connections for Thin Structural Wood Panels

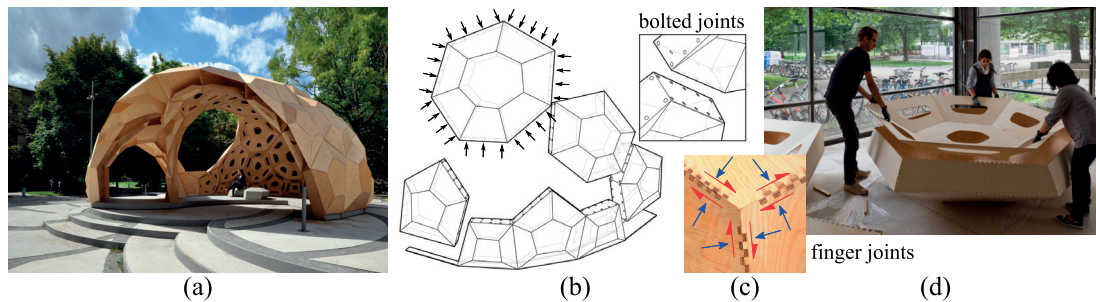


Figure 2.20 – 2011 - The ICD/ITKE Research Pavilion : (a) Pavillion inspired by sea urchin's plate morphology, (b) Assembly of the cell modules by bolts (c) 3-valent plate structures with in-plane forces and shear along the glued finger-joints (d) Pre-assembly of cells by gluing the finger joints.

was a birch plywood with a thickness of 6.5 mm. The pavilion of 4.3m height covered an ovoid-shaped surface of 10 meters by 9 meters.

The segmented structure is composed of prefabricated bi-layered hexagonal thin-paneled boxes(cells) which are, in a second step, assembled and bolted on site. For both steps of achievement, the trivalent strategy, where only three edges meet at each node, was adopted. The plates inside the cells are located and fixed relative to each other by finger joints, glued in the workshop(see Fig.2.20d). The finger joints were employed as locator feature and proposed a larger surface of gluing along the edges. The remaining three degrees of freedom were finally removed by gluing. The internal connection in the cells was considered as rigid. The resulting Y-vertices between the cells made the structure intrinsically stable without requiring special moment-resisting connections at the edges. The so-called pure plate behavior promoted the axial and shear in-plane forces (see Fig.2.20c). Hinges could be sufficient as connecting element between the cells. The face-to-face contact of the vertical plates of the double-layered cells, secured by bolts, also improved the stability of the structure by offering a vault effect (see Fig.2.20b).

2013 - A timber plate funicular shell, Ramboll Computational Design, London, UK [HL13]

Ramboll Computational Design (RCD) designed the TRADA Pavilion, a doubly curved compressive shell made from 152 unique flat timber panels, 900 stainless steel hinges and 3600 bolts. It served as a temporary trade fair stand. It was fully demountable and transportable. It could be packed flat on only two 2.4m×1.2m×0.9m palettes. 4 people were needed to erect the pavilion in one day. The implantation required only the marking on the ground of the leg locations. Neither formwork nor falsework were necessary at this scale. During the time of assembly, the legs were held alone by the fixation in feet before to be joined with the rest of the structure. The shell covered 8m by 6m and is 4m tall.

In order to get a funicular compression-only shell with no bending under self-weight, a structural form finding using zero-length springs with dynamic nodal masses was carried out. The form-finding algorithm started from an initial hexagonal zero-length spring system (in Fig.2.21a, left). The 8m×6m hexagonal network was connected by nodes where 3 springs met

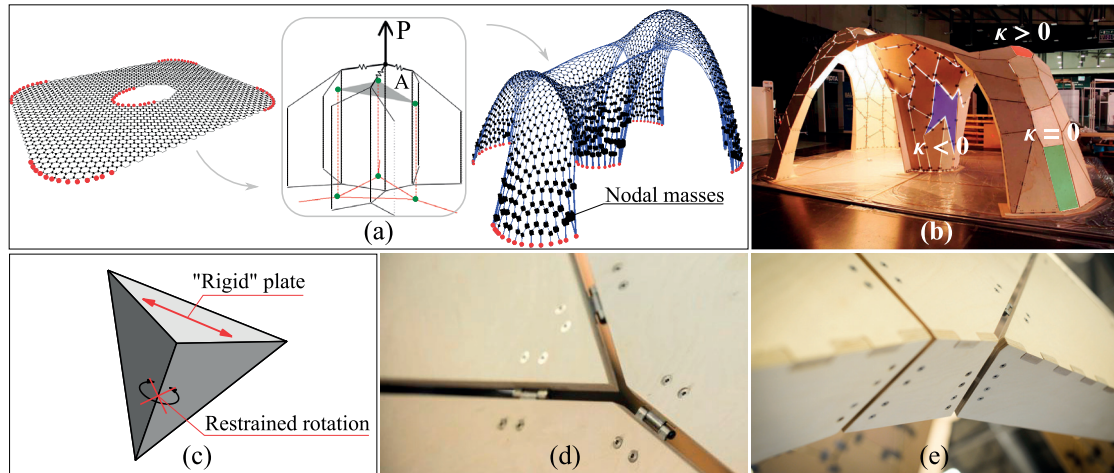


Figure 2.21 – 2013 - A timber plate funicular shell [HL13] : (a) Zero-length spring system, (b) Gaussian curvatures, (c) Restrained rotation, (d) Details of hinges, (e) Edge reinforcement

at a pinned connection. To tend towards a continuous surface shell, the lumped nodal masses were evaluated through the local area. The thickness of the shell was considered constant. The local area was calculated from the triangular surface which represents the hexagonal mesh dual of the neighboring hexagons. As the structure was supposed to be employed indoors, self-weight was the dominant load and nodal masses applied perpendicular to the ground plane (see Fig.2.21a, middle). The equilibrium between the spring forces and the vertical nodal forces was solved by dynamic relaxation method. By dynamically adjusting the spring stiffnesses, the gravitational constant and the boundary conditions, architects and engineers changed the shape until they reached the required geometry. The main requirements were to get a sort of a hollow column in the middle of the shell, for public access with enough headroom and a sufficient amount of double curvature to prevent buckling at the four corner legs (in Fig.2.21a, right).

At this stage, the geometry made of curved and deformed hexagonal mesh was discretized into planar elements. These planar elements were thus produced from flat cross-layered panels which resist well to tensile and compressive forces. The Variational Shape Approximation (VSA) method, adapted to architecture, was run to perform a polygonal discretization with only trivalent nodes. From a target number of plates decided by the designer, the method optimized the shape and the arrangement of the elements to minimize the deviation from the initial doubly-curved funicular shell surface. Smaller is the deviation, smaller is the risk of emergence of parasitic bending moments into the structure. The optimization was also focused on other topics like the assembly time, the fabrication costs and the aesthetic of the pattern. The appearance was typically governed by the panel shapes which are dictated by the Gaussian curvature of the surface (e.g. in Fig.2.21b, positive at the top dome and the panels are hexagonal and convex, zero at the quasi-cylindrical legs and the panels are rectangular, negative in the central hollow column and the panels are bow-tie-shaped).

Another advantage of the resulting hexagonal 3-valent topology was the torsional restraint it imposed to the edges. If two of the three plates in Fig.2.21c want to rotate about their shared

2.1. Angular Connections for Thin Structural Wood Panels

edge, they are blocked by the third one which maintains fixed the common edges it has with both plates. The flat plates were cut on 3-axis CNC machine from 15mm-thick fire-treated birch plywood. No bespoke and expensive connections were necessary for the assembly as M4-bolted standard stainless steel hinges suit with the trivalent topology of the discrete shell (in Fig.2.21d). The hinged connection indifferently adapted to positive and negative Gaussian curvatures. The free edges at the public entrances, which are insufficiently restrained and sensitive to buckling were reinforced with vertical plate stiffeners to ensure the stability (see Fig.2.21e). Like many others, RCD implemented its own C# plugins for Rhinoceros to manage the form-finding, planar discretization and fabrication. The construction principle was never validated at large scale with more critical external loads.

2016 - A double-layered timber plate shell, inspired by Dieste's Gaussian vault, EPFL-IBOIS, Switzerland [RKD⁺16]

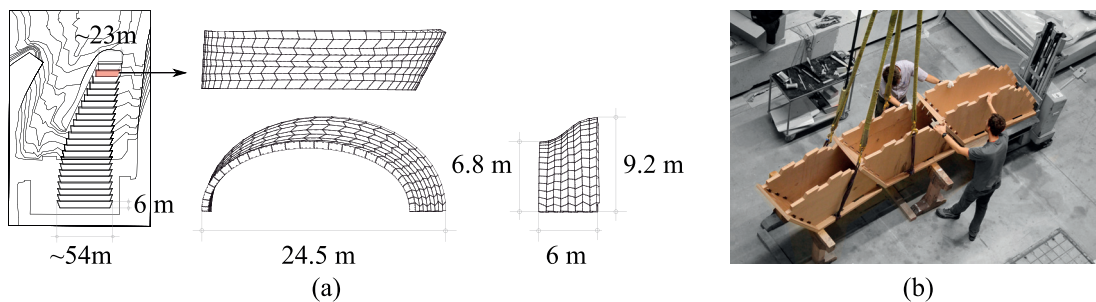


Figure 2.22 – 2016 - A double-layered timber plate shell [RKD⁺16] : (a) Full-scale project, (b) Full-scale mockup of 40mm Beech-LVL interconnected boxes.

This research work [RKD⁺16] was initiated in the context of an actual project to build a timber prefabrication facility (see layout and vault details in Fig.2.22a). It occupies an area of 5800 m². It consists of 23 juxtaposed double-curved shells inspired by the Gaussian vault masonry structure from the architect-engineer Eladio Dieste. The shells are constituted of two layers of relatively thin plates, made with 40mm-beech LVL panels. A mockup is shown in Fig.2.22b. The largest vault shells is segmented in 8×37 pieces for a total width of 6m and a span of 53.7m. The smallest one is segmented in 8×27 pieces for a span of 22.5m. The common height for all is 9 m. The 4 first meters from the floor are almost vertically aligned, thereby reducing the horizontal forces at the feet of the vaults.

A prototype (span 7.1m×width 1.75m×height 0.7-1.2m) was exhibited at AAG 2016 (see Fig.2.23a). It was built to validate the geometry, the digital fabrication, the assembly and the load transfer by jointing techniques which can be described as follows. Fig.2.23b details the internal assembly of an open box and the interconnection between the box modules. Each segment is constituted of a box with two open vertical faces. The upper and lower plates L_1 and L_2 of the box are spaced by the vertical side and end plates, W_0 and W_1 , respectively. These vertical plates set a constant distance between the layer and work as block shears in the overall behavior of the structure. Each box shares a vertical plates with its neighboring segments. Between the vertical plates, DJ variant with open slots are used. The absence

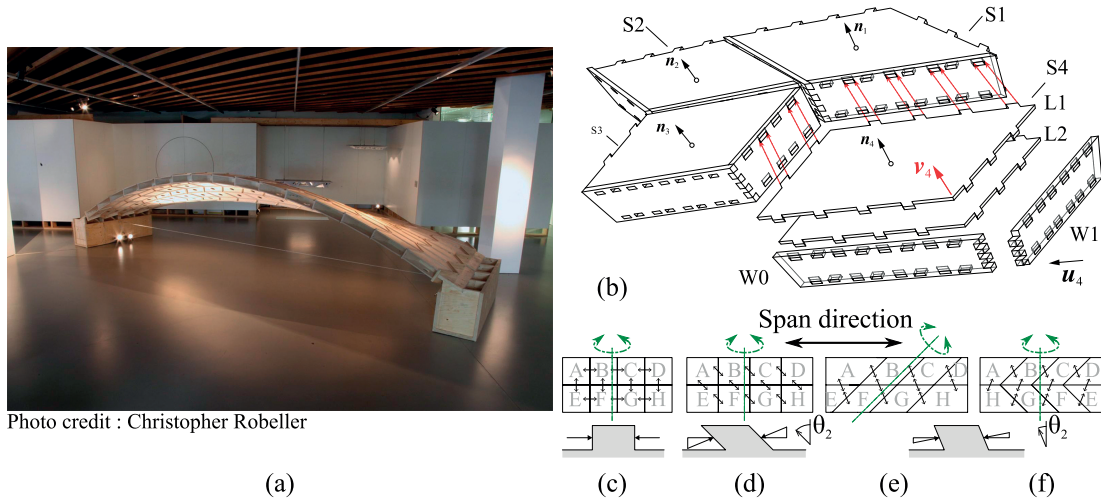


Photo credit : Christopher Robeller

Figure 2.23 – 2016 - A double-layered timber plate shell [RKD⁺16] : (a) 15mm birch plywood prototype, (b) Internal and external assembly of boxed segments, (c) Rectangular boxes with tabs perpendicular to the edges, (d) Rectangular boxes with parallel tabs, (e) rhombus-shaped boxes with parallel tabs, (f) rhombus-shaped boxes with parallel tabs, symmetrically arranged between row.

of protrusions ensures a contact without gap between the boxed segments. The connection between boxes which must transfer loads and participate to the rigidity of the structure along and across the span were achieved by TT connections and closed slots. They demonstrated their ability to withstand axial, shear and bending forces while also providing a sufficient stiffness. Both connections are 1-DOF joints but the TT variant provides bending strength and rigidity which are necessary to stabilize the segmented vault. The bending stiffness of each overall vault can also be improved by both pattern modification and joint orientation. In the first case (Fig.2.23c), only the moment-resisting effect of the connection can help. The rotation of tabs cause an oblique torsional effect across the span (Fig.2.23d). In Fig.2.23e, the torsional effect will be more global. The θ_2 angle of the tab can be reduced and the fabrication less constrained. Finally, the herringbone pattern rigidifies geometrically the structure against bending along the span. The end faces are not anymore parallel to the rotation axis (in green) and the oblique orientations of the tabs are symmetrically distributed perpendicular to this rotation axis, avoiding global torsion. On the external layers of the shells, the tab of L_1 and L_2 go directly trough every two slots W_0 and W_1 in contact with the edges of the neighboring plates. The compressive loads are thus transferred plate to plate, by direct contact in the main direction of the panel strength.

2.1.5 Free-form timber plate structures: Actual projects

2014 - The Landesgartenschau Exhibition Hall, Schwäbisch Gmünd, Germany [SKM14, LK15a, LK15b, KSM⁺14]

The peanut-shaped shell, presented in Fig.2.24a-b, was built as an exhibition hall for the 2014 Landesgartenschau (country garden show) in Schwäbisch Gmünd. This full scale project

2.1. Angular Connections for Thin Structural Wood Panels

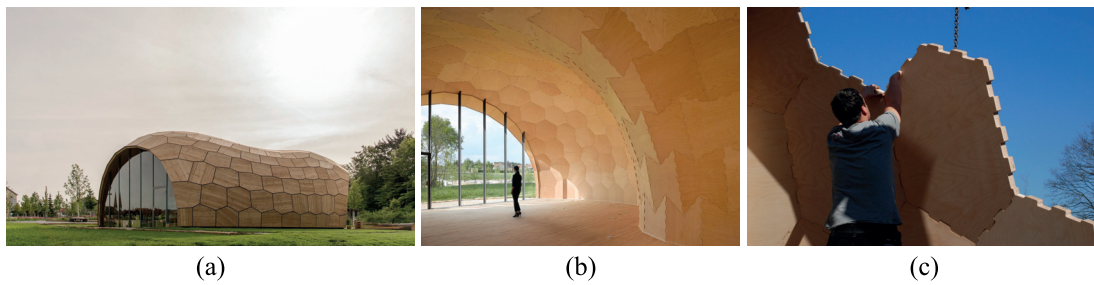


Figure 2.24 – 2014 - The Landesgartenschau Exhibition Hall [SKM14, LK15a, LK15b, KSM⁺14]: (a) Exterior view, (b) Interior view, (c) Segmental plates shell connected by cross-screwed finger joints.

served to apply a collaborative research between the Institute for Computational Design (ICD) and the Institute of Building Structures and Structural Design (ITKE) at the University of Stuttgart, in an actual insulated, waterproof and airtight building. The ambition was to combine structural performance, wood material constraints, geometry and fabrication in a fully automated process, with the criteria of an efficient architecture. As usual in non-standard geometry made with flat timber panels, the main steps were an initial freeform doubly-curved surface, a discrete approximation of the surface with planar elements and a customized computer aided design and manufacturing system to give flexibility in the design phase.

Among lightweight structures, this hall with dimensions 11m-span×17m-long×6m-height benefited of a very low wood to space ratio, only 12m³ for 605m³ of workspace. The arrangement of the 50mm-thick beech plywood segments in a single layer also contributed to optimize the ratio of self-weight to load-bearing capacity. The average size of the plates in the largest dimension was 1.2m.

The structure is viewed as a system of juxtaposed arches whose double-curvature provided a shell action. The external loads are mainly transfer directly to the support by the individual plates. A structural system which approached a pure plate behavior with trivalent nodes was chosen to improve the structural performance while reducing the thickness of the panels. As described by Wester [Wes84], a plate shell with 3-valent polyhedral flat element is the dual of a lattice shell with 6-valent triangular bar element. In theory, both are kinematically stable and moment-resisting connections are not mandatory. The trivalent plate shell will become unstable if two edges, whose the internal angle approach 180°, align with the bending axis.

Due to the peanut shape, shown in Fig.2.26a, left, the surface of this structure is predominantly synclastic ($\kappa > 0$) with just a few anticlastic ($\kappa < 0$) zones in the middle part. The TPI technique was used to discretize the NURBS surface into a set of planar polyhedral elements. Once again, the resulting irregular segmental pattern gave hexagons and pentagons in the area of positive curvature (red in Fig.2.26a, right), bow-tie hexagons in the area of negative curvature (blue in Fig.2.26a, right) and the sides of the same polygons will become flat along the length of the shell (see Fig.2.26f) at the transition zone between both kinds of Gaussian curvature. In this particular zone, the structural behavior differed a lot from that of a pure plate structure.

To connect by their bordering edges these different pattern shapes, a hybrid connection was developed as shown in Fig.2.25b. It includes finger joints with toe-screwing. The finger joints

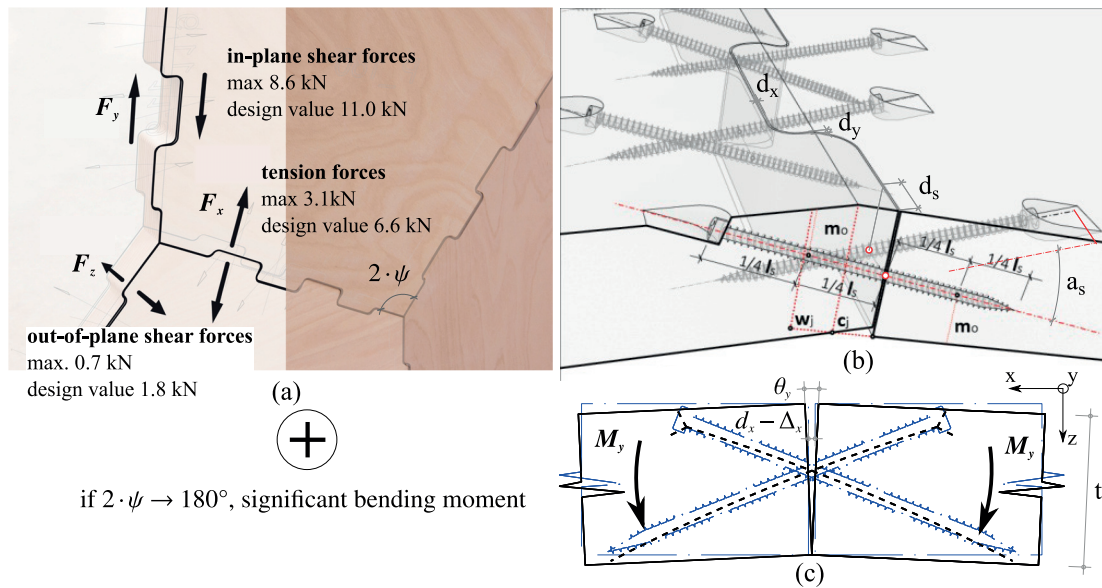


Figure 2.25 – Cross-screwed finger joint [LK15b, KSM⁺14] : (a) In-plane and out-of-plane forces in pure plate structure, (b) Details of the connection, (c) Bending moment taken up by the screws

absorb in-plane shear forces which are distributed along the plate edges. The self-tapping screws take up the axial forces and the out-of-plane shear forces as well as the bending moments at the place of local instability where the edge are almost perpendicular to the span in the transition zone (see Fig.2.25a & c) . The screw diameter ϕ_s and spacing d_s are 6mm and 20mm, respectively. CLT was rejected as the thickness of its internal layers is too large to enable screwing at the edge-to-edge connection. The screw threads could be embedded, parallel to the grain, in only one layer. This is usually not allowed by the building design codes. The thinner layers of the selected plywood guarantee the screws to stay at least in three cross-arranged layer.

The finger joints and the screw pockets were milled by robots at the outlines of the panels. The gap width between the panels was set to be 1 mm (both for d_x and d_y in Fig.2.25b), which was taken into consideration during the panel fabrication and the erection. The fabrication data are integrated in the parametric design and make it easily adaptable to local or global updates of the geometry.

Li [LK15a] carried out a practical study to demonstrate the theoretical analysis of Wester [Wes84, Wes93] on the pure plate structure behavior. He modeled four hexagonal-patterned flat shells. Each case of shells was blocked at the bottom and load at the top by a bending moment. The four shells differed both by their convex or concave patterns (red or blue in Fig.2.26a-e) and by their pattern orientation (0° where each of the 10 bending axes meet 6 edges or 90° where each of the 6 bending axes meet 12 edges, see Fig.2.26b&c and c&e). All the shells had a trivalent geometric pattern where three plates meet at one node. As imaged by Harding [HL13] in Fig.2.21c, the plates were mutually locked in rotation. Thus bending stiffness is generated even though the joints themselves are only hinged connections.

2.1. Angular Connections for Thin Structural Wood Panels

He proposed the following estimation of the bending stiffness for the convex pattern (hexagons) arranged at 0° . Fig.2.26b-e shows the parameters for the estimation of the rotational stiffness provided by topological restraints at the edges.

The rotational stiffness of one edge about the global axis X is

$$K_{\theta,edge,X} = \frac{M_{edge}}{\theta} = \frac{\sum V_{Z,i} \cdot Y_i}{\theta} \quad (2.1)$$

where M_{edge} is the bending moment about X taken by the edge, θ is the relative rotation about X of the two plate meeting at the edge, $V_{Z,i}$ is the out-of-plane shear force along the global axis Z of the i_{th} joint due to the relative rotation and Y_i is the distance from the X -axis to the i_{th} joint.

The shear can be calculated with

$$V_{Z,i} = K_z \cdot \Delta z_i = K_z \cdot (Y_i \cdot \theta) \quad (2.2)$$

where K_z is the joint stiffness in the local z -direction and Δz_i is the relative displacement of the i_{th} joint along z .

Hence, by substituting $V_{Z,i}$ in equation (2.1), we obtained

$$K_{\theta,edge,X} = K_z \cdot \sum Y_i^2 \quad (2.3)$$

Then as Y_i can be expressed as

$$Y_i = r_i \cdot \cos(\psi) \quad (2.4)$$

with r_i , the distance from the center to the edge to the i_{th} joint and ψ is the angle between y and Y , we finally get the rotational stiffness of one edge about the global axis as

$$K_{\theta,edge,X} = \cos^2(\psi) \cdot K_z \cdot \sum r_i^2 \quad (2.5)$$

Now, about the rotation axis of a row of 12 edges, the rotational stiffness is

$$K_{\theta,axis,X} = 12 \cdot K_{\theta,edge,X} \quad (2.6)$$

and the corresponding rotation is

$$\theta_{axis,X} = \frac{M}{K_{\theta,axis,X}} \quad (2.7)$$

If the bending of the plates is neglected and we consider the 6 rotation axes between end B and end A, we obtain the total rotation at end A,

$$\theta_{endA} = \frac{6M}{K_{\theta,axis,X}} = \frac{6M}{12 \cdot K_{\theta,edge,X}} = \frac{6}{12} \cdot \frac{M}{\cos^2(60^\circ) \cdot K_z \cdot \sum r_i^2} \quad (2.8)$$

Applying the same calculation to the pattern turns of a quadrant, the formula becomes

$$\theta_{endA,90^\circ} = \frac{10}{6} \cdot \frac{M}{\cos^2(30^\circ) \cdot K_z \cdot \sum r_i^2} \quad (2.9)$$

and the rotation ratio is

$$\frac{\theta_{endA}}{\theta_{endA,90^\circ}} = 0.9 \quad (2.10)$$

As shown by the previous calculation, the hexagonal patterns have close bending stiffness in the two major directions. The bow-tie hexagonal patterns have the exactly the same bending stiffness than the hexagonal pattern (same angles ψ and same number of edges and axes). A FEM analysis of the vertical flat shell models submitted to bending confirmed the value of the mechanical models with an average rotation θ_{endA} of 41 mrad and 46.5 mrad for the FE-model and the simplified model, respectively.

The load transfer under in-plane vertical loads was also numerically studied on the same simplified shells. Only the shear and axial stiffness were entered in the model. The results confirmed that the forces are mainly transferred by in-plane shear along the plate edges (local y -direction). The first hexagonal pattern presented more uniform stresses and reaction forces at the end B than 90°-rotated pattern. Like for bending, similar behavior were shown for the bow-tie patterns. In a segmented pattern, the connections are the weak points as they interrupt the continuity of the material. They influence the internal forces transfer. The stiffer joints drive the load path through them.

A global FEM analysis of the pavilion, including the necessary spring elements at the plate edges was also run considering two assumptions. First, when the bending stiffness provided by the cross screws is disregarded, the trivalent pattern of the structure provided enough bending stiffness where the Gaussian curvatures are positive or negative but not at the transition zone. Second, when the amount of bending stiffness obtained by experiments on screwed connections was considered, the rotation at the edges did not change significantly apart from the transition zone where the rotation was now under an acceptable limit.

The spring coefficient for the in-plane resistance was determined by a simplified step joint model while the spring coefficient for the bending resistance was directly determined by the four-point-bending test of a real size joint. The in-plane shear model of stiffness could be criticized as it did not take into account the other components; the bending of the beam-like teeth and the local compression at the contact between teeth.

In this structure, the pattern had a predominant influence on the stiffness. But it was confirmed than a better bending stiffness at the edge-to-edge connections would give more freedom to define the geometry of the plates and the arrangement of the curvatures.

2.1. Angular Connections for Thin Structural Wood Panels

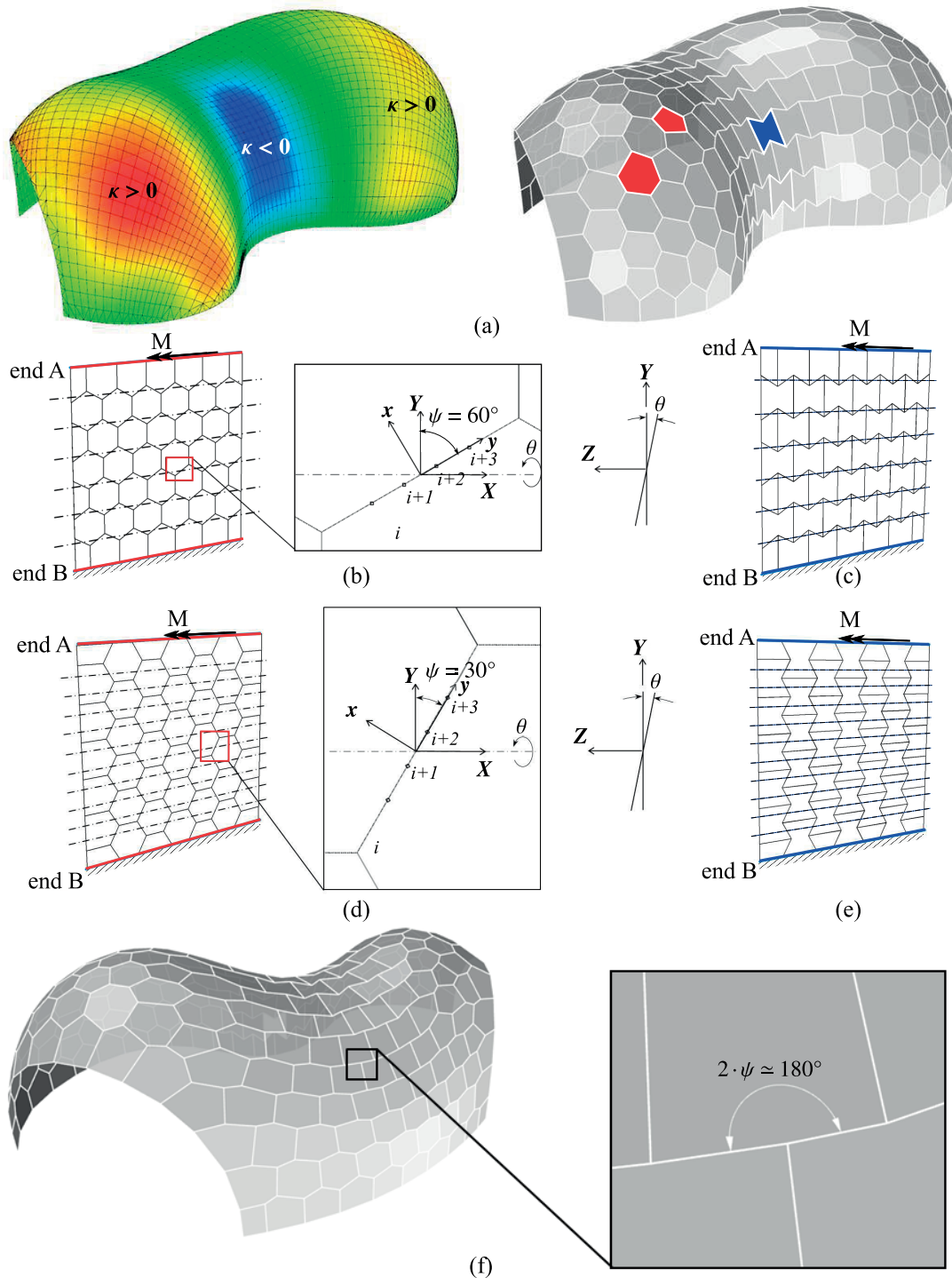


Figure 2.26 – 3-way vertices structure [SKM14, LK15a, LK15b, KSM⁺14]: (a) The distribution of Gaussian curvatures, Bending behavior (b) with positive Gaussian curvature, (c) with negative Gaussian curvature, (d) with positive Gaussian curvature in the transverse direction, (e) with negative Gaussian curvature in the transverse direction, (f) at the transition zone between positive and negative Gaussian curvature.

2015 - Solar energy house, Toul-Rosières, France

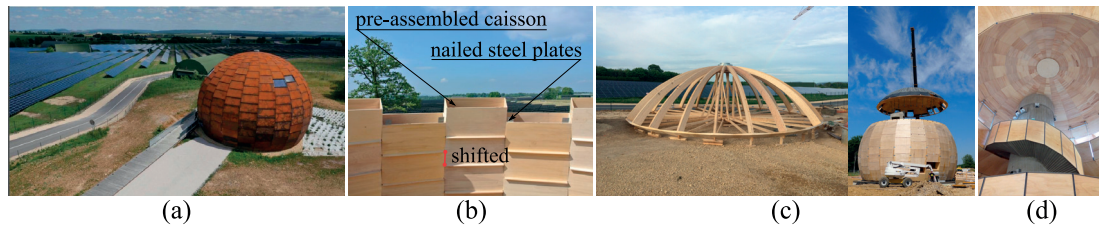


Figure 2.27 – 2015 - The Solar Energy House [A. CARTIGNIES, architect] : (a) Site layout, (b) 25mm-thick birch plywood caisson arrangement, (c) Glulam framed top dome, (d) concrete core and internal finishing.

This project was built in Toul-Rosières (France), in one of the largest photovoltaic facility in Europe (see Fig.2.27a). The architect Alain Cartignies and the timber engineer Jacques Anglade designed a 18m-diameter geodesic sphere for the reception and information building on solar energies. The shape was inspired by the geometry of the sun that floods the solar panel field. The constructive system is a kind of igloo based on Philibert de l'Orme techniques. The structure was based on 24 vertical slices (with reference to the solar stroke), constituted of prefabricated boxes made with 25mm-thick poplar plywood. However, the variable inertia of this geode along the slices had an obvious consequence: Not any boxed segments were similar in dimensions. The cutting on a CNC machine provided the adequate precision for the high level of requirements. The preassembled boxes were shifted by half a height from one slice to the other. This offset allowed to block the relatively rotation-free junction between two caissons with a rigid vertical plates of an adjoining boxes. The on-site connections between boxes were performed by nailed steel plate after filing with insulating material and interposing a seal between each element (see Fig.2.27b). The top of the sphere was finally closed with a glulam framed dome, lined with plywood panels (see Fig.2.27c). The structure is self-supporting and independent of the concrete core. The plywood was covered on the outside by a Corten steel cladding and left bare on the inside (see Fig.2.27a). All the internal finishing was also made with this same plywood to keep an aesthetic coherence (see Fig.2.27d).

2.1.6 Conclusion on the review

The case studies confirmed the conclusions from Tannert in chapter 1. They shown that connections which provide axial, shear and bending stiffness are highly recommended even for structures where the topology have been optimized to approach a pure plate behavior. As soon as the size grows, the shape irregularly varies and the external loads are more critical, moment-resisting joint are essential to ensure a certain continuity in the force distribution for Timber plate structures with discrete elements.

2.2 Moment-resisting Models of Timber Connections

The overview on research projects and actual buildings made with timber plates shown the lack of models on the rotational behavior of edge-to-edge connections for wood panels. Especially if we consider connection without adhesive bonding or mechanical fasteners, there is even no model at all. In the context of this research work, the investigation field for such model was thus redirected to the connections for timber frame structures with wood-to-wood contact only. The multiple tab and slot joint is studied here, considering not any additional parts or chemical products than the two panels to be connected at an adjoining edge. As usual in wood construction and confirmed in the previous sections, the MTSJ is classified among the semi-rigid connections.

2.2.1 Semi-rigid Joints

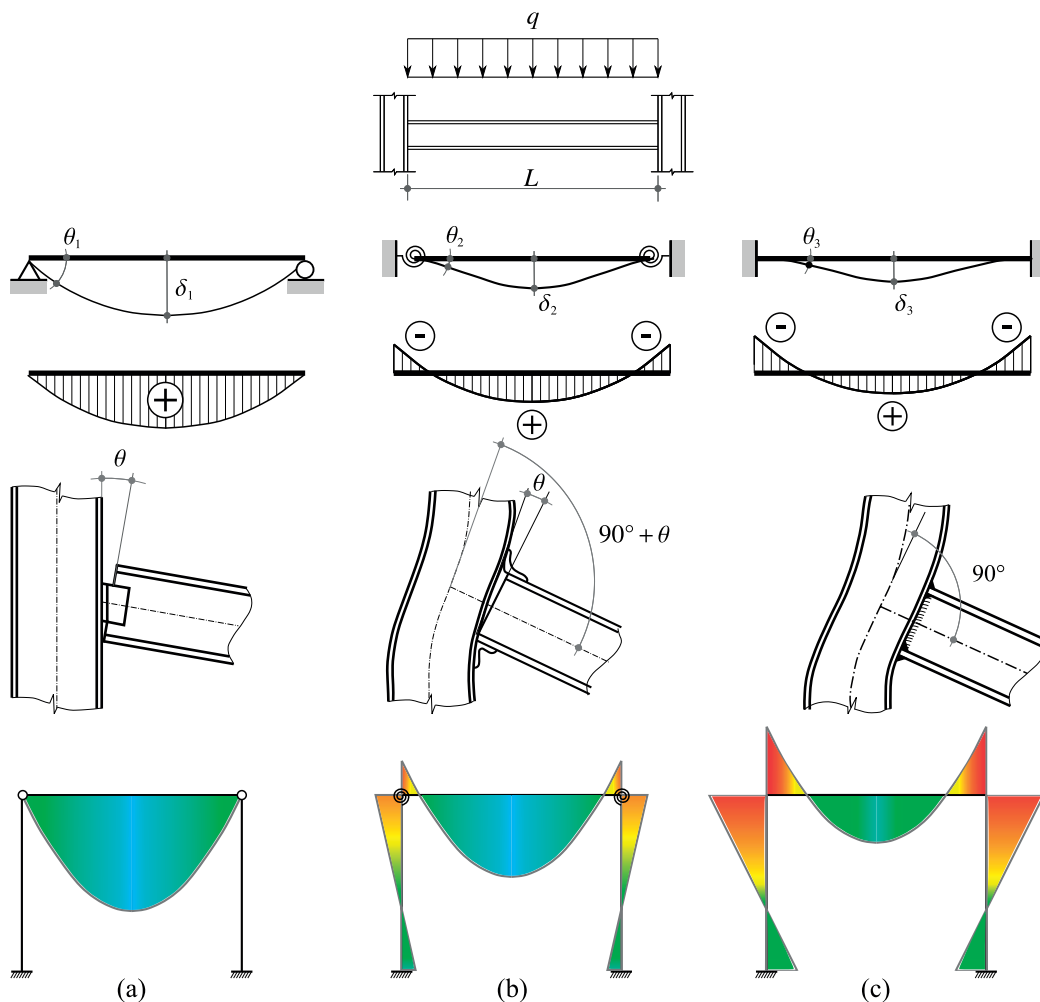


Figure 2.28 – Joint behavior in portal frames [DMVQ11, Cri97] : (a) Ideally pinned, (b) Semi-rigid, (c) Fully rigid.

Before the application of limit state codes to the design of structure as e.g. Eurocode [fSC08,

fSC05a], it was common to consider the joint behavior within a building frame as being either ideally pinned (in Fig.2.28a) or fully rigid (in Fig.2.28c) . The former is unable to transmit any bending moment and is only dimensioned by the transverse forces, the later blocks any rotation between columns and beams and takes up the bending moment. However, the usual connections in timber or steel structures actually behave as an intermediate between the rigid and hinged states. Such a connection is defined as semi-rigid (in Fig.2.28b), where the stiffness value is more than 0 (pinned) and less than ∞ (rigid). In the last thirty years, most of the research works on this topic have been dedicated to the issue of rotational stiffness of beam-to-column connections that can significantly influence the static or dynamic stability of a frame structure. Fig.2.28 gives an overview of the influence of the joint behavior on the bending responses of a steel beam or a portal frame [DMVQ11, Cri97].

The determination of the rotational behavior of joints was first addressed in the Annex J of the European Prestandard for the design of steel structures (ENV1993-1-1:1992, [fSC92]). The annex J was initially dedicated to the beam-to-column connections. Hence, it was extended to a larger catalog of connections and moved into the part-1-8 of the last revision of Eurocode 3 (EN1993-1-8:2005, [fSC05a, fSC05b]).

The determination of the rotational response of the joints, typically the rotational stiffness, the bending strength and the rotation capacity, consists of four steps [Jas00].

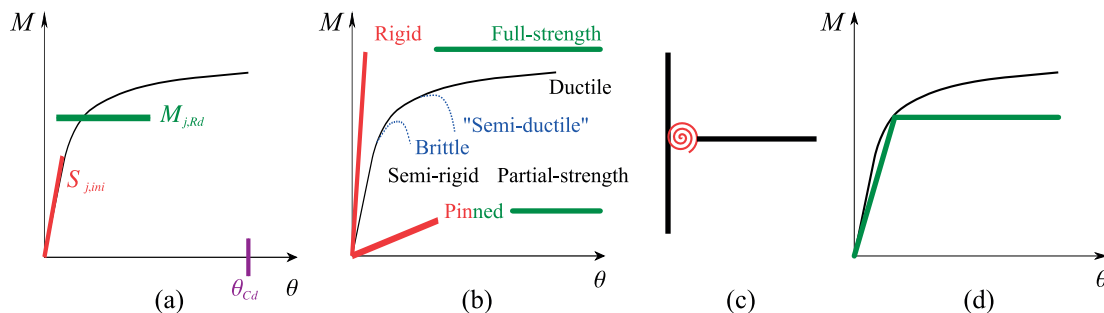


Figure 2.29 – Rotational response of joint : (a) Characterization, (b) Classification, (c) Modeling, (d) Idealization.

The joint **characterization** (see Fig.2.29a) preliminary provides, by full moment-rotation ($M - \theta$) curves or key values, the stiffness, the strength and the ductility of the joint. Experimental testing is the most accurate method but rather costly. Thus Numerical simulation are privileged. From both methods, curve fitting is a way to obtain the desired data. As they are based on mechanical and geometrical properties of the joints, the simplified analytical models are more versatile to cover without additional experiments different configurations of connections. One of this model called “the component method” has been selected in EN1993-1-8:2005. It will be described in the section 2.2.3.

As shown in Fig.2.29b, the **classification** of joint can be done with regard to the boundaries in stiffness and strength. The stiffness varies from pinned to rigid and the strength from pinned state to full-strength state. At an intermediate level of stiffness, semi-rigidity and

2.2. Moment-resisting Models of Timber Connections

partial-strength has to be considered. In EN1993-1-8:2005, the boundaries of the classification of connections by stiffness are defined by a non dimensional joint stiffness parameter k_b [CKK11]. This parameter is calculated as the ratio of the initial rotational spring stiffness $S_{j,ini}$ (the slope in the linear part of the M_θ curve) to the flexural stiffness of the beam EI/L .

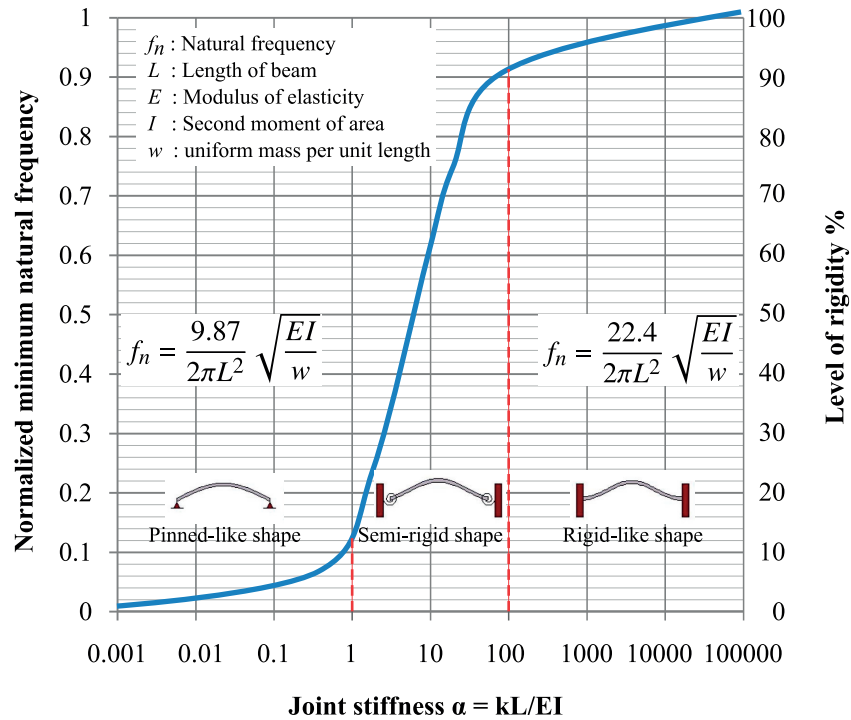


Figure 2.30 – Level of rigidity for timber beams [McG95, LHFC00, CK11]

Earlier in 1995, McGuire [McG95] demonstrated that beyond a significant variation in the bending moment distribution of a beam with hinged, semi-rigid or rigid joints, there is also a notable difference in the minimum natural frequency and mode shape. Moreover, the joint rigidity is influenced both by the rotational stiffness of the connection and the flexural stiffness of the beam. At the support, a stiff beam will appear less restrained in rotation than a flexible beam for the same level of partial rigidity at the joint. Using a finite element model, he proceeded to a normal modes analysis to obtain the minimum natural frequency for different rotational spring stiffness k (equivalent to $S_{j,ini}$). He also increased by 100 times in differentiated analysis both mass and flexural stiffness. The new mass changed the amplitude of the natural frequency but did not affect the rotational spring stiffness while the higher flexural stiffness did. From these conclusions, the plot of Fig.2.30 was proposed with normalized natural frequencies as ordinates and the joint stiffness ratios α (equivalent to k_b) instead of the rotational spring stiffness as abscissas. The boundaries of stiffness classification can be read on the plot. The pinned-pinned condition of the beam is reached within 10% when the joint stiffness ratio is less than 1. The rigid-rigid condition of the beam is reached within 10% when the joint stiffness ratio is more than 100. Based on the McGuire's work and assuming that the dynamic deformations of beams are similar to the static ones, Leitchi [LHFC00] proposed a continuum to "measure" the connection rigidity in static analysis of timber portal

frames. He completed the plot with a level of rigidity between 0 and 100% as second ordinates (see right ordinates in Fig.2.30). In steel structure, rigid joints with continuous models are quite easily achievable by welding. But for timber frames e.g., rigid connections at the knee is in practice not easily achievable. In case of unbraced frames, only the bolted connection with circular pattern of fasteners is supposed to overcome it but with some drawbacks as the generation of possible transverse tensile forces. Crovella [CK11] which proposed a non destructive experimental vibration technique as alternative to the numerical simulation of McGuire confirmed like others that it is difficult to go over 50% of rigidity level with timber fastened connection.

Following the classification step, the **model** of joint is allocated with respect to the global analysis to be performed on the structure (see Fig.2.29c). The different types of joint models are gathered in Table 2.1. According to EN1993-1-8:2005 [fSC05b], *simple model* means “in which the joint may be assumed not to transmit bending moments”; *continuous* means “in which the behavior of the joint may be assumed to have no effect on the analysis”; *semi-continuous* means “in which the behavior of the joint needs to be taken into account in the analysis”.

Method of global analysis	Classification of joint		
	Elastic	Nomally pinned	Rigid
Rigid-Plastic	Nomally pinned	Full-strength	Partial-strength
Elastic-Plastic	Nomally pinned	Rigid & full-strength	Semi-rigid & partial-strength Semi-rigid & full-strength Rigid & partial-strength
Type of joint model	Simple	Continuous	Semi-continuous

Table 2.1 – EN1993-1-8:2005 : Type of joint model [fSC05b]

At the last stage in Fig.2.29d, the joint spring **idealization** is governed by the type of global structural analysis. An elasto-plastic analysis will need a non linear idealization while an elastic analysis will need a linear idealization. The elastic-perfectly plastic moment-rotation model is commonly used as it is simple and very close to the model used for member in bending. The common goal of joint idealization is to provide a simplified moment-rotation curve for design practice with a minimum loss of accuracy.

Eurocode 3 is well advanced in the design of semi-rigid jointed frame structures. For the design of timber structures, Eurocode 5 did not proposed the characterization of joint based on the component model. Stiffness and strength models are proposed for connections with metal fasteners but not for direct assembly by wood-to-wood contact.

2.2.2 Component Method

A brief history

The credit of the component method (CM) principles is commonly given to Zoetemeijer [Zoe74, Zoe83]. In the early 1990s, the method was introduced in the European Prestandard Eurocode 3 and its annex J [fSC92] for the beam-to-column connections in design of steel structures. After gradual improvements, it was finally accepted to the European standard (CEN-EN1993-1-8 :2005 - Eurocode 3: Design of steel structures - Part 1-8: Design of joints) in 2005.

Introduction to the method

The method consists in applying the general principle of the Finite Element Method for a structure to a whole joint [JR94, Jas00]. The procedure of implementation can be described as

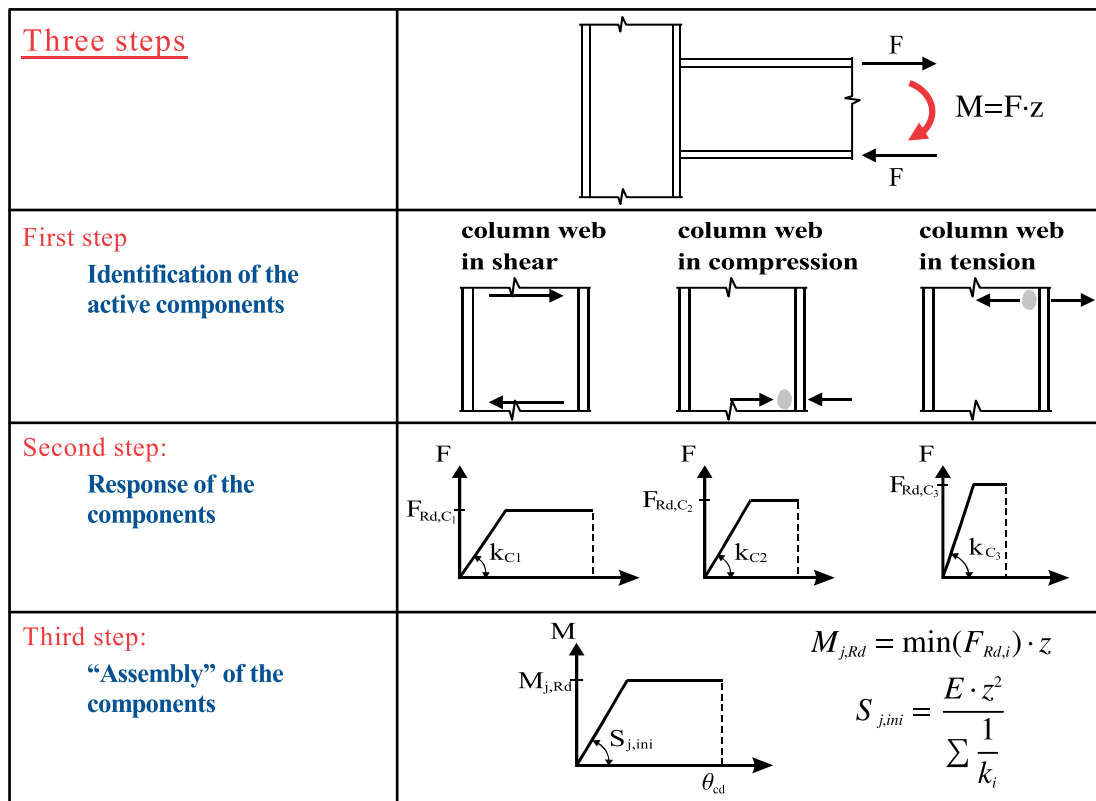


Figure 2.31 – Component method [Jas00]

Identification of the basic components: The joint is split into individual basic components as for a structure in finite elements (refer to Fig.2.31,1st row).

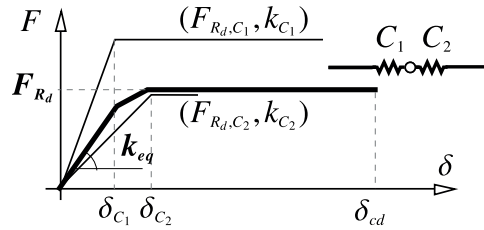
Modeling the response of the components according to mechanical, geometrical and material properties: The relevant strength, stiffness or load-slip responses are determined for every different components (refer to Fig.2.31,2nd row). This applies indifferently to components

Springs in Series,

$$F_{Rd} = \min(F_{Rd,C_1}; F_{Rd,C_2})$$

$$k_{eq} = \frac{k_{C_1} k_{C_2}}{k_{C_1} + k_{C_2}}$$

$$\delta = \frac{F_{Rd}}{k_{eq}} = \frac{F_{Rd}(k_{C_1} + k_{C_2})}{k_{C_1} k_{C_2}}$$

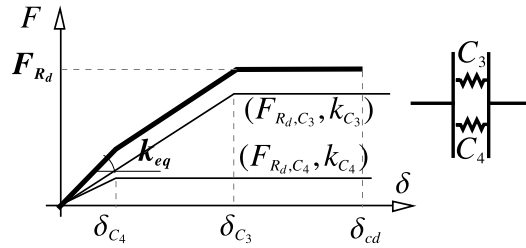


Spring in Parallel

$$F_{Rd} = F_{Rd,C_3} + F_{Rd,C_4}$$

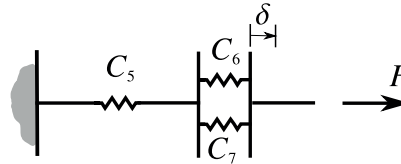
$$k_{eq} = k_{C_3} + k_{C_4}$$

$$\delta = \frac{F_{Rd}}{k_{C_3} + k_{C_4}}$$



General spring system

$$k_{eq} = \frac{k_{C_5}(k_{C_6} + k_{C_7})}{k_{C_5} + k_{C_6} + k_{C_7}}$$



Initial rotational spring stiffness

$$S_{j,ini} = \frac{M_j}{\theta_j} = \frac{F \cdot z}{\sum \frac{\delta_{C_i}}{z}} = \frac{F \cdot z^2}{\frac{F}{E} \sum \frac{1}{k_{C_i}}} = \frac{E \cdot z^2}{\sum \frac{1}{k_{C_i}}}$$

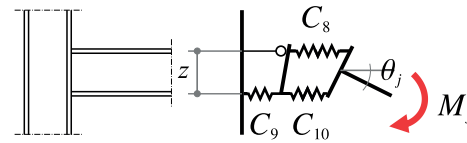


Figure 2.32 – Assembly of the components [WBC07, WJS96]

under compression, traction or shear forces. Certain interactions between basic components can be noted, but as these will effectively act merely on the shape of individual curves, an adjustment coefficient to take account of them can be added in the simplified analytical model. The responses of the components can be described by a linear or non linear load-slip curve. In case of non-linear behaviors, they can be approximated by bi-linear or tri-linear models. For each component, we can thus derive the design resistance F_{Rd,C_i} , the stiffness coefficient k_{C_i} and the deformation capacity δ_{C_i} . Simplified analytical models are also available for the most commonly encountered components in the design of joints for steel structures.

Assembly of the components to obtain the whole joint behavior (design strength, stiffness or entire load-slip curve). The assembly is based on the serial and /or parallel association of basic components (refer to Fig.2.31, 3rd row).. The external loads applied to the whole joint are distributed to the components through the internal forces as a function of the relative strength and stiffness of each component. To get a rotational spring stiffness, the lever arm is defined as the distance between the internal forces which create the resisting moment [WJS96]. In Fig.2.32 is presented the general method of assembly by spring models [WBC07].

2.2.3 Component method : Application to traditional timber joints

In Europe

An application of the CM to timber joint was initiated by **Drdácký et al.** [DWM99]. A halved joint from historic carpentry was divided into basic components all acting in compression. Component interactions were expected to be very limited and were therefore neglected. The stiffness of the deformed zone under compression was obtained using elastic soils mechanics equation of deformation under a rectangular rigid plate in an equivalent half space. It can be noticed that the CM was also derived for concrete-steel contacts [SWSS08].

In 2006, **Descamps et al.** [DLL06] carried out similar work to analyze the bending stiffness of barefaced shouldered tenon joints by performing theoretical, numerical and experimental analysis . The dowel was supposed to resist to shear force and define a fixed rotation center of the connection. Friction was neglected. The obtained rotational stiffness were equivalent for both numerical and component method. They introduced the stiffness of different geometries of joint in the framing of the Gothic choir of the Cathedral of Tournai and proceeded to the EC5's structural calculation. They confirmed the significant influence of the joint stiffness in the global behavior of the structure.

In 2009, **Descamps et al.** [DLL06, DG09, DL09, DN09] continued their work to analyze the rotational stiffness of a historic pegged tenon and mortise joint under static load . The CM was enhanced with adding cut factor to correct the young modulus value contained in the definition of the elementary stiffness. As the assumptions of an infinite half space shown their limitations, the cut factors were numerically adjusted for solicitations perpendicular and parallel to the grain. Additionally, the instantaneous center of rotation was this time iteratively calculated by equilibrium of the resisting forces and moments of the compressive zones of contact. The peg stiffness was introduced after experimental determination and a friction coefficient of 0.3 was applied in the numerical model. Although overestimated by 40%, the stiffness determined by the CM was quite satisfactory for the purpose of the global study

In an overview of the application of the CM to traditional dovetail joints for the connection of timber collar beam truss, **Sobra et al.** [SBA14] confirmed the lack of models for the stiffness of the timber components. However, they suggested ways of improving the previous studies on the topic. The Compressive area were expressed in a parametric form from the joint geometry and the angle between the member α . The strength of wood was obtained from the Hankinson formula [Han21] adopted by EC5 [fSC08].

$$f_{c,\alpha,d} = \frac{f_{c,0,d}}{\frac{f_{c,0,d}}{f_{c,90,d}} \sin^2 \alpha + \cos^2 \alpha} \quad (2.11)$$

To calculate the equilibrium in the joint knowing that the connected elements have different strength and difference in deformation under loads, the joint forces must be dependent on the contact stiffness between the elements. In addition, the loads in the joint are transferred by compression perpendicular to wood grain and the maximum strength from **Van der Put's** formula (2.12) may apply. The formula was derived from the equilibrium method of plasticity

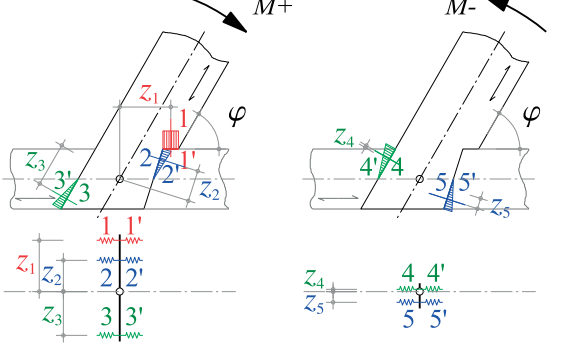
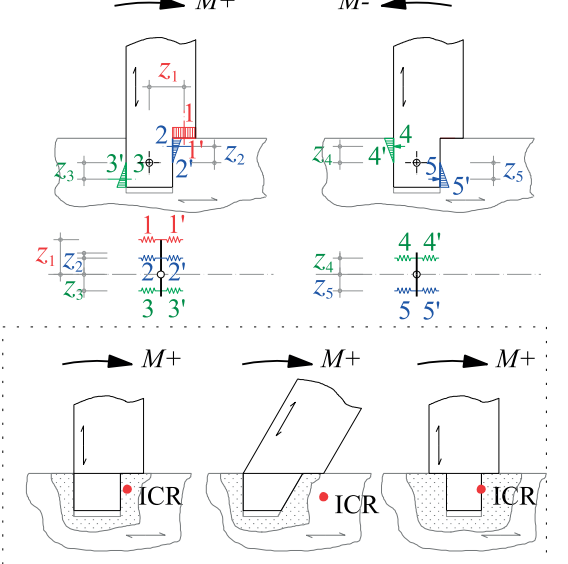
Author	Joint modeling	Stiffness model
Drdácký Wald Mareš Sokol Sobra		See : (SM1) Elastostatics of a Half Space in Soil Mechanics
Descamps		See : (SM1) Elastostatics of a Half Space in Soil Mechanics

Table 2.2 – Component method for timber

[dP90, dP08, dP12, LLdP10].

$$\sigma_{c,90,u} = c \cdot f_{c,90} \sqrt{\frac{A_s}{A_0}} = 1 \cdot f_{c,90} \sqrt{\frac{b \cdot l_{ef}}{b \cdot l}} = f_{c,90} \sqrt{\frac{l_{ef}}{l}} \quad (2.12)$$

Where $\sigma_{c,90,u}$ is the ultimate compressive stress perpendicular to grain, $f_{c,90}$ is the compression strength perpendicular to grain when the bearing load cover the full surface of the block, $A_0 = bl$ is the area below the load, A_s is the area of the spread stresses, b is the width of the member, l is the loading length and l_{ef} is the effective length corresponding to the spread of stresses. l_{ef} depends on the height of the beam h and the slope spreading (e.g if slope = 1:1.5, $l_{ef} = l + 3h$). Experimental campaign was settled to define the spring stiffness.

Meisel, Branco and Descamps also applied the component method to axial and shear response of joints. It is not developed in the scope of this research but detailed information can be found in [MMS10b, MMS10a, BD15, DG09, DL09, DN09]. Branco also proposed a complete review on the analysis of traditional carpentry joints.

In Asia

In Asia, many temples, shrines and town houses are registered as World Heritage, like the Grand Gate of Itsukushima shrine in Miyajima(Japan) and the ten thousands doors of Fushimi Inara shrine in Kyoto(japan), shown in Fig.2.33. Although they are subject to earthquakes



Itsukushima Shrine - Miyajima



Fushimi Inari Shrine - Kyoto

Figure 2.33 – Nuki joint in shrine

and typhons, these traditional timber constructions, perfect reflection of know-how in the art of timber carpentry, persist over the ages. However, they need reinforcements during their reconstruction. It is indeed classical ,in Japan for instance, to rebuild these monuments every 100 years to retain the knowledge of ancestral techniques. The structures consist mainly of columns and beams, assembled by wood-to-wood crosspiece joints without metal plates or mechanical fasteners. The mechanical behavior of such joints is the key point to assess the structural performance under static and dynamic external loads. These traditional timber joints absorb external force by an embedment mechanism between the members.

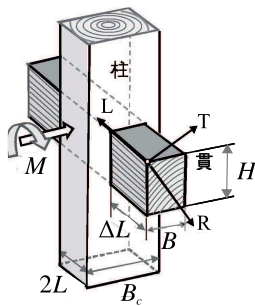


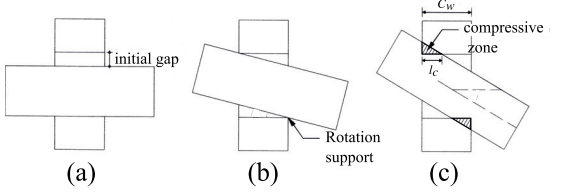
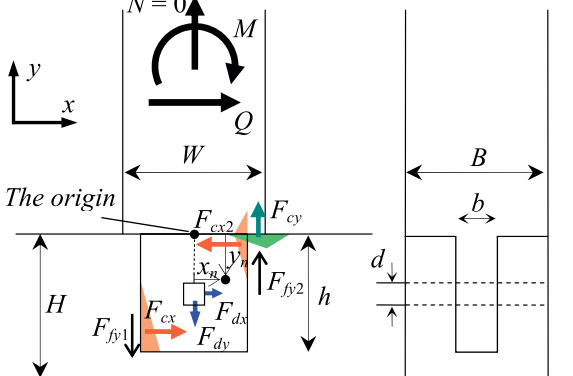
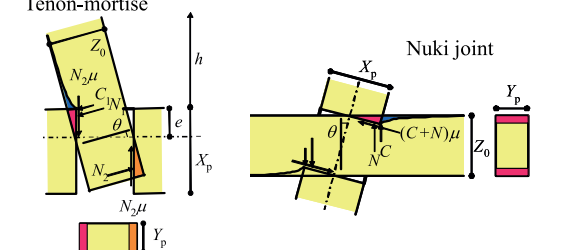
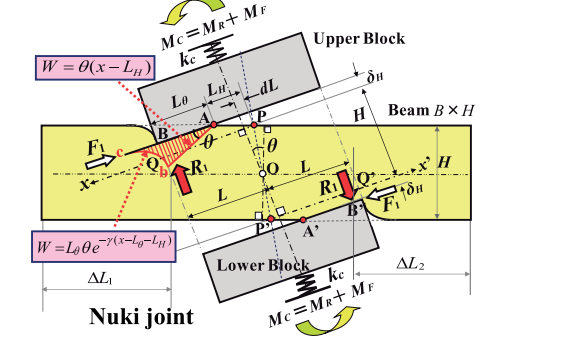
Figure 2.34 – Nuki joint [TS11]

If a moment is applied to the joint, the column-like element with an elastic modulus several dozen times greater than that of the beam-like element, inclines and the rotational partial compression (RPC), perpendicular to the grain, occurs at the surface of the beam. Each local force generated by the embedment mechanism opposes, by lever arm from the center of rotation, to the applied moment (e.g. Fig.2.38). The deformation due to embedment goes beyond the contact surface of the two elements as wood is a continuum. This additional indirectly loaded area (also found as “spring back effect” or “hammock effect” in the literature) benefits to the

increase of the reaction forces (e.g. see blue-colored surface in Fig.2.38). The embedment effect, combined to the diagonal effect (defined by Tanahashi [TS15], allows to load the joints well beyond its elastic limit, favorable to the ductility of the frame. Among these penetrating joints, Nuki and Watari-ago have been analytically modeled by Japanese and Taiwanese researchers. The “Nuki” is a tie beam which penetrates through a columns where a mortise have been previously cut. In Japan, unlike Taiwan, wedges are often used to tighten the joints as shown in Fig.2.33. The Japanese “Watari-ago” joint is a cogged right-angled joint which

Chapter 2. State-of-the-Art

consist roughly of two notched beams, as presented in Fig.2.39. It is a horizontal part of a floor or a roof of traditional timber construction. In that case, the embedment and diagonal effect allow the Watari-ago joint to resist the in-plane shear forces due to wind or seismic loads.

Author	Joint modeling	Stiffness model
<p>Chang (Taiwan)</p>	 <p>Figure 2.35 – Nuki joint [CHK06]</p>	<p>Triangular embedment without additional length</p>
<p>Sakata (Japan)</p>	 <p>Figure 2.36 – Tenon-mortise with dowel [SYO12]</p>	<p>See : (SM2) Triangular embedment with a linear additional length</p>
<p>Komatsu (Japan)</p>	 <p>Figure 2.37 – Penetrating joints [KKJM09]</p>	<p>See : (SM3) Triangular embedment with an exponential-shaped additional length</p>
<p>Tanahashi (Japan)</p>	 <p>Figure 2.38 – Nuki joint [TS12]</p>	<p>See : (SM4) Elasto-plastic Pasternak model of embedment behavior of wood</p>

2.2. Moment-resisting Models of Timber Connections

Author	Joint modeling	Stiffness model
Ogawa (Japan)	<p>3D Rotational embedment</p> <p>Watari-ago joint</p> <p>Figure 2.39 – Watari-ago joint [OSY15]</p>	See : (SM3) Triangular embedment with an exponential-shaped additional length

Table 2.3 – Models for traditional Asiatic penetrating joints

The following authors applied the embedment characteristics to develop moment-resisting models of timber crosspiece joints with different levels of complexity.

In Taiwan, where the Nuki joint are typically without wedges, **Chang et al.** [CHK06, CH07]

built a model considering gap between the beam and the column. In consequence, the joint undergoes an initial rigid body motion before activating the embedment effect. The embedment is assumed to be triangular without additional length. The distribution of stress is triangular in the elastic range and becomes trapezoidal in the non-linear plastic stage. It can be noticed that the way of addressing the plastic stage was not described in the paper. The elastic modulus is corrected during the evolution of the rotation by using the Hankinson's formula [Han21]. The elastic modulus corresponding to the compression perpendicular to the wood is calculated as a function of the rotation angle θ , the young modulus parallel to fiber $E_{//}$ and the young modulus perpendicular to fiber E_{\perp} . The contact length l_c in Fig.2.35 is expressed following the geometrical parameters as height, width of beam and column, the square angle between the member, the clearance due to the gap, the initial slip angle and the angle of rotation under the bending moment. Using stress formulation based on the above defined distribution, the bending moment M is formulated as a function of θ . It implies that the rotational stiffness K_i can be drawn from the final formula. By including the initial slip in the theoretical model, the hinge behavior of the joint at the early stage can be predicted. When a joint is free of gap, the contact length starts immediately with a value about half the mortise length C_w in Fig.2.35 while with an initial gap the value is much smaller when embedment begins. The friction was neglected. The theoretical model corresponded well with the experimental results of a total of 24 full-scale specimens (4 very close geometrical cases).

Sakata et al. [SYO12] typically conducted works similar to the European researchers Descamps, Drdácáký, Wald and others to model tenon-mortise joints with or without wedges (see Fig.2.36). However, the stiffness model for the components was different. It was based, this time, on the triangular embedment of wood (refer to section (SM2) Triangular embedment with a linear additional length). When considering joint without dowel, the failure point can be evaluated from the bending strength of the tenon.

Mud shear walls of ancestral shrines from Japan were studied by **Komatsu et al.** [KKJM09] to estimate non-linear behavior under lateral shear force. The walls are composed of joints which behave like Nuki and tenon-mortise joints (see Fig.2.37). This time, the theoretical development from AIJ (see section 2.2.4 “(SM3) Triangular embedment with an exponential-shaped additional length”) was adopted. The friction was taken into consideration without precising the value. An elastic perfectly plastic behavior was assumed, considering that the moment remains constant after yielding. The elastic modulus perpendicular to the grain is kept constant all along the rotational embedment.

The Pasternak model (PM) of orthotropic timber in partial transverse compression (EPM) published by **Tanahashi et al.** [TSH⁺08] was used to determine the relationship between the applied moment and the rotation angle in the Nuki joint. The model is described in section 2.2.4-“(SM4) Elasto-plastic Pasternak model of embedment behavior of wood”. The geometrical and material parameters of Fig.2.38 which represents the moment-resisting behavior are defined below :

2.2. Moment-resisting Models of Timber Connections

B : Beam width (mm),
 H : Beam height (mm),
 $\Delta L_1, \Delta L_2$: Beam end lengths (mm) ($\cong L_0 - L$ in PM),
 $2L$: Load bearing length on the column (mm),
 δH = gap between column mortise and beam (mm)
 $L_\theta : L + dL - L_H$: Contact length (mm),
 $dL = 0.5H \tan(\theta/2)$: offset as the rotation is about the point O (mm),
 $L_H = \delta H / \tan(\theta)$: offset due to gap (mm),
 $\rho = (L - L_\theta) / L_\theta = (L_H - dL) / L_\theta$
 $E = E_\perp$: Young's modulus of wood beam in transverse compression (N/mm²),
 $\gamma^* H$: Non-dimensional characteristic value depending on species and orthotropic plane,
 $k = E/H$: Compressive stiffness (N/mm),
 μ : coefficient of friction,
 W_i : Displacements due to the triangular embedment with additionnal length effect,
 R_1 : Normal force due to the triangular embedment with additionnal length effect,
 M_R : Moment due to the triangular embedment with additionnal length effect,
 M_F : Moment due to friction at embedment place.

If the end lengths are finite, the displacement, the forces and the moments listed above can be calculated using the following formulas:

$$\begin{aligned}
 W_1 &= \theta(x - L_H) & \text{if } L_H \leq x \leq L_H + L_\theta \\
 W_2 &= L_\theta \theta e^{-\gamma(x - L_H - L_\theta)} & \text{if } L_H + L_\theta \leq x \leq L_H + L_\theta + \Delta L
 \end{aligned} \tag{2.13}$$

Similarly to AIJ method [AIJ10], in the elastic state, the normal reaction force is obtained from the typical expression $R = E\varepsilon A = \int E(W(x)/H)Bdx$:

$$\begin{aligned}
 R1 &= \int_{L_H}^{L_H + L_\theta} kW_1 B dx + \int_{L_H + L_\theta}^{L_H + L_\theta + \Delta L} kW_2 B dx \\
 &= \frac{EBL_\theta^2}{2H} \left(1 + \frac{2(1 - e^{-\gamma\Delta L})}{\gamma L_\theta} \right) \theta \\
 &= \frac{EBL_\theta^2}{2H} \zeta_N \theta \\
 &= K_{N0} \zeta_N \theta
 \end{aligned} \tag{2.14}$$

The embedment occurs symmetrically with respect to the rotation center O and by a lever arm effect, the reaction forces create a resisting moment. Hence, Eq.(2.15) comes by multiplying by

* γ is equivalent to the decay coefficient a_e in stiffness model "(SM3) Triangular embedment with an exponential-shaped additional length" but it has a value which varies with the species, the orthotropic plane and the height of the beam.

2x the function within the integrals of Eq.(2.14).

$$\begin{aligned}
 M_R &= 2 \int_{L_H}^{L_H+L_\theta} kW_1 Bx dx + 2 \int_L^{L_H+L_\theta+\Delta L} kW_2 Bx dx \\
 &= \frac{2EBL_\theta^3}{3H} \left(1 + 1.5\rho + \frac{3}{\gamma L_\theta} \left(\left(1 + \rho + \frac{1}{\gamma L_\theta} \right) (1 - e^{-\gamma \Delta L}) - \frac{\Delta L}{L_\theta} e^{-\gamma \Delta L} \right) \right) \theta \\
 &= \frac{2EBL_\theta^3}{3H} \zeta_R \theta \\
 &= K_{R0} \zeta_R \theta
 \end{aligned} \tag{2.15}$$

The friction coefficient μ allows to estimate the friction force from the normal force R_1 . The lever arm distance for the moment due to friction M_F is assumed equal to $H + 2\delta_H$. Thereby the friction moment is

$$M_F = \mu R_1 (H + 2\delta_H) = \mu K_{F0} \zeta_F \left(1 + \frac{2\delta_H}{H} \right) \theta \tag{2.16}$$

where the basic stiffness factors K and the Increasing stiffness ratio ζ of the previous expressions are :

In compression,

$$K_{N0} = \frac{EBL_\theta^2}{2H} \tag{2.17a}$$

$$\zeta_N = 1 + \frac{2(1 - e^{-\gamma \Delta L})}{\gamma L_\theta} \tag{2.17b}$$

In rotation,

$$K_{R0} = \frac{2EBL_\theta^3}{3H} \tag{2.18a}$$

$$\zeta_R = 1 + 1.5\rho + \frac{3}{\gamma L_\theta} \left(\left(1 + \rho + \frac{1}{\gamma L_\theta} \right) (1 - e^{-\gamma \Delta L}) - \frac{\Delta L}{L_\theta} e^{-\gamma \Delta L} \right) \tag{2.18b}$$

In rotational friction,

$$K_{F0} = \frac{EBL_\theta^2}{2} \tag{2.19a}$$

$$\zeta_F = 1 + \frac{2(1 - e^{-\gamma \Delta L})}{\gamma L_\theta} \tag{2.19b}$$

Hence, The final expression of the moment due to embedment effect is

$$M = M_R + M_F = \left(K_{R0} \zeta_N + \mu K_{F0} \zeta_F \left(1 + \frac{2\delta_H}{H} \right) \right) \theta \tag{2.20}$$

θ is the rotation due to the embedment effect at the contact within the joint between beam and column. Tanahashi et al. [TS11, TSS12] expressed the total bending rotation θ of the

2.2. Moment-resisting Models of Timber Connections

system Beam-joint-column as $\theta_F = \theta + \theta_b + \theta_c + \theta_S$. θ_b and θ_c are the bending angle of beam and column, respectively. The classical formula of bending of beam can be used with respect to the actual boundary conditions of the system. θ_S is the shear deformation of the wood block of the beam which is inside the column.

The elastic analysis already well advanced is completed by taking into account the elasto-plastic behavior of the crosspiece joint. Hereafter is presented a very short picture of the principles. More details can be read in [TSS06b, TOS08].

The elasto-plastic relationship $M_P-\theta_P$ is obtained from Eq.(2.20) as follows :

$$M_P = \frac{M}{1 + mh_y} \quad (2.21)$$

where m is a multiplying factor of the yielding depth ratio h_y . h_y is equal to the ratio of yield depth H_y of the embedded area to the beam height H .

These two factors are expressed according to the yield parameters of transverse compression tests as :

$$m = C\left(1 - \frac{1}{\kappa}\right) \quad (2.22a)$$

$$h_y = \frac{H_y}{H} = \frac{1}{\eta} \ln \kappa \quad \text{with } 0 \leq h_y \leq 1 \quad (2.22b)$$

$$\kappa = \frac{\theta\eta}{\theta_y} = \frac{\varepsilon\eta}{\varepsilon_{y,F}} \quad (2.22c)$$

$$\eta = \frac{\varepsilon_{y,F}}{\varepsilon_{y,P}} \quad (2.22d)$$

$$\varepsilon = \frac{W}{H} \quad (2.22e)$$

$$W\phi' = \varepsilon\eta e^{-\eta \frac{z}{H}} = \varepsilon\phi_S \quad (2.22f)$$

$$\phi_S = \eta e^{-\eta \frac{z}{H}} \quad (2.22g)$$

where C is the plastic strain multiplier, κ is the yielding ratio. η is the parameter of strain profile $W\phi'$ through the height of the beam. ϕ_S is the shape function, in sense of Vlasov assumptions, for the simplified function presented in [TOIS11]. $\varepsilon_{y,F}$ and $\varepsilon_{y,P}$ are the yield strains in full and partial transverse compression, respectively. The elasto-plastic parameters are clarified in section 2.2.4-“(SM4) Elasto-plastic Pasternak model of embedment behavior of wood”.

As mentioned by the author, the procedure to implement the plasticity within the model is not trivial and require different steps and data before reaching an adequate result. The model was applied successfully to Nuki joints and other traditional Japanese joints where the same mechanism is acting [TSS12, TS15]. The model is however promising but deserves certain simplifications.

Ogawa et al. [OSY15] implemented a model to predict the resistance of Watari-ago joint to in-plane shear force. The behavior of such joint is similar to that of the Nuki joint. In that case, the width of the beam is not completely loaded like it was for the other authors. The compression is partial along two directions as the contact surface didn't cover the full width of the beams. The stiffness model that applies is therefore described in section 2.2.4-” (SM3) Triangular embedment with an exponential-shaped additional length”. The normal reaction forces are expressed from the deformed volume $P = V / H \cdot E$, where P is the local force, V is the deformed volume, H is the depth of the member where the embedment occurs and E is the Yong's modulus in full transverse compression. The deformed volume is divided in four elementary parts as shown in Fig.2.39 :

Deformed part 1 : directly loaded area

volume $V_1 \rightarrow$ triangular embedment as function of θ

Displacement function : $W_1(x) = x \tan \theta$,

Deformed part 2 : indirectly loaded area along the fiber (x -axis) beyond the directly loaded area

volume $V_2 \rightarrow$ additional length by an exponential shape function with a constant intercept fixed at the maximum displacement $\delta(\theta)$

Displacement function : $W_2(x) = \delta(\theta) \cdot \exp(-\gamma_2 x)$,

Deformed part 3 : indirectly loaded area across the fiber (y -axis) beside the directly loaded area

volume $V_3 \rightarrow$ additional length by an exponential shape function with an intercept $\delta(\theta, x)$ varying along x , Displacement function : $W_3(x, y) =$

$x \tan \theta \cdot \exp(-\gamma_3 y)$,

Deformed part 4 : indirectly loaded area, at the intersection of volumes V_2 and V_3

volume $V_4 \rightarrow$ the function for V_4 is defined in order to reach the function of V_2 when $y = 0$ and the function of V_3 when $x = 0$, the intercept value is fixed at the maximum displacement $\delta(\theta)$

Displacement function : $W_4(x, y) = \delta(\theta) \cdot \exp(-\gamma_2 x) \cdot \exp(-\gamma_3 y)$,

The above displacement function are written in the sense of Tanahashi for comparison but $\tan \theta$ was not simplified to θ as if the rotation angle goes over 10° , it does not stand anymore. The decay length where displacement vanishes to zero was fixed to $1.5z_0$ like Inayama did (z_0 and H represent indifferently the depth of the elastic layer according to the author in question). So the decay coefficient γ_2 of the exponential shape function for displacement spreading along x is taken as $1.5/z_0$ while γ_3 , that spreading along y is equal to $1.5n/z_0$. Here n is equal to 5. Each elementary volume is expressed in a closed form by integration. Two type of volumes are first computed : the total volumes V_i and the plastic volumes V_{pi} . The elastic volume V_{ei} come after subtracting V_{pi} to V_i . Indeed, after the yield point, the already deformed elastic part remains but becomes proportionally smaller and smaller as the plastic displacement increases. Unlike other authors, Ogawa et al. gave a differentiated form of the

2.2. Moment-resisting Models of Timber Connections

decay coefficient in the plastic range:

$$\gamma = a_e = \alpha = \begin{cases} \frac{3}{2z_0} & \text{if } \delta \leq \delta_y \\ \frac{3}{2z_0} - \frac{2}{3z_0} \ln \frac{\delta_y}{\delta} & \text{if } \delta \geq \delta_y \end{cases} \quad (2.23)$$

where the yield displacement δ_y is determined by Eq.(2.53) from model "(SM3) Triangular embedment with an exponential-shaped additional length".

The static equilibrium which leads to the determination of moment-rotation relationship $M-\theta$ is determined typically like AIJ [AIJ10], Inayama [Ina91, Ina93] and Komatsu [KKJM09]. First the local forces are obtained through deformed volumes by integration and then the moment is calculated with the lever arm while Tanahashi integrated a complete set to compute the moment. The resisting moment is finally expressed as $M = (E_{\perp} / H \sum_{i=1}^4 V_{ei} + r \cdot E_{\perp} / H \sum_{i=1}^4 V_{pi}) \times l_u \times 2$. E_{\perp} is the young's modulus of wood in transverse compression. The depth of the beam H is equal to a in Fig.2.39. l_u is the lever arm in the same figure. r is the penalization factor of the elastic modulus to address its weakening in the plastic range. By simplification the lever arm is taken $l_u/3$ without considering the effect of the additional length. The gap is introduced as a initial slip without considering its influence on the contact length.

The model was accurate but demonstrated a larger rotational stiffness than the test results.

The authors suggested improvements :

- + refine the elastic modulus by more compression tests on wood species sample
- + correct the lever arm with considering the additional length
- + add the friction forces in the model

Another ancestral technique gives its particularity to the temples, pagodas and other shrines. Exported in different Asian countries from China, the Dou-gong joints is an interlocking wooden brackets also called Tokyo, Kumimono or Masugumi in Japan and Dieh-dou in Taiwan. It is a complex stacking of bearing blocks and beams which are interlocked each other in three dimensions. This stacking of parts exclusively in wood invokes two different embedment mechanisms : the same than the crosspiece-type joints for the connection between Shu and Gong and a simplified block model pre-stressed by the vertical roof load and submitted to a moment (see Fig.2.40). For the latter, Kumatori proposed a model which differs from the Nuki joint. The block (Dou or Datoi) is this time loaded on its full surface without considering spring back effect. It is not described in the present thesis as no relevant to the behavior of our case study : the multiple tab-and-slot joint. A clear explanation of the block model is given both by Kitamori [KJH⁺10] and Yeo [YKHQ16, Yeo16]. In addition, Fig.2.41 shown the equivalent spring (or component) model of Dieh-dou joints [YKHQ16].

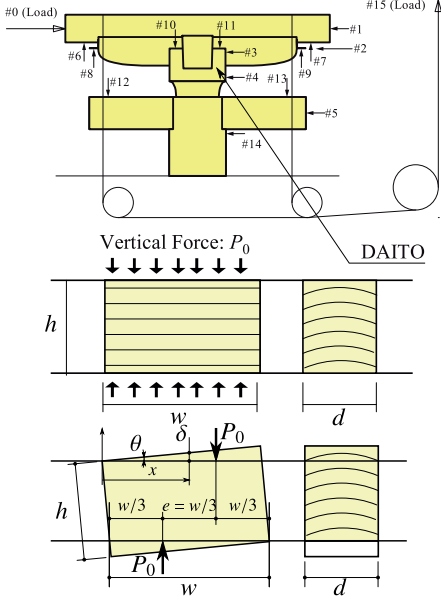
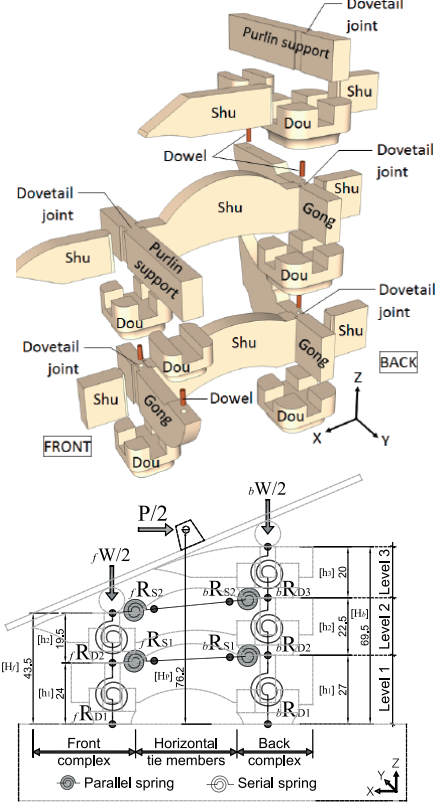
Author	Joint modeling	Stiffness model
<p>Kitamori (Japan)</p>	 <p>Figure 2.40 – Kumimono joint [KJH⁺10]</p>	<p>See : Simplified block model in Kitamori's paper [KJH⁺10]</p>
<p>Yeo (Taiwan)</p>	 <p>Figure 2.41 – Dieh-dou joint [YKHQ16]</p>	<p>See : Simplified block model in Kitamori's paper [KJH⁺10]</p> <p>(SM3) Triangular embedment with an exponential-shaped additional length</p>

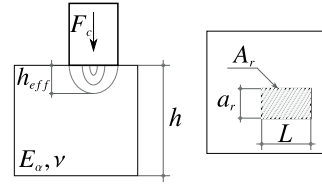
Table 2.4 – Models for traditional Asiatic interlocking brackets joints

2.2.4 Stiffness models for the components

(SM1) Elastostatics of a Half Space in Soil Mechanics

As presented in the previous section, some of the authors made the analogy with soil mechanics formulas to describe the contact law between blocks of wood in the noment-resisting behavior of traditional timber joints. For instance, Wald [WMSD00], Drdácký [DWM99, DWS99] and Descamps [DLL06, DG09, DL09, DN09] considered the wood-to-wood contact as a soil-foundation interaction problem. Thus the spring stiffness of the component of wood in compression is adapted from the settlement of a rectangular rigid shallow foundation resting on an elastic half space, in Eq.(2.24).

$$\delta_c = \frac{F_c I_{\delta_c} a_r}{E_\alpha A_r} \quad (2.24)$$



where

- δ_c^* = the deformation under compression
- F_c = the applied compressed force
- a_r = the width of the bearing block or equivalent rigid plate
- E_α = the young's modulus of wood at grain orientation α
- $A_r = a_r \cdot L$, the area of the bearing block or equivalent rigid plate surface
- $I_{\delta_c}^{**}$ = an Influence factor which depends on L/a_r and the Poisson's ratio ν

Budhu [Bud15] gave a short and clear definition of the half space in soil mechanics: “assuming that the soil is a semi-infinite, homogeneous, linear, isotropic, elastic material”, “an elastic half space” is a “semi-infinite mass bounded on one side and which extends infinitely in all other directions. For soils, the horizontal surface is the bounding side. Because of the assumption of a linear elastic soil mass, we can use the principle of superposition. That is, the stress increases at a given point in a soil mass from different surface loads can be added together”. These assumptions simplify the boundary conditions and the classical elasticity theory developed for the elastic half-space are largely applicable. Stress and displacements can be represented by mechanical or mathematical models derived from the characteristics of the soil where rests the foundation.

Most of the current models have inherited the work of the french mathematician Boussinesq's [Bou85]. The displacement components of the point N(x,y,z) due to a vertical punctual load acting on the surface of an elastic and isotropic half-space (see Fig.2.42a) are given by the following equations known as Boussinesq's equations.

*To avoid any confusion with the grain orientation, we replaced α by I_{δ_c} within the initial Wald's formula.
 ** δ_c is commonly denoted ρ , S_e , u_z or w in soil mechanics.

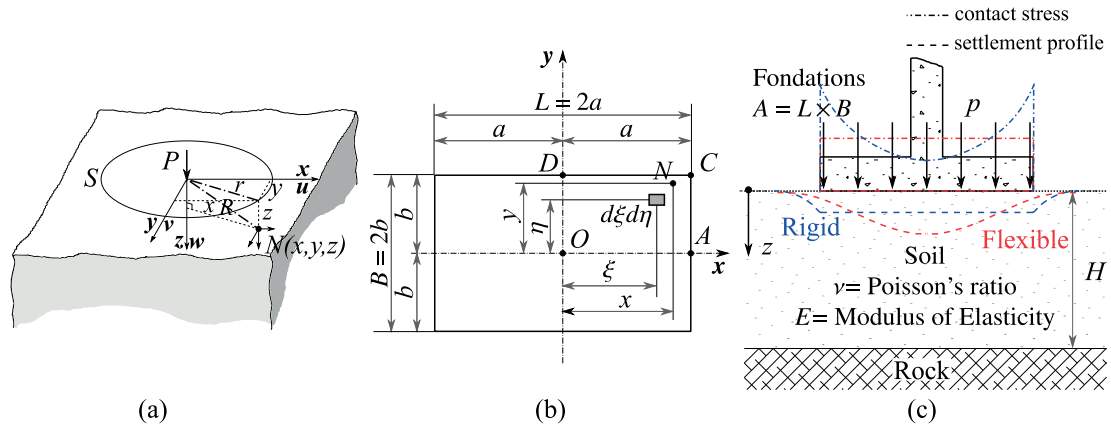


Figure 2.42 – (a) Point load on a half-space surface, (b) Vertical uniform load on a flexible rectangular footing, (c) General case of rectangular shallow foundation.

$$u(x, y, z) = \frac{P(1 + \nu)}{2\pi E} \frac{1}{R} \left[\frac{xz}{R^2} - \frac{(1 - 2\nu)x}{R + z} \right] \quad (2.25a)$$

$$v(x, y, z) = \frac{P(1 + \nu)}{2\pi E} \frac{1}{R} \left[\frac{yz}{R^2} - \frac{(1 - 2\nu)y}{R + z} \right] \quad (2.25b)$$

$$w(x, y, z) = \frac{P(1 + \nu)}{2\pi E} \frac{1}{R} \left[\frac{z^2}{R^2} + 2(1 - \nu) \right] \quad (2.25c)$$

Where x, y, z are the coordinates of an arbitrary point N in a Cartesian coordinate system whose origin $O(0, 0, 0)$ is in the boundary plane of the half-space. z -axis is positive downward into the body. u, v, w are the displacement components for the point $N(x, y, z)$ in the directions of the positive coordinate axes.

NOTA : A contemporary mathematical demonstration of the Boussinesq's equation have been proposed by Johnson in the chapter 3 of his book "Contact mechanics" [Joh85].

The relationship between the elastic modulus E , the Poisson's ratio ν and shear modulus G is $E = 2(1 + \nu)G$. For the points $(x, y, 0)$ of the boundary plane $z = 0$, the equations Eqs. (2.25a)–(2.25c) of the displacements become :

$$u(x, y, 0) = -(1 - 2\nu) \frac{P(1 + \nu)}{2\pi E} \frac{x}{R^2} = -(1 - 2\nu) \frac{P}{4\pi G} \frac{x}{R^2} = -\frac{m - 2}{m} \frac{P}{4\pi G} \frac{x}{R^2} \quad (2.26a)$$

$$v(x, y, 0) = -(1 - 2\nu) \frac{P(1 + \nu)}{2\pi E} \frac{y}{R^2} = -(1 - 2\nu) \frac{P}{4\pi G} \frac{y}{R^2} = -\frac{m - 2}{m} \frac{P}{4\pi G} \frac{y}{R^2} \quad (2.26b)$$

$$w(x, y, 0) = 2(1 - \nu) \frac{P(1 + \nu)}{2\pi E} \frac{1}{R} = (1 - \nu) \frac{P}{2\pi G} \frac{1}{R} = \frac{m^2 - 1}{m^2} \frac{P}{2\pi G} \frac{1}{R} \quad (2.26c)$$

In the previous equations Eqs. (2.26a)–(2.26c), we find the mathematical forms described by Johnson [Joh85] and Milović [Mil92] expressed with young modulus in the second member,

2.2. Moment-resisting Models of Timber Connections

with shear modulus in the third member and finally by Schleicher [Sch26] with $m = 1/\nu$ in the last member.

It can be noticed that the Poisson's ratio is sometimes defined as μ [Ter43, Bow87, Mil92, MR01] or $m = 1/\nu$ in soil mechanics. To avoid any confusion with the Lamé's elastic constants λ and μ [Bou85, Lov29], the symbol ν [Lov29, TG51, Bar62, RVW67, LW69, Joh85, DG86, Cra04, Wor07, Das07, Ver10], commonly adopted, e.g. in material science and mechanics, is used in the present dissertation for the Poisson's ratio. For clarification, the Lamé's constants are expressed according to the elastic properties of the material E and ν in the equations below.

$$\text{Lamé's elastic constants} \quad \lambda = \frac{\nu E}{(1 + \nu)(1 - 2\nu)}, \quad \mu = \frac{\nu E}{2(1 + \nu)} \quad (2.27)$$

At the boundary surface $z = 0$, the expressions can be expressed as functions of x and y .

As presented by Schleicher [Sch26] and reprinted by [Mil92], by replacing P by $p dA = p(\xi, \eta) d\xi d\eta$ and $R = \sqrt{x^2 + y^2}$ by $R = \sqrt{(x - \xi)^2 + (y - \eta)^2}$ in the last members of equations Eqs. (2.26a)–(2.26c), we get, in equations Eqs. (2.28a)–(2.28c), the displacement components considering an uniform vertical load continuously distributed over a certain area A . In fact, the principle of superposition apply and the results are obtained by integration of the concerned individual effects.

$$u(x, y) = -\frac{m-2}{2(m-1)} \frac{1}{\pi C} \iint_A \frac{p(\xi, \eta)(x - \xi)}{(x - \xi)^2 + (y - \eta)^2} d\xi d\eta \quad (2.28a)$$

$$v(x, y) = -\frac{m-2}{2(m-1)} \frac{1}{\pi C} \iint_A \frac{p(\xi, \eta)(y - \eta)}{(x - \xi)^2 + (y - \eta)^2} d\xi d\eta \quad (2.28b)$$

$$w(x, y) = \frac{1}{\pi C} \iint_A \frac{p(\xi, \eta)}{\sqrt{(x - \xi)^2 + (y - \eta)^2}} d\xi d\eta \quad (2.28c)$$

$$C \text{ is defined by } C = \frac{m^2 E}{m^2 - 1} = \frac{E}{1 - \nu^2} = \frac{2G}{1 - \nu}.$$

In response to gravity loads, the vertical settlement is more critical than the horizontal displacement fields. It governed the stability of the structure that rest on the foundations. The soil mechanics literature proposes many information about the topic. In order to explain more about the equation Eq.(2.24), the hereafter discussion restrict itself to the consideration of vertical settlement (or displacement) w for a flexible rectangular shallow foundation and then for a rigid one.

Flexible case

The parameters and variables used in the previous equations are shown in Fig.2.42b for the particular case of a flexible rectangular foundation under vertical uniform pressure. The rectangle footing of length $L = 2a$ and width $B = 2b$ has an area $A = B \times L = 2b \times 2a$. After the double integration of equation Eq.(2.28c) with boundaries $\xi \in [-a, +a]$ and $\eta \in [-b, b]$,

$$w(x, y) = \frac{1}{\pi C} \int_{-a}^a \int_{-b}^b \frac{p(\xi, \eta)}{\sqrt{(x-\xi)^2 + (y-\eta)^2}} d\xi d\eta \quad (2.29)$$

we obtain the equation Eq.(2.30) written in the compact and ordered form proposed by Schleicher [Sch26].

$$\begin{aligned} w(x, y) = \frac{p}{\pi C} & \left[(b-y) \ln \frac{\sqrt{(a-x)^2 + (b-y)^2} + (a-x)}{\sqrt{(a+x)^2 + (b-y)^2} + (a-x)} \right. \\ & + (b+y) \ln \frac{\sqrt{(a-x)^2 + (b+y)^2} + (a-x)}{\sqrt{(a+x)^2 + (b+y)^2} - (a+x)} \\ & + (a-x) \ln \frac{\sqrt{(a-x)^2 + (b-y)^2} + (b-y)}{\sqrt{(a-x)^2 + (b+y)^2} - (b+y)} \\ & \left. + (a+x) \ln \frac{\sqrt{(a+x)^2 + (b-y)^2} + (b-y)}{\sqrt{(a+x)^2 + (b+y)^2} - (b+y)} \right] \end{aligned} \quad (2.30)$$

At the particular points $O(0, 0)$, $A(a, 0)$, $C(a, b)$, $D(0, b)$ Fig.2.42b, the previous expression (2.30) can be written as :

$$O : w(0, 0) = \frac{2p}{\pi C} \left[a \ln \frac{\sqrt{a^2 + b^2} + b}{\sqrt{a^2 + b^2} - b} + b \ln \frac{\sqrt{a^2 + b^2} + a}{\sqrt{a^2 + b^2} - a} \right] \quad (2.31a)$$

$$A : w(a, 0) = \frac{2p}{\pi C} \left[a \ln \frac{\sqrt{4a^2 + b^2} + b}{\sqrt{4a^2 + b^2} - b} + b \ln \frac{b}{\sqrt{4a^2 + b^2} - 2a} \right] \quad (2.31b)$$

$$C : w(a, b) = \frac{2p}{\pi C} \left[a \ln \frac{a}{\sqrt{a^2 + b^2} - b} + b \ln \frac{b}{\sqrt{a^2 + b^2} - a} \right] \quad (2.31c)$$

$$D : w(0, b) = \frac{2p}{\pi C} \left[a \ln \frac{a}{\sqrt{a^2 + 4b^2} - 2b} + b \ln \frac{\sqrt{a^2 + 4b^2} + a}{\sqrt{a^2 + 4b^2} - a} \right] \quad (2.31d)$$

and an average settlement is given for an absolute flexible footing with rectangular base under uniform distributed vertical pressure. The average settlement is defined by the following double integration,

$$w_{mean} = \frac{\int_0^a dx \int_0^b w(x, y) dy}{ab} \quad (2.32)$$

2.2. Moment-resisting Models of Timber Connections

and considering $A = 4ab$, $\alpha = \frac{b}{a}$, $a = \frac{\sqrt{A}}{2\sqrt{\alpha}}$ and $b = \frac{\sqrt{AF}}{2}$, an analytical form is provided as

$$w_{mean} = \frac{p\sqrt{A}}{\pi C\sqrt{\alpha}} \left[\ln \frac{\sqrt{1+\alpha^2} + \alpha}{\sqrt{1+\alpha^2} - \alpha} + \alpha \ln \frac{\sqrt{1+\alpha^2} + 1}{\sqrt{1+\alpha^2} - 1} - \frac{2}{3} \cdot \frac{(1+\alpha^2)^{3/2} - (1+\alpha^3)}{\alpha} \right] \quad (2.33)$$

and

$$O : w(0,0) = \frac{p\sqrt{A}}{\pi C\sqrt{\alpha}} \left[\ln \frac{\sqrt{1+\alpha^2} + \alpha}{\sqrt{1+\alpha^2} - \alpha} + \alpha \ln \frac{\sqrt{1+\alpha^2} + 1}{\sqrt{1+\alpha^2} - 1} \right] \quad (2.34a)$$

$$A : w(a,0) = \frac{p\sqrt{A}}{\pi C\sqrt{\alpha}} \left[\ln \frac{\sqrt{4+\alpha^2} + \alpha}{\sqrt{4+\alpha^2} - \alpha} + \alpha \ln \frac{\alpha}{\sqrt{4+\alpha^2} - 2} \right] \quad (2.34b)$$

$$C : w(a,b) = \frac{p\sqrt{A}}{\pi C\sqrt{\alpha}} \left[\ln \frac{1}{\sqrt{1+\alpha^2} - \alpha} + \alpha \ln \frac{\alpha}{\sqrt{1+\alpha^2} - 1} \right] \quad (2.34c)$$

$$D : w(0,b) = \frac{p\sqrt{A}}{\pi C\sqrt{\alpha}} \left[\ln \frac{1}{\sqrt{1+4\alpha^2} - 2\alpha} + \alpha \ln \frac{\sqrt{1+4\alpha^2} + 1}{\sqrt{1+4\alpha^2} - 1} \right] \quad (2.34d)$$

The settlement for a flexible rectangular foundation under uniform pressure is usually found in a simplified form in the soil mechanics literature as

$$w = \frac{p\sqrt{A}}{C} I_{schl} \quad (2.35)$$

The values of I_{schl} at different points of a flexible rectangular plate are given in table 2.5.

For clarity, the expression of the mean influence factor coming from Eq.(2.33) and Eq.(2.35) is given below.

$$I_{schl,mean} = \frac{1}{\pi\sqrt{\alpha}} \left[\ln \frac{\sqrt{1+\alpha^2} + \alpha}{\sqrt{1+\alpha^2} - \alpha} + \alpha \ln \frac{\sqrt{1+\alpha^2} + 1}{\sqrt{1+\alpha^2} - 1} - \frac{2}{3} \cdot \frac{(1+\alpha^2)^{3/2} - (1+\alpha^3)}{\alpha} \right] \quad (2.36)$$

The mean spring stiffness can be expressed as usual by $k_{mean} = \frac{p}{w_{mean}}$ and from equation (2.33), we get

$$k_{mean} = \frac{C}{\sqrt{F}} \cdot \frac{\pi\sqrt{\alpha}}{\ln \frac{\sqrt{1+\alpha^2} + \alpha}{\sqrt{1+\alpha^2} - \alpha} + \alpha \ln \frac{\sqrt{1+\alpha^2} + 1}{\sqrt{1+\alpha^2} - 1} - \frac{2}{3} \cdot \frac{(1+\alpha^2)^{3/2} - (1+\alpha^3)}{\alpha}} \quad (2.37)$$

$\frac{L}{B}$	I_{sch}				
	O	A	C	D	mean
1	1.12	0.76	0.56	0.76	0.95
1.5	1.11	0.79	0.55	0.73	0.94
2	1.08	0.79	0.54	0.69	0.92
3	1.03	0.78	0.51	0.64	0.88
5	0.94	0.75	0.47	0.57	0.82
10	0.80	0.67	0.40	0.47	0.71

Table 2.5 – Influence factor for the settlement of rectangular flexible area

The formula for settlement can be found in literature written in different forms :

$$\text{Schleicher (flexible) [Sch26]} \quad w = \frac{(1 - \nu^2)}{E} p \sqrt{A} I_{sch} \quad (2.38a)$$

$$\text{Schleicher (flexible) [Sch26]} \quad w = \frac{(1 - \nu^2)}{E} \frac{P}{\sqrt{A}} I_{sch} \quad (2.38b)$$

$$\text{Giroud (flexible) [Gir68, PD74]} \quad w = \frac{(1 - \nu^2)}{E} p B I_{gir} \rightarrow I_{gir} = \frac{I_{sch}}{\sqrt{L/B}} \quad (2.38c)$$

$$\text{Barkan (rigid) [Bar62]} \quad w = \frac{(1 - \nu^2)}{E} \frac{P}{\sqrt{A}} \frac{1}{\beta_z} \quad (2.38d)$$

$$\text{Wald (rigid) [WMSD00]} \quad w = \frac{P I_{wal} B}{EA} = \frac{P I_{wal}}{E \sqrt{A} \sqrt{L/B}} \rightarrow I_{wal} = \frac{(1 - \nu^2) \sqrt{L/B}}{\beta_z} \quad (2.38e)$$

$$\text{Pais (rigid) [PK88]} \quad w = \frac{(1 - \nu^2)}{E} \frac{P}{\sqrt{A}} \frac{4 \sqrt{L/B}}{[3.1 (L/B)^{0.75} + 1.6]} \quad (2.38f)$$

Some rigid-case formulations were also added as matter of comparison.

Rigid case

When the foundation is considered as flexible and loaded with a uniformly distributed load, the settlement profile has a bowl shape and the contact stress over the base is uniform (see red lines Fig.2.42c). The maximum deflection is at the center (point O, Fig.2.42b). A rigid foundation similarly loaded has an uniform settlement profile over the footing and generates vertical stress such as shown in Fig.2.42c (blue dotdash). The stress grow continually with the distance from the center and , in theory, should reach infinity at the edges. But not any material is infinitely elastic and can sustain infinity stresses. Plastic deformations will begin and stresses, although much larger than at the center, will reach a finite limit. These two assumptions supposed that the soil is cohesive like saturated clay [Das07, Bar62].

For the rigid case, only Schleicher [Sch26] gave an exact solution for a circular foundation. For

2.2. Moment-resisting Models of Timber Connections

rectangular rigid foundation, several authors proposed approximated solutions with influence factors as function of the ratio L/B . A condensed form of such solution is given in Eq.(2.39).

$$w = \frac{(1 - \nu^2)}{E} \frac{P}{\sqrt{A}} \cdot I_{w,rigid} \quad (2.39)$$

A list of values that depend on which author provided it is summarized in the table 2.6. The

$\frac{L}{B}$	$I_{w,rigid}$						
	I_{whr}	I_{bar}	I_{mil}	I_{gor}	I_{dem}	I_{pai}	$I_{sch,rigid}$
1	0.93	0.93	0.92	0.88	0.87	0.85	0.88
1.5	0.93	-	0.92	0.87	0.86	0.84	0.87
2	0.90	0.91	0.91	0.86	0.85	0.83	0.86
3	0.86	0.87	0.87	0.84	0.82	0.80	0.82
5	0.79	0.81	0.81	0.78	0.76	0.75	0.76
10	0.70	0.71	0.71	0.67	-	0.66	0.66

Table 2.6 – Influence factor for the settlement of rectangular rigid plate

influence factor I_{whr} can be obtained by divided 2 by β_z , the value read from Whitman and Richart curves [RVW67]. Barkan [Bar62] proposed two different coefficients for flexible and rigid(I_{bar}) rectangular foundation. Milovic [Mil92] provided a simple table of coefficients I_{mil} while Gorbunov-Possadov expressed the settlement by a double power series and built a graph to read the values of I_{gor} . Dempsey [DL89] numerically solved the rigid case and filled a table to determine I_{dem} . The values of I_{pai} came from Pais's approximate formula [PK88] shown by eq.(2.38f). It was commonly adopted in soils foundations [Bow96, Wor07] that the settlement for rigid bases is about 7% less than the average settlement of flexible bases so $I_{sch,rigid} = 0.93 \cdot I_{sch,flexible}$.

Limitations of the models for timber connections

A certain analogy can be made with connection for timber as foundations are neither perfectly flexible nor infinitely rigid. The actual behavior depends on the elastic properties of the footing and the nature of the soil. In their respective works, Descamps [DLL06, DG09, DL09, DN09], Drdácý [DWM99, DWS99] and Wald [WMSD00] considered the case of rigid foundations. Descamps enhanced the stiffness definition arising from elastostatics of a half space with correction factors. This fully support the conclusions, among others authors, of Terzaghi [Ter43] and Scott [Sco13]. In all the results presented above, it was assumed that the compressible soil is of infinite depth, meaning $H \rightarrow \infty$ in Fig.2.42c. In practice, the elastic layer of compressible soil is resting on a relatively incompressible base located at a finite depth H . As the depth is limited by a rigid boundary, the lateral spread of the load through the elastic stratum is reduced and the vertical component of stress increases below the directly loaded area. An

over influence shall be taken into consideration. In the above formulas, the rigidity properties of the foundation have never been reported, only the mechanical properties of the soil are used. Some authors like Milovic [Mil92] defined a system stiffness K factor which considers both properties of soil and raft. Then a new set of influence coefficient I_w is established to consider stiffness factor K and the ratios L/B , relative to the geometry of the raft and H/B , relative to the finite depth from bottom surface of the raft and the rigid boundary of the elastic layer. For all these reasons, the estimation of the settlement in soil foundations is often subject to uncertainties. Hence, using it to estimate the stiffness in the case of timber connections is really limited to simplified elastic analysis. Descamps mentioned that the stiffness was overestimated by 40% with the component method while numerical and experimental analyzes gave corroborating results. In his case study, the overestimation was not of importance on the global analysis of the frame structure.

This model was not adopted in this thesis as it is based on isotropic linear elastic continuum assumptions and does not cover the plastic range in the described formulations.

2.2. Moment-resisting Models of Timber Connections

(SM2) Triangular embedment with a linear additional length

To conduct tests in rotational partial compression, Sakata et al. [SYO12] developed a specific setup shown in Fig.2.43. The design allows to constraint the rotation center at the bottom left edges of the vertical part. The lying part is thus compressed by the full area $x \times B$ of the standing part during rotation and application of load. x and B are the thickness and the width of the vertical wooden part. The strain distribution is defined with a triangular shape beneath

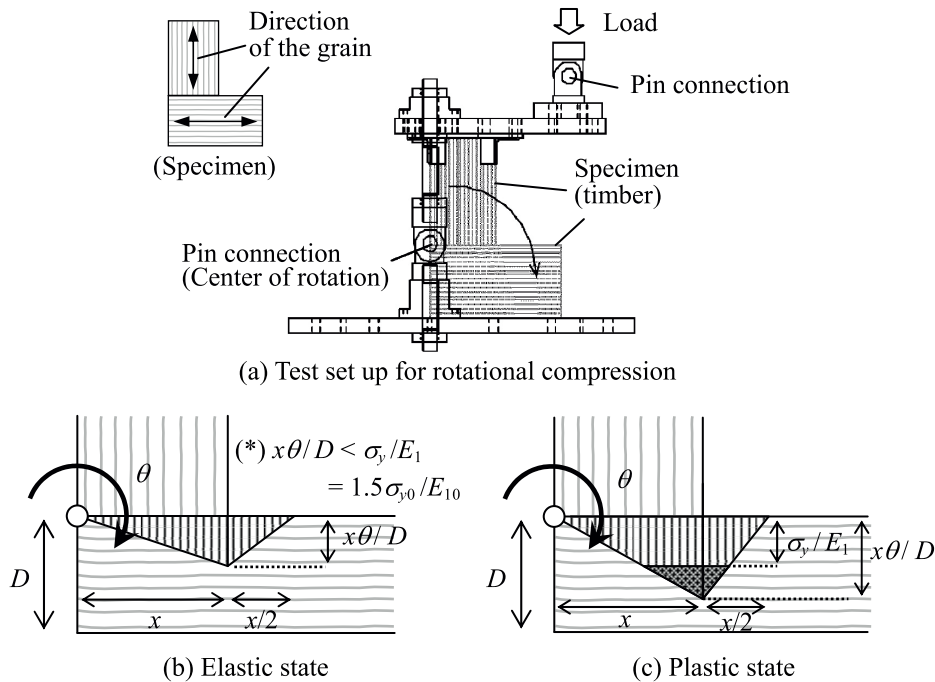


Figure 2.43 – Triangular embedment : test setup and deformation profile with additional length [SYO12]

the rigid contact, like Chang et al., and an additional length effect is taken into account and set to half the initial contact length. The deformed volume due to the additional length effect is simplified as a triangle. As shown in Fig.2.36, frictional forces F_{fyi} are part of the model by multiplying the embedment resisting forces between the tenon and mortise faces F_{cx_i} by a friction coefficient μ of 0.2. The elastic and plastic young's modulus, E_1 and E_2 , respectively, are taken from bi-linear approximation of the translational compression test curves. The yield stress σ_{y0} coming from the same graph is multiplied by 1.5 to get the one in rotational compression (σ_{y0}). The strain distribution is also derived in the plastic state with a yield displacement threshold fixed at σ_y/E_1 .

(SM3) Triangular embedment with an exponential-shaped additional length

The “Fundamental Theory of Timber Engineering” book [AIJ10] of the Architectural Institute of Japan (AIJ) retained the work from Inayama [Ina91, Ina93] to propose design formulas for partial compression of wood perpendicular to the fiber. The problem was addressed both for translational (refer to Fig.2.44a) and rotational partial compression (refer to Fig.2.44c).

Since wood has a structure like bundled hollow cylindrical cells, the material properties in the transverse direction are smaller than that in the longitudinal direction of grain. Therefore, the embedment which develops in the transverse direction on a local area of timber members, becomes the determining factor for the structural strength. On the other hand, it is possible to make use of this in order to exhibit characteristically ductile behavior for the previously presented wood-to-wood joints. In general, wood subjected to full transverse compression shows an elasto-plastic behavior. In partial transverse compression, like a raft can do on a saturated clay soil, the directly pressured surface is extended by extra lengths all over the direct contact area if the distance to the member edges are sufficient (see Fig.2.44b,d,e). In the condition of embedment, the stress is gradually spread from the vicinity of the directly pressurized surface due to the additional length effect. As a result, Fig.2.44f shows a bi-linear stress-strain curve of partial compression where yield strength, initial stiffness and tangent stiffness increase relatively to full compression. The positive rising slope of the plastic part, in partial compression, explained also the contribution observed for the ductility.

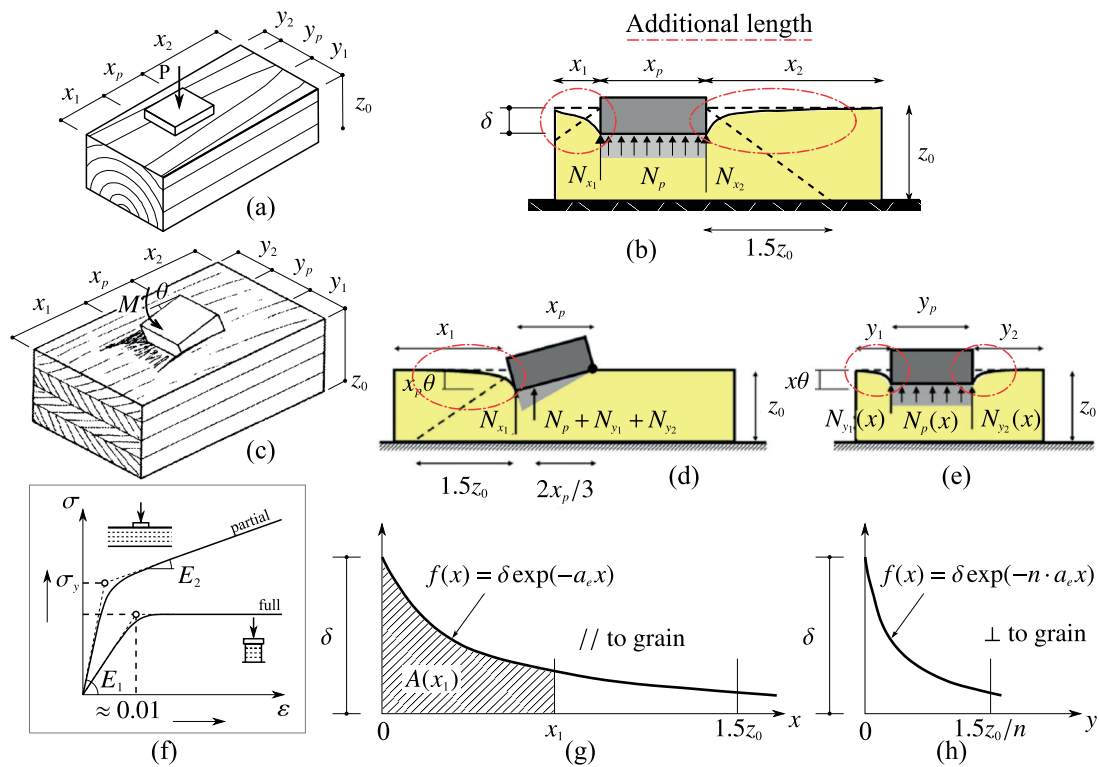


Figure 2.44 – Additional length effect on rotational partial compression [Ina91, Ina93, AIJ10]

2.2. Moment-resisting Models of Timber Connections

As a result of past experiments and above explanations, AIJ listed the characteristics of the embedment as follows

- initial stiffness (E_1) and tangent stiffness (E_2) are both improved. A simplified calculation formula of $E_2 = 0.13(E_1 - E_{\perp})$ is provided by AIJ but complementary studies are needed as the value is not accurate.
- the improvement of stress in partial compression is due to the spreading of stress beyond the directly loaded surface,
- the additional length in the fiber direction with high bending and shear rigidity is more effective than that in the fiber perpendicular direction,
- for the same additional length, the smaller the width of the stressed surface is, the higher the effect is.
- Even with a short additional length, the effect is largely significant, and as the additional length gets longer than a certain limit, no more increasing is noticed. Along the fiber AIJ proposed like Madsen [MHH82, Mad00] did, that the additional length threshold is $1.5 \times$ the material thickness.
- The improvement rate of yield strength is not as large as the improvement rate of elastic stiffness. Therefore, strain at yield decreases.
- The increase in yield stress tends to take a constant upper limit value regardless of member thickness.

The assumptions used for deriving the design formulas for embedment described hereinafter are :

1. Within the elastic range, the volume deformed by embedment and the applied force are proportional.
2. Assuming that the stress spread along fiber is proportional to the material thickness, the additional length from the edge of the loaded block is 1.5 times the thickness of the material (refer to Fig.2.44 b,d,e).
3. The additional length in the direction perpendicular to the grain is that in the parallel direction divided by n (AIJ currently admitted values of n between 5 and 7 for Japanese coniferous wood).
4. The additional length profile is defined by an exponential function.
5. Even in the case where the additional length can not get the assumed vanishing point ($1.5 \cdot z_0$), the exponential function shape remains the same.

Translational partial compression

Before presenting the design formulas for RPC, the translational behavior has to be introduced.

Using the classical Hook's formula, in the elastic range, the local force is expressed as $F = \sigma \cdot A = E \cdot \varepsilon A = E \frac{\delta_h}{h} A = E \frac{V}{h}$. F is the local force, σ is the transverse stress, A is the area of the loaded surface, E is the elastic modulus, ε is the strain, δ_h is the transverse displacement, h is the height of the wood member and $V = \delta_h \cdot A$ is the deformed volume.

By the application of the previous expression, the local force N_p , directly under the loaded area is obtained as

$$N_p = x_p y_p \frac{\delta}{z_0} E_{\perp} \quad (2.40)$$

The symbols of Eq.(2.40) are shown in Fig.2.44b. E_{\perp} is the young modulus in the transverse direction to the grain (in Japan, $E_{\perp} = E_{\parallel}/25 \sim 50$).

In the case of the indirectly loaded area, as shown in Fig.2.44g, the exponential function shape applied and the section of the deformed volume is calculated by integration of $f(x) = \delta e^{-a_e x_i}$.

$$A(x_i) = \int f(x) dx = \frac{\delta}{a_e} (1 - e^{-a_e x_i}) \quad (2.41)$$

How the value of the decay coefficient was fixed by AIJ has been clarified by Kitamori [KMKK09]. First, if we consider the limit edges of the member at an infinite distance from the edge of the bearing blocks, $A(x)$ is reduced to

$$A(\infty) = \frac{\delta}{a_e} \quad (2.42)$$

As assumed, the threshold of the additional length is $1.5 \times z_0$. At this limit, the integrated area is considered covering 90% of the full area under the curve $f(x)$. So, it can be expressed as

$$\frac{A\left(\frac{3z_0}{2}\right)}{A(\infty)} = 1 - \exp\left(-a_e \frac{3z_0}{2}\right) = 0.9 \quad (2.43)$$

and the decay coefficient a_e is approximated thereby

$$-a_e \frac{3z_0}{2} = \ln(0.1) \cong -2.3 \implies a_e \cong \frac{3}{2z_0} \quad (2.44)$$

Finally N_{x_i} , the local forces due to the additional length effect, are taken from $N_{x_i} = E_{\perp} \frac{A(x_i) y_p}{z_0}$, Eq.(2.41) and Eq.(2.44). For both x -sides of the bearing block, they are described by the

2.2. Moment-resisting Models of Timber Connections

following expression.

$$N_{x_1} = \frac{2y_p E_{\perp} \delta}{3} \left(1 - e^{-\frac{3x_1}{2z_0}}\right) = \frac{2z_0}{3x_p} \left(1 - e^{-\frac{3x_1}{2z_0}}\right) N_p \quad (2.45a)$$

$$N_{x_2} = \frac{2y_p E_{\perp} \delta}{3} \left(1 - e^{-\frac{3x_2}{2z_0}}\right) = \frac{2z_0}{3x_p} \left(1 - e^{-\frac{3x_2}{2z_0}}\right) N_p \quad (2.45b)$$

A similar method is used for the direction y , perpendicular to fibers, in the plane of the loaded surface. The symbol x replaced y in Eqs.(2.45a) & (2.45b). The decay coefficient for the y -sides is now $a_e \cong \frac{3n}{2z_0}$. N_{y_i} is given by

$$N_{y_1} = \frac{2x_p E_{\perp} \delta}{3n} \left(1 - e^{-\frac{3ny_1}{2z_0}}\right) = \frac{2z_0}{3ny_p} \left(1 - e^{-\frac{3ny_1}{2z_0}}\right) N_p \quad (2.46a)$$

$$N_{y_2} = \frac{2x_p E_{\perp} \delta}{3n} \left(1 - e^{-\frac{3ny_2}{2z_0}}\right) = \frac{2z_0}{3ny_p} \left(1 - e^{-\frac{3ny_2}{2z_0}}\right) N_p \quad (2.46b)$$

The four components of the local forces due to the additional length effect and the local force under the directly loaded area are summed to calculate the total resisting force in translational partial compression (TPC) perpendicular to the grain.

$$P(N) = N_p + N_{x_1} + N_{x_2} + N_{y_1} + N_{y_2} = \frac{x_p y_p C_x C_y E_{\perp}}{z_0} \delta = x_p y_p C_x C_y \sigma \quad (2.47)$$

C_x and C_y are the increasing ratio of elastic stiffness due to partial compression when the distance to the edge of the wood member is not infinite. C_{xm} and C_{ym} are the increasing ratio of elastic stiffness when the distance to the edge of the wood member is infinitely long. Their condensed expressions are summarized below.

$$C_x = 1 + \frac{2z_0}{3x_p} \left(2 - e^{-\frac{3x_1}{2z_0}} - e^{-\frac{3x_2}{2z_0}}\right) \quad (2.48a)$$

$$C_{xm} = 1 + \frac{4Z_0}{3x_p} \quad (2.48b)$$

$$C_y = 1 + \frac{2z_0}{3ny_p} \left(2 - e^{-\frac{3ny_1}{2z_0}} - e^{-\frac{3ny_2}{2z_0}}\right) \quad (2.48c)$$

$$C_{ym} = 1 + \frac{4Z_0}{3ny_p} \quad (2.48d)$$

With regard to yield displacement, according to Inabaya's experiment [Ina91, Ina93], the assumption that the strain energy U_0 at the yield is a constant value holds,

$$U_0 = \frac{1}{2} \sigma_y \epsilon_y = \frac{\sigma_y^2}{2E_{el}} \quad (2.49)$$

where the increased elastic modulus are defines as

$$E_{el} = C_x C_y E_{\perp} \quad (2.50a)$$

$$E_{el-max} = C_{xm} C_{ym} E_{\perp} \quad (2.50b)$$

Therefore, when the edge-to-edge distance (also called end length) is infinite and the elastic limit response is F_m , the formula (2.51) is established, and leads to Eq.(2.52).

$$\frac{\sigma_y^2}{E_{el}} = \frac{F_m^2}{E_{el-max}} \quad (2.51)$$

$$\sigma_y(N) = F_m \sqrt{\frac{C_x C_y}{C_{xm} C_{ym}}} \quad (2.52)$$

F_m is the embedment yielding stress in case of infinitely long end length. In AIJ's formula, F_m in (N/mm²) is regulated to $F_m = 0.8 \times F_{cv}$. F_{cv} is the yielding stress of partial compression perpendicular to grain in case of 5% strain. For spruce, in Japan, $F_{cv} = 6.0$ N/mm².

From Eq.(2.52), we can derive the equation of the yield displacement in translational partial compression.

$$\delta_y(\text{mm}) = \frac{z_0 F_m}{E_{\perp} \sqrt{C_x C_y C_{xm} C_{ym}}} \quad (2.53)$$

Rotational partial compression

The rotational partial compression is typically the case of the triangular embedment in the traditional Japanese timber joints. The loaded surface is, this, time, deformed by a the rotation of the bearing block. In the AIJ formulation, the center of the rotation is taken ,at an edge of the bearing block, parallel to the y -axis (see Fig.2.44c,d). Therefore, the vertical displacement δ depends on the abscissa x . $N_p(x)$, $N_{y_1}(x)$ and $N_{y_2}(x)$, listed below, are expressed similarly to Eq.(2.40), Eq.(2.46a) and Eq.(2.46b), respectively. They are defined as a function of x and δ is replaced by θx in the referred equations.

$$N_p(x) = \frac{\theta x y_p E_{\perp}}{z_0} \quad (2.54a)$$

$$N_{y_1}(x) = \frac{2\theta x E_{\perp}}{3} \left(1 - e^{-\frac{3ny_1}{2z_0}}\right) = \frac{2}{3ny_p} \left(1 - e^{-\frac{3ny_1}{2z_0}}\right) N_p(x) \quad (2.54b)$$

$$N_{y_2}(x) = \frac{2\theta x E_{\perp}}{3} \left(1 - e^{-\frac{3ny_2}{2z_0}}\right) = \frac{2}{3ny_p} \left(1 - e^{-\frac{3ny_2}{2z_0}}\right) N_p(x) \quad (2.54c)$$

The symbols of the equation are shown in Fig.2.44e. The final expression of these local forces are finally obtained in Eq.(2.55) by summing them and integrating the result from 0 to x_p . x_p

2.2. Moment-resisting Models of Timber Connections

is the direct contact length.

$$N_p + N_{y_1} + N_{y_2} = \int_0^{x_p} (N_p(x) + N_{y_1}(x) + N_{y_2}(x)) dx = \frac{x_p^2 y_p C_y E_{\perp} \theta}{2 z_0} \quad (2.55)$$

C_y is given by Eq.(2.48c). For the last indirectly loaded area which starts at the edge where the vertical displacement $\delta = \theta x_p$ is maximum, the local force N_{x_1} is defines by Eq.(2.56a). At the other x-side of the bearing block, there is no embedment and the local force N_{x_2} can be neglected.

$$N_{x_1} = \frac{2 x_p y_p E_{\perp} \theta}{3} \left(1 - e^{-\frac{3x_1}{2z_0}} \right) \quad (2.56a)$$

$$N_{x_2} \approx 0 \quad (\text{neglected because of no embedment on that side}) \quad (2.56b)$$

Fig.2.44d shows the two different lever arms to be used for the calculation of the resisting moment due to the four embedded parts of the deformed volume. x_p and $2x_p/3$ stands for N_{x_1} and $(N_p + N_{y_1} + N_{y_2})$, respectively. The condensed formula of the resisting moment is written as follows

$$M(\text{N} \cdot \text{mm}) = N_{x_1} \times x_p + (N_p + N_{y_1} + N_{y_2}) \times \frac{2x_p}{3} = \frac{x_p^3 y_p C_y E_{\perp} \theta}{z_0} \left[\frac{1}{3} + \frac{2z_0}{3x_p} \left(1 - e^{-\frac{3x_1}{2z_0}} \right) \right] \quad (2.57)$$

The design formula for the yield angle is derived from the yield displacement formulation Eq.(2.53) where δ is replaced by θx_p .

$$\theta_y(\text{rad}) = \frac{z_0 F_m}{x_p E_{\perp} \sqrt{C_x C_y C_{xm} C_{ym}}} \quad (2.58)$$

C_x , C_y , C_{xm} and C_{ym} are respectively provided by Eqs.Eqs. (2.48a)–(2.48d). For C_x in triangular embedment, x_2 shall be taken equal to x_1 .

Simplified formula for crosspiece joints

The above calculation of triangular embedment is useful for penetrating joints like Nuki joint shown in Fig.2.45.

On this purpose, AIJ proposes simplified formulas which take into account the following assumptions :

1. the triangular embedment is present on both side of the beams and the resisting moment of Eq.(2.57) is multiplied by 2,
2. the end length along the x-direction is long enough to be considered as infinite,
3. no end length along the y-direction,
4. friction μ at the contact surface.

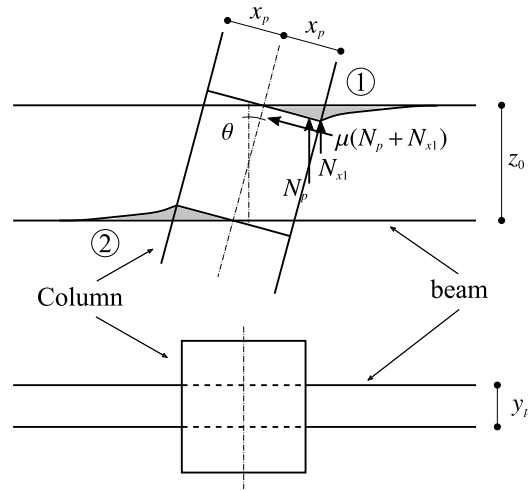


Figure 2.45 – Triangular embedment in penetrating joint

For the structural calculation of such joint in a global structure, the rotational stiffness K_θ and the yield moment M_y can be introduced as

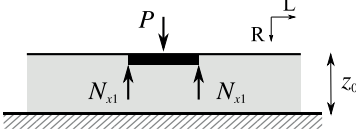
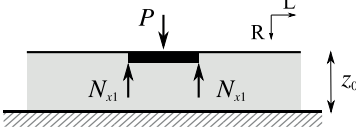
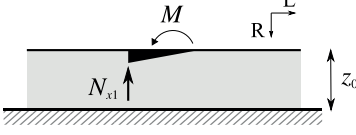
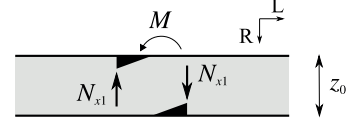
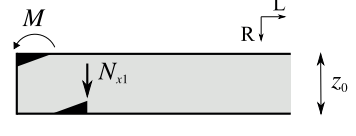
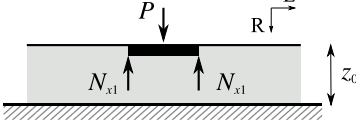
$$K_\theta (\text{N} \cdot \text{mm} / \text{rad}) = x_p^2 y_p E_\perp \left[\frac{x_p}{z_0} \left(C_{xm} - \frac{1}{3} \right) + 0.5 \mu C_{xm} \right] \quad (2.59a)$$

$$M_y (\text{N} \cdot \text{mm}) = \frac{K_\theta z_0 F_m}{x_p E_\perp C_{xm} \sqrt{C_{ym}}} \quad (2.59b)$$

Complementary studies on the decay coefficient a_e

AIJ used the conclusion from Inayama to fix the decay coefficient at $a_e = 1.5/z_0$. Kitamori et al. [KMKK09] conducted a test campaign to evaluate the decay coefficient according to the support conditions (rigid base, cantilever, discrete support), the type of embedment (TPC or RPC) and the number of simultaneous contacts (single or double). They also established the stiffness equation of each case shown in Figs. 2.47–2.50, typically using the AIJ’s formula with $x_1 = \infty$ and $y_1 = y_2 = 0$. Tanahashi et al. [TSS06a, TSS06b, TSH⁺08] used the Pasternak model to determine the decay coefficient $a_e = \gamma \cdot z_0/z_0$. The value of $\gamma \cdot z_0$ was found with matching the results of a FEM analysis with the equations of the Pasternak model (see 2.2.4 “(SM4) Elasto-plastic Pasternak model of embedment behavior of wood”). They addressed only the TPC in single contact. The values of the various decay coefficients are summarized in table 2.7, where L,R and T, are the longitudinal, tangential and radial direction of wood, respectively.

2.2. Moment-resisting Models of Timber Connections

Author	Figure	decay coefficient	x	y	z
Inayama, AIJ [Ina91, Ina93, AIJ10]	 <p style="text-align: center;">Figure 2.46 – TPC - LR Plane</p>	$a_e = \frac{1.5}{z_0}$	L	T	R
Kitamori [KMKK09]	 <p style="text-align: center;">Figure 2.47 – TPC - LR Plane</p>	$a_e = \frac{2.5}{z_0}$	L	T	R
Kitamori [KMKK09]	 <p style="text-align: center;">Figure 2.48 – RPC - single contact</p>	$a_e = \frac{3}{z_0}$	L	T	R
Kitamori [KMKK09]	 <p style="text-align: center;">Figure 2.49 – RPC - double contact</p>	$a_e = \frac{5.5}{z_0}$	L	T	R
Kitamori [KMKK09]	 <p style="text-align: center;">Figure 2.50 – RPC(end) - double contact</p>	$a_e = \frac{5.5}{z_0}$	L	T	R
Tanahashi [TSS06a, TSS06b, TSH ⁺ 08]	 <p style="text-align: center;">Figure 2.51 – TPC - LR plane</p>	$a_e = \frac{3.1}{z_0}$	L	T	R

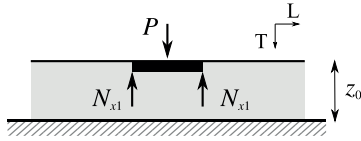
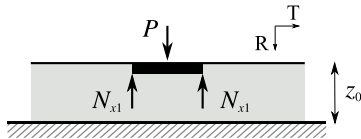
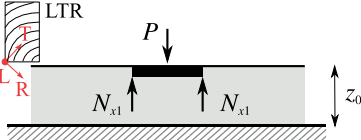
Author	Figure	decay coefficient	x	y	z
Tanahashi [TSS06a, TSS06b, TSH ⁺ 08]	 <p>Figure 2.52 – TPC - LT plane</p>	$a_e = \frac{3.0}{z_0}$	L	R	T
Tanahashi [TSS06a, TSS06b, TSH ⁺ 08]	 <p>Figure 2.53 – TPC - RT plane</p>	$a_e = \frac{9.0}{z_0}$	T	L	R
Tanahashi [TSS06a, TSS06b, TSH ⁺ 08]	 <p>Figure 2.54 – TPC - LTR plane</p>	$a_e = \frac{2.3}{z_0}$	L	T ↷	R ↷

Table 2.7 – Decay coefficients in partial compression - TPC = translational, RPC = rotational.

2.2. Moment-resisting Models of Timber Connections

(SM4) Elasto-plastic Pasternak model of embedment behavior of wood

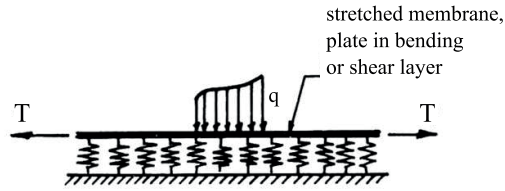


Figure 2.55 – Two parameter soil models [Ker64]

The analytical treatment of partial transverse compression of wood is typically addressed here by using models of soil response with exhibit purely elastic behavior.

Most of the models proposed in the literature restrict on relationship between the applied loads and the resulting displacements given by linear functions. In the case of a rectangular plate resting on an elastic medium, the different options can be summarized as :

Op1- Winkler model : $q(x, y) = kw(x, y)$

Op2- Two parameter model : $q(x, y) = kw(x, y) - G\nabla^2 w(x, y)$

Op3- isotropic elastic medium : $w(x, y) = \frac{1}{\pi C} \int_{-a}^a \int_{-b}^b \frac{p(\xi, \eta)}{\sqrt{(x-\xi)^2 + (y-\eta)^2}} d\xi d\eta$

where q is the load and w is the displacement.

The third option was already presented in section 2.2.4-”(SM1) Elastostatics of a Half Space in Soil Mechanics”. The Winkler model has inherent deficiency to characterize the real behavior of soils; the deflection of the soil layer at any point on the surface is directly proportional to the stress applied at the same point and independent of stresses applied at other locations.

The models with two independent elastic constants overcome the limit of the Winkler model by adding interaction between the isolated springs [Ker64, Ker66]. Filonenko-Borodich [FB40], Hetényi [Het46] and Pasternak [Pas54] proposed mechanical interaction by stretched elastic membrane, elastic plate, or elastic shear layers, respectively.

Vlasov and Leontiev [VL66] started from the elastic continuum model and formulated the problem by a variational method. After introducing constraints and simplifying assumptions on the distribution of stress and displacements, they provided a relation similar to Op2.

Tanahashi et al. used the Pasternak model with Vlasov’s assumptions to depict the behavior of wood under partial transverse compression considering a infinite end lengths [TSS06a, TSS06b] and a finite end lengths [TSH⁺08, TOS08]. Their work is presented below.

Governing equation of the Pasternak model

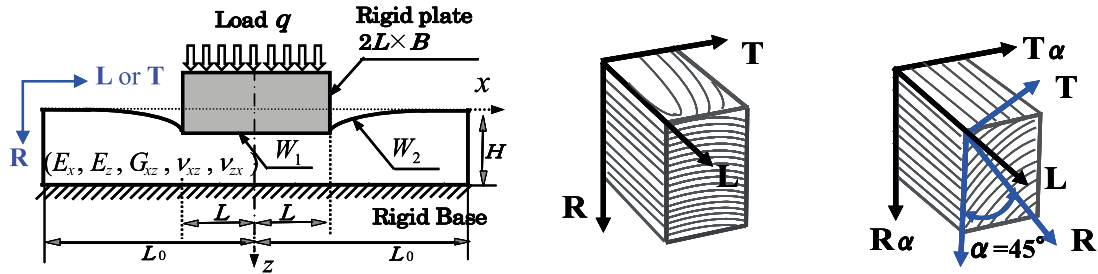


Figure 2.56 – Pasternak model for embedment of orthotropic wood, perpendicular to the grain [TSH⁺08]

The constitutive equations for an orthotropic wood are as follows

$$\begin{bmatrix} \sigma_x \\ \sigma_z \\ \tau_{xz} \end{bmatrix} = \frac{1}{(1 - \nu_{xz}\nu_{zx})} \begin{bmatrix} E_x & E_x\nu_{zx} & 0 \\ E_z\nu_{xz} & E_z & 0 \\ 0 & 0 & (1 - \nu_{xz}\nu_{zx})G_{xz} \end{bmatrix} \begin{bmatrix} \epsilon_x \\ \epsilon_z \\ \gamma_{xz} \end{bmatrix} \quad (2.60)$$

where $\sigma_x, \sigma_z, \tau_{xz}$ are the stresses and ϵ_x, ϵ_z and γ_{xz} , the corresponding strains. E_x, E_z and G_{xz} are the Elastic and Shear modulus in the orthotropic directions, respectively. ν_{xz} and ν_{zx} are the Poisson's ratio. x and z can be indifferently replaced by L,R and T, the longitudinal, tangential and radial direction of wood, respectively.

Vlasov [VL66] proposed a soil elastic model based on a variational method. Constraints on distribution of displacement are introduced to simplify the equations for a linear elastic continuum. Considering plane strain state of the elastic layer on a rigid base in the x - z plane, Vlasov made the following assumptions:

- 1- the horizontal displacement is neglected compared to the vertical displacement under a vertical load. It implies

$$u(x, z) = 0 \quad (2.61)$$

- 2- The vertical displacement $w(x, z)$ is defined using a vertical surface displacement $W(x)$ and a shape function $\phi(x)$. It implies

$$w(x, z) = W(x)\phi(z) \quad (2.62)$$

u and w are the horizontal and vertical displacements, respectively. The function $\phi(z)$ represents the variation of displacement $w(x, Z)$ in the z -direction, typically the depth or the thickness of the elastic layer.

2.2. Moment-resisting Models of Timber Connections

A linear form was proposed for thin layer,

$$\phi(x) = 1 - z/h \quad (2.63)$$

and an exponential form, assumed for deep layer, was used by Tanahashi [TSH⁺08, TOS08] :

$$\phi(z) = \frac{\sinh(\eta(1 - z/H))}{\sinh(\eta)} \quad (2.64)$$

η is the decrease parameter with depth in the formulation of the vertical displacement. The boundary conditions of the function are, in that case,

$$\phi(0) = 1, \quad \phi(H) = 0, \quad w(x, 0) = W(x) \quad (2.65)$$

These shape functions were initially proposed by Vlasov et al., in 1966, on the basis of experimental analysis. In 1977, Jones et al. [JX77] theoretically demonstrated the shape function written in Eq.(2.64). It is worth noting that if $\eta = 0$, Eq.(2.64) is simplified to the linear form in Eq.(2.63).

The displacements due to a uniform load q are considered constrained by the rigid foundation. Therefore, the total potential energy Π of the system can be calculated using a Lagrange multiplier λ . Since the displacement below the rigid plate is assumed to be a constant C , the total potential energy Π is expressed as

$$\begin{aligned} \Pi = & \int_{-L_0}^{L_0} \int_0^H \frac{1}{2} (\sigma_x \varepsilon_x + \sigma_z \varepsilon_z + \tau_{xz} \gamma_{xz}) dz dx - \int_{-L}^L q w(x, 0) dx \\ & + \int_{-L}^L \lambda [w(x, 0) - C] dx \end{aligned} \quad (2.66)$$

Eq.(2.67) is obtained with substituting Eqs.(2.60) and (2.2.4) in Eq.(2.66).

$$\begin{aligned} \Pi = & \int_{-L_0}^{L_0} \int_0^H \left[\frac{E_z}{2(1 - \nu_{xz} \nu_{zx})} \left(\frac{d\phi}{dz} \right)^2 W^2 + \frac{G_{xz}}{2} \phi^2 \left(\frac{dW}{dx} \right)^2 \right] dz dx - \int_{-L}^L q W dx \\ & + \int_{-L}^L \lambda [W - C] dx \end{aligned} \quad (2.67)$$

Hence, the system of governing differential equations is obtained by minimizing the function Π with respect to W and λ on the basis of the variational principles ($\partial\Pi = 0$).

$$\begin{aligned} kW_1 - G \frac{d^2 W_1}{dx^2} &= q - \lambda & \text{if } |x| \leq L \\ W_1 - C &= 0 \\ kW_2 - G \frac{d^2 W_2}{dx^2} &= 0 & \text{if } L < |x| \leq L_0 \end{aligned} \quad (2.68)$$

where

$$\begin{aligned}
 \gamma &= \sqrt{\frac{k}{G}} && : \text{characteristic value of the system} \\
 k &= \frac{E_z}{1 - \nu_{xz}\nu_{zx}} \int_0^H \left(\frac{d\phi}{dz}\right)^2 dz && : \text{vertical spring constant} \\
 G &= G_{xz} \int_0^H \phi^2 dz && : \text{shear stiffness}
 \end{aligned} \tag{2.69}$$

Note that W_1 is the displacement beneath the rigid plate and W_2 is the displacement due to the additional length effect.

Parameters of the Pasternak model

When the load is uniformly distributed over the entire surface ($L \rightarrow \infty$), the strain is constant at all points in the elastic body, and the vertical displacement is linearly distributed in the vertical direction, corresponding to the expression Eq.(2.64). By substituting Eq.(2.63) into Eq.(2.69) and proceeding to the integration, the fundamental parameters are obtained as

$$\begin{aligned}
 k_0 &= \frac{E_z}{(1 - \nu_{xz}\nu_{zx})H} \\
 G_0 &= \frac{G_{xz}H}{3}
 \end{aligned} \tag{2.70}$$

When substituting the exponential form Eq.(2.64) of the shape function into into Eq.(2.69) and still integrating, k and G become

$$\begin{aligned}
 k &= \frac{E_z}{1 - \nu_{xz}\nu_{zx}H} \eta \frac{\sinh \eta \cosh \eta + \eta}{2 \sinh^2 \eta} = k_0 \varphi_k \\
 G &= \frac{G_{xz}H}{3} \frac{1}{\eta} \frac{\sinh \eta \cosh \eta - \eta}{2 \sinh^2 \eta} = 3G_0 \varphi_G
 \end{aligned} \tag{2.71}$$

where

$$\begin{aligned}
 \varphi_k &= \eta \frac{\sinh \eta \cosh \eta + \eta}{2 \sinh^2 \eta} \\
 \varphi_G &= \frac{1}{\eta} \frac{\sinh \eta \cosh \eta - \eta}{2 \sinh^2 \eta}
 \end{aligned} \tag{2.72}$$

Considering the ratio Φ as

$$\Phi = \sqrt{\frac{\varphi_k}{\varphi_G}} = \eta \sqrt{\frac{\sinh \eta \cosh \eta + \eta}{\sinh \eta \cosh \eta - \eta}} \tag{2.73}$$

the non-dimensional characteristic value γH , which depends on the young modulus and the

2.2. Moment-resisting Models of Timber Connections

Poisson's coefficients is written by expression Eq.(2.74).

$$\gamma H = \sqrt{\frac{k}{G}} H = \sqrt{\frac{k_0 \varphi_k}{3G_0 \varphi_G}} H = \sqrt{\frac{E_z}{1 - \nu_{xz}\nu_{zx}G_{xz}}} \Phi \quad (2.74)$$

Solution of the Pasternak model

Like for the case of infinite end length, the displacements W_1 , W_2 are constant at the limit of the rigid plate for $|x| = L$. When the end lengths are considered to be infinite, the displacement in the indirectly loaded areas vanish to 0 at an infinite distance from the edge of plate ($W_2(\pm\infty = 0)$). In the present case with finite lengths, the second equation of Eq.(2.75) comes from the fact that there is no loading at the beam end of Pasternak Model, therefore the tangent of the displacement curve, at the ends must be horizontal. The resulting boundary conditions are as follows

$$\begin{aligned} W_1(\pm L) &= W_2(\pm L) = C \\ \frac{dW_2(x)}{dx} &= 0 \quad \text{if } x = \pm L_0 \end{aligned} \quad (2.75)$$

The equilibrium between the vertical loads and the reaction forces of the support is shown in Eq.(2.76).

$$2qL = 2 \int_0^L kW_1 dx + 2 \int_L^{L_0} kW_2 dx \quad (2.76)$$

The system (2.75) is finally solved with applying the boundary conditions (2.75) and (2.76). It gives the exact solution of the surface displacement as

$$\begin{aligned} W_1 &= \frac{S}{1 + \frac{\tanh(\gamma \cdot \Delta L)}{\gamma \cdot L}} \quad \text{if } |x| \leq L \\ W_2 &= \frac{S}{1 + \frac{\tanh(\gamma \cdot \Delta L)}{\gamma \cdot L}} \frac{\cosh(\gamma(L_0 - x))}{\cosh(\gamma \cdot \Delta L)} \quad \text{if } L < |x| \leq L_0 \end{aligned} \quad (2.77)$$

and the multiplier λ of Lagrangian is given by the expression (2.80).

$$\lambda = \frac{\tanh(\gamma \cdot \Delta L)}{\gamma \cdot L + \tanh(\gamma \cdot \Delta L)} q \quad (2.78)$$

The assumption of having an horizontal asymptote at the ends is not experimentally valid. Under load, the ends of the elastic layer on a rigid base combine an horizontal displacement and a rotation. Hence the displacement profile is more probably governed by an exponential function (see Fig.6 in [TSH⁺08]). Hence, Tanahashi et al. provided an approximate solution

which depicts better the real behavior.

$$\begin{aligned}
 W_1 &= \frac{S}{1 + \frac{1 - e^{\gamma \cdot \Delta L}}{\gamma \cdot L}} & \text{if } |x| \leq L \\
 W_2 &= \frac{S}{1 + \frac{1 - e^{\gamma \cdot \Delta L}}{\gamma \cdot L}} e^{-\gamma|x-L|} & \text{if } L < |x| \leq L_0
 \end{aligned} \tag{2.79}$$

with the multiplier λ of Lagrangian,

$$\lambda = \frac{1 - e^{\gamma \cdot \Delta L}}{\gamma \cdot L + 1 - e^{\gamma \cdot \Delta L}} q \tag{2.80}$$

S is expressed with the fundamental vertical displacement S_0 . S_0 is the vertical displacement in case of $L \rightarrow \infty$.

$$S = \frac{q}{k} = \frac{q}{k_0 \varphi_k} = \frac{(1 - \nu_{xz} \nu_{zx}) q H}{E_z \varphi_k} = \frac{S_0}{\varphi_k} \tag{2.81a}$$

$$S_0 = \frac{q}{k_0} = \frac{(1 - \nu_{xz} \nu_{zx}) q H}{E_z} \tag{2.81b}$$

In addition, as wood embedment is rather shallow, Tanahashi assumed $\eta < 1$ in Eq.(2.64), and referring to Fig.3 in [Tan04] fixed $\varphi_k = 1$. Following his assumptions, the increasing ratio of stiffness of partial compression displacement compared to full compression displacement is

$$\zeta_P = \frac{k_P}{k_0} = \frac{q/W_1}{q/S_0} = \frac{S \varphi_k}{W_1} \cong \frac{S}{W_1} \tag{2.82}$$

and in an expanded form,

$$\zeta_P = \frac{S}{W_1} = 1 + \frac{1 - e^{-\gamma \cdot \Delta L}}{\gamma \cdot L} = 1 + \frac{1 - e^{-\gamma H \cdot \beta}}{\gamma H \cdot \alpha} \tag{2.83}$$

with

$$\begin{aligned}
 \alpha^* &= \frac{L}{H} \\
 \beta^{**} &= \frac{\Delta L}{H} = \frac{L_0 - L}{H}
 \end{aligned}$$

The stress-strain relationship in partial compression is expressed from the full compression

*Note that α replaced λ from [TSH⁺08] to avoid any confusion with the Lagrangian multiplier.

**Note that β replaced δ from [TSH⁺08] to avoid any confusion with the displacement.

2.2. Moment-resisting Models of Timber Connections

strain ε_F by

$$\sigma_P = \zeta_p E \varepsilon_F \quad (2.84)$$

and the following set of equations Eqs. (2.85a)–(2.85d) can be applied for the characterization of orthotropic-assumed wood in partial compression also denoted embedment.

$$W_1 = \frac{S}{\zeta_p} \quad \text{if } |x| \leq L \quad : \text{direct contact} \quad (2.85a)$$

$$W_2 = \frac{S}{\zeta_p} e^{-\gamma|x-L|} \quad \text{if } L < |x| \leq L_0 \quad : \text{additional length effect} \quad (2.85b)$$

$$S = S_0 = \frac{(1 - \nu_{xz}\nu_{zx})qH}{E_z} \quad : \text{Vertical displacement (full compression)} \quad (2.85c)$$

$$\zeta_p = 1 + \frac{1 - e^{-\gamma H \cdot \frac{L_0-L}{H}}}{\gamma H \cdot \frac{L_0-L}{H}} \quad : \text{Increasing stiffness ratio (partial compression)} \quad (2.85d)$$

Of course, it has to be adapted to the particular kinematics of the problem (translational or rotational compression). The expression in rotational compression for the case of Nuki joints is expressed by Eq.(2.13) in section 2.2.3.

Tanahashi et al. summarized in table 2.8 the comparison of the increasing stiffness ratio from different authors, already cited in the present document.

Author	Increasing stiffness ratio	Method
Madsen (Canada) [MHH82]	$\zeta_p = \begin{cases} 1 + \frac{\sqrt{\frac{L_0-L}{H}}}{2.38 \frac{L}{H}} & \text{if } L_0 - L < 1.6 \\ 1 + \frac{1}{1.89 \frac{L}{H}} & \text{if } L_0 - L \geq 1.6 \end{cases}$	Beam on elastic foundation model FEM analysis Experiments
Inayama (Japan) [Ina91, Ina93]	$C_x = 1 + \frac{1 - e^{-1.5 \frac{L_0-L}{H}}}{1.5 \frac{L}{H}} \quad // \text{ to fiber in plane x-y}$ $C_y = 1 + \frac{1 - e^{-1.5n \frac{L_0-L}{H}}}{1.5n \frac{L}{H}} \quad \perp \text{ to fiber in plane x-y}$	Experiments $n = 5 \sim 7$ for coniferous

Chapter 2. State-of-the-Art

Author	Increasing stiffness ratio	Method
Tanahashi ([TSH ⁺ 08])	$\zeta_p = 1 + \frac{1 - e^{-\gamma H \cdot \frac{L}{H}}}{\gamma H \cdot \frac{L_0 - L}{H}}$	Pasternak model FEM analysis

Table 2.8 – Increasing stiffness ratio in partial compression [TSH⁺08]

Simplification of the shape function

Tanahashi [TOIS11] compared four types of shape functions (see table 2.9) and selected the simplified exponential function when comparing with FEM in Fig.2.57. This simplified function was adopted for the moment-resisting model of Nuki joints.

Curve	Type	Shape function ϕ_S	h_y
(1)	Hyperbolic function	$\frac{\eta \cosh(\eta(1 - z/H))}{\sinh \eta}$	$1 - \frac{1}{\eta} \cosh^{-1}\left(\frac{1}{\kappa} \sinh \eta\right)$
(2)	Exponential function (Simplified)	$\eta e^{-\eta \frac{z}{H}}$	$\frac{1}{\eta} \ln \kappa$
(3)	Exponential function (Exact)	$\frac{\eta}{1 - e^{-\eta}} e^{-\eta \frac{z}{H}}$	$\frac{1}{\eta} \ln\left(\frac{\kappa}{1 - e^{-\eta}}\right)$
(4)	Exponential function (Revised)	$\eta e^{-\eta \sqrt{\frac{z}{H}}}$	$\left(\frac{1}{\eta} \ln \kappa\right)^2$

Table 2.9 – Increasing stiffness ratio in partial compression [TSH⁺08]

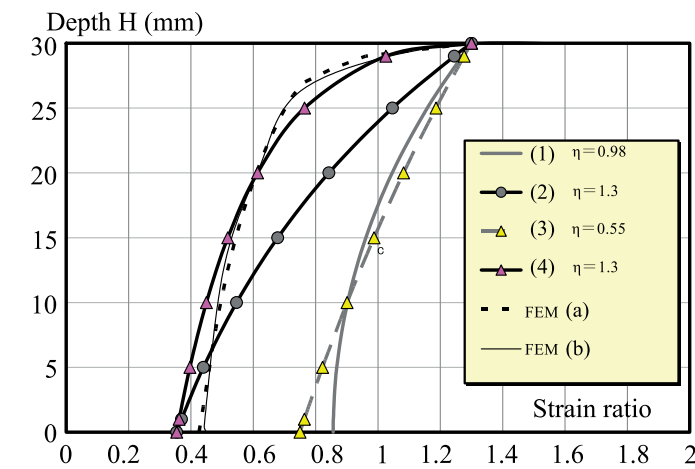


Figure 2.57 – Shape function for Pasternak model [TOIS11]

Elasto-plastic parameters for PM

The elasto-plastic parameters of the PM are obtained from the simulation of stress–strain relation in TPC or moment–rotation relation in RPC. The shape of test curves is given by Fig.2.58.

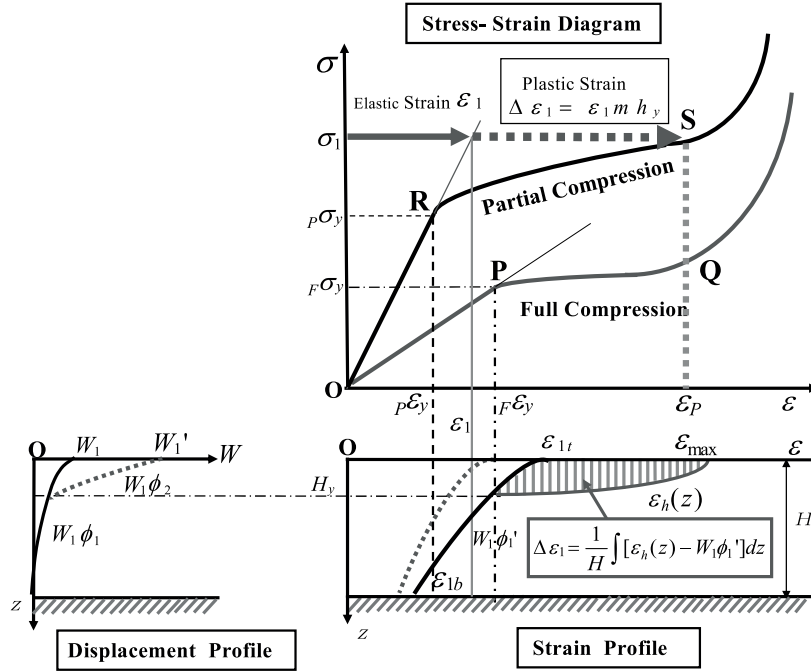


Figure 2.58 – Yielding mechanism for PM [TOIS11]

The average strains beneath the loading plate are assumed to distribute from the top ϵ_{1t} to the bottom ϵ_{1b} in Fig.2.58 (bottom right), where

$$W\phi' = \epsilon_1\phi_S = \epsilon_1\eta e^{-\eta \frac{z}{H}} \quad (2.86a)$$

$$\epsilon_{1t} = \epsilon_1\eta e^{-\eta \frac{0}{H}} = \epsilon_1\eta \quad (2.86b)$$

$$\epsilon_{1b} = \epsilon_1\eta e^{-\eta \frac{H}{H}} = \epsilon_1\eta e^{-\eta} \quad (2.86c)$$

The yielding takes place from the top to the depth H_y where strain equals to $\epsilon_{y,F}$ which is the yielding strain in full compression(FC). Here,

$$h_y = \frac{H_y}{H} = \frac{1}{\eta} \ln \kappa \quad : \text{Strain yielding depth ratio} \quad (2.87a)$$

$$\kappa = \frac{\epsilon\eta}{\epsilon_{y,F}} \quad : \text{Yielding ratio in FC} \quad (2.87b)$$

$$\kappa = \eta \frac{\epsilon}{\epsilon_{y,F}} = \eta \frac{L\theta/H}{L_F\theta_y/H} = \eta \frac{\theta}{\theta_y} \quad : \text{Yielding ratio in RPC} \quad (2.87c)$$

The total yielding strains $\Delta\epsilon_1$ correspond to the dark hatched area of Fig.2.58 (bottom right)

and the plastic strain multiplier C is obtained by curve fitting of the stress–strain or the moment–rotation relation of the test results.

$$\Delta\varepsilon_1 = \frac{1}{H} \int [\varepsilon_h(z) - W\phi'] dz = \varepsilon_1 m h_y \quad : \text{Total yielding strains} \quad (2.88a)$$

$$m = C \left(1 - \frac{\theta_y}{\eta\theta} \right) = C \left(1 - \frac{1}{\kappa} \right) \quad : \text{Equivalent multiplying factor} \quad (2.88b)$$

m and h_y are finally used in the nonlinear moment-resisting relationship Eq.(2.21) of the Nuki joint.

2.3 Laminated veneer lumber for timber plate structures

Traces of composite wood made with veneer date back to the antiquity but the industrial production of wood panels with cross-layered veneer appeared in the late 19th century. During the Second World War, particular plywood called Laminated Veneer Lumber (LVL) with veneers parallel to the long edge of the panels strengthened critical parts of aircraft. Starting in the early 1970s, LVL panels were really optimized with ultrasonically sorting of veneers, high-performance gluing and veneer thickness around 3 mm. Metsäwood, Steico, Stora Enso and Pollmeier, today's producers of engineered wood products propose two main LVL; one with all layer in the same direction and another with a certain percentage of cross layer.

Regarding the present research work, we are looking for panels with the following features :

- Approved mechanical properties regarding European standard
- Optimal strength and good stiffness
- Large range of thickness but with thin panel available - to meet design requirements
- Cross-layered composite, load can be transferred edgewise and flatwise parallel and perpendicular to the grain of the outer layer
- Preservative impregnation and water-resistant gluing shall be possible
- High stability along the life time
- Homogeneity across the thickness
- Various species and density of wood on the market (softwood and hardwood)
- Large dimensions of delivered panels for both cutting optimization and large elements
- Ability to be cut on CNC machines

In conclusion, LVL suits with requirements and spruce Kerto-Q has been selected for supporting the scope of this research work.

LVL is a composite product manufactured with thin layers of sorted wood veneers glued together to form an homogeneous and orthotropic structural material. Species are selected mostly from softwood (e.g. Spruce, Douglas fir, Pine) but use of hardwood (e.g. Beech, Polar, Birch, Alder, Turkey oak) increases. Veneers are peeled from log under constant pressure. The controlled process allows to get ribbon-like veneer without any cracks and with an uniform thickness. Typically, the veneer thickness is between 2.5 and 5 mm. During manufacturing steps the moisture content is reduced below 10% by hot air drying. Adhesive applied on both surfaces of veneer before hot pressing is mainly phenol resorcinol formaldehyde. A big effort is on going for reducing the formaldehyde emission value at the level of natural wood. LVL is also available with polyurethane (PUR) and isocyanate (EPI) glues exempt of formaldehyde.

The final multi-layered wood composite called LVL is usually with grain of all veneers along the major axis. Due to manufacturing process and random distribution of remaining surface defects, LVL strength is often superior to the high-grade lumber. Moreover size is not limited and thin panels from 21 mm thickness can be ordered. Mechanical properties can be easily predicted and replicated. LVL has one of the best ratio strength to self-weight in the engineered wood products. To improve the product for flatwise loading in the weak direction, perpendicular to the grain, most of the manufacturers are proposing LVL with a percentage of cross-layered veneers in the compound. The cross-banded veneers stabilize the panel when loads are applied in all directions and limit warping and twisting during storage or under humid conditions. Outdoor use is also compatible with solutions like Kerto-Bloc, a re-glued and pressure impregnated raw material [Met14]. All the certified mechanical properties can be found in the VTT certificate from Metsäwood [VESL16].

Cutting of LVL panels is as easy as cutting regular softwood. Wear on tooling can be a little bit higher if glue with abrasive components is used. Machining with diamond or tungsten carbide tools demonstrated very good results for surface quality. For all these reasons, LVL is a valuable material to characterize the semi-rigid behaviour of wood-to-wood connection; disturbance will not come from instability of material properties.

2.4 Research motivation

Problem statement

Freeform timber plate structures are built with lightweight panels which sustain multidirectional loads. Moreover, the polygonal mesh of such structure needs a multi-edge assembly in space. The resulting random arrangement of the connected edges makes difficult to orient the plates along their strongest orthotropic axis. For these reasons, multi-layered panels with a certain percentage of cross-layers are essential. To be economically produced from these flat panels, the structures are discretized and planarized. Digital fabrication is now quite efficient to provide algorithm of tessellation, algorithm of planarization and five-axis cutting. However, despite some innovative proposals without further development, connecting thin panels at various dihedral angles remains a crucial problem. The assumption of shell behavior so often made needs to ensure the continuity of force transfer in the structure. Even if a pure plate system can help, it can not apply to any irregular form that architects could imagine. Hence, connections should tend to provide the better possible stiffness at the edges. The rotational stiffness is one of the most important and difficult to settle, like for instance in case of quadrangular mesh. The presented review on research and actual projects confirmed the lack of appropriate joint models. Integral mechanical attachment developed at IBOIS seems promising. The joint is cut simultaneously with the contour of the plates and no additional part, fastener or bonding are necessary. It offers an all-in-one solution with in-space locator and connector features. Unfortunately, while the automation of the geometry and fabrication of the joint is well advanced, understanding the local mechanical behavior of the joint is not yet completed.

Main objective

The research work is focused on the moment-resisting behavior of multiple tab-and-slot joint (MTSJ) for edge-to-edge angular assembly of thin LVL panel. MTSJ is an integral mechanical attachment cut at the outline of engineered wood panels. The work content consists on the theoretical and experimental local analysis of the rotational semi-rigidity of the through tenon variant of MTSJ.

Chapter 2. State-of-the-Art

Objective ①

Initiatory work on the Integral Mechanical Attachment (IMA)

- Continue the preliminary work on beam,
- Select the material within spruce solid wood, SWP and LVL Kerto-Q,
- Learning the joint geometry,
- Joint geometry limited to open slots : Finger joint(FJ) and Dovetail joint (DJ) variant,
- Learning fabrication and testing process,
- Testing the mechanical behavior on a simple bending test,
- Analyze of the semi-rigid effect of the joint geometry on the deflection of a three-layered beam,
- initial definition of *multiple Tab-and-slot joint* (MTSJ).

Reference to Chapter

3. On the semi-rigidity of dovetail joint for the joinery of LVL panels

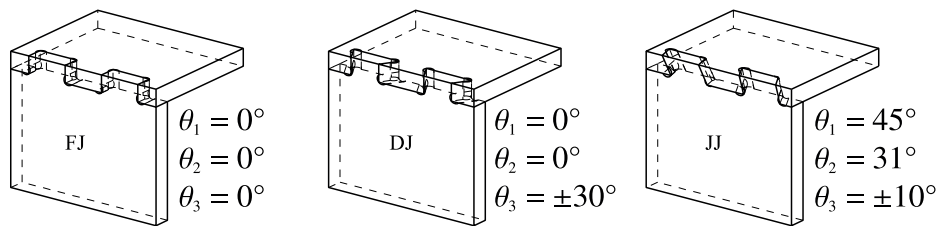


Figure 2.59 – MTSJ with open slots

Objective ②

- *Testing the rotational stiffness of multiple Tab-and-slot joint,*
- Develop a dedicated experimental setup to fold angularly connected LVL panels,
- Limit the joint geometry to open slots, without protrusion : FJ, DJ and Japanese joint (JJ) variant,
- Monitor the influence of the Bryant's angle θ_1 , θ_2 , θ_3 on the rotational stiffness,
- Conclude on the rotational stiffness of open slot joints.

Reference to Chapter

4. Rotational Stiffness at Ridges of Timber Folded-plate Structures

Objective ③

- *Improve the rotational stiffness*
- Introduce a MTSJ geometry with closed slots and protrusion : Through Tenon (TT),
- Simplify the geometry with all Bryant's angles set to zero,
- Identify the components : embedment due to rotational partial compression (RPC),
- Introduce the notion of single contact (SC) and double contact (DC),
- Qualify the additional length effect in RPC,
- Develop a setup for RPC tests.

Reference to Chapter

5. Improvement of the Rotational Stiffness for the Connection of Thin Structural Wood Panels

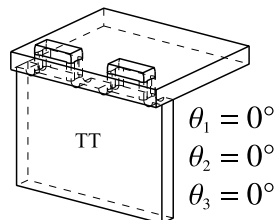


Figure 2.60 – MTSJ with closed slots and protrusion

Objective ④

- *Characterize spruce LVL Kerto-Q in RPC* (embedment and additional length effect),
- Build a simplified model for SC and DC in full width embedment,
- Provide the material characteristics of the additional length effect :
 - Decay coefficient in SC and DC,
 - Yield angles in SC and DC.

Reference to Chapter

6. Material characterization of spruce LVL in rotational partial compression

Objective ⑤

- *Provide a non linear moment-resisting model of the MTSJ TT-variant,*
- Feed the model with the material characteristics of the additional length effect,
- Experimentally confirm the model reliability.

Reference to Chapter

7. Semi-rigid Moment-resisting Model of the Through Tenon variant of Multiple Tab-and-Slot Joint for LVL panels

2.5 Scope of research

Material

As described in section 2.3, LVL product was selected and for the following chapters the range of products conforms to :

Manufacturer	: Metsäwood™
Species	: spruce veneer
Thickness	: $21^{+1.43}_{-1.03}$, $27^{+1.61}_{-1.21}$, $39^{+1.97}_{-1.57}$ mm
Panel dimensions	: 1.25 × 2.5m
Storage conditions	: Temperature $20^{\circ} \pm 2^{\circ}$, HR% 60% ~ 65%
Moisture content	: 11% ~ 12%

The most concern came from the thickness variability. For the range of considered thicknesses, the interval of tolerances is between 2.46mm ($\approx 11\%$) and 3.74mm ($\approx 10\%$). The tolerance interval is not distributed on the panel and adjoining areas of the panel can differ a lot. Indeed, the over-thickness is due to the superposition of 2 veneers of a same layer at the place where they intersect. The veneers are never longer and wider enough to cover the surface of very long produced panels. This thickness variability causes uncertainties to manage the transversal clearance between tab and slot. To improve the accuracy, the thickness is checked on the part with tabs and adjust for the part with slots in the Excel sheet before generating the outlines. It is clear that such procedure can not apply in practice.

Type of joint

The IMA in object of the study is the one-degree-of-freedom (1-DOF) joint developed in 2015 by Robeller in his thesis [Rob15]. The rotational stiffness is evaluated and compared for the FJ, DJ, JJ and TT variants but a non linear moment-resisting model is only provided for TT variant. The geometries of the samples for the tests were generated automatically in Rhinoceros©3D 5.0 from an Excel table previously filled with all the parameters. The parameters are clearly explained in the chapters of the thesis. From the bottom and top outlines of each of the two parts of a sample, the G-code is directly written by a Grasshopper©components implemented by C.Robeller. The G-code is the language that drives the 5-axis CNC machine in charge of cutting 1.25m×2.5m spruce LVL Kerto-Q panels into samples. The milling machine is a MAKAMM7s.

Development of dedicated test setup

A significant part of the research work was to develop dedicated test equipments like :

- R1 Four point bending rig for testing LVL (to be mounted on Static Universal Testing Machine Walter+Bai 200kN)
- R2 Folding machine to test closing and opening of MTSJ joints with open slot, limited to

450mm long (see chapter 4),

R3 Rotational compressing system for SC embedment (see chapters 5 & 6),

R4 Four points bending rig for angular edge-to-edge connected panels of any dihedral angle and any length (see chapter 7),

R5 Adaptation of R4-setup to DC embedment (refer to chapter 6),

Rotational stiffness

The review of connections within freeform timber plate projects, presented in section 2.1, emphasizes the influence of axial, shear and bending stiffness in the behavior of such structure. The level of rigidity dictates the ability of the structural system to limit the deflection and distribute the stresses. The rigidity is induced both by the topology of the structure and the performance of the connections. Nevertheless, in places where the curvature changes, which is often the case with very irregular structures, the problem must be dealt with connections most able to transmit the bending forces. Although axial and shear stiffnesses are important, the present study privileges the rotational stiffness

Type of analysis

Apart in the design of the project “2014 - The Landesgartenschau Exhibition Hall, Schwäbisch Gmünd, Germany [SKM14, LK15a, LK15b, KSM⁺14]” where a stiffness model is proposed, the connection behavior is mostly figured out by experiments and numerical analysis. The present work combined experimental and theoretical analysis. The short introduction on a finite element modeling (FEM) analysis of the MTSJ in bending was conducted in collaboration with G.Mattoni [Mat14] and will be achieved later by another research team.

References

- [AIJ10] AIJ. *Fundamental Theory of Timber Engineering, 1st edn.* Architectural Institute of Japan (AIJ), Maruzen, Tokyo, Japan, 2010. (in Japanese).
- [Bar62] D.D. Barkan. *Dynamics of Bases and Foundations.* McGraw-Hill series in soils engineering and foundations. McGraw-Hill, 1962.
- [BD15] J. M. Branco and T. Descamps. Analysis and strengthening of carpentry joints. *Construction and Building Materials*, 97:34 – 47, 2015. Special Issue: Reinforcement of Timber Structures.
- [Bou85] J. Boussinesq. *Application des potentiels à l'étude de l'équilibre et du mouvement des solides élastiques: principalement au calcul des déformations et des pressions que produisent, dans ces solides, des efforts quelconques exercés sur une petite partie de leur surface ou de leur intérieur : mémoire suivi de notes étendues sur divers points de physique, mathématique et d'analyse.* Mémoires de la société des sciences, de l'agriculture et des arts de Lille. Gauthier-Villars, 1885.
- [Bow87] J. E. Bowles. Elastic foundation settlements on sand deposits. *Journal of Geotechnical Engineering*, 113(8):846–860, 1987.
- [Bow96] J. E. Bowles. Foundation settlements. In *Foundation Analysis and Design Fifth Edition*, volume Chap. 5, pages 284–343. The McGraw-Hill Companies, Inc., 1996.
- [Bud15] M. Budhu. *Soil Mechanics Fundamentals.* Wiley, 2015.
- [Bur10] H. U. Buri. *Origami - Folded Plate Structures.* PhD thesis, Ecole Polytechnique Fédérale de Lausanne, 2010.
- [BW08a] H. Buri and Y. Weinand. Origami - folded plate structures, architecture. In *World Conference on Timber Engineering, Miyazaki, Japan.* Proceedings WCTE 2008, 2008.
- [BW08b] H. U. Buri and Y. Weinand. Origami - folded plate structures, architecture. In *World Conference on Timber Engineering, Miyazaki, Japan.* Proceedings WCTE 2008, 2008.
- [BW08c] Hani Buri and Yves Weinand. Die provisorische Kapelle von St. Ioup. *Bulletin Schweizerische Arbeitsgemeinschaft für Holzforschung SAH*, (2):16–20, 2008.
- [CH07] W.-S. Chang and M.-F. Hsu. Rotational performance of traditional nuki joints with gap ii : the behavior of butted nuki joint and its comparison with continuous nuki joint. *Journal of Wood Science*, 53(5):401–407, 2007.
- [CHK06] W.-S. Chang, M.-F. Hsu, and K. Komatsu. Rotational performance of traditional nuki joints with gap i : Theory and verification. *Journal of Wood Science*, 52(1):58–62, 2006.

- [CK11] Paul Crovella and George Kyanka. Use of vibration techniques to determine the rotational stiffness of timber joints. In *SHATIS'11 International Conference on Structural Health Assessment of Timber Structures*, 2011.
- [CKK11] W.F. Chen, N. Kishi, and M. Komuro. *Semi-rigid Connections Handbook*. Civil and environmental engineering series. J. Ross Pub., 2011.
- [Cra04] R.F. Craig. *Craig's Soil Mechanics, Seventh Edition*. Taylor & Francis, 2004.
- [Cri97] M. Crisinel. Dimensionnement des assemblages mixtes semi-rigides (i). *Bulletin technique de la Suisse romande, Cahier 11*, pages 180 – 187, 1997.
- [Das07] B.M. Das. *Advanced Soil Mechanics*. Taylor & Francis, 2007.
- [DG86] R. Dobry and G. Gazetas. Dynamic response of arbitrarily shaped foundations. *Journal of Geotechnical Engineering*, 112(2):109–135, 1986.
- [DG09] T. Descamps and G. Guerlement. Component method for the assessment of the axial, shear and rotational stiffness of connections in old timber frames. In *9ième Congrès de Mécanique, Marrakech*. FS Semlalia, 2009.
- [DL89] J. P. Dempsey and H. Li. A rigid rectangular footing on an elastic layer. *Géotechnique*, 39(1):147–152, 1989.
- [DL09] T. Descamps and P. Lemlyn. Effects of the rotational, axial and transversal stiffness of the joints on the static response of old timber framings. In Federico Mazzolani, editor, *Protection of Historical Buildings*, volume 1, pages 281–286. PROHITECH 09, 2009.
- [DLL06] T. Descamps, J. Lambion, and D. Laplume. Timber structures: Rotational stiffness of carpentry joints. In *9th World Conference on Timber Engineering, Portland, Oregon, USA*. Proceedings WCTE 2006, 2006.
- [DMVQ11] C. Díaz, P. Martì, M. Victoria, and O. M. Querin. Review on the modelling of joint behaviour in steel frames. *Journal of Constructional Steel Research*, 67(5):741 – 758, 2011.
- [DN09] T. Descamps and J. Noël. Semi-rigid analysis of old timber frames : Definition of equivalent springs for joints modeling. enhancement of the method, numerical and experimental validation. *International Review of Mechanical Engineering*, 3(issue 2):230 – 239, 2009.
- [Dox15] Doxygen. Shapeop 0.1.0, 2015.
- [dP90] T. A. C. M. Van der Put. Tension perpendicular at notches and joints. In *CIB-W18 paper 23-10-1, Lisboa*, 1990.

- [dP08] T. A. C. M. Van der Put. Derivation of the bearing strength perpendicular to the grain of locally loaded timber blocks. *Holz als Roh und Werkstoff*, 66(6):409–417, 2008.
- [dP12] T. A. C. M. Van der Put. Restoration of exact design for partial compression perpendicular to the grain. *Wood Material Science & Engineering*, 7(4):225–236, 2012.
- [DWM99] M. Drdácký, F. Wald, and J. Mareš. Modelling of real historic timber joints. *WIT Transactions on the Built Environment*, 39:169–178, 1999.
- [DWS99] M. Drdácký, F. Wald, and Z. Sokol. Sensitivity of historic timber structures to joint response. In R. Astudillo and A. J. Madrid, editors, *Proceedings of the 40th Anniversary Congress of IASS Madrid*, volume II, pages G1–G10. CEDEX Madrid, September 1999.
- [FB40] M. M. Filonenko-Borodich. Some approximate theories of the elastic foundation. *Uchenyie Zapiski Moskovskogo Gosudarstvennogo Universiteta. Mekhanika*, (46):3–18, 1940. (in Russian).
- [fSC92] European Committee for Standardization (CEN). *ENV 1993-1-1:1992 - Eurocode 3: Design of steel structures - Part 1-1: General rules and rules for buildings, European Prestandard*. (CEN), Brussels, 1992.
- [fSC05a] European Committee for Standardization (CEN). *CEN-EN1993-1-1:2005 - Eurocode 3: Design of steel structures - Part 1-1: General rules and rules for buildings*. (CEN), Brussels, 2005.
- [fSC05b] European Committee for Standardization (CEN). *CEN-EN1993-1-8 :2005 - Eurocode 3: Design of steel structures - Part 1-8: Design of joints*. (CEN), Brussels, 2005.
- [fSC08] European Committee for Standardization (CEN). *CEN-EN1995-1-1:2005+A1 - Eurocode 5: Design of timber structures - Part 1-1: General - Common rules and rules for buildings*. (CEN), Brussels, 2008.
- [Gir68] J. P. Giroud. Settlement of a linearly loaded rectangular area. *Journal of the Soil Mechanics and Foundations Division*, 94(Issue 4):813–832, 1968.
- [GRW17] J. Gamero, C. Robeller, and Y. Weinand. Rotational mechanical behaviour of wood-wood connections with application to double-layered folded timber-plate structure. *Construction and Building Materials*, 2017. (Submitted).
- [Han21] R. L. Hankinson. Investigation of crushing strength of spruce at varying angles of grain. *Air Force Information Circular No. 259*, 1921.

- [Het46] M. Hetényi. *Beams on Elastic Foundation: Theory with Applications in the Fields of Civil and Mechanical Engineering*. University of Michigan studies: Scientific series. University of Michigan Press, 1946.
- [HL13] J. Harding and H. Lewis. The trada pavilion – a timber plate funicular shell. *Proceedings of the International Association for Shell and Spatial Structures (IASS) Symposium, Beyond the Limits of Man, 23-27 September, Wroclaw University of Technology, Poland, 2013*, 2013.
- [HW08] M. Haasis and Y. Weinand. Origami - folded plate structures, engineering. In *World Conference on Timber Engineering, Miyazaki, Japan*. Proceedings WCTE 2008, 2008.
- [Ina91] M. Inayama. *Wooden Embedment Theory and its Application*. PhD thesis, The University of Tokyo, Tokyo, Japan, 1991. (in Japanese).
- [Ina93] M. Inayama. Study on compression perpendicular to the grain in wood, part 4: analytic functions for the relation between compression load and elastic deformation perpendicular to the grain in wood. In *Proceedings of AIJ, Tokyo, Japan*, pages 907–908, 1993. (in Japanese).
- [Jas00] J. P. Jaspart. General report : Session on connections. *Journal of Constructional Steel Research*, 55:68–89, 2000.
- [Joh85] K. L. Johnson. *Contact Mechanics*. Cambridge University Press, 1985.
- [JR94] J. P. Jaspart and R. Maquoi. Prediction of the semi-rigid and partial-strength properties of structural joints. In *Proceedings of the annual Technical Session, SSRC, Lehigh, USA*, 1994.
- [JX77] R. Jones and J. Xenophontos. The vlasov foundation model. *International Journal of Mechanical Sciences*, 19(6):317 – 323, 1977.
- [Ker64] A. D. Kerr. Elastic and viscoelastic foundation models. *Journal of Applied Mechanics*, 31(3):491–498, 1964.
- [Ker66] A. D. Kerr. *A Study of a New Foundation Model*. 186 Research report. Hanover, N.H. : U.S. Army Materiel Command, Cold Regions Research & Engineering Laboratory, 1966, 1966.
- [KJH⁺10] A. Kitamori, K. Jung, I. Hassel, W.-S. Chang, K. Komatsu, and Y. Suzuki. Mechanical analysis of lateral loading behaviour on japanese traditional frame structure depending on the vertical load. In *11th World Conference on Timber Engineering (WCTE)*, 2010.
- [KKJM09] K. Komatsu, A. Kitamori, K. Jung, and T. Mori. Estimation of the mechanical properties of mud shear walls subjected to lateral shear force. In *Proceedings of the*

11th International Conference on Non-conventional Materials and Technologies (NOCMAT 2009), Bath, UK, 6-9 September 2009.

- [KMKK09] A. Kitamori, T. Mori, Y. Kataoka, and K. KOMATSU. Effect of additional length on partial compression perpendicular to the grain of wood. *Journal of Structural and Construction Engineering (Transactions of AIJ)*, 74(642):1477–1485, 2009.
- [KSM⁺14] Oliver David Krieg, Tobias Schwinn, Achim Menges, Jian-Min Li, Jan Knippers, Annette Schmitt, and Volker Schwieger. *Biomimetic Lightweight Timber Plate Shells: Computational Integration of Robotic Fabrication, Architectural Geometry and Structural Design*, pages 109–125. Springer International Publishing, Cham, 2014.
- [Lei04a] K. Leitner. Models of new folded plate structures of timber boards and the textile junction. *Proceedings of the IASS 2004 Symposium, Montpellier 2004*, 2004.
- [Lei04b] K. Leitner. *Tragkonstruktionen aus plattenförmigen Holzwerkwerkstoffen mit der TEXTILEN FUGE*. PhD thesis, RWTH Aachen University, 2004.
- [LHFC00] R. J. Leichti, R. A. Hyde, M. L. French, and S. G. Camillos. The continuum of connection rigidity in timber structures. *Wood and Fiber Science*, (1):11–19, 2000.
- [LK15a] J.-M. Li and J. Knippers. Pattern and form—their influence on segmental plate shells. *Proceedings of the International Association for Shell and Spatial Structures (IASS) Symposium 2015, Amsterdam Future Visions, August 17-20, Amsterdam, The Netherlands, 2015*, 2015.
- [LK15b] J.-M. Li and J. Knippers. Segmental timber plate shell for the landesgartenschau exhibition hall in schwäbisch gmünd—the application of finger joints in plate structures. *International Journal of Space Structures*, 30(2):123–139, 2015.
- [LLdP10] A.J.M. Leijten, H.J. Larsen, and T.A.C.M. Van der Put. Structural design for compression strength perpendicular to the grain of timber beams. *Construction and Building Materials*, 24(3):252–257, 2010.
- [Lov29] A. E. H. Love. The stress produced in a semi-infinite solid by pressure on part of the boundary. *Philosophical Transactions of the Royal Society of London A: Mathematical, Physical and Engineering Sciences*, 228(659-669):377–420, 1929.
- [LW69] T. W. Lambe and R. V. Whitman. *Soil mechanics*. Series in soil engineering. Wiley, 1969.
- [Mad00] B. Madsen. *Behaviour of Timber Connections*. North Vancouver, British Columbia : Timber Engineering, Ltd, 2000.
- [Mat14] G. Mattoni. Folded plate structure – design and analysis of woodworking joints for structural timber panels. Master’s thesis, Ecole Nationale des Ponts et Chaussées and Ecole Polytechnique Fédérale de Lausanne, 2014.

- [McG95] J. McGuire. Notes on semi-rigid connections. <https://femci.gsfc.nasa.gov/semirigid/>, 1995.
- [Mes11] R.W. Messler. *Integral Mechanical Attachment: A Resurgence of the Oldest Method of Joining*. Elsevier Science, 2011.
- [Met14] Metsäwood. Kerto for advanced structural engineering. (<http://www.metsawood.com/products/kerto>), 2014. Kerto brochure and VTT certificate and others.
- [MHH82] B. Madsen, R. F. Hooley, and C. P. Hall. A design method for bearing stresses in wood. *Canadian Journal of Civil Engineering*, 9(2):338–349, 1982.
- [Mil92] D. Milović. *Stresses and displacements for shallow foundations*. Developments in Geotechnical Engineering Series. Elsevier Science Limited, 1992.
- [MM11] W. Munoz M. Mohammad. *Chapter 5 – Connections in cross-laminated timber buildings*. Special publication. FPInnovations, 2011.
- [MMS10a] A. Meisel, T. Moosbrugger, and G. Schickhofer. Realistic modelling and repair of ancient austrian roof structures, part ii. In University of British Columbia N. Banthia, A. Mufti, editor, *Proceedings of Conservation of Heritage Structure (CSHM-3), Ottawa, Canada*, pages 495–508, 2010.
- [MMS10b] A. Meisel, T. Moosbrugger, and G. Schickhofer. Survey and realistic modelling of ancient austrian roof structures, part i. In University of British Columbia N. Banthia, A. Mufti, editor, *Proceedings of Conservation of Heritage Structure (CSHM-3), Ottawa, Canada*, pages 481–494, 2010.
- [MR01] F.S. Merritt and J.T. Ricketts. *Building Design and Construction Handbook, 6th Edition*. Building Design & Construction Handbook. McGraw-Hill, 2001.
- [MWK12] R. La Magna, F. Waimer, and J. Knippers. Nature-inspired generation scheme for shell structures. *Proceedings of the International Symposium of the IASS-APCS Symposium, Seoul, South Korea, 2012*, 2012.
- [OSY15] K. Ogawa, Y. Sasaki, and M. Yamasaki. Theoretical modeling and experimental study of japanese “watari-ago” joints. *Journal of Wood Science*, 61(5):481–491, 2015.
- [Pas54] P. L. Pasternak. *On a New Method of Analysis of an Elastic Foundation by Means of Two Foundation Constants*. Moscow, 1954. (Gosudarstvennoe Izdatelstvo Literaturi po Stroitelstve i Arkhitekture, in Russian).
- [PD74] H. G. Poulos and E. H. Davis. *Elastic Solutions for Soil and Rock Mechanics*. John Wiley & Sons, Inc., 1974.

- [PK88] A. Pais and E. Kausel. Approximate formulas for dynamic stiffnesses of rigid foundations. *Soil Dynamics and Earthquake Engineering*, 7(4):213–227, 1988.
- [RGCW16] C. Robeller, J. Gamarro, P.-O. Coanon, and Y. Weinand. Théâtre vidy lausanne-ein zweischichtiges gefaltetes flächentragwerk aus brettsperrholz. In *Tagungsband S-WIN FBK Weinfelden 2016: Digitale Fertigung im Holzbau*, volume 48, pages 9–20. Swiss Wood Innovation Network S-WIN, 2016.
- [RKD⁺16] C. Robeller, M. A. Konakovic, M. Dedijer, M. Pauly, and Y. Weinand. A double-layered timber plate shell-computational methods for assembly, prefabrication, and structural design. In *Advances in Architectural Geometry 2016*, volume 5, pages 104–122. vdf Hochschulverlag AG, 2016.
- [RMW14] C. Robeller, P. Mayencourt, and Y. Weinand. Snap-fit joints - cnc fabricated, integrated mechanical attachment for structural wood panels. In *ACADIA 14: Design Agency, Proceedings of the 34th Annual Conference of the Association for Computer Aided Design in Architecture (ACADIA), Los Angeles, October 23-25, 2014*, pages 189–198, 2014.
- [RNW14] C. Robeller¹, S. S. Nabae², and Y. Weinand². Design and fabrication of robot-manufactured joints for a curved-folded thin-shell structure made from clt. In *Rob|Arch, Robotic Fabrication in Architecture, Art, and Design*. Springer, 2014.
- [Rob15] C. Robeller. *Integral Mechanical Attachment for Timber Folded Plate Structures*. PhD thesis, Ecole Polytechnique Fédérale de Lausanne, 2015.
- [RSMW14] C. Robeller, A. Stitic, P. Mayencourt, and Y. Weinand. Interlocking folded plate - integrated mechanical attachment for structural wood panels. In *Advances in Architectural Geometry 2014*. Springer - submitted may 2014, 2014. <http://www.architecturalgeometry.org/aag14/>.
- [RVW67] F. E. Richart Jr R. V. Whitman. *Design Procedures for Dynamically Loaded Foundations*. The University of Michigan, 1967. Industry Program of The College of Engineering.
- [RW16] C. Robeller and Y. Weinand. Fabrication-aware design of timber folded plate shells with double through tenon joints. In *Robotic Fabrication in Architecture, Art and Design 2016*, pages 166–177. Springer, 2016.
- [SBA14] K. Sobra, J. M. Branco, and Ch. A. Aranha. Application of the component method to traditional dovetail joints of timber trusses. In *Materiais de Construção Sustentáveis, Universidade do Minho, Braga, Portugal*, pages 187–196, 2014.
- [Sch26] F. Schleicher. Zur theorie des baugrundes. *Der Bauingenieur*, pages 931–935, 1926.

- [Sch04] Regina Schineis. Gefalteter klangkoerper musikprobensaal thannhausen / thannhausen rehearsal room. In *10. Internationales Holzbau Forum (IHF), Garmisch-Partenkirchen, 2004*.
- [Sco13] C.R. Scott. *An Introduction to Soil Mechanics and Foundations*. Springer US, 2013.
- [SDWM12] H. Schimek, E. Dominguez, A. Wiltsche, and M. Manahl. Sewing timber panels: an innovative digitally supported joint system for self-supported timber plate structures. pages 213–222, 04/2012 2012.
- [SKM12] T. Schwinn, O. D. Krieg, and A. Menges. Robotically fabricated wood plate morphologies, robotic prefabrication of a biomimetic, geometrically differentiated, lightweight, finger joint timber plate structure. In *Rob|Arch, Robotic Fabrication in Architecture, Art, and Design*. Springer Wien New York, 2012.
- [SKM14] T. Schwinn, O. D. Krieg, and A. Menges. Behavioral strategies: Synthesizing design computation and robotic fabrication of lightweight timber plate structures. In *ACADIA 14: Design Agency, Proceedings of the 34th Annual Conference of the Association for Computer Aided Design in Architecture (ACADIA), Los Angeles, October 23-25, 2014*, pages 177–188, 2014.
- [SMB10] H. Schimek, A. Meisel, and T. Bogenperger. On connecting panels of freeform building envelopes. *CAAD – Cities – Sustainability [5th International Conference Proceedings of the Arab Society for Computer Aided Architectural Design], Fez (Morocco), 19-21 October 2010*, pages 171–178, 2010.
- [SWSS08] M. Steenhuis, F. Wald, Z. Sokol, and J.W.B. Stark. Concrete in compression and base plate in bending. *Heron*, 53(1/2):51–68, 2008.
- [SYO12] H. Sakata, Y. Yamazaki, and Y. Ohashi. A study on moment resisting behavior of mortise-tenon joint with dowel or split wedge. In *15th World Conference on Earthquake Engineering, Lisbon, Portugal, 24-28 September 2012*.
- [Tac10] T. Tachi. Geometric considerations for the design of rigid origami structures. In *Proceedings of International Symposium of the International Association for Shell and Spatial Structures (IASS) : Spatial Structures - temporary and permanent*, Beijing, China, 2010. China Architecture & Building Press.
- [Tan04] H. Tanahashi. Formulas for an infinitely long bernoulli-euler beam on the pasternak model. *Soils and Foundations*, 44(5):109–118, 2004.
- [Ter43] K. Terzaghi. *Theoretical Soil Mechanics*. J. Wiley and Sons, inc., 1943.
- [TG51] S. P. Timoshenko and J. N. Goodier. 124. load distributed over a part of the boundary of a semi-infinite solid. In *Theory of elasticity*, pages 366–373. New York McGraw-Hill, 1951.

- [TMI12] T. Tachi, M. Masubuchi, and M. Iwamoto. Rigid origami structures with vacuumatics: Geometric considerations. *Proceedings of the International Symposium of the IASS-APCS Symposium, Seoul, South Korea, 2012*, 2012.
- [TMNM15] T. Tannert, A. Meyboom, O. Neumann, and I. Macdonald. Shell structures in wood, technical research & testing final report. Technical report, Centre for Advanced Wood Processing, Department of Wood Science, Department of Civil Engineering, and the School of Architecture and Landscape Architecture (SALA), 2015.
- [TOIS11] H. Tanahashi, Y. Ooka, K. Izuno, and Y. Suzuki. Yielding mechanism of embedment of wood and formulation of elasto-plastic embedded displacements. *Journal of Structural and Construction Engineering (Transactions of AIJ)*, 76(662):811–819, 2011. (in Japanese).
- [TOS08] H. Tanahashi, M. Okamura, and Y. Suzuki. Simple formulation of elasto-plastic embedment behavior of orthotropic wood considering densification. In *World Conference on Timber Engineering, Miyazaki, Japan*. Proceedings WCTE 2008, 2008.
- [TS11] H. Tanahashi and Y. Suzuki. Characteristics of elasto-plastic rotational embedment of traditional wooden joints and formulation of crosspiece joints. *Journal of Structural and Construction Engineering (Transactions of AIJ)*, 76(667):1675–1684, 2011. (in Japanese).
- [TS12] H. Tanahashi and Y. Suzuki. Embedment mechanism and formulation of major types of traditional wooden joints in japan. In *World Conference on Earthquake Engineering, Lisbon, Portugal*, 2012.
- [TS15] H. Tanahashi and Y. Suzuki. Three effects of mechanisms in traditional timber structures. In *IABSE Conference Elegance of Structures, Nara, Japan*, May 13-15, 2015.
- [TSH⁺08] H. Tanahashi, H. Shimizu, H. Horie, P. Yang, and Y. Suzuki. Elastic embedded displacements of orthotropic wood with a finite length based on pasternak model. *Journal of Structural and Construction Engineering (Transactions of AIJ)*, 73(625):417–424, 2008. (in Japanese).
- [TSS06a] H. Tanahashi, H. Shimizu, and Y. Suzuki. Elastic surface displacements of orthotropic wood due to partial compression based on pasternak model. *Journal of Structural and Construction Engineering (Transactions of AIJ)*, (609):129–136, 2006. (in Japanese).
- [TSS06b] H. Tanahashi, H. Shimizu, and Y. Suzuki. Formulation of elasto-plastic moment-resisting performance of timber connections using pasternak model. In *World Conference on Timber Engineering, Portland, USA*. Proceedings WCTE 2006, 2006.

- [TSS12] H. Tanahashi, H. Shimizu, and Y. Suzuki. Basic concept and general formulation of restoring force characteristics of traditional wooden joints. In *World Conference on Timber Engineering, Auckland, New Zealand*. Proceedings WCTE 2012, 2012.
- [Ver10] A. Verruijt. *An Introduction to Soil Dynamics*. Theory and Applications of Transport in Porous Media. Springer Netherlands, 2010.
- [VESL16] Finland VTT Expert Services Ltd. *Kerto-VTT-C-184-03-Certificate:2016 Kerto-S and Kerto-Q Structural Laminated Veneer Lumber, Certificate NO.184/03*. 2004, Updated 17.5.2016.
- [VL66] V. Z. A. Vlasov and U. N. Leont'ev. *Beams, Plates and Shells on Elastic Foundations: (Balki, Plity i Obolochki Na Uprugom Osnovanii)*. Technical Translation / NASA. Israel Program for Scientific Translations, 1966.
- [WBC07] D. C. Weggel, D. M. Boyajian, and S.-E. Chen. Modelling structures as systems of springs. *World Transactions on Engineering and Technology Education*, 6(1):169–172, 2007.
- [Wes84] T. Wester. *Structural Order in Space: The Plate-Lattice Dualism*. Plate Laboratory, Royal Academy of Arts, School of Architecture, 1984.
- [Wes93] T. Wester. *Efficient faceted surface structures*. Number vol.1. Thomas Telford, 1993.
- [Wil12] A. Wiltsche. Non-standard formen in der architektur. *IBDG 2012/1*, pages 13–18, 2012.
- [WJS96] K. Weynand, J.-P. Jaspart, and M. Steenhuis. The stiffness model of revised annex j of eurocode 3. In R. Bjorhovde, A. Colson, and R. Zandonini, editors, *Connections in Steel Structures {III}*, pages 441–452. Pergamon, Oxford, 1996.
- [WMSD00] F. Wald, J. Mareš, Z. Sokol, and M. Drdácý. Component method for historical timber joints. In C.C. Baniotopoulos and F. Wald, editors, *The Paramount Role of Joints into the Reliable Response of Structures*, volume 4 of *NATO Science Series*, pages 417–424. Springer Netherlands, 2000.
- [Wor07] A. Worku. The use of springs in static analysis of structures to account for short and long term subgrade deformations. *Zede, Journal of the Ethiopian Engineers and Architects, EEA*, 24:11–21, 2007.
- [Yeo16] S.-Y. Yeo. *Structural Performance of Taiwanese Traditionnal Dieh-Dou Timber Frame*. PhD thesis, National Cheng Kung University, Taiáwan, 2016.
- [YKHQ16] S.-Y. Yeo, K. Komatsu, M.-F. Hsu, and Z. Que. Mechanical model for complex brackets system of the taiwanese traditional dieh-dou timber structures. *Advances in Structural Engineering*, 19(1):65–85, 2016.

Chapter 2. State-of-the-Art

- [Zoe74] P. Zoetemeijer. A design method for the tension side of statically loaded, bolted beam-to-column connections. 1974.
- [Zoe83] P. Zoetemeijer. Summary of the research on bolted beam-to-column connections (period 1978 - 1983). Technical report, University of Technology Delft, 1983. Report No. 6-85-M, Steven Laboratory.

Investigations and Publications



3 On the semi-rigidity of dovetail joint for the joinery of LVL panels

Stéphane Roche, Christopher Robeller, Laurent Humbert and Yves Weinand

Published in European Journal of Wood and Wood Products, vol. 73, num. 5, p. 667-675, 2015, DOI 10.1007/s00107-015-0932-y.

Abstract

This paper focuses on Multiple Tab-and-Slots Joints (MTSJ) for load-carrying assembly of structural wood elements, which are inspired by traditional cabinetmaking joints and adapted for automatic fabrication and engineered wood panels such as Laminated Veneer Lumber (LVL). It is first presented a numerical method for the estimation of the connections semi rigid properties based on box beam samples. In a simplified model, the mechanical behavior of the joint is represented by potential elastic slips at interfaces. These are handled by the model, with the help of rigidity modulus, which are determined by matching simulated and experimental deflections. Finally, the influence of tab length and contact face angle on the semi-rigidity of the joint is discussed considering a dovetail geometry of the Multiple tab-and-Slot joint. Glued and screwed samples serve as references during this study.

Keywords Integral Mechanical Attachment, Semi-rigidity, Wood Machining, LVL, Dovetail Joint.

Objective ① *

Initiatory work on the Integral Mechanical Attachment (IMA)

*This additional section was not included in the original publication.

3.1 Introduction

Multiply cross-laminated wood panels such as LVL have received increasing usage in engineering structures over the last decades. These panels are particularly suitable for the design and fabrication of lightweight structural components, such as roof and floor box elements, webbed beams or folded-plate structures as presented by [RSMW14]. The construction of such components requires several panels to be jointed along their edges, where the connections between panels play a significant role in the load-carrying capacity of these structural elements.

State of the art connections include adhesives, which provide a high stiffness of the connection, but the jointing must be done off-site, applying a defined, distributed pressure for a certain amount of time. Alternatively, metal fasteners such as screws can be used for the edge-jointing; however a large amount of screws will be necessary to achieve a sufficient stiffness of the connection. The direct application of metal fasteners to the edge of panels is not possible on thin LVL panels [20113]. Furthermore, for both screws and adhesive joints, a precise and fast alignment of parts may be difficult, especially for non-orthogonal edge connections.

The multiple tab-and-slot joints (MTSJ) applied in this paper is re-considering the advantages of traditional connections from cabinetmaking [Gra87], while taking advantage of the efficiency and precision of Computer Numerical Control (CNC) fabrication technology. It demonstrates an alternative technique, especially for the jointing of thin panels which cannot be connected with screws [fSC04], and allows for a fast and precise assembly of structural components. The final alignment of parts, the angles in between parts and the direction of their assembly can be pre-defined through the geometry of the joint. A more detailed description of the joint is given by [RSMW14] within a folded-plate prototype, digitally fabricated and experimentally tested.

However, when designing new types of timber structures, stiffness remains one of the most important structural parameters that may be affected by the performance of the connection. Therefore, it is important to provide quantitative estimation of the joint degree of rigidity through well-controlled tests and analyses with reasonable generality and simplicity. While several previous studies [D.B99, SS10] have examined the mechanical behavior of conventional connections, the present work presents an analysis of CNC fabricated MTSJ on a case-study (LVL box beams with uniform cross section). For introducing the assumptions of semi-rigidity, the geometry of the joint is simply defined as a dovetail-joint (DJ) type similar to furniture connections in woodworking. Then the MTSJ is longitudinally loaded during a three-points bending test.

3.2 Numerical Model

In this section, a one-dimensional simplified method is applied for the analysis of multi-layered elastic beams which permits reversible horizontal slip between the layers without vertical separation. Friction and irreversible gaps between successive layers are not addressed. This method, initially referred to as “Gamma method”, originates from the pioneer work of Möhler [M56] for up to three-layered composite systems subjected to cosine/sine load functions. Möhler's analysis was extended by Schelling [Sch68] to laminated composite beams

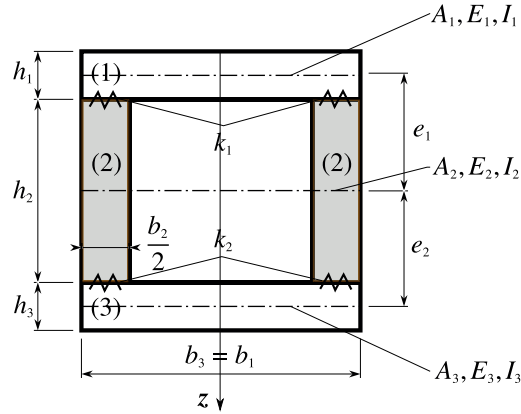


Figure 3.1 – Box beam cross section with semi-rigid interfaces

made of an arbitrary number of layers and more complex loading cases such as piecewise, uniformly distributed loads of practical interest. Recent applications and developments of the method are proposed in the references [Kre95, NSRF04] among others. Besides these works, analytical solutions were also proposed at the beginning of the fifties by Newmark et al. [NSV51] for two-layered semi-rigid systems and extended by Goodman et al. [NSV51] to three-layered (timber) composite beams of rectangular and equal cross-sections. Recent developments on the subject can be found by instance in [KFZ07] and [JS10].

Practical and representative solutions may easily be derived for simply supported composite beams with arbitrary cross-sections and load distributions under the following basic assumptions: (1) the materials and interfaces behave linearly, (2) plane sections remain plane inside each connected element and (3) the same rotation θ and vertical displacement w of the centroidal axis is considered for every element assuming that the slope of the deflection curve is small.

The boxed beam is viewed here as a three-layered beam that lies in the x, z plane, with two slipping interfaces. Relevant cross-sectional properties as well as the layer numbering are defined in Fig.3.1, where the transverse coordinate z is taken positive downward from the upper face. For each beam element i of cross sectional area A_i and vertical position of the reference (centroidal) axis z_i , the centroidal moment of inertia of the element cross section is denoted $I_i = \int_{A_i} (z - z_i)^2 dA_i = \frac{1}{12} b_i h_i^3$. The distance between the reference (centroidal) axis of the first and second elements and second and third elements is given by $e_1 = (h_1 + h_2)/2$, $e_2 = (h_2 + h_3)/2$, respectively. E_i and G_i are the elastic and shear modulus of the element i .

The two slipping interfaces are associated with the rigidity modulus k_1 and k_2 (see Fig.3.1) that are kept constant along the beam length. Consequently, it is admitted that every dovetail joints behave in a similar manner along the interface.

Denoting θ the rotation of the beam element sections, the displacement field for the beam is expressed by

$$\begin{aligned} u_i(x, z) &= u_i(x) - (z - z_i)\theta(x) \\ w_i(x, z) &= w(x) \end{aligned} \quad (3.1)$$

Chapter 3. On the semi-rigidity of dovetail joint for the joinery of LVL panels

where w is the transverse displacement. The functions $u_i(x)$ represent the horizontal displacements of the reference axis of each layer.

The axial strain ϵ_i and corresponding stress σ_i for each layer are given by

$$\epsilon_i = \frac{du_i}{dx} - (z - z_i) \frac{d\theta}{dx} \quad (3.2)$$

$$\sigma_i = E_i \epsilon_i = E_i \left(\frac{du_i}{dx} - (z - z_i) \frac{d\theta}{dx} \right) \quad (3.3)$$

At the elements centroids, when $z = z_i$, one has $\sigma_i = E_i du_i/dx$. For brevity, the dependence with x is not explicitly indicated here and in what follows.

From the kinematical hypothesis Eq.(3.1), the following set of differential equations linking the unknown θ , u_i and w can be obtained.

$$\begin{aligned} E_1 A_1 \frac{d^2 u_1}{dx^2} + k_1 (u_2 - u_1 + e_1 \cdot \theta) &= 0 \\ E_2 A_2 \frac{d^2 u_2}{dx^2} + k_1 (u_2 - u_1 + e_1 \cdot \theta) + k_2 (u_3 - u_2 + e_2 \cdot \theta) &= 0 \\ E_3 A_3 \frac{d^2 u_3}{dx^2} - k_2 (u_3 - u_2 + e_2 \cdot \theta) &= 0 \\ GA \left(\frac{d^2 w}{dx^2} - \frac{d\theta}{dx} \right) &= q \\ EI \frac{d^2 \theta}{dx^2} - GA \left(\frac{dw}{dx} - \theta \right) - e_1 k_1 (u_2 - u_1 + e_1 \cdot \theta) \\ &\quad - e_2 k_2 (u_3 - u_2 + e_2 \cdot \theta) = 0 \end{aligned} \quad (3.4)$$

where $EI = E_1 I_1 + E_2 I_2 + E_3 I_3$, $GA = G_1 A_1 + G_2 A_2 + G_3 A_3$, is the cross-sectional transverse stiffness of the multilayered beam and $q(x)$ is the distributed lateral load acting along the beam direction. The second-order differential system Eq.(3.4) couples the displacements u_i , w and rotation angle θ in the framework of Timoshenko beam theory. By definition, the transverse shear force $V(x)$ is given as

$$V = GA \left(\theta - \frac{dw}{dx} \right) \quad (3.5)$$

such that $q = -\frac{dV}{dx}$, as usual. Note that the fourth equation in Eq.(3.4) comes from the derivative of Eq.(3.5) with respect to x , coupling thus the beam curvature w'' with θ' and q . The prime symbol is also used to denote the derivative of a function with respect to x .

Next, the differential system Eq.(3.4) can be transformed to a system of ordinary differential equations (ODEs) of the form

$$\frac{dy}{dx} = \mathbf{f}(x, \mathbf{y}), \quad 0 \leq x \leq L \quad (3.6)$$

where L stands for the beam span. For the Timoshenko theory, one has to consider the 10×1 column vector $\mathbf{y} = (u_1 \ u'_1 \ u_2 \ u'_2 \ u_3 \ u'_3 \ w \ w' \ \theta \ \theta')^T$.

From Eq.(3.4), the components of the 10×1 vector function \mathbf{f} are given by

$$\mathbf{f} = \begin{pmatrix} u_1' \\ -\frac{k_1}{E_1 A_1} (u_2 - u_1 + e_1 \cdot \theta) \\ u_2' \\ \frac{k_1}{E_2 A_2} (u_2 - u_1 + e_1 \cdot \theta) - \frac{k_2}{E_2 A_2} (u_3 - u_2 + e_2 \cdot \theta) \\ u_3' \\ \frac{k_2}{E_3 A_3} (u_3 - u_2 + e_2 \cdot \theta) \\ \theta + \frac{V}{GA} \\ \theta' + \frac{q}{GA} \\ \theta' \\ \frac{1}{EI} \left(GA(w' - \theta) + e_1 k_1 (u_2 - u_1 + e_1 \cdot \theta) + e_2 k_2 (u_3 - u_2 + e_2 \cdot \theta) \right) \end{pmatrix}$$

The solution of the problem requires the specification of two-point boundary conditions given here in the generic form

$$\mathbf{g}(\mathbf{y}(0), \mathbf{y}(L)) = \mathbf{0} \quad (3.7)$$

or explicitly,

$$\begin{aligned} w(0) &= w(L) = 0, \\ w''(0) &= \theta'(0) + V(0)/GA = 0, \\ w''(L) &= \theta'(L) + V(L)/GA = 0, \\ u_1'(0) &= u_2'(0) = u_3'(0) = 0, \\ u_1(0) + u_1(L) &= 0, \\ u_2(0) + u_2(L) &= 0, \\ u_3(0) + u_3(L) &= 0. \end{aligned} \quad (3.8)$$

The first four boundary conditions in Eq.(3.8) impose that vertical displacements and curvatures are zero at the supports. Axial deformations and stresses are taken to be zero at $x = 0$ using the three subsequent conditions. Finally, the remaining conditions lead to opposite values for the axial displacement at the end points, assuming thus that symmetrical loads with respect to mid span prevail here.

For a three-point bending configuration, with load F at $L/2$, $q(x)$ is evaluated using the Heaviside function

$$H(x) = \begin{cases} 0 & \text{if } x < 0 \\ 1 & \text{if } x \geq 0 \end{cases} \quad \text{as}$$

$$q(x) = q_0 \cdot \left(H\left(x - \frac{L}{2} + \frac{l_0}{2}\right) - H\left(x - \frac{L}{2} - \frac{l_0}{2}\right) \right) \quad (3.9)$$

where $q_0 = F/l_0$ and $l_0 = L/100$ is typically considered. Accordingly, the central load is described as a constant load q_0 acting on a small domain of size $2l_0$, centered at the position $x = L/2$.

3.3 Experimental study

3.3.1 Introduction to the MTSJ geometry

Based on linear connections for furniture such as dovetail or Japanese nejiri arigata joints, the MTSJ without adhesive bonding or fasteners allow assembly and direct interlocking of two panel edges at their final in-space location.

As a detailed description of this "integrated mechanical attachment" is given by [Rob15], the next section briefly introduces the geometrical parameters of the joint. The connection employed here is a one-degree-of-freedom connection (for the purpose of assembly) where tabs are inserted in slots Fig.3.2b. "Multiple" refers to the reiteration of interlocked tab and slot along the common edge of two connected panels. The geometry of the connection defines the relative positioning of the panels and allows a certain degree of load-transfer between them. The assembly of the two panels is directed along a vector of insertion (see below). The tab contact faces of each part belong to the same contact plane after insertion. In general, the insertion vector and the normal to the locking face are obtained by the following sequence (see Fig.3.2a).

If \mathbf{n}_0 and \mathbf{n}_1 are the normal of the two considered panels, the frame of the joint $F = (\mathbf{u}_1, \mathbf{u}_2, \mathbf{u}_3)$ can be calculated, as $\mathbf{u}_1 = \mathbf{n}_0 \times \mathbf{n}_1$, $\mathbf{u}_2 = \mathbf{n}_0$ and $\mathbf{u}_3 = \mathbf{u}_1 \times \mathbf{u}_2$. Then, the line segment representing the intersection of the two panel mid-planes can be uniformly divided into N points $(X_i)_{(i=1..N)}$, the distance between points is the tab length of the joint L_t (Fig.3.3). The plane P_i is the plane of normal \mathbf{u}_1 , and contains the point X_i . Thus by three successive rotations of this plane and its attached frame as,

$$\begin{aligned} & \{P_i, F = (\mathbf{u}_1, \mathbf{u}_2, \mathbf{u}_3)\} \\ & \quad \downarrow R(\mathbf{u}_1, \theta_1) \\ & \{P'_i, F' = (\mathbf{u}'_1 = \mathbf{u}_1, \mathbf{u}'_2, \mathbf{u}'_3)\} \\ & \quad \downarrow R(\mathbf{u}'_2, \theta_2) \\ & \{P''_i, F'' = (\mathbf{u}''_1, \mathbf{u}''_2 = \mathbf{u}'_2, \mathbf{u}''_3)\} \\ & \quad \downarrow R(\mathbf{u}''_3, \pm\theta_{3,i}) \\ & \{P'''_i, F''' = (\mathbf{u}'''_{1,i}, \mathbf{u}'''_{2,i}, \mathbf{u}'''_{3,i} = \mathbf{u}''_3)\} \end{aligned} \quad (3.10)$$

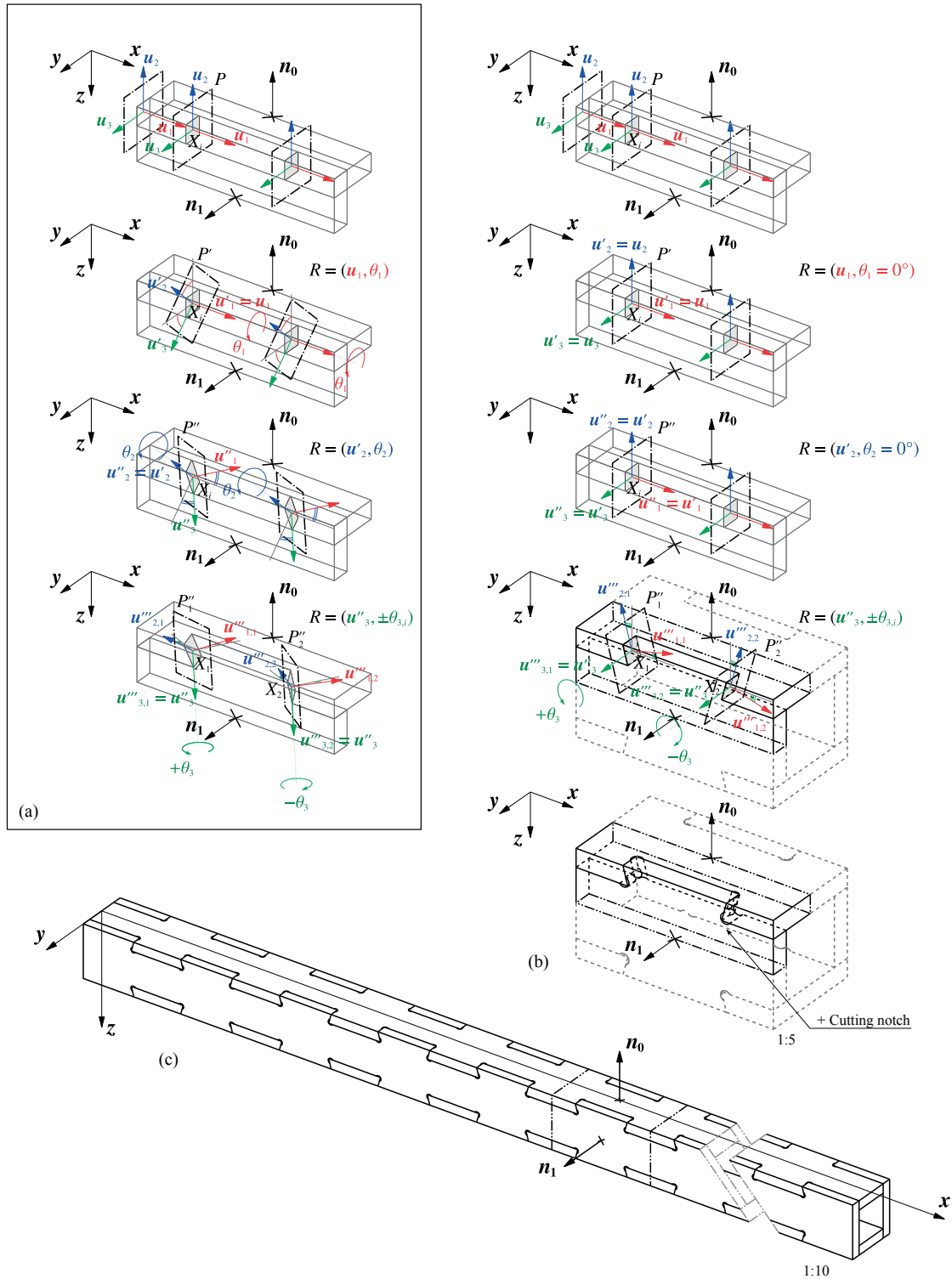


Figure 3.2 – f
 or beam(a) General sequence of plane & frame rotations for a MTSJ, (b) Result for a dovetail-type connection with $\theta_1, \theta_2 = 0^\circ$, (c) boxed beam.

Chapter 3. On the semi-rigidity of dovetail joint for the joinery of LVL panels

the final joint is obtained defining the planes P_i''' , $u_{1,i}'''$ and $u_{3,i}''' = u_3''$ as the tab contact faces, their normal and the insertion vector, respectively. In the present paper, the θ_1, θ_2 angles are taken equal to 0° (Fig.3.2b) and the θ_3 angle is set successively to 0° (finger joint), $\pm 15^\circ$ (DJ), $\pm 25^\circ$ (DJ). Then, four panels are connected with the MTSJ to build a square box beam (Fig.3.2c). Note that in this subsection, θ_i and the prime symbol denote the rotation angles and the successive rotated planes and frames, respectively.

3.3.2 Description of the samples

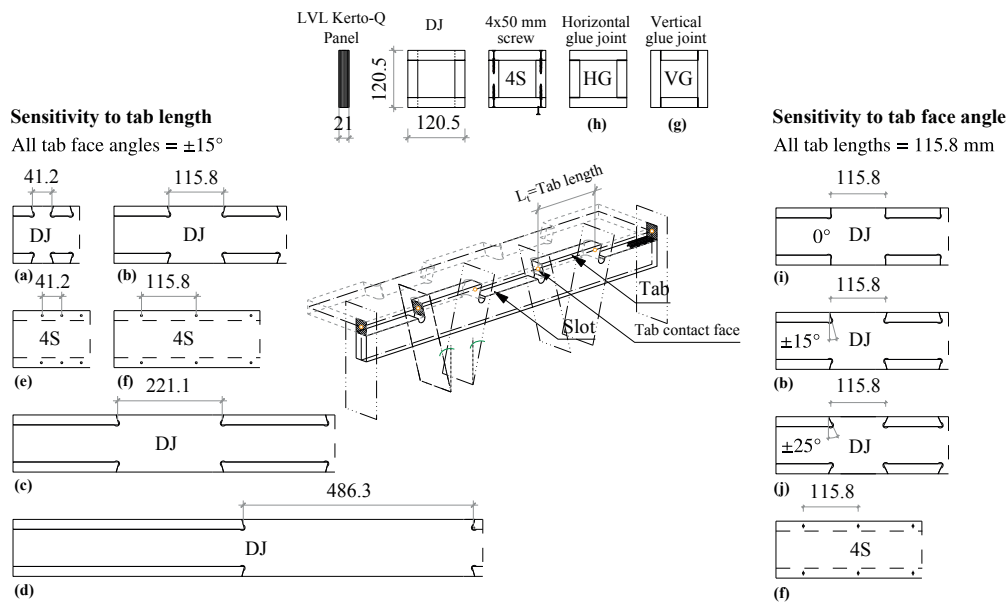


Figure 3.3 – Sample connection specifications : (a) DJ15 41 mm, (b) DJ15 116 mm, (c) DJ15 221 mm, (d) DJ15 486 mm, (e) 4mm-screw 41 mm, (f) 4mm-screw 116 mm, (g) Vertical glue joint, (h) Horizontal glue joint, (i) DJ00 116 mm, (j) DJ25 116 mm.

Ten series of box beams with different connection types have been constructed using LVL Kerto-Q panels of 21 mm thickness with spruce ply (0-90-0-0-0-90-0). The Kerto-Q panels were supplied by the Company Metsäwood. Geometrical and mechanical properties of the experimental specimens are used and gathered for clarity in Table 3.1. The same values are taken for elastic modulus E_1, E_3 and the shear modulus G_1, G_3 , corresponding to the values (relative to actions perpendicular to the panel plate) of the VTT certificate provided by Metsäwood [Met14]. Similarly, E_2, G_2 are the values relative to actions in the panel plate. A common beam length of 2432 mm for the specimens is considered here.

The ten series (a) to (j) (see Fig.3.3) consist of hollow square beams that are assembled with ten particular sequences of joint elements. Depicted on Fig.3.3 is the cross-sectional area of the box beams where the mid-thickness profile corresponds to a square of 99.5 mm side. Nevertheless, no glue has been added during the assembly process of samples (a) to (f) and (i) to (j).

	Layer 1	Layer 2	Layer 3
Height h_i (mm)	21	78.5	21
Width b_i (mm)	120.5	42	120.5
Elastic modulus E_i (N/mm ²)	10000	10000	10000
Shear modulus G_i (N/mm ²)	60	600	60

Table 3.1 – Geometrical and mechanical properties for the 3-layered boxed beams (LVL Kerto-Q from Metsäwood).

Three replicates of each sample (Fig.3.3) were tested using a three-point bending setup as outlined in Fig.3.4. Samples **(a)** **(b)** **(c)** **(d)** each have a joint geometry with angles $\theta_1 = 0^\circ$, $\theta_2 = 0^\circ$, $\theta_3 = \pm 15^\circ$, namely dovetail joint (DJ15) and tabs ranging from 41 mm to 486 mm in length. The slot lengths are equal to the tab lengths for each configuration. The samples **(i)** and **(j)** differs in joint geometry to the previous ones, having $\theta_3 = 0^\circ$ (DJ00) and $\theta_3 = \pm 25^\circ$ (DJ25) respectively, while their tab length are identical to that of samples **(b)** and **(f)**(spacing). Recall that lateral panels have identical joint profiles. The upper and lower panels present also the same joint profile that starts this time with a tab element. Samples **(e)** and **(f)** are screwed using Würth ASSY screws of 4x50mm with spacings identical to tab lengths of samples **(a)** and **(b)** respectively. Samples **(g)** and **(h)** are bonded by PUR gluing via a horizontal and a vertical joint, respectively. These last two samples serve as reference for rigid behaviour of the tested beams. Finally, a total of 30 beams were loaded until failure (3 replicates of each sample).

3.3.3 Method

The test beams of length 2432 mm are simply supported on steel rollers over a span L of 2210.5 mm. The actuator motion is controlled automatically, allowing the load to be applied at a constant rate. The load is measured at mid-span using an external load cell placed under the actuator. Vertical displacements (deflections) are recorded using seven linear variable differential transducers (LVDTs) equally spaced along the beam span (spacing = 368.4 mm). Measurements are performed at the middle of the beam's upper panel, so that transducers (d0) and (d6) are positioned at the support locations and at the actuator (d3), which is placed at mid-span (Fig.3.4). Experimental results are given in the next section.

3.3.4 Experimental results

During the experiment, the box beam specimens in each series have been exposed to a simple quasi static loading cycle until failure of the beams.

Sensitivity to tab length

In Fig.3.5, deflection profiles at a maximal load of 3.0 kN are compared for the **(a)** to **(h)** series of tests; DJ15 type with various tab lengths. For each curve, plot symbols represent data points provided by the transducers equally spaced along the beam length (see Fig.3.4). In fact each measurement point is obtained by averaging all the measurements taken from the replicates in a series. For comparison, the curve representing a rigid beam model is included in Fig.3.5.

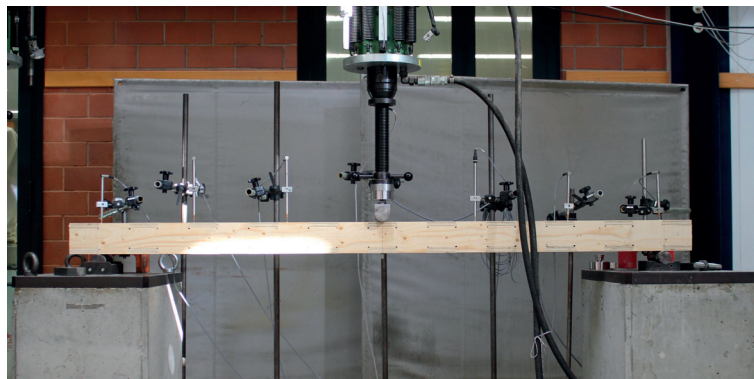
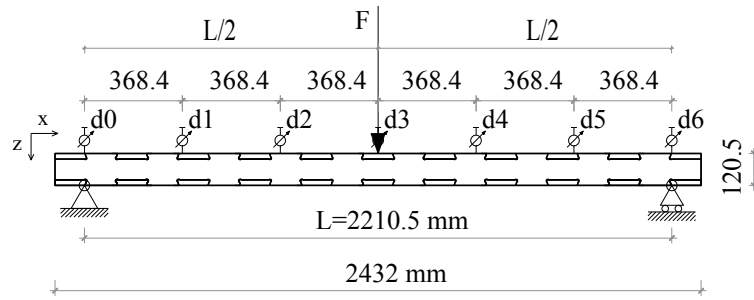


Figure 3.4 – Three-point bending tests with LVDT locations.

Practically, the system Eq.(3.6) subjected to the two-point boundary value conditions Eq.(3.7) can be integrated numerically using the so-called *bvp4c* routine of the Matlab software [SRK]. This routine implements an effective collocation method for the resolution of practical boundary value problems. The solution y_{sol} is a continuous function that is computed by discretizing the domain on K subintervals $[x_k, x_{k+1}]$ such as $0 = x_1 < x_2 < \dots < x_K = L$. Over each subinterval, y_{sol} is approximated by a cubic polynomial function and satisfies the differential equations Eq.(3.4) at both ends and the midpoint of the subinterval. In the present case, accurate results are obtained by taking $K = 1201$ and constant step sizes of 1.84 mm. This value of K guarantees a good execution time without diverging more than 1.2% from a K -value ten times higher. Next, it is worth noting that the rigidity modulus k_1 and k_2 appear as parameters in the model that will be determined from the experimental deflections given in Fig.3.5.

Semi-rigid values for each connection type are obtained by assuming the same value k for the two interface rigidities, i.e. $k_1 = k_2 = k$. In each case, this value is determined iteratively by matching the experimental deflections to the simulated ones. The final k -value is fixed when the deviation between the experimental and numerical points at $x = \{0, L/6, L/3, L/2, 2L/3, 5L/6, L\}$ is minimum. The amplitude of the deviation is sufficiently low for attesting of the overall elastic behavior of the beams. Experimental and simulated deflections are plotted with dotted and solid lines respectively.

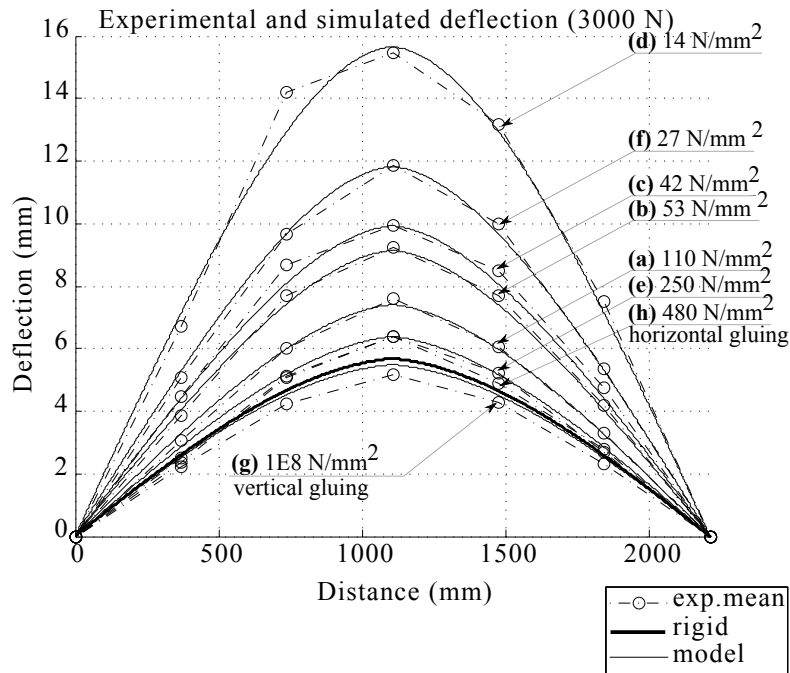


Figure 3.5 – Deflection curves of the tested beams for $F=3000$ N, average of 3 runs per specimens : (a) DJ15-41 mm, (b) DJ15-116 mm, (c) DJ15-221 mm, (d) DJ15-486 mm, (e) 4mm-screw 41 mm, (f) 4mm-screw 116 mm, (g) Vertical glue joint, (h) Horizontal glue joint.

The force varies linearly with the displacement during the loading step and a maximum value of about 16 mm ((d), 486 mm Tab length) is recorded with LVDT (d3) at 3kN.

The effect of shear was included in the models (about 10% of additional deformation for this beam geometry). As expected the deflection curves of the glued beam, the rigid model and the numerical model with rigidity of 10^8 N/mm² match rather well (see Fig.3.5). In Fig.3.6, the rigidity coefficient is represented as a function of the tab length of the MTSJ (or spacing for screws). The screw connection is indicated by a cross and DJ15 is indicated by a circle. The ratio of the stiffness (k_{DJ15}/k_{screw}) is higher when increasing screw spacing/tab length. It goes from $k_{(a)}/k_{(e)} = 0.44$ for 41 mm to $k_{(b)}/k_{(f)} = 1.96$ for 116 mm. The DJ15-connected beam shows a better rigidity when reducing the number of tab elements than the screwed beam when reducing the number of screws (236 elements to 84 elements). Below 116 mm (samples (c) and (d)), DJ15 does not offer adequate performance as low stiffness is accommodated through a low ultimate strength (see table 3.2) due to the shear force being distributed on only a few contact surfaces.

To complete the semi-rigid analysis, the different joint configurations were compared for a maximum beam deflection corresponding to $1/200^{th}$ of the span L . The 486mm-DJ15 connected beam is out of the considered elastic range (0.1 to $0.4F_{max}$). The 116mm-DJ15 connection acts mechanically better than a 116mm-spacing screwed joint with a load of 3.5 kN as against 2.79 kN (25 % more). Within the elastic range, the 41mm-spacing screwed beam and the 41mm-DJ connected beam show not more than 7% of difference between their centre point loads of 4.52 kN and 4.22 kN, respectively.

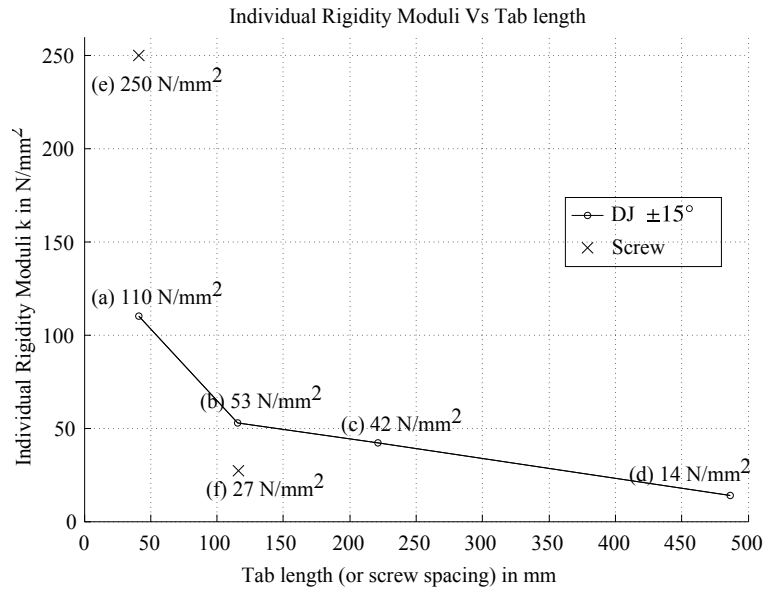


Figure 3.6 – Individual rigidity modulus vs tab length or screw spacing : (a) DJ15-41 mm, (b) DJ15-116 mm, (c) DJ15-221 mm, (d) DJ15-486 mm, (e) 4mm-screw 41 mm, (f) 4mm-screw 116 mm.

rep	deflection(1/200) mm	F(1/200) kN	0.1 Fmax kN	0.4 Fmax kN	Fmax kN	deflection max mm
(d) DJ15-486		2.19	0.52	2.08	5.19	35.24
(f) S4mm-116		2.79	0.77	3.07	7.67	71.06
(i) DJ00-116		2.78	1.16	4.65	11.63	50.53
(c) DJ15-221		3.19	1.05	4.19	10.48	52.55
(b) DJ15-116	11.05	3.50	1.14	4.55	11.37	43.80
(a) DJ15-41		4.22	1.22	4.89	12.23	41.65
(e) S4mm-41		4.52	1.20	4.80	12.01	62.11
(h) H-glued		4.92	1.29	5.17	12.92	40.30
(g) V-glued		6.32	1.83	7.31	18.28	36.42

Table 3.2 – Deflection of beam samples at 1/200th of span.

Sensitivity to tab contact face angle

The Figure 3.7 shows deflection profiles at a maximal load of 3.0 kN for the samples (i)-DJ00, (b)-DJ15, (j)-DJ25 and (f)-4mm screw). The tab length (or screw spacing) is set to 116 mm for each sample.

The geometry of the (i)-DJ00 is similar to the one of a traditional finger joint. Consequently, the upper and lower panels are only blocked from a vertical displacement by a possible friction between the contact faces of the tabs and the slots. As soon as the tab face angle increases to 15° and 25° the rigidity grows with 26% and 38%, respectively. A difference of less than 10% between (b)-DJ15 and (j)-DJ25 can not be considered as significant. Using larger angles, as 25° for instance, induces an inclination of the contact normal that increases the transverse components of stresses. The loads, perpendicular to the panel grain, are higher. So the presence of cross layers in the panel plies takes all its importance. Simek et al. [SS10] mention

that previous studies have shown an optimal angle between 10° and 14°.

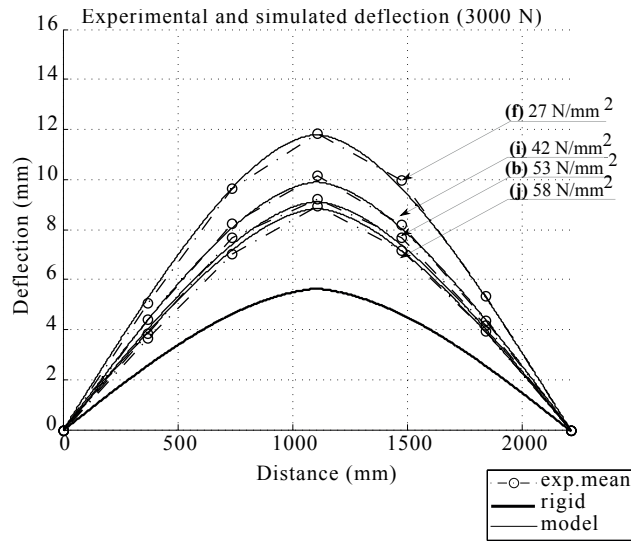


Figure 3.7 – Deflection curves of the tested beams for $F=3000$ N, average of 3 runs per specimens : **(i)** DJ00-116 mm, **(b)** DJ15-116 mm, **(j)** DJ25-116 mm, **(f)** 4mm-screw 116 mm.

3.4 Conclusion

This paper focuses not directly on geometrically complex assemblies, but on the development and improvement of joints that allow for the design and fabrication of those. From the architectural point of view, the main priorities are considered to be geometric variability, efficient design, fabrication and assembly, as well as a visual appearance that must not be hidden. However, in order to develop such connections for structural building components, the mechanical behavior must be analyzed thoroughly. The specimens have therefore been chosen with a simple geometry for these first experiments and models, although the connections have already been successfully applied on various other assemblies, as shown in Fig.3.8 [RSMW14]. The experimental results presented in this paper, allow for a comparison with other state-of-the-art joints. The MTSJ provides a highly feasible alternative to the traditional screwed connection. Compare to a reasonable screw spacing (116 mm, 84 screws), a box beam connected with MTSJ-dovetail type gets 96% of rigidity with a much lower assembly time. One should note that a screwed assembly would not comply to the desired standard [fSC04] when used in conjunction with the 21 mm Kerto-Q panels employed for the study. Typically, A minimal thickness of 40 mm (at least ten times the screw diameter) is required for connecting edgewise panels with 4 mm-screw in the absence of dedicated testing. The experimental results are generally encouraging; they figure out that the MTSJ joints behave efficiently as a semi-rigid connection. Within the field of complex geometry, IBOIS has initiated teamwork to design different timber folded-plate structures connected with MTSJ joint. Modeling the semi-rigid behavior of the connection is of main importance for their global structural analysis. The behavior of these joints will be further explored under other loading cases (e.g. moment about edges of short-plate elements).



Figure 3.8 – The MTSJ joints have already been successfully applied to more complex assemblies, where the joint angles θ_1 , θ_2 and θ_3 are not zero (Robeller et al, 2014).

Outcomes ① *

The outcomes of the present chapter are synthesized as follows.

From the mathematical description of the MTSJ with open slots and the combination of the rotation angles which followed the Bryant sequence, three practical variants were identified.

The more versatile is the Japanese joint variant (JJ) with $\theta_1, \theta_2, \theta_3 \neq 0^\circ$. Fig.3.9 shows the unique degree of freedom (1DOF) consisting on a oblique out-of-plane insertion. The milling imposes a five-axis router to achieve the locking face orientation.

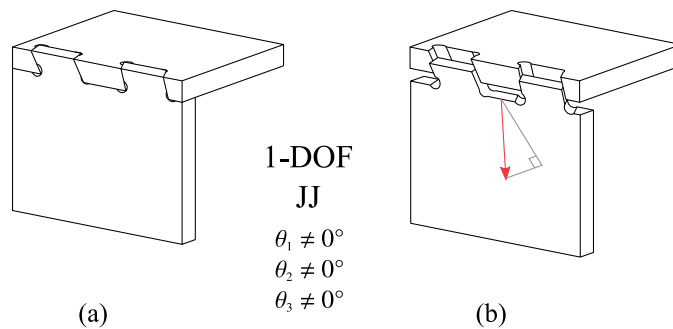


Figure 3.9 – (a) MTSJ Japanese variant (JJ) : 1 degree of freedom (1-DOF), (b) 1 out-of plane translation.

The simplest one is the Finger joint variant (FJ) with $\theta_1, \theta_2, \theta_3 = 0^\circ$. Fig.3.10 shows the three degrees of freedom (3DOF) consisting on two in-plane translations and one rotation about the joint axis. The milling is achieved with only three-axis router.

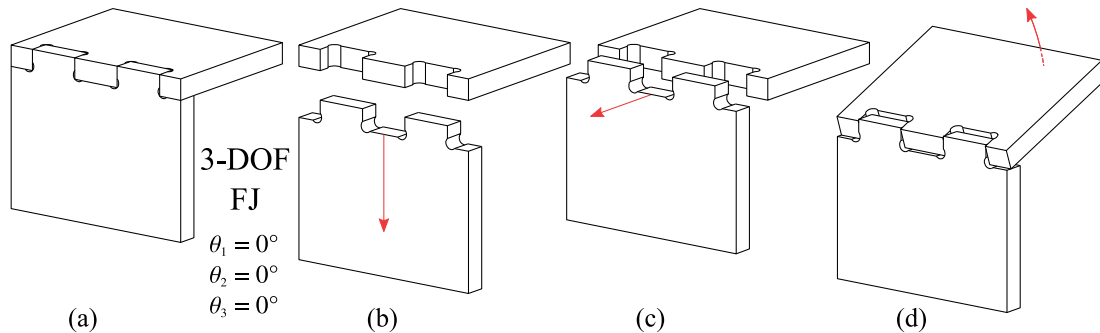


Figure 3.10 – (a) MTSJ Finger joint variant (FJ) : 3 degree of freedom (1-DOF), (b) 1st in-plane translation, (c) 2nd in-plane translation, (d) 1 rotation about joint axis.

*This additional section was not included in the original publication.

Chapter 3. On the semi-rigidity of dovetail joint for the joinery of LVL panels

An intermediate variant, the Dovetail joint (DJ) with $\theta_1, \theta_2 = 0^\circ$ and $\theta_3 \neq 0^\circ$ was tested in shear. Fig.3.11 shows the unique degree of freedom (1DOF) consisting on one in-plane translation. The milling imposes a five-axis router to achieve the locking face orientation.

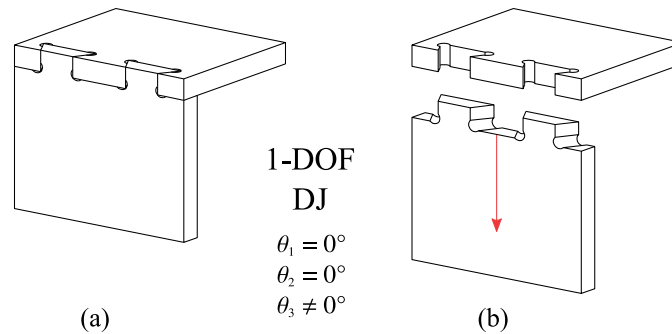


Figure 3.11 – (a) MTSJ Dovetail joint variant (DJ) : 1 degree of freedom (1-DOF), (b) 1 in-plane translation.

A three-point bending test on boxed beams, where the sides are assembled with the upper and lower parts by different geometries of DJ, demonstrated the ability of the semi-rigid connection to resist shear at least as well as screws. The individual shear rigidity moduli k of a beam connected with DJ variant ($\theta_3 = 15^\circ$, $L_{tab} = 116\text{mm}$) was twice the one of a screwed beam ($\phi 4 \times 70\text{mm}$, 116mm screw spacing). In addition, the stiffness with DJ connection also increased with the decrease in tab length L_{tab} while θ_3 angle had no significant influence.

The particularity of the JJ and DJ variants is to restrain five degree of freedom. Compared with the different solutions introduced in the section 2.1.1, these two wood-to-wood connections are the only one that could theoretically restrain the rotation about their axis without glue or additional fastener. Quantifying this level of semi-rigidity is the objective of the next chapter.

What about the moment-resisting performance of 1DOF MTSJ with open slots ?

→ **Objective ②** (see chapter 4)

References

- [20113] *European Technical Approval ETA-11/0190 Würth self-tapping screws for use in timber constructions*. European Organisation for Technical Approvals, 2013.
- [D.B99] D.B.Engströ. Evaluation of connections by the use of semi-rigidity. In *COST C1, Semi-rigid Timber Joints - Structural Behaviour, Modelling and New Technologies: Final Report of Working Group "Timber Joints"*. Technische Universität Dresden, 1999.
- [fSC04] European Committee for Standardization (CEN). *CEN-EN1995-1-1:2004+A1 - Eurocode 5: Design of timber structures - Part 1-1: General - Common rules and rules for buildings*. (CEN), Brussels, 2004.
- [Gra87] W. Graubner. *Gegenüberstellungen japanischer und europäischer Lösungen, 2nd edition*. Deutsche Verlags-Anstalt, Stuttgart, 1987.
- [JS10] J. B. M. Sousa Jr. and A. R. Da Silva. Analytical and numerical analysis of multilayered beams with interlayer slip. *Engineering Structures*, 32:1671–1680, 2010.
- [KFZ07] P. Krawczyk, F. Frey, and A.P. Zieliński. Large deflections of laminated beams with interlayer slips: Part 1: model development. *Engineering Computations*, 24(1):17–32, 2007.
- [Kre95] H. Kreuzinger. *Mechanically jointed beams and columns*, pages B11/1–8. Centrum Hout, The Netherlands, 1995.
- [M56] K. Möhler. *Über das Tragverhalten von Biegeträgern und Druckstäben mit zusammengesetzten Querschnitten und nachgiebigen Verbindungsmitteln*. Habilitation, Technische Universität Karlsruhe, Germany, 1956.
- [Met14] Metsäwood. Kerto for advanced structural engineering. (<http://www.metsawood.com/products/kerto>), 2014. Kerto brochure and VTT certificate and others.
- [NSRF04] J. Natterer, J.L. Sandoz, M. Rey, and M. Fiaux. *Construction en Bois: Matériau, Technologie et Dimensionnement, 2nd edition*, volume 13 of *Traité de génie civil de l'Ecole polytechnique fédérale de Lausanne*. Presses Polytechniques et Universitaires Romandes, 2004.
- [NSV51] N.M. Newmark, C.P. Siess, and I.M. Viest. Tests and analysis of composite beams with incomplete interaction. volume 9, pages 75–92. Proceedings of Society for Experimental Stress Analysis, 1951.
- [Rob15] C. Robeller. *Integral Mechanical Attachment for Timber Folded Plate Structures*. PhD thesis, Ecole Polytechnique Fédérale de Lausanne, 2015.

Chapter 3. On the semi-rigidity of dovetail joint for the joinery of LVL panels

- [RSMW14] C. Robeller, A. Stitic, P. Mayencourt, and Y. Weinand. Interlocking folded plate - integrated mechanical attachment for structural wood panels. In *Advances in Architectural Geometry 2014*. Springer - submitted may 2014, 2014. <http://www.architecturalgeometry.org/aag14/>.
- [Sch68] W. Schelling. *Die Berechnung nachgiebig verbundener, zusammengesetzter Biegeträger im Ingenieurholzbau, Dissertation*). PhD thesis, TH Karlsruhe, Germany, 1968.
- [SRK] L. F. Shampine, M. W. Reichelt, and J. Kierzenka. Solving boundary value problems for ordinary differential equations in matlab with bvp4c. <http://www.architecturalgeometry.org/aag14/>.
- [SS10] V. Sebera and M. Simek. Finite element analysis of dovetail joint made with the use of cnc technology. *Acta Universitatis Agriculturae Et Silviculturae Mendelianae Brunensis*, LVIII, 3:321–328, 2010.

4 Rotational Stiffness at Ridges of Timber Folded-plate Structures

Stéphane Roche, Geoffroy Mattoni and Yves Weinand

Published in International Journal of Space Structures, vol. 30, num. 2, p. 153-168, 2015, DOI 10.1260/0266-3511.30.2.153

Abstract

Folded-plate structures provide an efficient design using thin laminated veneer lumber panels. Inspired by Japanese furniture joinery, the multiple tab-and-slot joint was developed for the multi-assembly of timber panels with non-parallel edges without adhesive or metal joints. Because the global analysis of our origami structures reveals that the rotational stiffness at ridges affects the global behaviour, we propose an experimental and numerical study of this linear interlocking connection. Its geometry is governed by three angles that orient the contact faces. Nine combinations of these angles were tested and the rotational slip was measured with two different bending set-ups: closing or opening the fold formed by two panels. The non-linear behaviour was conjointly reproduced numerically using the finite element method and continuum damage mechanics.

Keywords Semi-rigid, Connection, Moment-Rotation, Folded-plate, Timber.

Objective ② *

Testing the rotational stiffness of multiple Tab-and-slot joint

*This additional section was not included in the original publication.

4.1 Introduction

The first folded-plate roofs were built in the mid-50s using plywood [War01]. However, technical problems arose from the variations in the plywood's structural properties, the aesthetics of the outer layers were paramount while its characteristic strength could not be fully controlled. Single-fold plate roofs behave as a series of V-section beams (Fig.4.1). The plywood skin transmits shear like a web and transfers in-plane forces to the ends of the roof where the walls and transverse stiffeners bear the vertical and horizontal load components, respectively [War01, MLP07]. Fifty years after the first attempts at folded-plate roof structures [War01], Jaksch et al. [JFW12] proposed a similar pitched roof of lightweight cross-laminated timber (CLT) rather than plywood. More recent attempts have adopted glue and nails or cold-formed thin steel plate to create a rigid joint at the ridge. Today, laminated veneer lumber (LVL), CLT, and solid wood panels (SWP) are the most commonly used materials for highly stressed structures. These high-performance panels inspired other architects and researchers to develop novel solutions for reviving folded-plate structures. In 2008, Buri et al. described the application of origami paper folding to timber folded-plate structures at the 10th World Conference on Timber in Japan [BW08]. The structure's 21 mm plywood panels were assembled with 5 mm self-drilling screws arranged in staggered rows at the mitre joints of the panels. Both sides were bevelled at a 60° angle to form a 120° corner. Because the relative position of the parts had to be set before screwing, pre-mounting with jigs was required. Failure during a loading test occurred through tearing at the ridges and valleys, a direct result of the weakness of the connection [Bur10]. Although origami folded-plate structures are promising complex timber structures, the connections of their thin panels must be improved. Robeller et al. described the first approach to the problem in 2014 [RSMW14]. A double-curved folded-plate prototype was constructed using a five-axis CNC machine. The cut LVL plates had integrated jointing at their edges. Based on linear connections used in furniture (e.g., dovetail or Japanese nejiri arigata joints), these multiple tab-and-slot joints (MTSJ) with no adhesive bonding allow simultaneous assembly of up to three ridges or valleys. The panels can then be directly interlocked in situ at their final location. All these previous studies noted a lack in the connection stiffness model that could affect the global behaviour. Literature on timber connection rarely addresses the structural behaviour of panel connections. Most research on connections over the last thirty years has examined joint stiffness within the context of frame structures. Among many others, H.J. Larsen, A.J.M. Lejiten, A. Kevarinmaki and D.B. Engstrom, the Scandinavian members of the Timber Joints working group of the European Cooperation in Science and Technology (COST action C1, Semi-rigid behaviour of civil engineering structural connections), have reported specific works on the rotational stiffness of timber joints [HJ99]. They showed that the inclusion of semi-rigidity in the structural analysis gave more realistic frame stress resultants and deflection, and thus demonstrated its significant effect on stability. Before the application of limit-state codes, such as Eurocode (EC), to the design of structures, joints were commonly considered as either hinged or rigid. However, the fastened connections usual in timber or steel structures actually behave as semi-rigid connections [HJ99, Jas00]. These works led EC5 [fSC04] to take fastener stiffness into consideration in the design of timber structures. The new rules are nonetheless unsuitable for traditional carpentry joints. Research programs on

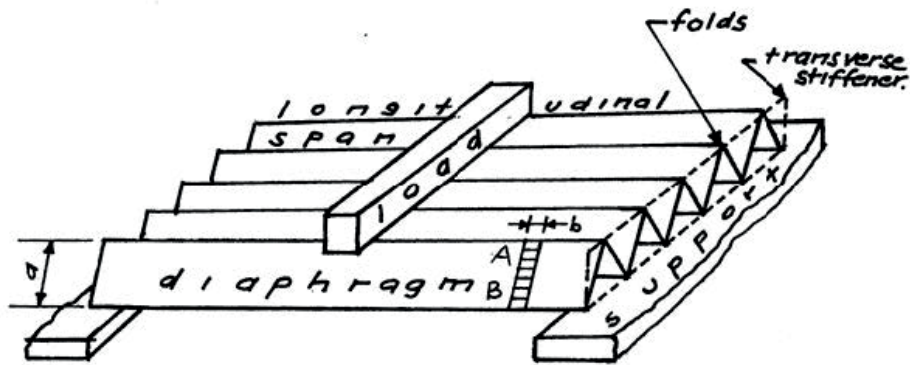


Figure 4.1 – Single-fold plate roof as V-section beams [MLP07].

the moment-rotation behaviour of this type of connections include a project by the Czech Ministry of Culture, which is dedicated to investigating the timber joints in historical structures (“Design and Assessment of Timber Joints of Historical Structures”, started February 2012). A study of the bending stiffness of a through dovetail joint for plywood panels has also been reported. Again, friction is implemented in the 3D-solid finite element model, but the studied orthotropic material, used for furniture, was only considered in its elastic stage as the final displacement was limited to 2 mm [SS10]. Robeller et al. [RSMW14] presented a linear interlocking connection of plates for the in-space assembly of folded plate shells. They introduced a geometrical solution for simultaneously joining plates with multiple non-parallel edges, and calculated the mechanical performance of the overall structure by a finite element method (FEM) analysis of perfectly rigid joints. It was completed by a local simulation of bending on a dovetail joint connecting two panels. The bending moment was transformed into compression, normal and shear forces parallel to the locking faces. Conjointly, Roche et al. [RMW15] conducted numerical and experimental work to test the assumptions of semi-rigid behaviour of such a connection. Three-layered box beams assembled at the inter-layers with dovetail joints with differing tab lengths and tab angles were loaded to failure in three-point bending tests. The connection showed promising stiffness results. For instance a 110 mm-tab-length dovetail joint was stiffer than 110-mm-spaced screws. The previous results confirmed the good strength/stiffness ratio of the MTSJ in shear. The shear due to the inter-layer slip is transferred by compression on the locking faces. The moment-resisting performance discussed in Ref. [RSMW14] should be also confirmed. This paper presents a study of the rotational stiffness of a MTSJ as a structural connection in architecture. A dedicated folding machine was developed to test the Japanese pattern of the MTSJ under bending moments. A parametric experimental study explored the rotational stiffness through different combinations of the three angles governing the joint geometry. The non-linear behaviour is reproduced by finite element analysis using an adaptation of the continuum damage model of Sandhaas [San01].

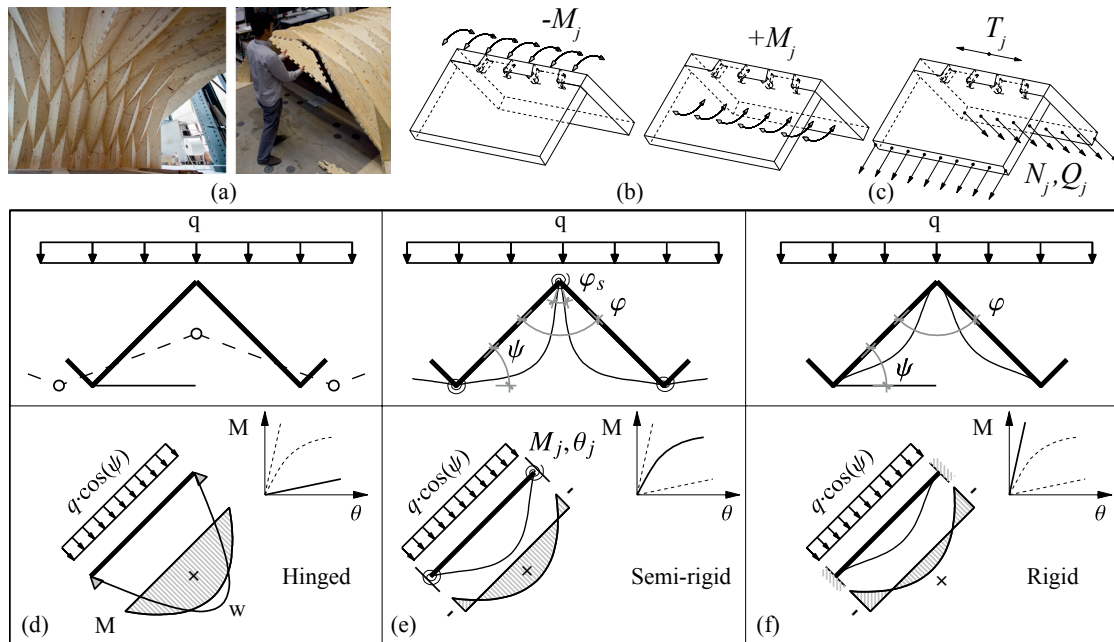


Figure 4.2 – (a) Origami double-curved folded-plate prototype, reported by Robeller et al [RSMW14]. (b) Bending moments at the ridge. (c) Forces along and perpendicular to the ridge. (d) Hinged joint at ridge. (e) Semi-rigid joint at the ridge. (f) Rigid joint at the ridge.

4.2 The Multiple Tab-and-Slot Joint as a Structural Panel Connection

4.2.1 Forces at ridges and valleys

When a folded-plate structure is uniformly and vertically loaded, slab and plate action induce transverse and longitudinal action in the folds [JFW12]. The ridges typically experience the bending moment, M_j (Fig.4.2b), forces perpendicular to the ridge in the panel plane, N_j , and out of the panel plane, Q_j (Fig.4.2c), and forces along the ridge, T_j (Fig.4.2c). The study is limited to the behaviour under the bending moment, and neglect the effect of the transverse forces at this stage. As the model of this joint is assumed to be semi-rigid (Fig.4.2e) during bending of the plates, an additional rotation is induced at the ridges. This is in contrast to the rigid model, where the initial angle, φ , between the panels remains unchanged after deformation (Fig.4.2f). The MTSJ offers a moment-resisting connection that a hinge cannot supply (Fig.4.2d). Here, we seek to understand the way in which geometry, particularly the angles directing the normal to the locking face, affects this semi-rigidity.

4.2.2 Description of the MTSJ

A detailed description of this “integrated mechanical attachment” is given in [RSMW14]; thus, in the next section a brief introduction to the geometrical parameters of the joint is included. The ridge (or valley) connection employed here is a one-degree-of-freedom connection (for the purpose of assembly) that has tabs inserted in slots (Fig.4.3e). “Multiple” refers to the interlocked tabs and slots, which are repeated along the common edge of two connected

4.2. The Multiple Tab-and-Slot Joint as a Structural Panel Connection

panels. The geometry of the connection defines the relative positioning of the panels, and allows a certain degree of load-transfer between them. The assembly of the two panels is directed along the vector of insertion. The locking faces of each part belong to the same contact plane after insertion. The insertion vector and the vector normal to the locking face are obtained by the sequence of rotations Eq.(4.1) following the convention of the Bryant angles (Fig.4.3a–d).

$$\begin{aligned}
 & \{P_i, F = (\mathbf{u}_1, \mathbf{u}_2, \mathbf{u}_3)\} \\
 & \quad \downarrow R(\mathbf{u}_1, \theta_1) \\
 & \{P'_i, F' = (\mathbf{u}'_1 = \mathbf{u}_1, \mathbf{u}'_2, \mathbf{u}'_3)\} \\
 & \quad \downarrow R(\mathbf{u}'_2, \theta_2) \\
 & \{P''_i, F'' = (\mathbf{u}''_1, \mathbf{u}''_2 = \mathbf{u}'_2, \mathbf{u}''_3)\} \\
 & \quad \downarrow R(\mathbf{u}''_3, \pm\theta_{3,i}) \\
 & \{P'''_i, F''' = (\mathbf{u}'''_{1,i}, \mathbf{u}'''_{2,i}, \mathbf{u}'''_{3,i} = \mathbf{u}''_3)\}
 \end{aligned} \tag{4.1}$$

If \mathbf{n}_0 and \mathbf{n}_1 are the normals of the two panels, the frame of the joint $F = (\mathbf{u}_1, \mathbf{u}_2, \mathbf{u}_3)$ can be calculated as $\mathbf{u}_1 = \mathbf{n}_0 \times \mathbf{n}_1$, $\mathbf{u}_2 = \mathbf{n}_0$ and $\mathbf{u}_3 = \mathbf{u}_1 \times \mathbf{u}_2$. Then, the line segment representing the intersection of the two panel mid-planes can be uniformly divided into N points $(X_i)_{(i=1\dots N)}$, the distance between points will be the tab length L_j of the joint. The plane P_i will be the plane of normal \mathbf{u}_1 , containing the point X_i (see Fig.4.3a). Thus, by three successive rotations of this plane, P_i , and its attached frame, F (see Fig.4.3a–d), the final joint will be obtained, defining for both the tab and slot, the planes, P'''_i , as the locking faces and the vectors, $\mathbf{u}'''_{1,i}$ and $\mathbf{u}''_3 = \mathbf{u}'''_{3,i}$, as their normals and insertion vector, respectively (Fig.4.3d). This elemental sequence of rotations is represented by the Bryant angles, θ_1 , θ_2 and θ_3 . In this study, the principle of the nejiri arigata joint described by Robeller [RSMW14, Rob15] is adopted, where $+\theta_3$ is applicable from P_1 to $P_{N/2}$ and $-\theta_3$ from $P_{N/2}$ to P_N .

This geometry allows a multi-edge assembly of one panel with three adjoining plates. From the origami folded-plate structure (see Fig.4.4a), the four plates k ($k = 0, 1, 2, 3$) are taken (see Fig.4.4b). Plate ‘0’ (i.e., $k = 0$) shares edges ‘01’, ‘02’, and ‘03’ with plates ‘1’, ‘2’, and ‘3’, respectively. For each edge, the eligible subset of insertion vectors is defined as E^{01} , E^{02} , and E^{03} (see Fig.4.4c). The fabrication constraint, β_{max} , referring to the maximal tool inclination, then sets the limits of the dihedral angle φ^{0k} and the angles θ_1^{0k} , θ_2^{0k} , and θ_3^{0k} that govern the insertion vector subsets and the tab angle, respectively [RSMW14, Rob15, Mat14]. For example, for a 12- mm-diameter milling tool with a cutting length of 28 mm, β_{max} is 30° , which prevents spindle collision when machining 21 mm panels. If the dihedral angle, φ , is set to 120° (Fig.4.3f) or if θ_3 is set to 30° (Fig.4.3g), then the maximum tool inclination is already reached and θ_1 and θ_2 cannot be different from 0° . Finally, θ_1 , θ_2 , and θ_3 can only all have non-zero values if $\beta_{max} < 30^\circ$ and $60^\circ < \varphi < 120^\circ$. Mattoni showed that the interdependency between the Bryant angles, dihedral angle, and tool inclination limits the possible combinations [Mat14]. By intersecting the three constrained local vector subsets, a unique vector subset is finally

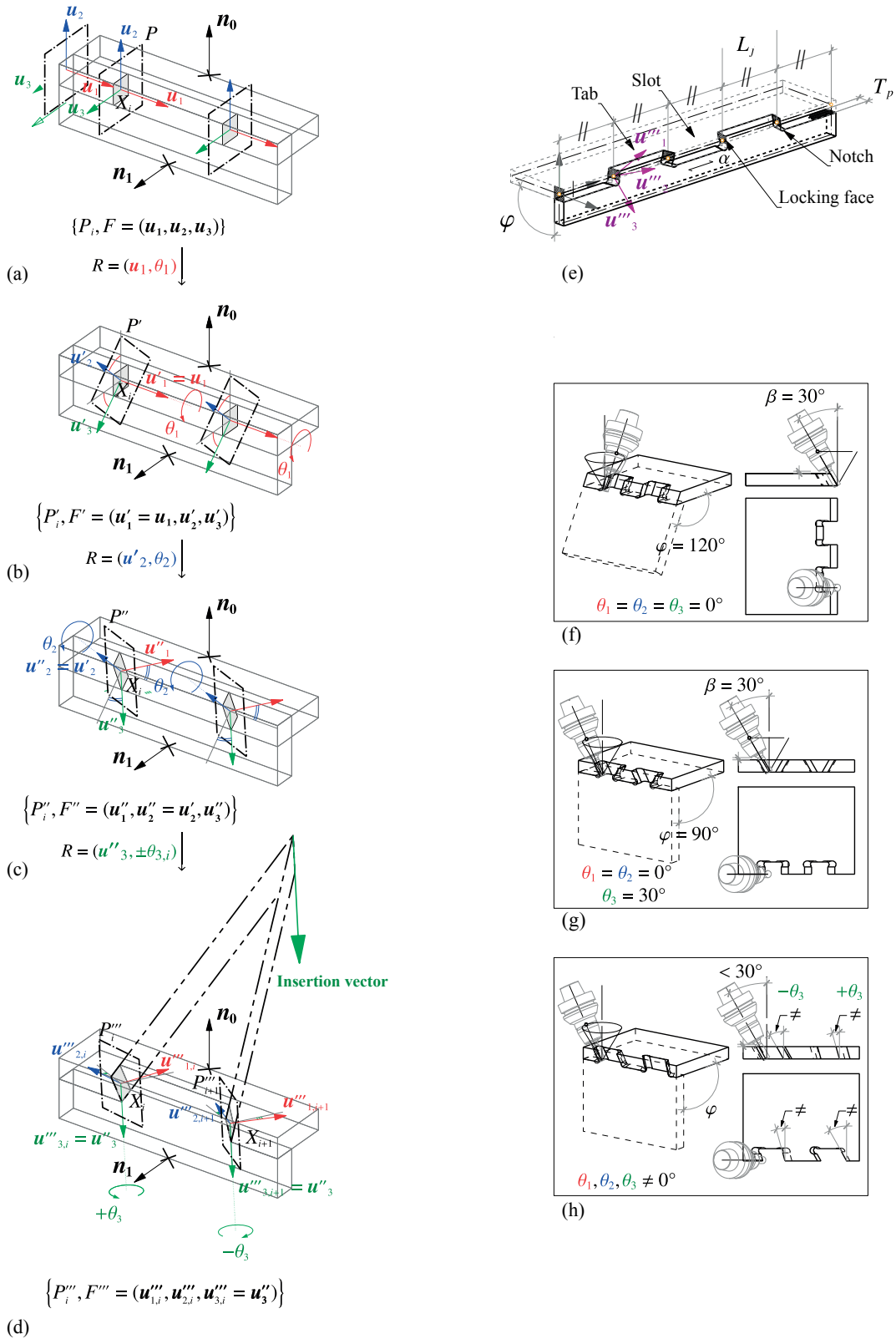


Figure 4.3 – (a)–(d) Rotation sequence for designing the locking face. (e) Terminology of the MTSJ. (f) Fabrication constraint due to the dihedral angle. (g) Fabrication constraint due to the tab angle. (h) Constrained combination of θ_1, θ_2 , and θ_3 .

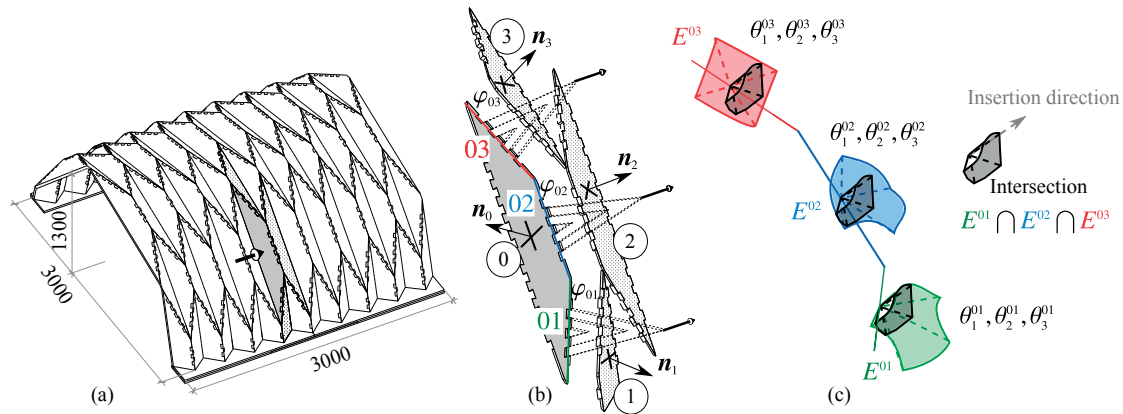


Figure 4.4 – Assembly constraints. (a) Plates in situ in the global geometry. (b) Three-edge simultaneous assembly. (c) Selection of the insertion vector in the intersection space.

obtained where the insertion vector must be selected.

Given that we intend to analyse the rotational stiffness of the joint, the angle θ_3 will be taken to be at least 10° where the locking faces are definitely not parallel and offer a certain resistance to rotation about the ridge axis. Detailed analysis determining the parameters for our sample is given in Ref. [Mat14].

4.3 Experimental study

4.3.1 Description of the samples

Eleven series of two 21 mm LVL Kerto-Q panels with spruce ply (0-90-0-0-0-90-0) were assembled with eleven particular sequences of joint elements. The geometric properties of the specimens are summarised in Table 4.1 and Fig.4.5. No glue was added during the assembly of samples (a) to (i), which correspond to nine characteristic combinations of the Bryant angles [Mat14]. All had the same tab length of 50 mm. The two panels F0 and F1 were 200 mm long (along the ridge) and 150 mm wide; they had two and one full tab, respectively. One series (j)

Parameters	Symbol	Unit	Val
Insertion angle (1)	θ_1	°deg	
Insertion angle (2)	θ_2	°deg	→
Tab angle	θ_2	°deg	
Dihedral angle	φ	°deg	90
Tab length	L_t	mm	50
Panel thickness	T_p	mm	21
Panel density	ρ_k	kg/m ³	480
Angle edge to grain	α	°deg	0
Notch 12 mm	r	t or b	b
Tool angle T241	β	°deg	30

Table 4.1 – Sample parameters

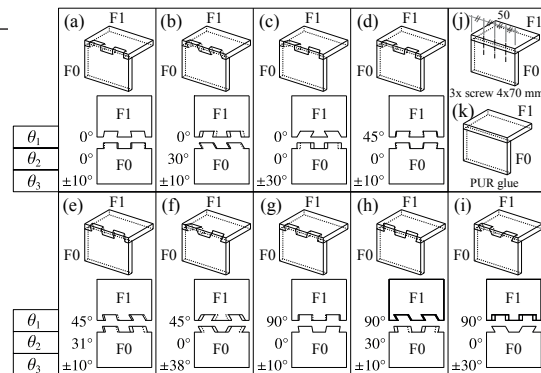


Figure 4.5 – Combination of Bryant angles.

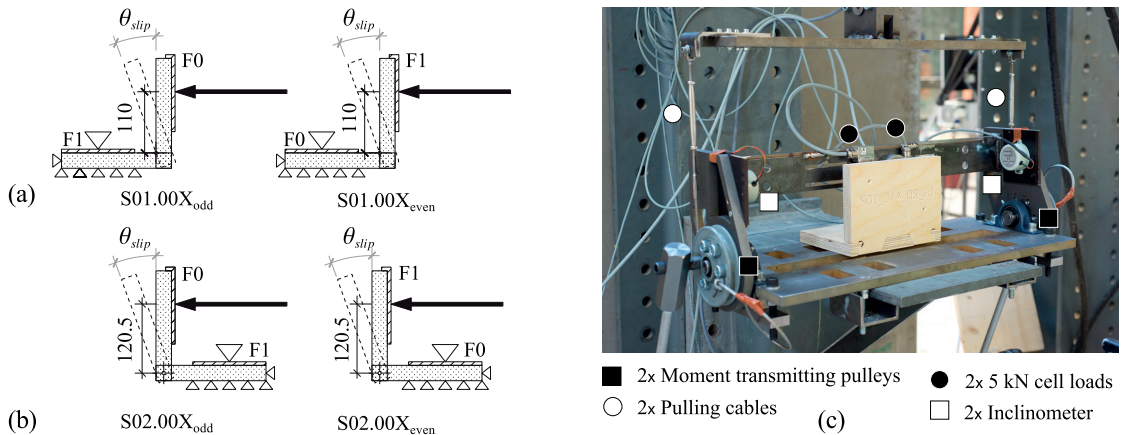


Figure 4.6 – Bending tests. (a) Closing mode, (b) Opening mode, and (c) Sample geometries.

was screwed using three Würth ASSY screws (4 mm × 70 mm) with 50 mm spacing. The last series (k) was bonded by PUR gluing. These last two series had butt joints.

4.3.2 Method

Four specimens of each sample were tested using a dedicated folding-test machine (Fig.4.6). To reflect the asymmetry of the joint along the bisector plane of the connected panels, the tests of pushing F0 and F1 were each repeated twice. A 20 kN cylinder pulled two cables to drive the rotation of two moment-transmitting pulleys. Then the plate supporting two 5 kN cell loads acted as a level arm on the vertical panel F0 (or F1) of the sample. The horizontal F1 (or F0) panel was rigidly clamped onto the base plate. The location of the rotation centre of the rig could be set to coincide with the rotation centre of the joint. Rotation and loads were recorded by averaging values of two inclinometers and summing data from the cell loads, respectively. This method was applied in both closing (S01) and opening (S02) tests. A total of 88 specimens were tested.

4.4 Numerical model

4.4.1 Material model

The LVL Kerto-Q material is implemented as multi-layered due to the circular notch (Fig.4.7), which is required for the digital manufacture of the joint, reducing the contact surface to a few layers. As through-thickness stress cannot be ignored, the model uses linear hexahedral elements with reduced integration (C3D8R). Each of the seven layers has its own orientation (0-90-0-0-0-90-0). The Coulomb friction coefficient is set to 0.3.

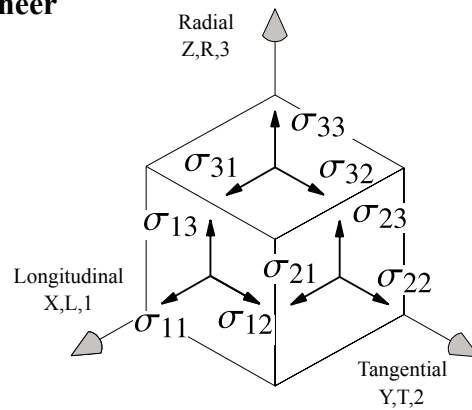
4.4.2 Elastic behaviour

Each northern spruce veneer is typically considered orthotropic, and behaves elastically in its local orientation frame (Fig.4.8). Interfaces are considered to be rigid, so inter-laminar failure is not addressed. Elastic properties are summarised in Table 4.2 [San12, ISFK08]. Reliable values for spruce veneer are relatively rare in the published literature.



Figure 4.7 – Reduced contact on the locking faces.

Veneer



$$\underline{\varepsilon} = (\varepsilon_{11}, \varepsilon_{22}, \varepsilon_{33}, 2\varepsilon_{12}, 2\varepsilon_{13}, 2\varepsilon_{23})^T$$

$$\underline{\sigma} = (\sigma_{11}, \sigma_{22}, \sigma_{33}, \sigma_{12}, \sigma_{13}, \sigma_{23})^T$$

**LVL Kerto-Q
21 mm**

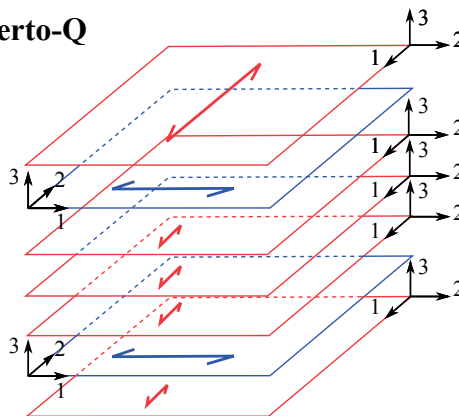


Figure 4.8 – Material frame and orientation.

Property	Symbol	Value	Unit
Elastic modulus 11	E_{11}	6200	Mpa
Elastic modulus 22	E_{22}	210	Mpa
Elastic modulus 33	E_{33}	210	Mpa
Shear modulus 12	G_{12}	350	Mpa
Shear modulus 13	G_{13}	200	Mpa
Shear modulus 23	G_{23}	40	Mpa
Poisson's ratio 12	ν_{12}	0.61	
Poisson's ratio 13	ν_{13}	0.60	
Poisson's ratio 23	ν_{23}	0.50	

Table 4.2 – Elastic properties of spruce

4.4.3 Damage approach

To approach the non-linear behaviour of the joint, we use a wood model based on continuum damage mechanics (CDM) (generously provided by C. Sandhass, and described in detail in Ref. [San01, San12]). A main feature of the model is its penalization of the elastic moduli. The compliance matrix \mathbf{C}^{dam} , derived for the elastic compliance matrix, defines the new behaviour of damaged elements (see Eqs. 4.2–4.5).

$$\boldsymbol{\varepsilon} = \mathbf{C}^{dam} \boldsymbol{\sigma} \quad (4.2)$$

$$\begin{bmatrix} \varepsilon_{11} \\ \varepsilon_{22} \\ \varepsilon_{33} \\ 2\varepsilon_{12} \\ 2\varepsilon_{13} \\ 2\varepsilon_{23} \end{bmatrix} = \begin{bmatrix} \mathbf{C}_1^{dam} & 0 \\ 0 & \mathbf{C}_2^{dam} \end{bmatrix} \begin{bmatrix} \sigma_{11} \\ \sigma_{22} \\ \sigma_{33} \\ \sigma_{12} \\ \sigma_{13} \\ \sigma_{23} \end{bmatrix} \quad (4.3)$$

$$\mathbf{C}_1^{dam} = \begin{bmatrix} \frac{1}{(1-d_{11})E_{11}} & \frac{-\nu_{12}}{E_{22}} & \frac{-\nu_{31}}{E_{33}} \\ \frac{-\nu_{12}}{E_{11}} & \frac{1}{(1-d_{22})E_{22}} & \frac{-\nu_{32}}{E_{33}} \\ \frac{-\nu_{13}}{E_{11}} & \frac{-\nu_{23}}{E_{22}} & \frac{1}{(1-d_{33})E_{33}} \end{bmatrix} \quad (4.4)$$

$$\mathbf{C}_2^{dam} = \begin{bmatrix} \frac{1}{(1-d_{12})G_{12}} & 0 & 0 \\ 0 & \frac{1}{(1-d_{13})G_{13}} & 0 \\ 0 & 0 & \frac{1}{(1-d_{23})G_{23}} \end{bmatrix} \quad (4.5)$$

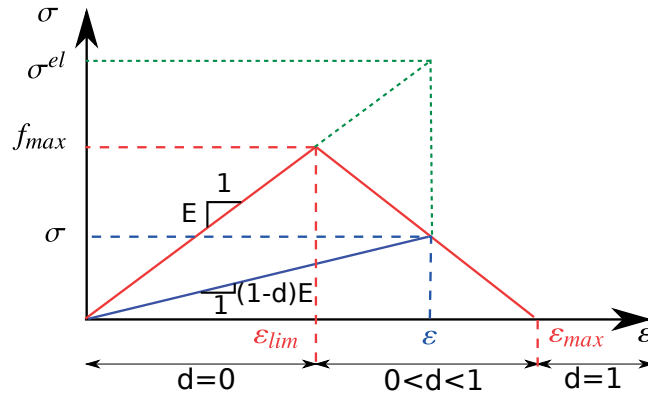


Figure 4.9 – Brittle behaviour.

d_{ij} are the damage variables, which depend on the strain state. Here we recall the failure modes F_m (described in Ref. [San12]) that control the onset of damage.

Brittle behaviour

- In tension :

$$F_{t,1} = \frac{\sigma_{11}}{f_{t,0}} \leq 1 \quad (4.6)$$

- In tension and shear:

$$F_{t,2} = \frac{(\sigma_{22})^2}{(f_{t,90})^2} + \frac{(\sigma_{12})^2}{(f_v)^2} + \frac{(\sigma_{23})^2}{(f_{roll})^2} \leq 1 \quad (4.7)$$

$$F_{t,3} = \frac{(\sigma_{33})^2}{(f_{t,90})^2} + \frac{(\sigma_{13})^2}{(f_v)^2} + \frac{(\sigma_{23})^2}{(f_{roll})^2} \leq 1 \quad (4.8)$$

- In shear under compression perpendicular to grain:

$$F_{v,2} = \frac{(\sigma_{12})^2}{(f_v)^2} + \frac{(\sigma_{23})^2}{(f_{roll})^2} \leq 1 \quad (4.9)$$

$$F_{v,3} = \frac{(\sigma_{13})^2}{(f_v)^2} + \frac{(\sigma_{23})^2}{(f_{roll})^2} \leq 1 \quad (4.10)$$

Ductile behaviour

- In compression:

$$F_{c,1} = \frac{-\sigma_{11}}{f_{c,0}} \leq 1 \quad (4.11)$$

$$F_{c,2} = \frac{-\sigma_{22}}{f_{c,90}} \leq 1 \quad (4.12)$$

$$F_{c,3} = \frac{-\sigma_{33}}{f_{c,90}} \leq 1 \quad (4.13)$$

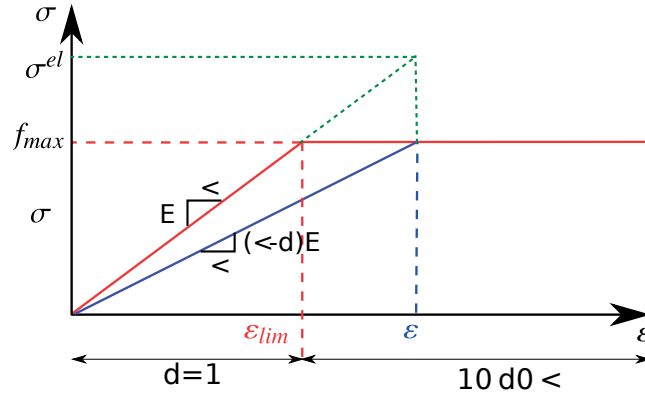


Figure 4.10 – Ductile behaviour.

Damage in tension or related to shear will be brittle ($F_{t,1}, F_{t,2}, F_{t,3}, F_{v,2}, F_{v,3}$), whereas modes in compression will be ductile ($F_{c,1}, F_{c,2}, F_{c,3}$). While $F_m \leq 1$ or $(F_m - \kappa_m) \leq 0$, the material is in the elastic range, and the damage parameter, $d_m(\kappa_m \leq 1) = 0$. Damage for mode m initiates when $F_m \geq 1$; thus, the history parameter, κ_m , and consequently the damage parameter, d_m , then grow. When $d_m(\kappa_m \rightarrow \infty)$ approaches 1, the material is fully damaged; it is calculated according to the failure modes. Fig.4.10 for ductile failure shows that the stress will stay constant after failure initiation, and d_m is expressed as

$$d_m = 1 - \frac{1}{\kappa_m} \quad (4.14)$$

However, for brittle failure, the stress diminishes with the strain increment (Fig.4.9). This decrease is defined by the failure energy (the area below the curve). In this case, the damage parameter, d_m , can be calculated as

$$d_m = 1 - \frac{f_{max}^2 - \frac{2g_f E}{\sqrt{\kappa_m}}}{f_{max}^2 - 2g_f E} \quad (4.15)$$

where $g_f = \frac{G_f}{l_e}$. G_f is the fracture energy, and l_e is the characteristic length of the element in the numerical model (CELENT parameter in ABAQUS). Replacing G_f with g_f in Eq.4.15 minimizes the mesh dependency [San12]. κ_m is the track parameter of the loading history, defined as $\kappa_m^t = \max(1, F_m, \kappa_m^{t-1})$. The mechanical properties are given in Table 4.3 [San12, ISFK08].

4.4.4 User Defined Field (USDFLD) in Abaqus

To modify the compliance matrix, we implement our CDM by an USDFLD subroutine, whereas Sandhass developed a user material subroutine (UMAT). The elastic properties of the material were declared in Abaqus as “field dependent”. Six fields are defined to represent the damage: $E_{ii} = (1 - f_i)E_{ii}^0$ for $1 \leq i \leq 3$, $G_{ij} = (1 - f_{i+j+1})G_{ij}^0$ for $1 \leq i < j \leq 3$, $\nu_{ij} = (1 - f_i)\nu_{ij}^0$ for

Property	Symbol	Value	Unit
Tensile strength // to grain f_{11}^t	$f_{t,0}$	78	Mpa
Compressive strength // to grain f_{11}^c	$f_{c,0}$	50	Mpa
Tensile strength \perp to grain f_{22}^t	$f_{t,90}$	2.2	Mpa
Compressive strength \perp to grain f_{22}^c	$f_{c,90}$	10	Mpa
Tensile strength \perp to grain f_{33}^t	$f_{t,90}$	2.2	Mpa
Compressive strength \perp to grain f_{33}^c	$f_{c,90}$	10	Mpa
Longitudinal shear strength f_{12}	f_v	6.9	Mpa
Longitudinal shear strength f_{13}	f_v	6.9	Mpa
Rolling shear strength f_{23}	f_{roll}	2.5	Mpa
Fracture energy tension // to grain	$G_{f,0}$	1.6	N/mm
Fracture energy tension \perp to grain	$G_{f,90}$	0.5	N/mm
Fracture energy longitudinal shear	$G_{f,v}$	1.2	N/mm
Fracture energy rolling shear	$G_{f,roll}$	0.6	N/mm

Table 4.3 – Mechanical properties of spruce

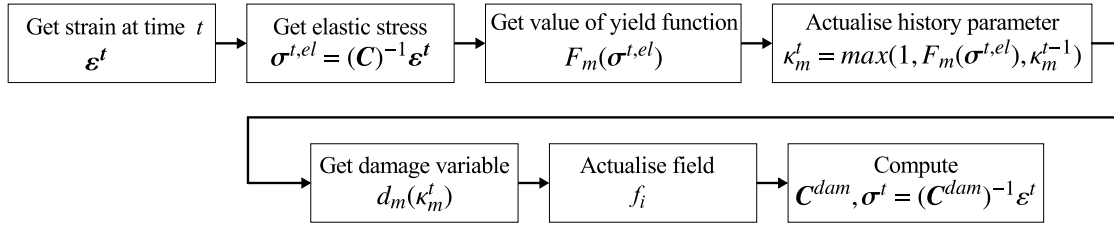


Figure 4.11 – Algorithm of the USDFLD subroutine.

$1 \leq i < j \leq 3$, where $f_1 = d_{11}$, $f_2 = d_{22}$, $f_3 = d_{33}$, $f_4 = d_{12}$, $f_5 = d_{13}$ and $f_6 = d_{23}$. The subroutine fixes the value of the field according to strain and stress verifications. Fig.4.11 presents the simplified algorithm of the subroutine.

4.5 Results and discussion

4.5.1 Experimental results

Replicate comparison

The sequence of rotations that defined the final geometry of each sample gave an asymmetry with respect to the bisector plane of the two connected panels. For each sample, four replicates were tested by pushing the F0 panel for the two first samples and on F1 for the last two. Figs. 4.12 (S01, closing) and 4.13 (S02, opening) present the ultimate moment and stiffness of each replicate. Despite the asymmetry of the joint, we did not observe any large difference between pushing on F0 or F1, both for S01 and S02. Therefore, the rest of the analysis considers the average of the four replicate values.

Non-linear moment-rotation curves

Figs. 4.14 (S01, closing) and 4.15 (S02, opening) show the average moment-rotation full curves. The sample names in the legend correspond to those in Tables 4.4 and 4.5.

After failure, a residual moment remains for all the samples. It never drops below 50% of

Chapter 4. Rotational Stiffness at Ridges of Timber Folded-plate Structures

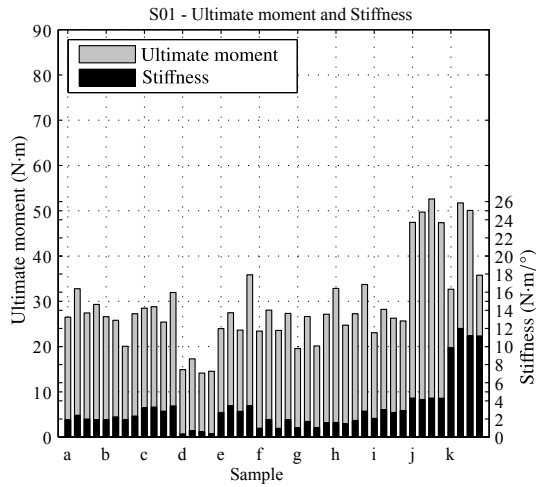


Figure 4.12 – S01–Moment max and Stiffness.

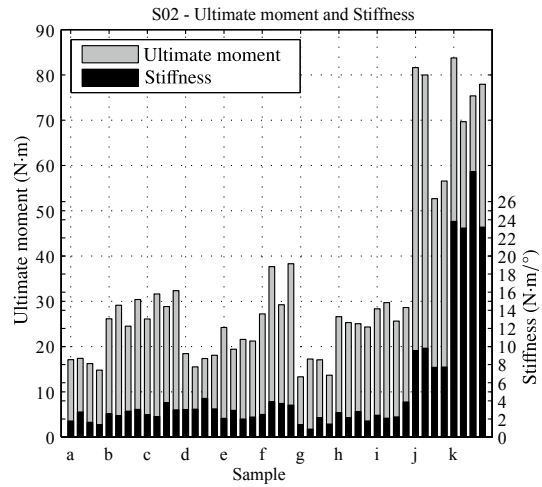


Figure 4.13 – S02–Moment max and stiffness.

Sample	θ_1 - θ_2 - θ_3	Moment max.		Stiffness	
		Mean N·m	Std.	Mean N·m/°	SD
a	00-00-10	29	2.8	2.0	0.2
b	00-30-10	25	3.3	2.2	0.3
c	00-00-30	29	2.7	3.1	0.2
d	45-00-10	15	1.4	0.5	0.1
e	45-31-10	28	5.7	3.1	0.4
f	45-00-38	26	2.4	1.4	0.6
g	90-00-10	23	4.1	1.3	0.3
h	90-30-10	30	4.3	2.0	0.5
i	90-00-30	26	2.1	2.7	0.4
MTSJ		25.5	4.4	2.04	0.9
j	screwed	49	2.5	4.3	0.1
k	glued	43	9.7	11.3	1.0

Table 4.4 – S01 - Mean and SD

Sample	θ_1 - θ_2 - θ_3	Moment max.		Stiffness	
		Mean N·m	Std.	Mean N·m/°	SD
a	00-00-10	16	1.2	1.7	0.6
b	00-30-10	28	2.7	2.8	0.4
c	00-00-30	30	2.9	2.8	0.8
d	45-00-10	17	1.3	3.2	0.7
e	45-31-10	22	2.0	2.4	0.4
f	45-00-38	33	5.7	3.0	0.6
g	90-00-10	15	2.1	1.6	0.7
h	90-30-10	25	0.9	2.4	0.5
i	90-00-30	28	1.7	2.6	0.7
MTSJ		23.8	6.41	2.5	0.6
j	screwed	68	15.2	8.9	1.1
k	glued	77	5.8	25.3	2.9

Table 4.5 – S02 - Mean and SD

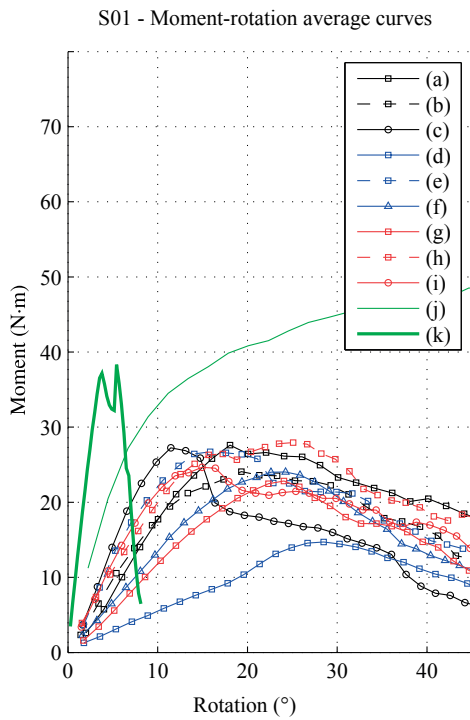


Figure 4.14 – S01 - Moment-rotation average non-linear curves for bending in closing.

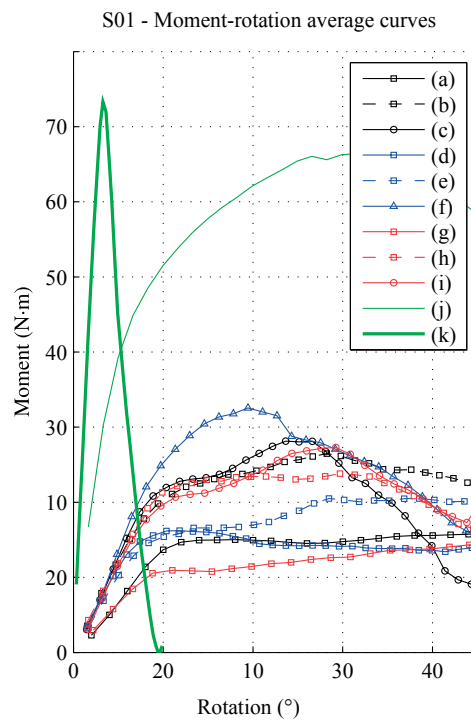


Figure 4.15 – S02 - Moment-rotation average non-linear curves for bending in opening.

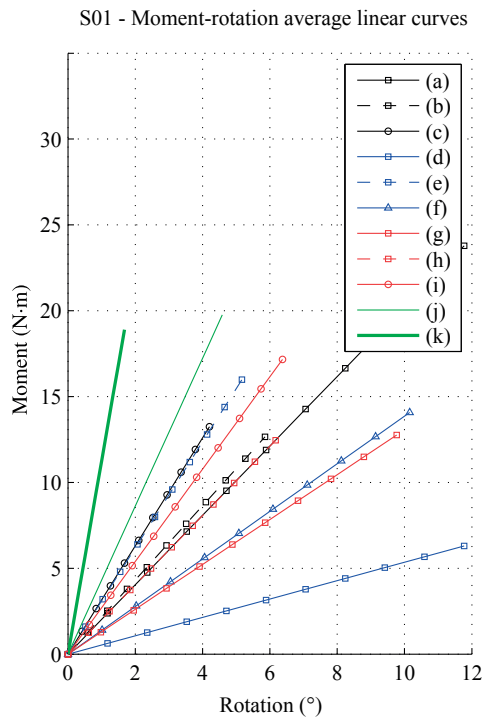


Figure 4.16 – S01 - Moment-rotation average linear curves (between 10% and 40% of M_{max}) for bending in closing.

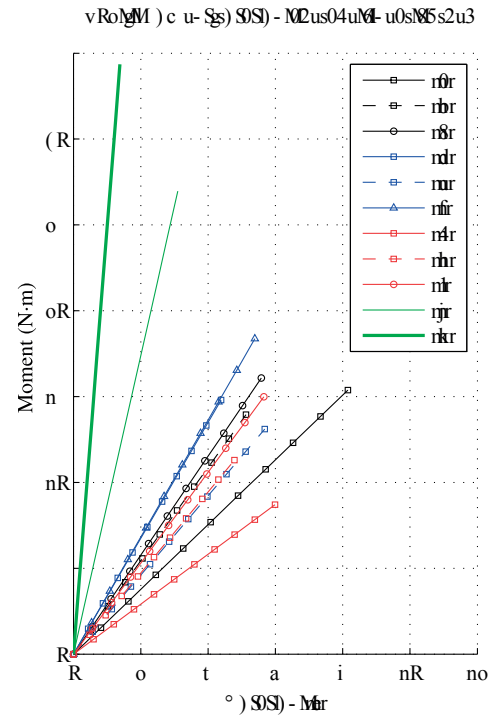


Figure 4.17 – S02 - Moment-rotation average linear curves (between 10% and 40% of M_{max}) for bending in opening.

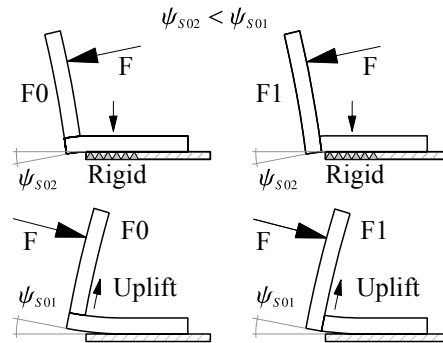


Figure 4.18 – High-stiffness effect on glued and screwed joints.

the ultimate moment except in the case of sample (c), which it does in both directions (S01 and S02). This sample later showed the best compromise of stiffness in closing and opening (0° , 0° , 30°). Samples with the most rigid connections generally showed quicker softening after damage. The hardening differed between closing (S01) and opening (S02), with only sample (h) hardening in S01 and all but (f) and (d) hardening in S02. The MTSJ is globally quite ductile, although its stiffness in bending is much weaker than that of the screwed and glued connections. The fastened and bonded samples showed different experimental results for closing and opening. These types of connection are much more rigid than the MTSJs; they were stronger than the panel strength and stiffness during deformation. Bending occurred in panels F0 and F1, and Fig.4.18 explains this effect on the stiff joint. In S02, the reference panel was pressed onto the support with increasing load, reducing local bending near the joint. In S01, the reference panel was lifted by the loading, and was free to bend. Under a given load, the sample deflected more in S01 than in S02. In both cases, the glue was subjected to tensile stress, which was in the direction unfavourable for adhesive bonding. As the glued and screwed samples were stiffer in S02, their moments in S02 were higher than in S01 for a given rotation. The highly brittle failure of the glued connection is clearly visible in Figs. 4.14 and 4.15. The less stiff screwed joint behaved similarly to the glued joint but with smaller differences between S01 and S02. Both connections were tested as elements of comparison. After testing, the samples connected with MTSJs showed no bending within the panels. The relative weakness of the connection resulted in no high-stiffness effect. The rest of the analysis will focus only on the MTSJs.

Linear moment-rotation curves

Figs. 4.16 and 4.17 were obtained by averaging the linear fits of the four replicates of each sample. The limits of the linear range were chosen between 10% and 40% of the ultimate moment. The curves are displayed in this range. The sample names in the legend correspond to those in Tables 4.4 and 4.5.

Global analysis

The total average stiffness in closing (2.04 N.m/°) was 18.5% lower than the stiffness in opening (2.5 N.m/°), whereas the ultimate moments were not significantly different ($25.5 \text{ N.m} \longleftrightarrow 23.8$

N.m, less than 8%). The range of S02 stiffnesses were also narrower than those of S01. This is confirmed by the standard deviations listed in Tables 4.4 and 4.5. In the tables, 'MTSJ' means the group of nine MTSJ samples (36 samples per loading case).

Comparative analysis of stiffness

To evaluate the effects of the Bryant angles and their partial combinations on the semi-rigidity of the MTSJ, mean values of stiffness are listed in Table 4.6. For each group of samples that has the same values for θ_1 , θ_2 or θ_3 or any combination thereof, the mean value of stiffness is compared with the mean of all samples (see Tables 4.4 and 4.5) for both S01 and S02. The deviations from the global means are listed in the columns headed 'dev.%', and they are considered meaningful when greater than 10%. The full combinations ($\theta_1 \theta_2 \theta_3$) are listed in Tables 4.4 and 4.5, but trends cannot be clearly extracted from them. We here analyse trends revealed in the experimental results. Each sample was tested in four replicates. For brevity, the combinations are written as ($\theta_1 \theta_2 _$), ($\theta_1 _ \theta_3$) and ($_ \theta_2 \theta_3$) in the text. Any value greater or equal to 30° is noted as 30° in the brackets.

$\theta_1 = 0^\circ$ gives the best stiffness in closing (S01), whereas $\theta_1 = 45^\circ$ reduces the stiffness in opening (S02). Connections with $\theta_1 = 90^\circ$ are possibly weaker, particularly in S02. The effect of θ_3 is obvious, as increasing the value to 30° or more, increases the rigidity in both loading directions. For θ_2 , which seems to improve the stiffness in S01, the analysis must be completed in combination with θ_1 . (00 00 $_$) and (45 00 $_$) provide opposite results, with stiffness increasing in S01 and decreasing in S02 for the former, and opposite behaviour for latter. In contrast, (00 30 $_$) was stiffer in S02 and (45 30 $_$) was stiffer in S01.

Combining θ_2 with $\theta_1 = 90^\circ$ did not greatly alter the results relative to the total mean. The combinations ($_ \theta_2 \theta_3$) confirmed the positive effect of θ_3 on the stiffness, except in the case of sample (f) ($\theta_3 = 38^\circ$), which showed a rather low stiffness in closing. The tabs were stretched in S01 for this configuration. Above a certain value ($>30^\circ$), the normal of the locking faces approaches the orientation where the tension perpendicular to the grain starts reducing the strength and stiffness. The sensitivity to large θ_3 angles could be explored in future works. ($_ 00 30$) and ($_ 30 10$) both have a similar effect on S01, and again highlights the beneficial effect of $\theta_3 = 30^\circ$. However, $\theta_2 \geq 30^\circ$ had no major effect during opening (S02).

Finally, the best compromise of the nine samples is $\theta_1 = 0^\circ$, $\theta_2 = 0^\circ$, $\theta_3 = 30^\circ$, which takes advantages of the positive effects described above. According to the trends shown in this study, a joint definition with $\theta_1 = 0^\circ$, $10^\circ \leq \theta_2 \leq 30^\circ$, $15^\circ \leq \theta_3 \leq 30^\circ$ could behave efficiently. As described in section 4.2.2, the available combination are limited by the tool inclination and the multi-edge assembly constraints. The range of possible tool inclinations could be increased by altering the shank length and the tool-holder geometry.

4.5.2 Numerical model versus experiments

A numerical model was built to reproduce the experimental set-up as faithfully as possible. For analysing the rotational stiffness, the elastic range would have been sufficient. As the ultimate moment of the connection is monitored experimentally, comparison with a numerical value

Chapter 4. Rotational Stiffness at Ridges of Timber Folded-plate Structures

Row	Samples	θ_1	θ_2	θ_3	Mean S01 N·m/°	Dev. %	Mean S02 N·m/°	Dev. %
1	a,b,c	0			2.44	20	2.44	-2
2	d,e,f	45			1.67	-18	2.86	14
3	g,h,i	90			2.01	-2	2.21	-12
4	a,c,d,f,g,i		0		1.85	-9	2.50	0
5	b,e,h		≥ 30		2.42	19	2.52	1
6	a,b,d,e,g,h			10	1.86	-9	2.35	-6
7	c,f,i			≥ 30	2.41	18	2.82	13
8	a,c	0	0		2.59	27	2.26	-10
9	b	0	≥ 30		2.16	6	2.82	13
10	a,b	0		10	2.09	2	2.25	-10
11	c	0		≥ 30	3.15	54	2.83	13
12	d,f	45	0		0.97	-53	3.11	24
13	e	45	≥ 30		3.09	51	2.36	-6
14	d,e	45		10	1.82	-11	2.78	11
15	f	45		≥ 30	1.39	-32	3.02	21
16	g,i	90	0		2.00	-2	2.12	-15
17	h	90	≥ 30		2.02	-1	2.39	-5
18	g,h	90		10	2.00	-2	2.12	-15
19	i	90		≥ 30	2.69	32	2.62	5
20	a,d,g		0	10	1.29	-37	2.17	-13
21	c,f,i		0	≥ 30	2.41	18	2.82	13
22	b,e,h		≥ 30	10	2.42	19	2.52	1

Table 4.6 – Comparative analysis of the combination of Bryant angles

would be useful, and a damage model was implemented to achieve this.

Some preliminary results are presented as follows.

Both in S01 and S02, numerical strain and damaged element were well observed experimentally. Consider, for example, sample (a) in Fig.4.19: the numerical model matched the experimental curves well under closing. However, at this stage, our model aborted before reaching the ultimate strength when the samples were tested in opening(Fig.4.20). The jobs stopped before reaching the yield point, and so the ultimate moment could not be observed. The continuum damage model worked well, but convergence problems were encountered during the contact step. So that only the stiffness values of the model in S01 were listed in Table 4.7 and compared to experimental values. They were generally significantly lower than the averages of the experimental results. It was probably due to the deviation from actual values of both material properties and friction coefficient (set to 0.3 in our case). The development of the numerical model remains ongoing, and pending issues have to be solved by:

- re-defining the contact step and the Coulomb friction coefficient.
- refining the elastic and mechanical properties by material testing on Kerto-Q panel and spruce veneer.
- identifying dislocated elements with large rotation and mesh modification,
- controlling the time increment,
- conducting mesh optimization, and

- passing from Abaqus/Standard to Abaqus/Explicit.

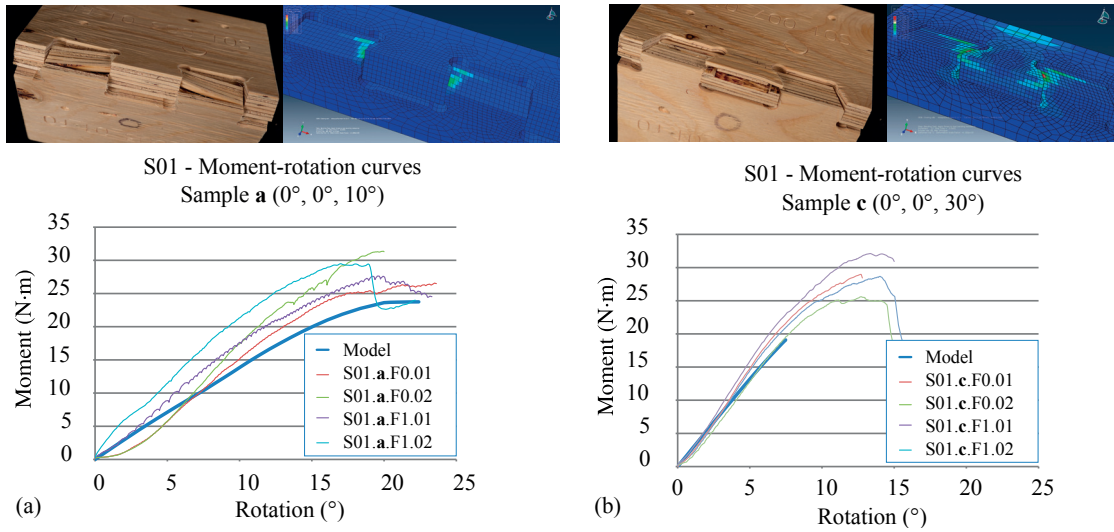


Figure 4.19 – S01 - Numerical curves versus experimental results, (a) Sample **a** ($0^\circ, 0^\circ, \pm 10^\circ$), (b) Sample **c** ($0^\circ, 0^\circ, \pm 30^\circ$)

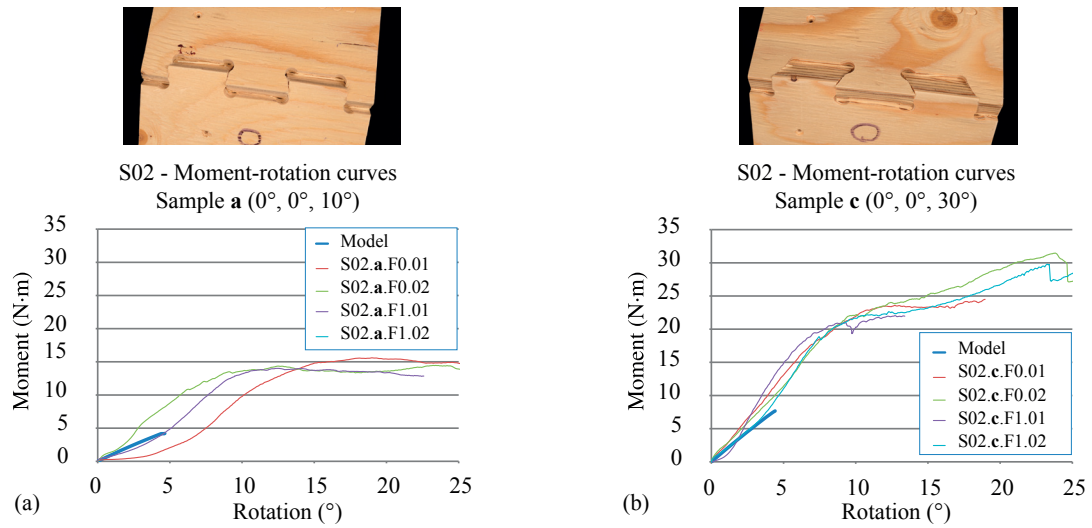


Figure 4.20 – S02 - Numerical curves versus experimental results, (a) Sample **a** ($0^\circ, 0^\circ, \pm 10^\circ$), (b) Sample **c** ($0^\circ, 0^\circ, \pm 30^\circ$)

Sample	θ_1 - θ_2 - θ_3	Model stiffness	Exp. Stiffness	
		mean N·m/°	mean N·m/°	std
a	00-00-10	1.4	2.0	0.2
b	00-30-10	1.7	2.2	0.3
c	00-00-30	2.6	3.1	0.2
d	45-00-10	0.6	0.5	0.1
e	45-31-10	1.4	3.1	0.4
f	45-00-38	1.1	1.4	0.6
g	90-00-10	0.7	1.3	0.3
h	90-30-10	1.0	2.0	0.5
i	90-00-30	1.8	2.7	0.4

Table 4.7 – S01 - Model stiffness vs Experimental stiffness

4.6 Conclusions

Producing strong edge-to-edge connections in thin panels is challenging. Usual metal fasteners such as screws may not comply with the required edge distance. The MTSJ presented in this paper is an innovative solution. It allows the in-space multi-edge interlocking connection of panels. The joint is milled during cutting. Its shear performance has already been assessed mechanically [RMW15], and the semi-rigidity of the MTSJ has demonstrated properties competitive with wood screws. The bending stiffness at the ridges of the folded-plate structures is considered here. The first tests on the rotational stiffness of MTSJ with nejiri arigata design revealed ductile behaviour with relatively low stiffness compared with screwed and glued joints. The joints were tested in their minimal configuration with one and two tabs per panel. The effect of the tab angle θ_3 is significant, and its combination with the other angles is promising for further analyses. The sample with $\theta_1 = 0^\circ$, $\theta_2 = 0^\circ$, $\theta_3 = 30^\circ$ behaved well, but joints defined as $\theta_1 = 0^\circ$, $10^\circ \leq \theta_2 \leq 30^\circ$, $15^\circ \leq \theta_3 \leq 30^\circ$ could be even more efficient. A numerical model based on continuum damage mechanisms showed promising results, although it showed limitations that must be addressed. These preliminary results will facilitate the development of stiffer joints, and further work is already under way. Fig.4.21 presents the evolution of the MTSJ with closed slots, the sample (a) ($\theta_1 = 0^\circ$, $\theta_2 = 0^\circ$, $\theta_3 = 30^\circ$) is shown joined for comparison. Bending experiments have already demonstrated its stiffness to be equivalent to that of a screwed joint. The connections have been already used in a double-layer curved shell.



Figure 4.21 – MTSJ: open slot (left), closed slot (right).

Outcomes ②*

The outcomes of the present chapter are synthesized as follows.

From bending tests, by folding in closing and opening of two panels connected at 90°, the rotational performance of 1DOF MTSJ with open slots revealed the following behavior :

The experimental results shown a ductile behavior, ranging from hinged to semi-rigid and more or less symmetric in closing and opening with respect to the combination of the Bryant's angles.

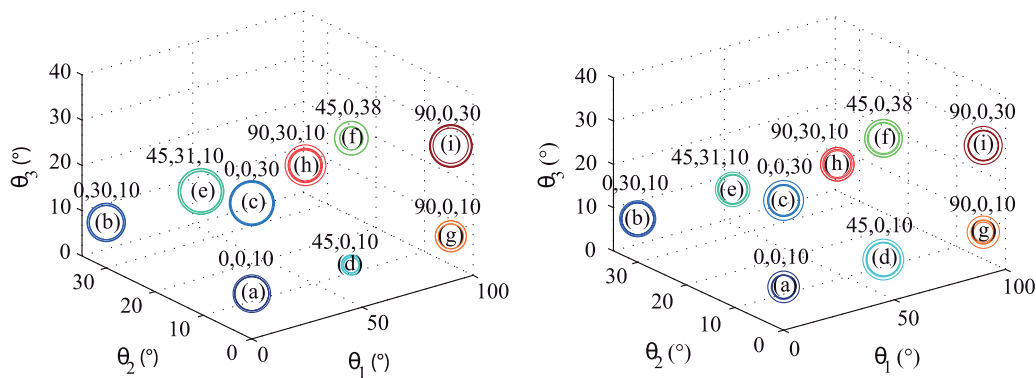


Figure 4.22 – MTSJ-JJ - Average stiffness : closing (left), opening (right) with bigger the circle, higher the stiffness.

The comparison of the nine combinations of the Bryant's angles, presented in Fig.4.22 led to three main tendencies :

- The MTSJ-JJ with $\theta_3 = \pm 30^\circ$ tend to the best stiffness (see Fig.4.23),

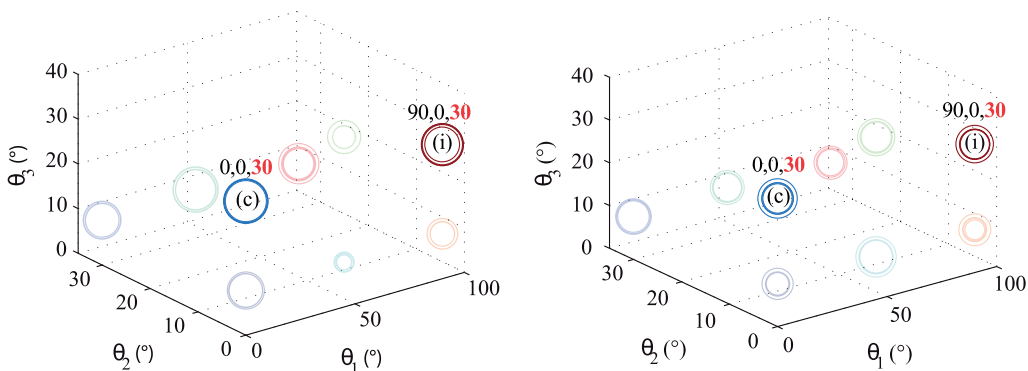


Figure 4.23 – MTSJ-JJ - Best stiffness : closing (left), opening (right).

*This additional section was not included in the original publication.

Chapter 4. Rotational Stiffness at Ridges of Timber Folded-plate Structures

- The MTSJ-JJ with $\theta_2 = \pm 0^\circ$, $\theta_3 = \pm 10^\circ$ tend to the worst stiffness (see Fig.4.24),

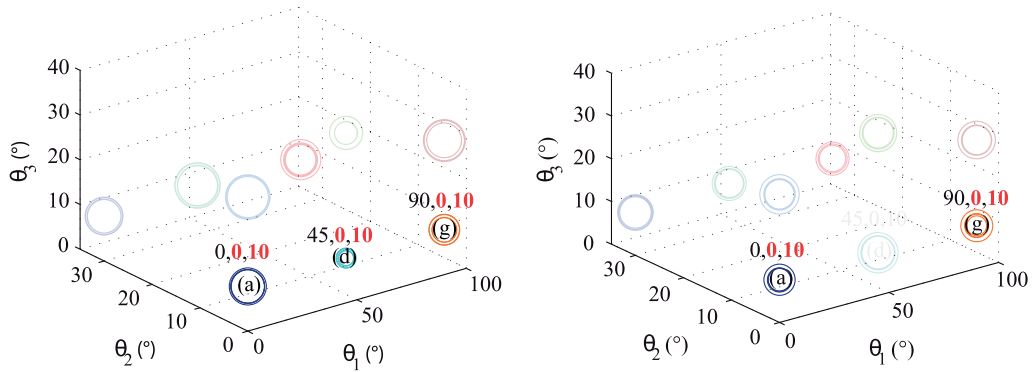


Figure 4.24 – MTSJ-JJ - Best stiffness : closing (left), opening (right).

- The MTSJ-JJ with $\theta_1 = 45^\circ$, $\theta_2 = 0^\circ$, $\theta_3 = \pm 10^\circ$ reveal dissymmetry in closing versus opening (see Fig.4.25).

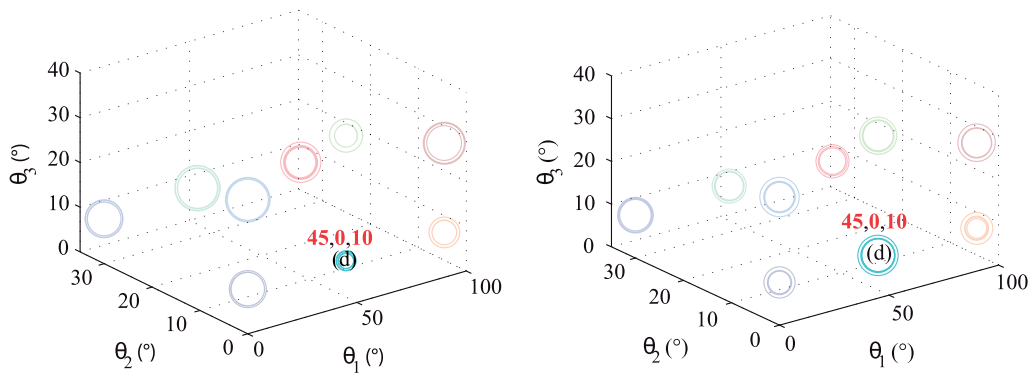


Figure 4.25 – MTSJ-JJ - Dissymmetry in stiffness : closing (left), opening (right).

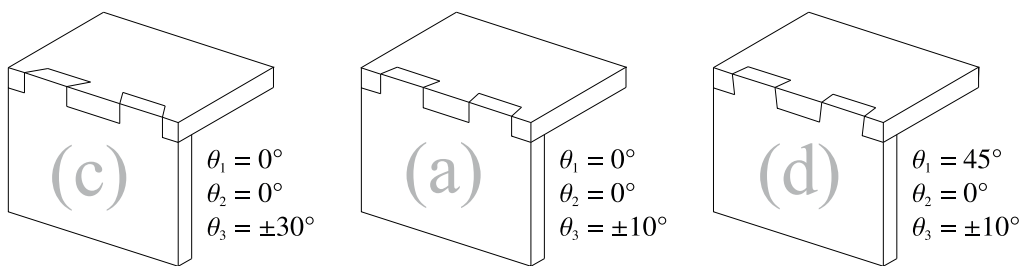


Figure 4.26 – MTSJ-JJ : sample (c), sample (a), sample (d).

But in any case, the different geometries of MTSJ-JJ were significantly less stiffer than glue and screws.

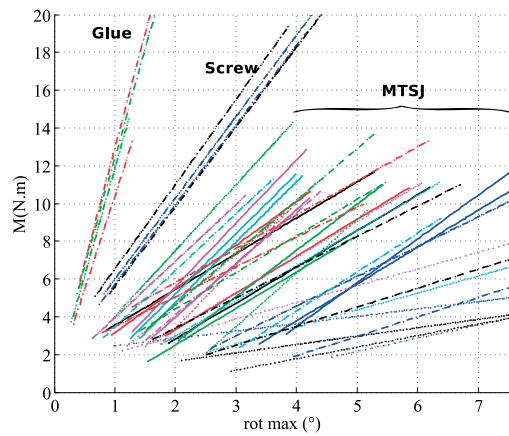


Figure 4.27 – Closing - Moment-rotation linear range from 10% to 40% M_{max} .

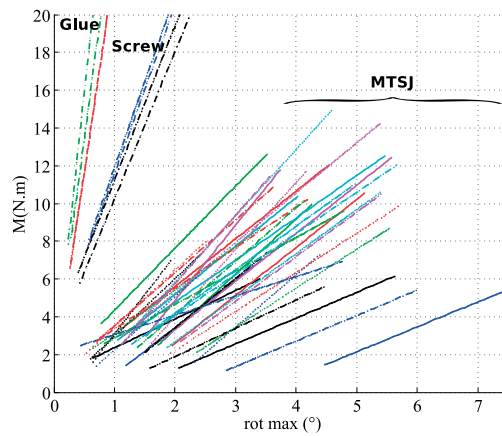


Figure 4.28 – Opening - Moment-rotation linear range from 10% to 40% M_{max} .

How the rotational stiffness can be improved to compete with screws ?

→ **Objective ③** (see chapter 5)

References

- [Bur10] H. U. Buri. *Origami - Folded Plate Structures*. PhD thesis, Ecole Polytechnique Fédérale de Lausanne, 2010.
- [BW08] H. U. Buri and Y. Weinand. Origami - folded plate structures, architecture. In *World Conference on Timber Engineering, Miyazaki, Japan*. Proceedings WCTE 2008, 2008.
- [fSC04] European Committee for Standardization (CEN). *CEN-EN1995-1-1:2004+A1 - Eurocode 5: Design of timber structures - Part 1-1: General - Common rules and rules for buildings*. (CEN), Brussels, 2004.
- [HJ99] P. Haller and COST C1. Working Group "Timber Joints". *Semi-rigid Timber Joints - Structural Behaviour, Modelling and New Technologies: Final Report of Working Group "Timber Joints"*. Technische Universität Dresden, 1999.
- [ISFK08] I. V. Ivanov, T. Sadowski, M. Filipiak, and M. Kneć. Experimental and numerical investigation of plywood progressive failure in ct tests. *Budownictwo i Architektura*, 2:79–94, 2008.
- [Jas00] J. P. Jaspart. General report : Session on connections. *Journal of Constructional Steel Research*, 55:68–89, 2000.
- [JFW12] S. Jaksch, A. Fadai, and W. Winter. Folded clt structures - developments in design and assembly strategies. In *World Conference on Timber Engineering, Auckland, New Zealand*, volume 1, pages 18–22. Proceedings WCTE 2012, 2012.
- [Mat14] G. Mattoni. Folded plate structure – design and analysis of woodworking joints for structural timber panels. Master's thesis, Ecole Nationale des Ponts et Chaussées and Ecole Polytechnique Fédérale de Lausanne, 2014.
- [MLP07] M. McDowall, M. Leigh, and M. Punton. Exotic structural forms - folded plates. In *Structural Plywood & LVL Design Manual*, volume Chap. 12, pages 154–158. Engineered Wood Products Association of Australasia, 2007. <http://www.ewp.asn.au>.
- [RMW15] S. Roche, G. Mattoni, and Y. Weinand. Rotational stiffness at ridges of timber folded-plate structures. *International Journal of Space Structures*, 30(2):153–168, 2015.
- [Rob15] C. Robeller. *Integral Mechanical Attachment for Timber Folded Plate Structures*. PhD thesis, Ecole Polytechnique Fédérale de Lausanne, 2015.
- [RSMW14] C. Robeller, A. Stitic, P. Mayencourt, and Y. Weinand. Interlocking folded plate - integrated mechanical attachment for structural wood panels. In *Advances in Architectural Geometry 2014*. Springer - submitted may 2014, 2014. <http://www.architecturalgeometry.org/aag14/>.

- [San01] C. Sandhaas. 3d material model for wood, based on continuum damage mechanics. Technical report, University of Technology Delft, 2001. Stevinrapport 6-11-4, Stevin II Laboratory.
- [San12] C. Sandhaas. *Mechanical Behaviour of Timber Joints With Slotted-In Steel Plates*. PhD thesis, University of Technology Delft, 2012.
- [SS10] V. Sebera and M. Simek. Finite element analysis of dovetail joint made with the use of cnc technology. *Acta Universitatis Agriculturae Et Silviculturae Mendelianae Brunensis*, LVIII, 3:321–328, 2010.
- [War01] T. Wardle. Old growth : Our timber engineering heritage. design notes for plywood folded-plate roofs. *New Zealand Timber Design Journal, Issue 1*, 19:548–551, 2001.

5 Improvement of the Rotational Stiffness for the Connection of Thin Structural Wood Panels

Stéphane Roche, Julien Gamarro and Yves Weinand

Published in the Proceedings of the World Conference on Timber Engineering, Vienna, Austria, August 22-25, 2016.

Abstract

Researchers in Asia have focused on analyzing the rotational performance of traditional connections based on embedment. The Nuki through-joint has inspired work at the laboratory of wood construction (IBOIS), Ecole Polytechnique Fédérale de Lausanne, to improve the rotational behavior of the multiple tab and slot joint (MTSJ). In this work, through tenon (TT) and closed slot joints were added to initial dovetail and Nejiri arigata joints used for folded-plate structures. The bending performance of the improved MTSJ-TT joint was higher than that of screwed angular connections. Numerical monitoring of the embedded volumes under partial compression on the contact surfaces was used to characterize the directly and indirectly loaded areas. The decay coefficients for the exponential form, which defined the additional length in the indirectly loaded area, were quantified for both single (SC) and double contact (DC). The evolution of these coefficients was also monitored along the angular deformation. Finally, an analytical formulation of the embedded volumes was provided to prepare an analytical model for the MTSJ-TT joint subjected to bending.

Keywords Timber, Panel, Through-connection, Rotational Embedment, Multiple Tab-and-Slot Joint.

Objective ③ *

Improve the rotational stiffness.

*This additional section was not included in the original publication.

5.1 Introduction

In 2014, Robeller described structural connections for thin engineered edge-joined wood panels [RNW14]. The multi-edge in-situ connection of laminated veneer lumber (LVL) panels was demonstrated on a folded-plate prototype (Fig.5.1a), and a Yoshimura tessellation of trapezoidal plates was assembled with multiple tab-and-slot joints (MTSJs). Despite significant rigidity in rotation, the connections were weaker under bending than screws and adhesives [RMW15].

At the same conference, Krieg et al. presented a pavilion that had a free-form geometry discretized with planar hexagonal meshes, which resulted in trivalent connections [KSM⁺14]. Except in the transition region between positive and negative Gaussian curvatures, where the plates approached a rectangle, the trivalent geometry resulted in bending stiffness despite each pair of connected edges being hinged. The mixed connection had finger joints bearing the in-plane shear forces and crossing screw joints bearing the axial and out-of-plane shear forces. In the transition zone, the screws provided the required bending stiffness.

Segmental plate shells with a trivalent geometry partially solved the bending stiffness, while a folded-plate structure improved the static height using thinner panels. For folded-plate structures (FPS), the rotational stiffness of the edge connection greatly affects the overall structural behavior.

Fig.5.1b shows a double layered FPS based on the Miura-ori pattern [RW16]. The connection of a maximum of two edges at a time made possible the in-plane insertion and the use of through tenon joints (TTs).

The embedment effect in a MTSJ with TT causes it to behave similarly to traditional Japanese through-joints in rotational partial compression. Researchers in Asia have studied the elasto-plastic rotational behavior of such joints [CHK06, TS12, TSS12, OSY15], confirming their great rotational stiffness and ductility, which contributes to the stability of ancient structures, even during earthquakes. They based their models on embedment theory developed in Japan. Local compression loading produces directly and indirectly loaded areas. Inayama established an elastic formulation of this phenomenon for wood loaded perpendicular to the grain [Ina93]. Tanahashi et al. derived the elasto-plastic embedment behavior of orthotropic wood analytically from the Pasternak soil model [TSH⁺08, TOS08]. Tanahashi and Suzuki also worked on the rotational compression of the Nuki joint using this model [TS12, TSS12]. Other works (e.g., Kitamori [KMKK09][MDS⁺02]) compared the additional length profile of the embedment areas for different contact cases (single/double, axial/rotational). Most of these works show that the indirectly loaded area is characterized by an exponential curve with a decay coefficient, γ (Eq.5.1).

$$f(x) = a \times \exp(-\gamma x) \quad (5.1)$$

Here, x is the abscissa on the non deformed surface and a is the maximum surface displacement. The coefficient γ defines the amplitude of the indirectly loaded area, and it varies according to the type of embedment and the material geometry and properties.

Inspired by the performance of Nuki joints in rotation, the present article examines the

5.2. MTSJ design for improved rotational stiffness

embedment behavior of TTs and closed slots that drastically improves the moment-resisting performance of a MTSJ. The deformed volume is defined in the elastic and plastic range, and the decay coefficient is experimentally obtained for single contact (SC) and double contact (DC) with the grain parallel to the joint axis.

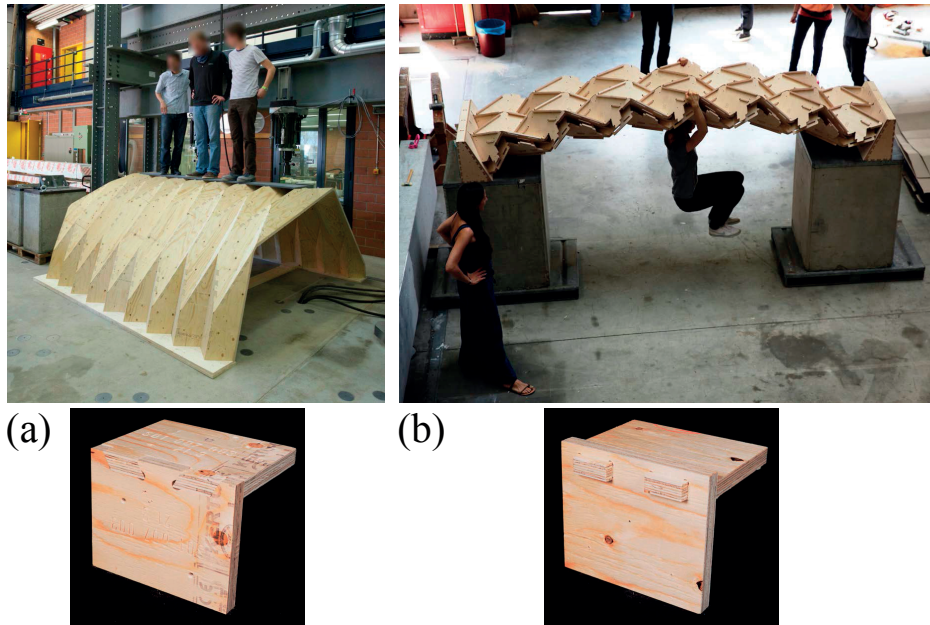


Figure 5.1 – (a) Yoshimura pattern and MTSJ ($0^\circ, 0^\circ, \pm 30^\circ$), (b) Double-layer Miura-ori pattern and TTs.

5.2 MTSJ design for improved rotational stiffness

The Nuki joint, a tie beam penetrating a mortise cut in a column, performs well as a moment-resisting connection. To improve the rotational stiffness of a MTSJ, a TT and closed slots were added to achieve a similar embedment effect to a Nuki joint under rotation. Eight geometries, including a MTSJ-TT, were tested to validate the improvement (Fig.5.2). The first group (samples (a) to (d)) has open slots. Sample (a) had the geometry of the sample that has been reported to provide the best compromise between stiffness in closing and opening [RMW15]. The principle of the Nejiri arigata joint (MTSJ-JJ) is used with an insertion oriented by $\theta_1 = 0^\circ, \theta_2 = 0^\circ$ and a tab angle θ_3 equal to $\pm 30^\circ$ for the first and second half of the edge, respectively [RNW14] [RMW15]. Sample (b) is the MTSJ dovetail variante (DJ) of the same joint, and $\pm \theta_3$ is applied to each locking face. To limit kinematic slip during rotation, sample (c) was the same as sample (b) except it included one screw per tab, whereas sample (d) is a screwed MTSJ finger joint (FJ) alternative with $\theta_1, \theta_2, \theta_3 = 0^\circ$. The next three samples (e, f, g) were designed with TTs and closed slots. Samples (e) and (f) had elastic tabs whose snap-fit (SF) function removed the last degree of freedom after insertion [RSMW14]. Sample (g) is a MTSJ with TTs (MTSJ-TT); the effect of embedment in this joint is investigated in more detail in the following sections (Fig.5.3). For comparison, sample (h) was only connected with a screw on a butt joint.

Chapter 5. Improvement of the Rotational Stiffness for the Connection of Thin Structural Wood Panels

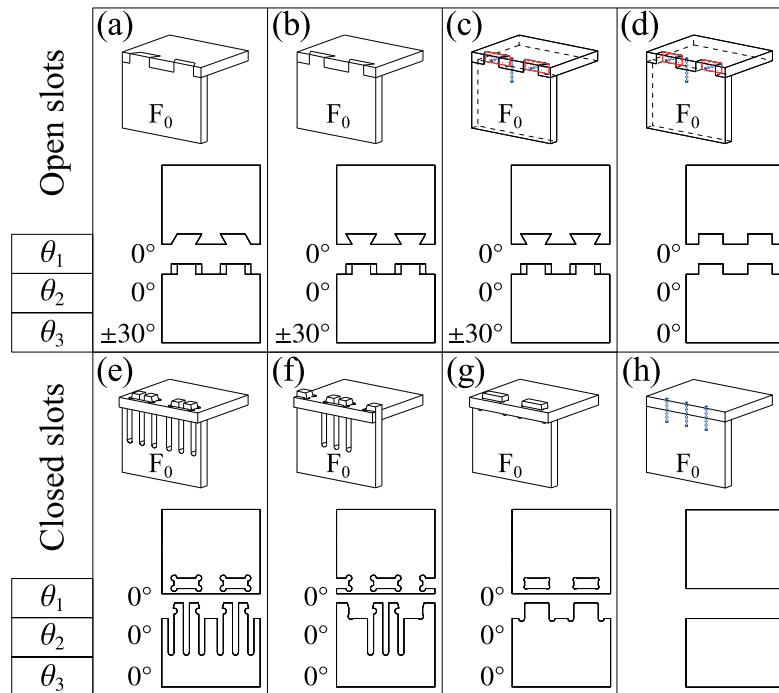


Figure 5.2 – MTSJ sample design.

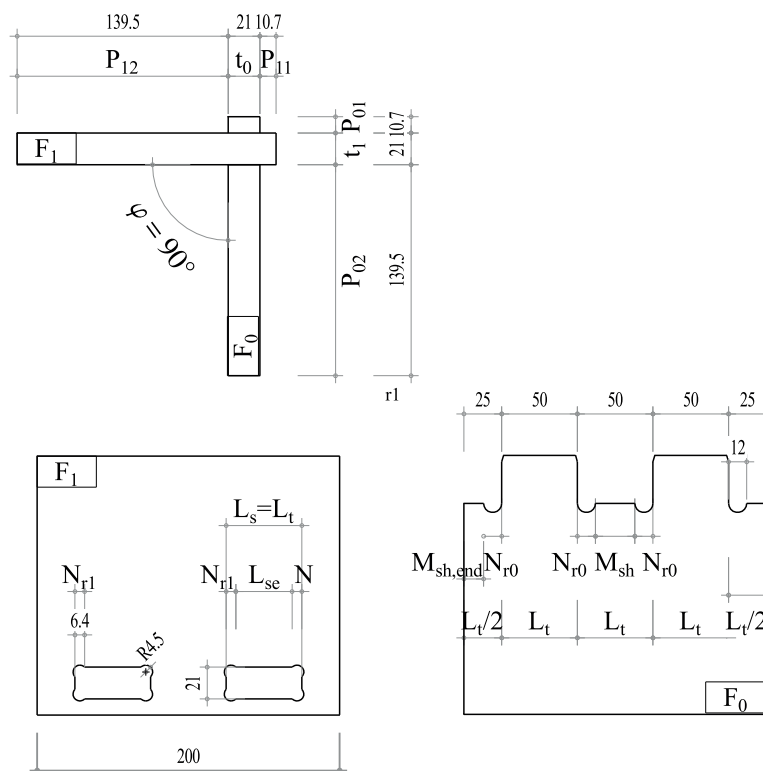


Figure 5.3 – Geometry of MTSJ with TTs.

5.3 Bending experiments

Folding tests compared sample (g) in bending with the other configurations of MTSJ. Its performance is also rated with respect to screwed assemblies (Fig.5.2c,d,h).

5.3.1 Method

The test setup was the same as that introduced by Roche et al. [RMW15]. A dedicated folding machine applied a moment by pushing perpendicularly to the loaded panel (F_0) during the rotation (Fig.5.4). The orientation of the sample in the machine determined whether the angle between the two panels was reduced (closing, Fig.5.4a) or increased (opening, Fig.5.4b) during the deformation. The deformation was measured by averaging measurements from two inclinometers, and the load by summing two load cell responses.

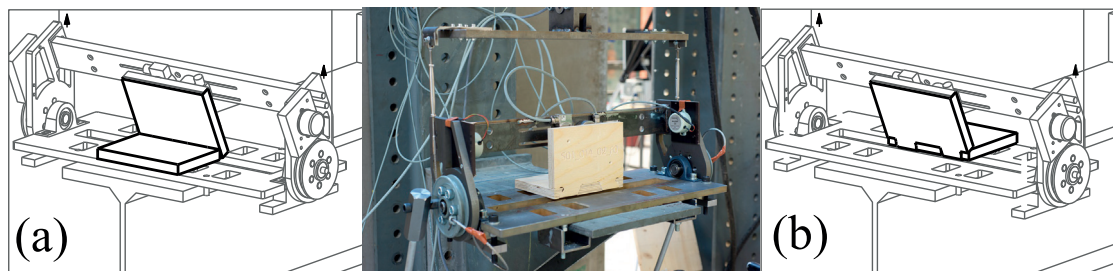


Figure 5.4 – Folding machine: (a) closing and (b) opening.

Five replicates of each geometry were tested in opening and closing (Fig.5.4a,5.4b), giving a total of 80 results.

5.3.2 Results

The experimental results are represented as non-linear average moment–rotation curves (Fig.5.5 and 5.6). The linear part fits between 10% and 40% of the ultimate moment in each case. Tables 5.1 and 5.2 present the values of average stiffness and ultimate moment for each sample (from five replicates) in the two directions of loading. The MTSJ with closed slots and TTs (sample (g)) was more than twice as stiff and twice as strong as the screwed connection (sample (h)) in closing. Combining DJ or FJ with crossing screws improved the stiffness of the connections asymmetrically. Screwed connections generally show a significant difference of stiffness between closing and opening owing to the rig effect described in Ref. [RMW15] combined with the screw pressing effect. In Fig.5.2, the red contact surfaces of samples (c) and (d) are pre-stressed by the screwing. These surfaces are then fully carried with limited slip during the opening of the joint. In closing, the screw heads are pulled out, and only the threads resist comparatively weakly against the induced tension.

Fig.5.7 shows the symmetric behavior of the MTSJ-TT for both loading directions. The elastic part of the curves ends after a very limited rotation of less than 5° . The next section focuses on the embedment volume geometry of this particular type of MTSJ.

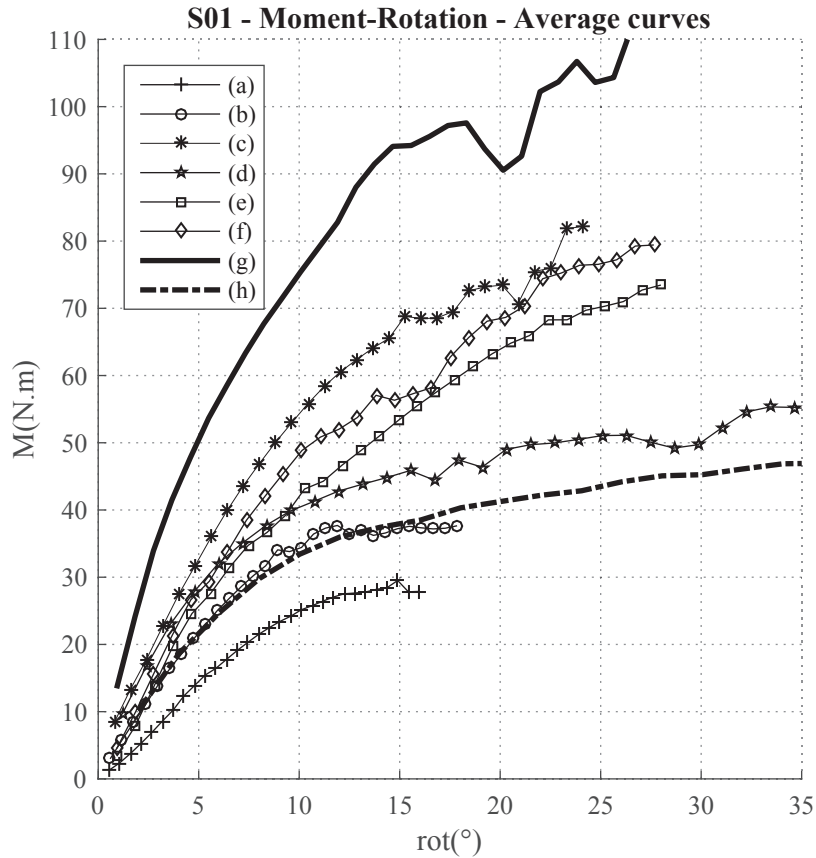


Figure 5.5 – S01 (closing): moment–rotation curves up to the maximum point.

Sample	Type	θ_1 - θ_2 - θ_3	Moment max.		Stiffness	
			Mean N·m	Std. -	Mean N·m/°	Std. -
a	(JJ)	00-00-30	28	2.5	3.1	0.2
b	(DJ)	00-00-30	37	4.2	4.5	0.1
c	(DJ+S)	00-00-30	72	7.2	6.3	0.2
d	(FJ+S)	00-00-00	53	5.0	5.8	0.9
e	(2SF)	00-00-00	70	4.4	5.1	0.2
f	(1SF)	00-00-00	76	5.7	5.9	0.7
g	(TT)	00-00-00	106	10.6	9.9	0.8
h	(S)	3xscrew4.5	49	1.6	4.3	0.07

Table 5.1 – Average stiffness and ultimate moment for S01.

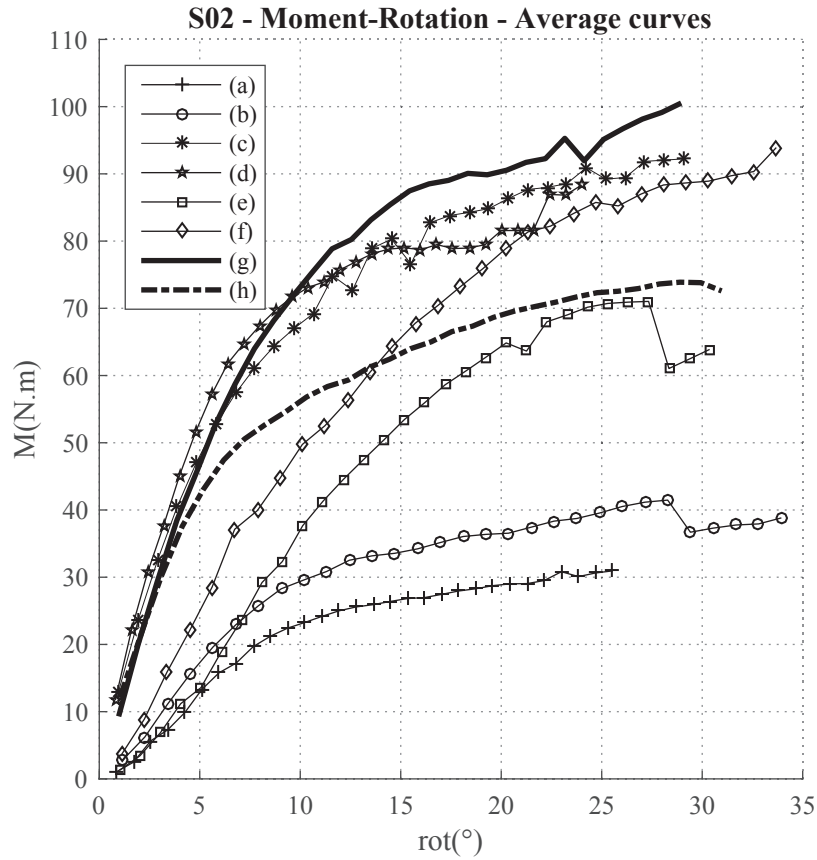


Figure 5.6 – S02 (opening): moment–rotation curves up to the maximum point.

Sample	Type	θ_1 - θ_2 - θ_3	Moment max.		Stiffness	
			Mean N·m	Std. -	Mean N·m/°	Std. -
a	(JJ)	00-00-30	31	2.7	3.2	0.6
b	(DJ)	00-00-30	42	3.4	4.0	0.6
c	(DJ+S)	00-00-30	84	13.3	10.5	1.1
d	(FJ+S)	00-00-00	82	6.2	10.8	1.0
e	(2SF)	00-00-00	71	5.8	4.9	0.4
f	(1SF)	00-00-00	86	7.5	5.5	0.7
g	(TT)	00-00-00	95	5.6	9.4	0.9
h	(S)	3xscrew4.5	74	1.0	9.0	0.12

Table 5.2 – Average stiffness and ultimate moment for S02.

Chapter 5. Improvement of the Rotational Stiffness for the Connection of Thin Structural Wood Panels

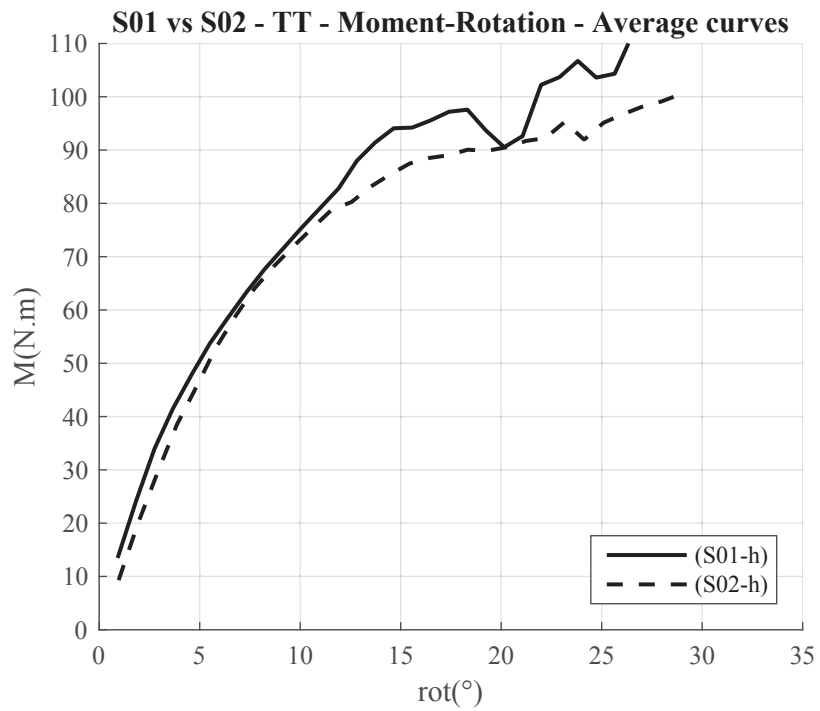


Figure 5.7 – Symmetrical behavior of TT.

5.4 Embedment Effect on MTSJ with TT

5.4.1 Contact surfaces

After testing, sample (g) was cut and scanned to identify the contact surface and the geometry of the deformed volumes (Fig.5.8). As the behavior is symmetric, Fig.5.9 presents only the embedment effect in closing. Where the tenons go through the slots, an embedment zone is present at each side of the tab faces (DC, Fig.5.9a). It results in a self-locking effect. In addition, the shoulders of the F_0 panel compressed the surface of the F_1 panel, leading to a single deformation on the bottom face F_{1-} (SC, Fig.5.9b). The internal local forces at each deformed zone counterbalance the external bending moment. The total resisting moment of the joint is obtained by multiplying each local force by its respective lever arm measured from the rotation center of the joint. This study is limited to the geometry of the deformed volumes, from which the local forces can be determined by using Eq.(5.2).

$$P_\theta = \frac{V_\theta}{t} \cdot E_\theta \quad \text{with} \quad E_\theta = \frac{E_{90,edge,mean} \cdot E_{90,flat,mean}}{E_{90,edge,mean} \sin^{1.8} \theta + E_{90,flat,mean} \cos^{1.8} \theta} \quad (5.2)$$

Here, P_θ , V_θ , t , and E_θ are the local force, the embedded volume, the reference thickness (here $t = t_0 = t_1$), and the elastic modulus of LVL Kerto-Q at θ angle, respectively. Inspection of the surfaces also confirmed the exponential form of the indirectly loaded surfaces, as analyzed by Japanese researchers [Ina93][KMKK09][MDS⁺02]. Additional experiments formalized the mechanical behavior of the embedment and the decay coefficients.

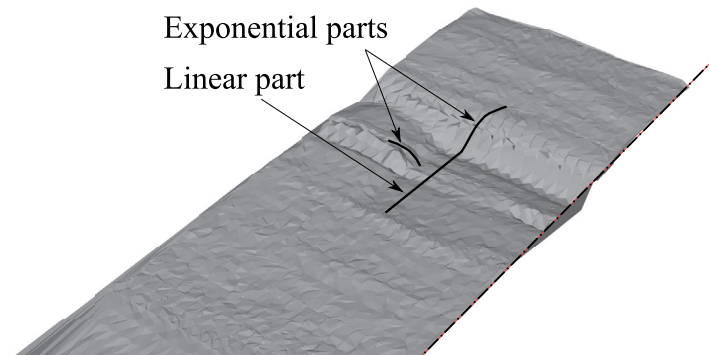


Figure 5.8 – Scan of F_{0+} embedment area with a FaroArm.

5.4.2 Embedment by rotational partial compression

Description of the tests

The test comprised two parts: the first characterized the mechanical behavior of the MTSJ in partial compression with rotation, and the second analyzed the additional length profile. As described in the previous section, a MTSJ shows two types of rotational compression, SC and DC. Both phenomena were studied here. For each test, six series of samples with different geometries and with wood and steel matrices for the standing panel (SP) were tested (Fig.5.10). The geometric properties and characteristics of each sample are listed in Table 5.3.

Samples were tested using a setup designed for partial compression with rotation (Fig.5.11). A

Chapter 5. Improvement of the Rotational Stiffness for the Connection of Thin Structural Wood Panels

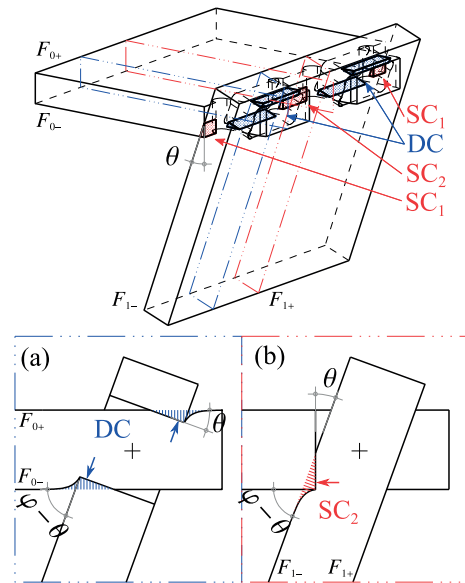


Figure 5.9 – Embedment effect in MTSJ-TT: (a) DC and (b) SC.

Parameters	Symb.	Unit	a	b	c	d	e	f
Joint length	JL	mm	50	50	50	50	30	30
Panel thickness	t	mm	21	21	21	21	21	21
Standing panel	SP	-	S	K	K	S	K	S
Lying panel	LP	-	K	K	K	K	K	K
Edge distance	ED	mm	0	0	63	63	50	50
Tab protrusion	P	mm	-	-	-	-	10.5	10.5
Replicate	-	-	8	8	4	1	5	5

K = LVL Kerto-Q, S = Steel

Table 5.3 – Sample parameters for partial compression.

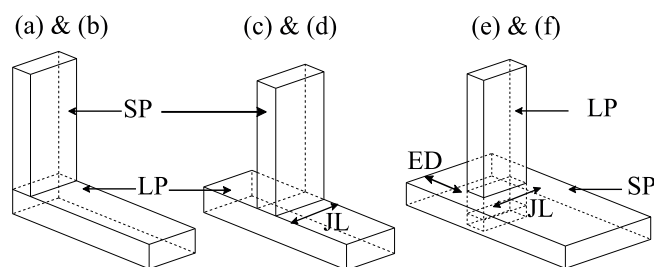


Figure 5.10 – Sample geometries.

20 kN cylinder pressing on a steel lever arm was used to transmit rotation θ on the SP, which bore the surface of the lying panel (LP). The lever arm kept the load perpendicular to the standing panel in any position. The LP was rigidly fixed by a steel clamp. The location of the rotation center could be set depending on the geometry of the test sample. Rotation and load were recorded by two inclinometers and the cell load. A total of 31 specimens were tested. All

these tests were performed with the grain parallel to the length of the joint with a dihedral angle equal to 90° .

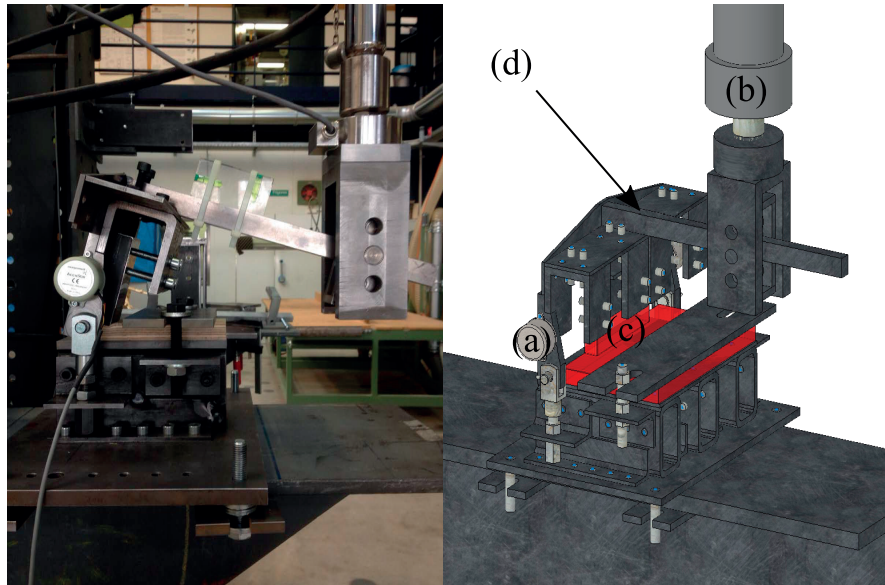


Figure 5.11 – Rotational partial compression setup: (a) 2x inclinometers, (b) cylinder and 20kN cell loads, (c) sample, and (d) lever arm.

Moment–rotation behavior in partial compression

All the tests explored the mechanical behavior of this joint in partial compression with rotation angles from 0° to 25° (Fig.5.12). First, the clearance of the joint caused an initial displacement, and special attention was given to the production of the samples to minimize it. This deformation is an essential consideration in structure design, and receives particular attention in the current European standards. Secondly, the joint stiffness was determined in the elastic region by a linear regression from 0.1 to 0.4 $M_{u,D}$. The yield point was defined as the intersection of the elastic and the plastic regression lines. Densification was not achieved, because the rotation angle should have been much larger; however, a joint with such a large strain is structurally useless. As a consequence of the setup limitation, the maximum moment observed in the test was not the real ultimate moment of the joint. An average of all the replicates of each sample was taken, so only average curves are displayed in the figures.

Wood's anisotropic properties mean that its elastic modulus changes with its grain orientation. The use of a steel punch avoided parasitic effects due to the edge deformation of the standing panel after a certain rotation angle. Nevertheless, some tests were also conducted with a wood punch to reproduce the actual behavior of the joint. The mechanical behavior of the joint was more homogeneous with the steel punch (Fig.5.12): its standard deviation with a wood punch was almost 4 times larger than that with a steel one. As a result, the SP distortion at the corner of the contact surface was not negligible, and could be considered in the theoretical estimation of mechanical performance. The Hankinson empirical formulas can help to characterize the elastic modulus in different orientations [Han21].

Chapter 5. Improvement of the Rotational Stiffness for the Connection of Thin Structural Wood Panels

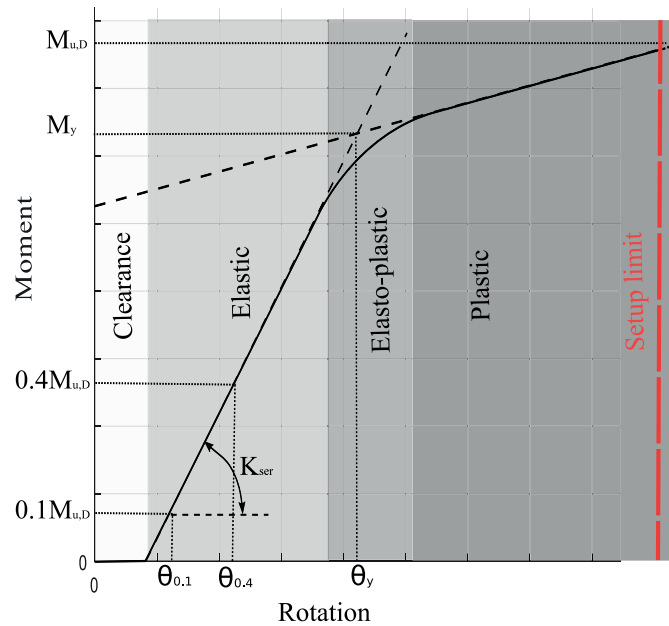


Figure 5.12 – Mechanical behavior in rotational partial compression.

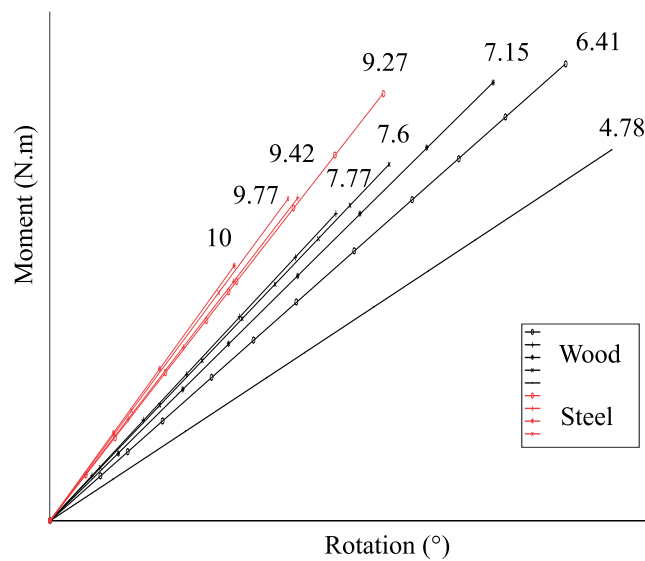


Figure 5.13 – Corresponding stiffness with steel or Kerto Q punch.

All the stiffness and the yield point results are listed in Table 5.4. The curves are presented for SC and DC (Fig.5.14 and 5.15). Using the steel punch gave higher results than those from using wood for the reasons described above. For SC, when the edge distance was 63 mm, the elastic stiffness increased by 21% compared with no edge distance. The increase did not affect the yield moment. Further tests will be conducted to characterize the stiffness with respect to this distance.

Table 5.5 gives a comparative analysis of the SC and DC joints. The joint length is 40% lower in

Sample	Elastic stiffness (N·m/°)	Plastic stiffness (N·m/°)	Yield moment (N·m)	Yield rotation (°)
a	10.9	4.6	99.2	7.5
b	12.1	4.1	64.7	4.6
c	15.1	4.4	69.5	4.1
d	14.1	6.3	92.3	5.6
e	6.1	3.1	38.0	6.1
f	9.5	2.6	47.1	5.1

Table 5.4 – Elasto-plastic values for rotational partial compression.

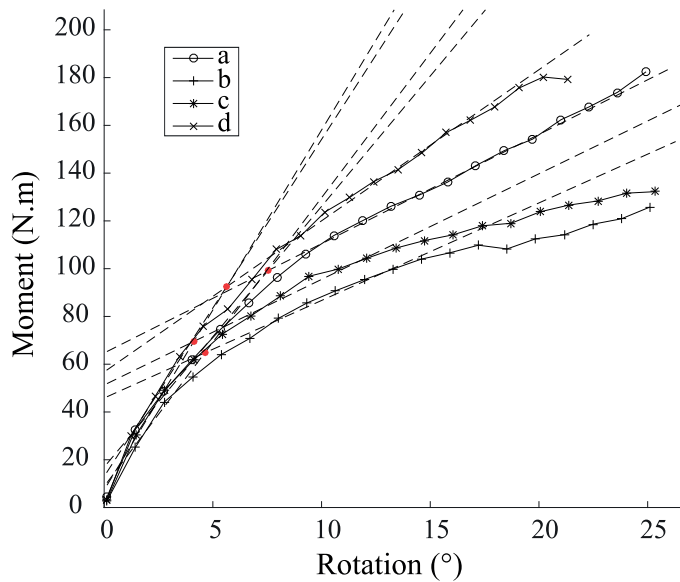


Figure 5.14 – SC moment-rotation curves.

the DC configuration than in the SC one. Given that the mechanical strength is proportional to the joint length, the yield rotation behavior is not similar in both configurations. Based on these results, the mechanical performances of the SC and the DC configurations are largely quasi equal. The exception is the yield moment, which is more important in the DC configuration according to the proportionality of this test. A setup with a higher rotation range could refine the linear regression in the plastic part, and thus provide a more accurate yield point. In the current setup, the MTSJ showed homogeneous behavior in its different loaded areas, leading to the stress distributing uniformly in the joint and so avoiding failure at a singular weak point.

Analysis of the additional length profile

The additional length takes the form of an exponential curve whose shape is determined by the γ coefficient, which needs to be set according to the different geometries of the MTSJs.

Chapter 5. Improvement of the Rotational Stiffness for the Connection of Thin Structural Wood Panels

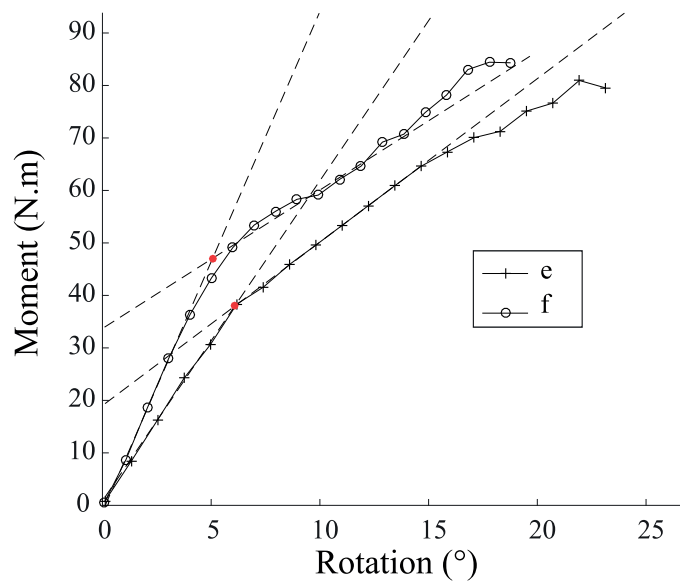


Figure 5.15 – Double contact moment–rotation curves.

Contact	Elastic stiffness (N·m/°)	Plastic stiffness (N·m/°)	Yield moment (N·m)	Yield rotation (°)	Joint length mm
SC	13.1	4.9	81.5	5.5	50
DC	7.8	2.9	42.5	5.6	30
≠	40 %	41 %	48 %	2 %	40 %

Table 5.5 – Comparison of SC and DC.

The rotation angle and strain are both small in the elastic part. For this reason, the additional length was studied only in the plastic part (Fig.5.16). The deformations were monitored with a high-resolution camera during the experiment. Afterwards, the final deformations were scanned with a FaroArm to compare the data processing from the camera pictures (Table 5.6). The results from both data processes appeared almost equal, with a difference of just 0.5%. The reliability of the data processes was therefore verified.

Type	Scan	Camera
ID Time	t4	t4
Time(s)	600	600
γ	0.4407	0.4432
Adj. Rsquare	0.96	0.99
Nb. curves	7	5

Table 5.6 – Comparative fit of γ coefficient - Scan vs camera.

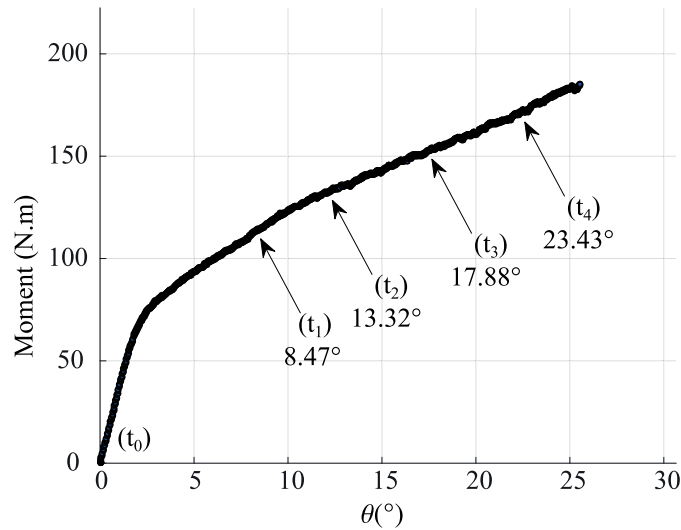


Figure 5.16 – Selected times on the moment–rotation curve.

First, the effect of geometry on the γ coefficient was studied (for the same 25° rotation angle). All the γ coefficients for the different geometries are listed in Table 5.7. The additional length of sample (d) was not studied owing to the lack of consistent values from the few specimens available. Table 5.8 compares the values between SC and DC. The additional length in the DC was small, which may account for most of the disparity in the results. The γ coefficient for the DC was 77% bigger than that for the SC. As a result, the additional length was less important in the DC area of the joint for a given rotation angle.

Sample	a	b	c	d	e	f
γ_{min}	0.27	0.22	0.15	-	1.77	1.11
γ_{max}	1.14	1.34	0.89	-	4.51	3.58
γ_{mean}	0.50	0.53	0.55	-	2.95	1.76
SD	0.21	0.28	0.24	-	0.88	0.95
Adj. Rsquare	0.95	0.97	0.95	-	0.94	0.93
Nb.samples	8	8	4	-	5	5
Nb.curves	21	25	10	-	12	6

Table 5.7 – γ coefficient at 25° of rotation.

In the second step, the evolution of the additional length was studied using time-lapse photography (Fig.5.8). Sample (a) is shown with a fixed interval of 120 seconds between each picture. Fig.5.18a displays the area of additional length with respect to different angles of rotation. The shape of the exponential curve varied with the angle of rotation, although there was a linear correlation between the γ coefficient and the strain of the LP in this configuration (Fig.5.18b and Table 5.9). The larger the rotation, the smaller the γ coefficient was. The effect of this coefficient was understood and observed at a given rotation angle (time= t_4 , $\theta = 23.43^\circ$): the higher the γ coefficient, the smaller the additional length was (Fig.5.18c). However, the additional length represented a small part of the total deformed area. Considering

Chapter 5. Improvement of the Rotational Stiffness for the Connection of Thin Structural Wood Panels

Sample	SC	DC
γ_{min}	0.21	1.44
γ_{max}	1.12	4.04
γ_{mean}	0.53	2.35
SD	0.24	0.91
Adj. Rsquare	0.96	0.93
Nb.samples	7	5
Nb.curves	19	9

Table 5.8 – γ coefficients for SC or DC.

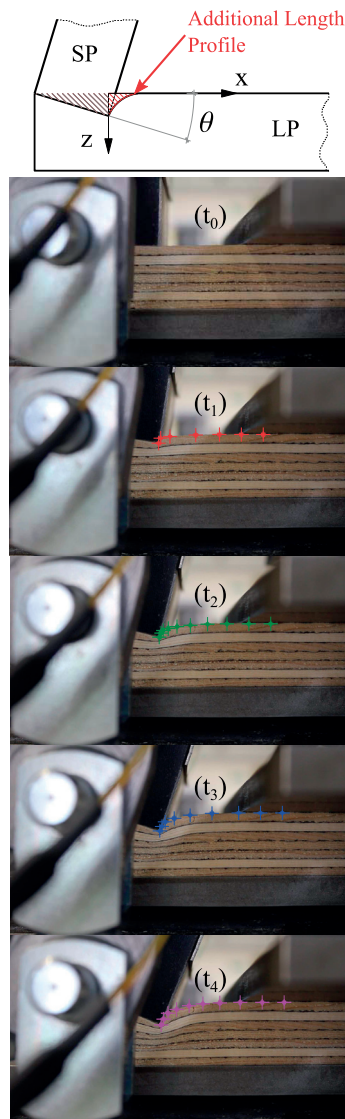


Figure 5.17 – Time-lapse photographs of the displacement profile.

5.4. Embedment Effect on MTSJ with TT

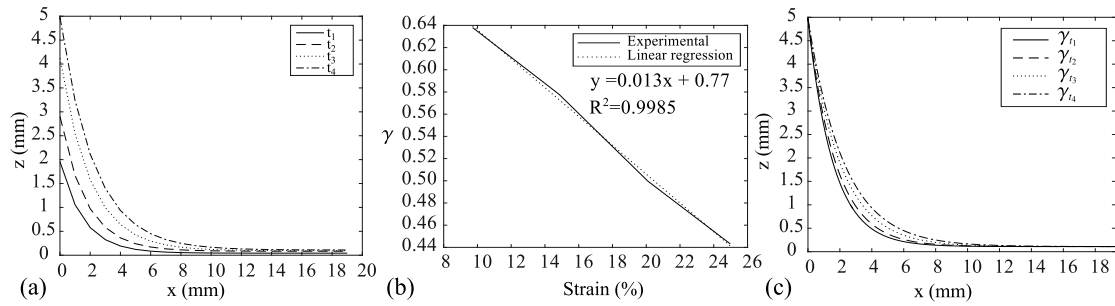


Figure 5.18 – γ coefficients: (a) at each step t_i , (b) linear regression of $\gamma = f(\text{strain})$, and (c) comparison with t_4 displacement.

Time step	t_1	t_2	t_3	t_4
Time(s)	240	360	480	600
$\theta(^{\circ})$	8.47	13.32	17.88	23.43
γ	0.638	0.578	0.500	0.443
SD	0.06	0.07	0.06	0.06
Adj. Rsquare	0.99	0.98	0.99	0.99
$\delta(\text{mm})$	1.96	3.03	4.17	5.14
Strain (%)	9.6	14.7	20	25

Table 5.9 – Evolution of γ with rotation steps.

a constant γ coefficient during the rotation of the joint, the average error was only 3.5%. A uniform value of γ could be used with little effect on the result.

Embedded volumes

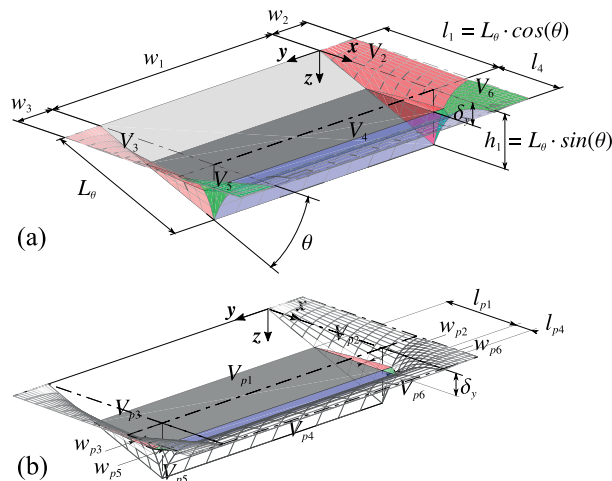


Figure 5.19 – (a) Elasto-plastic deformed volumes. (b) Details after yield point.

The total deformed volume due to the rotational partial compression can be divided into elementary volumes (V_i , Fig.5.19). Each volume is described by the following integrations (Eqs.(5.3) to (5.8)), which are expressed with the geometrical parameters of the directly and

Chapter 5. Improvement of the Rotational Stiffness for the Connection of Thin Structural Wood Panels

indirectly loaded area given in Fig.5.3 and Table 5.10.

$$V_1 = \frac{1}{2} \cdot w_1 \cdot l_1 \cdot h_1 \quad (5.3)$$

$$V_2 = \int_0^{l_1} \int_0^{w_2} x \cdot \tan \theta \cdot \exp(-\gamma y) dy dx \quad (5.4)$$

$$V_3 = \int_0^{l_1} \int_0^{w_3} x \cdot \tan \theta \cdot \exp(-\gamma y) dy dx \quad (5.5)$$

$$V_4 = w_1 \cdot \int_0^{l_4} h_1 \cdot \exp(-\gamma x) dx \quad (5.6)$$

$$V_5 = \int_0^{l_4} \int_0^{w_3} h_1 \cdot \exp(-\gamma x) \cdot \exp(-\gamma y) dy dx \quad (5.7)$$

$$V_6 = \int_0^{l_4} \int_0^{w_2} h_1 \cdot \exp(-\gamma x) \cdot \exp(-\gamma y) dy dx \quad (5.8)$$

Param.	SC1		SC2		DC*	
	Name	Value	Name	Value	Name	Value
w_1	$M_{sh,end}$	13	M_{sh}	26	L_{se}	37.2
w_2	-	0	N_{r0}	12	N_{r1}	6.4
w_3	N_{r0}	12	N_{r0}	12	N_{r1}	6.4
l_1	$L_{\theta,SC} \cos \theta$	-	$L_{\theta,SC} \cos \theta$	-	$L_{\theta,DC} \cos \theta$	-
l_4	P_{22+}	139.5	P_{22}	139.5	P_{01} (P_{02})	10.7 (139.5)
h_1	$L_{\theta,SC} \sin \theta$	-	$L_{\theta,SC} \sin \theta$	-	$L_{\theta,DC} \sin \theta$	-
γ	γ_{SC}	0.53	γ_{SC}	0.53	γ_{DC}	2.35

* For each of the two embedded volumes, P_{01} and P_{02} set the l_4 value, respectively.

Table 5.10 – Embedded volume parameter values

The length of the directly loaded surface is $L_{\theta,k} = t/2(1 + \tan \theta/2) - C/\tan \theta$, where t is the panel thickness and C is the clearance between the tab and slot.

The plastic range is reached quickly during the deformation. If we consider that δ_y is the point where the plastic deformation starts, then the elementary plastic volumes are defined by Eqs.(5.9) to (5.14).

$$V_{p1} = \frac{1}{2} \cdot w_1 \cdot l_{p1} \cdot (h_1 - \delta y) \quad (5.9)$$

$$V_{p2} = \int_{l_1 - l_{p1}}^{l_1} \int_0^{w_{p2}} (x \cdot \tan \theta \cdot \exp(-\gamma y) - \delta y) dy dx \quad (5.10)$$

$$V_{p3} = \int_{l_1 - l_{p1}}^{l_1} \int_0^{w_{p3}} (x \cdot \tan \theta \cdot \exp(-\gamma y) - \delta y) dy dx \quad (5.11)$$

$$V_{p4} = w_1 \cdot \int_0^{l_{p4}} (h_1 \cdot \exp(-\gamma x) - \delta y) dx \quad (5.12)$$

$$V_{p5} = \int_0^{l_{p4}} \int_0^{w_{p5}} (h_1 \cdot \exp(-\gamma x) \cdot \exp(-\gamma y) - \delta y) dy dx \quad (5.13)$$

$$V_{p6} = \int_0^{l_{p4}} \int_0^{w_{p6}} (h_1 \cdot \exp(-\gamma x) \cdot \exp(-\gamma y) - \delta y) dy dx \quad (5.14)$$

with

$$l_{p1} = l_1 - \frac{\delta y}{\tan \theta} \quad (5.15)$$

$$w_{p2} = -\frac{1}{\gamma} \ln \frac{\delta y}{x \tan \theta} \quad \text{with } l_1 - l_{p1} \leq x \leq l_1 \quad (5.16)$$

$$w_{p3} = -\frac{1}{\gamma} \ln \frac{\delta y}{x \tan \theta} \quad \text{with } l_1 - l_{p1} \leq x \leq l_1 \quad (5.17)$$

$$l_{p4} = -\frac{1}{\gamma} \ln \frac{\delta y}{h_1} \quad (5.18)$$

$$w_{p5} = \frac{1}{\gamma} \ln \frac{\delta y}{h_1 * \exp(-\gamma x)} \quad \text{with } l_1 - l_{p1} \leq x \leq l_1 \quad (5.19)$$

$$w_{p6} = -\frac{1}{\gamma} \ln \frac{\delta y}{h_1 * \exp(-\gamma x)} \quad \text{with } l_1 - l_{p1} \leq x \leq l_1 \quad (5.20)$$

The elastic embedded volumes are obtained by

$$V_{ei} = V_i - V_{pi}.$$

5.5 Conclusions

The rotational stiffness of an edge-to-edge connection of a timber folded-plate structure was increased by using a TT and closed slots. The effect of embedment, which provided strength, stiffness, and ductility to the connection, was identified and explained. Quantitative analysis provided values for the decay coefficients of the additional length curves in single and double contact. The embedded volumes were analytically described. Their use in the description of the local forces will allow subsequent work to formulate an analytical model of the MTSJ rotational behavior. Further works will aim to determine the γ coefficient with respect to the material properties (LVL), panel thickness, grain orientation, protrusion lengths, dihedral angle φ , tab number, and types of contact. This paper demonstrates that a MTSJ with TT performs better under a bending moment than a screwed angular connection for thin LVL panels.

Chapter 5. Improvement of the Rotational Stiffness for the Connection of Thin Structural Wood Panels

Outcomes ③*

The outcomes of the present chapter are synthesized as follows.

Bending tests, by folding two connected panels, revealed that the TT-variant of the MTSJ, without glue or metal fastener, was significantly stiffer than screws with a symmetric behavior in closing and opening for $\varphi = 90^\circ$.

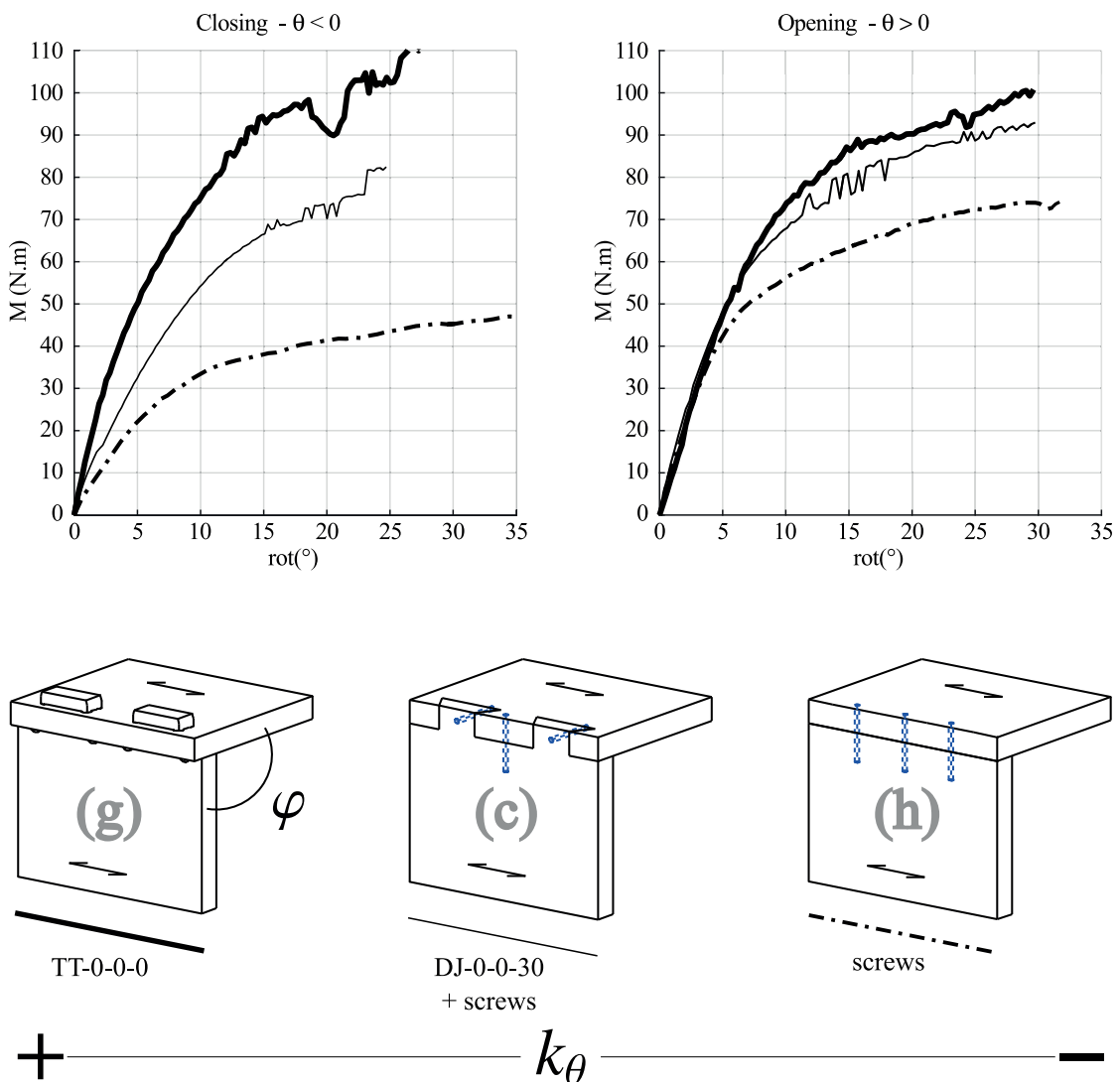


Figure 5.20 – Comparison between TT-variant and screws.

*This additional section was not included in the original publication.

The TT-variant of the MTSJ resists the applied moment with activating the components in rotational partial compression perpendicular to the panel plane. This mechanism is similar to that of the Nuki joint.

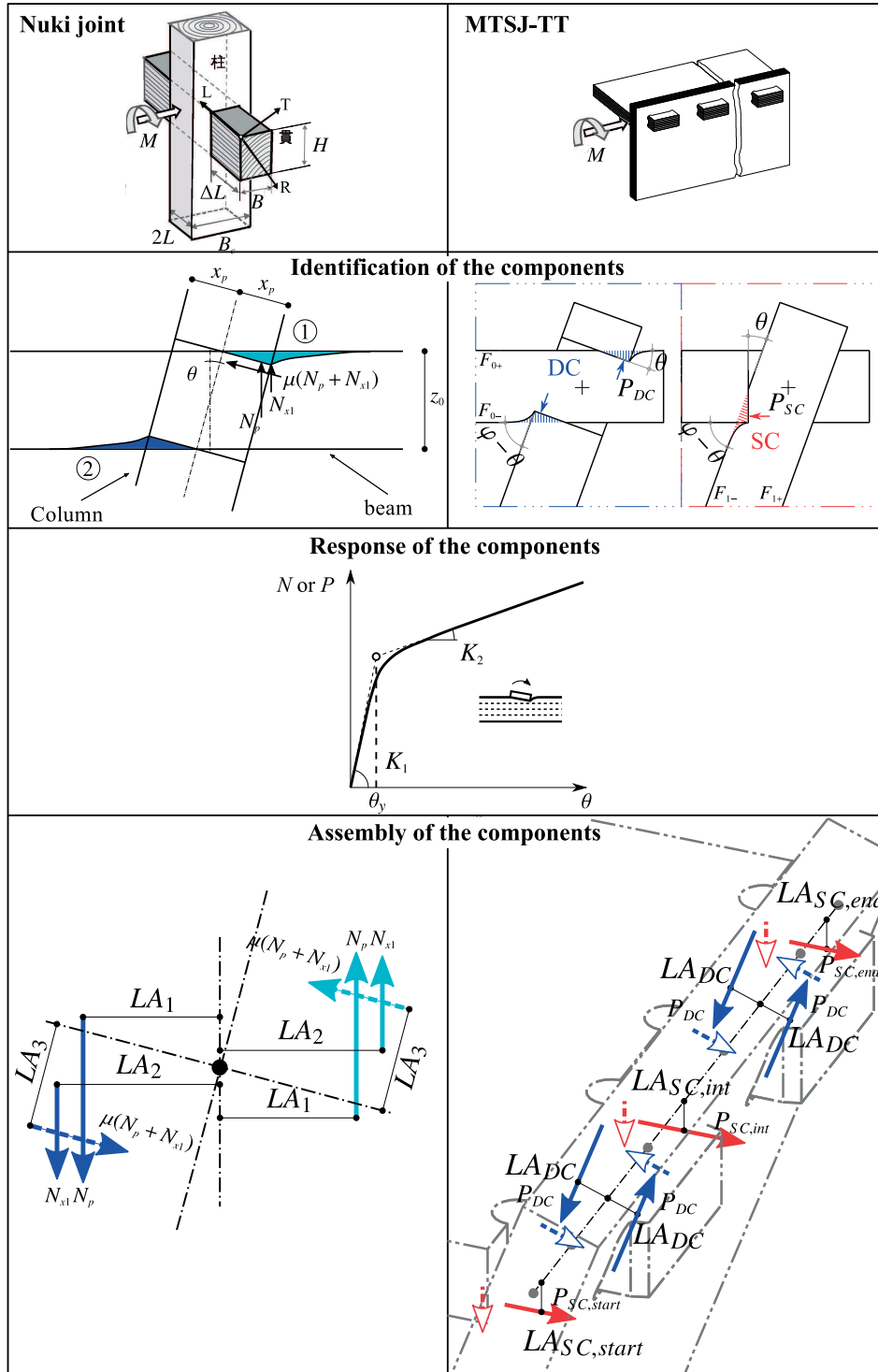


Figure 5.21 – Analogy MTSJ-TT to Nuki joint by component method.

Chapter 5. Improvement of the Rotational Stiffness for the Connection of Thin Structural Wood Panels

In addition to the embedment effect by double contact in the tabs of panel F_0 (components similar to Nuki joints), other components in single contact occur in the panel F_1 at the start and end of the MTSJ-TT as well as the areas between slots.

The characterization of the embedment effect was limited to Kerto-Q material with only a thickness of 21mm. The joint-to-grain angle α was set to 0°

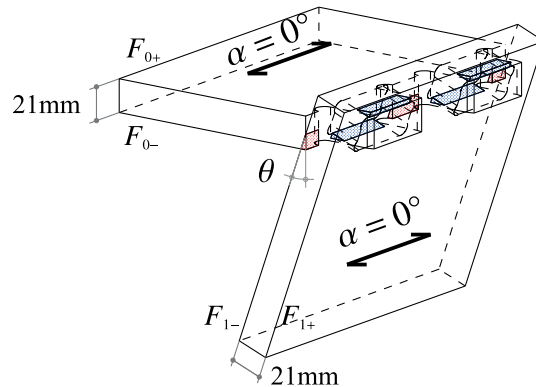


Figure 5.22 – Embedment in single (SC) and double (DC) contact : Kerto-Q 21mm, joint-to-grain angle $\alpha = 0^\circ$.

Under the previous limitations of the study, the decay coefficients which define the exponential profiles of the indirectly deformed parts were obtained only by image processing. The yield angles, used to calculate the plastic part of the deformed volumes were determined by bi-linear approximation of the nonlinear moment-rotation curves. However, in freeform timber plate structures, the thickness and the grain orientation of the panels vary according to the structural requirements and the global geometry. It implies the following question.

How to extend the embedment characteristics of LVL Kerto-Q to different thicknesses and joint-to-grain angles ?

→ **Objective ④** (see chapter 6)

References

- [CHK06] W.-S. Chang, M.-F. Hsu, and K. Komatsu. Rotational performance of traditional nuki joints with gap i : Theory and verification. *Journal of Wood Science*, 52(1):58–62, 2006.
- [Han21] R. L. Hankinson. Investigation of crushing strength of spruce at varying angles of grain. *Air Force Information Circular No. 259*, 1921.
- [Ina93] M. Inayama. Study on compression perpendicular to the grain in wood, part 4: analytic functions for the relation between compression load and elastic deformation perpendicular to the grain in wood. In *Proceedings of AIJ, Tokyo, Japan*, pages 907–908, 1993. (in Japanese).
- [KMKK09] A. Kitamori, T. Mori, Y. Kataoka, and K. KOMATSU. Effect of additional length on partial compression perpendicular to the grain of wood. *Journal of Structural and Construction Engineering (Transactions of AIJ)*, 74(642):1477–1485, 2009.
- [KSM⁺14] Oliver David Krieg, Tobias Schwinn, Achim Menges, Jian-Min Li, Jan Knippers, Annette Schmitt, and Volker Schwieger. *Biomimetic Lightweight Timber Plate Shells: Computational Integration of Robotic Fabrication, Architectural Geometry and Structural Design*, pages 109–125. Springer International Publishing, Cham, 2014.
- [MDS⁺02] Y. Matsubara, Z. Du, H. Sakata, A. Wada, H. Ito, and R. Kataoka. 22014 experimental study on the behavior of rotational embedment between douglas fir glulams. *Summaries of technical papers of Annual Meeting Architectural Institute of Japan. C-1, Structures III, Timber Structures, Steel Structures, Steel Reinforced Concrete Structures*, 2002:27–28, 2002.
- [OSY15] K. Ogawa, Y. Sasaki, and M. Yamasaki. Theoretical modeling and experimental study of japanese “watari-ago” joints. *Journal of Wood Science*, 61(5):481–491, 2015.
- [RMW15] S. Roche, G. Mattoni, and Y. Weinand. Rotational stiffness at ridges of timber folded-plate structures. *International Journal of Space Structures*, 30(2):153–168, 2015.
- [RNW14] C. Robeller¹, S. S. Nabae², and Y. Weinand². Design and fabrication of robot-manufactured joints for a curved-folded thin-shell structure made from clt. In *Rob|Arch, Robotic Fabrication in Architecture, Art, and Design*. Springer, 2014.
- [RSMW14] C. Robeller, A. Stitic, P. Mayencourt, and Y. Weinand. Interlocking folded plate - integrated mechanical attachment for structural wood panels. In *Advances in Architectural Geometry 2014*. Springer - submitted may 2014, 2014. <http://www.architecturalgeometry.org/aag14/>.

Chapter 5. Improvement of the Rotational Stiffness for the Connection of Thin Structural Wood Panels

- [RW16] C. Robeller and Y. Weinand. Fabrication-aware design of timber folded plate shells with double through tenon joints. In *Robotic Fabrication in Architecture, Art and Design 2016*, pages 166–177. Springer, 2016.
- [TOS08] H. Tanahashi, M. Okamura, and Y. Suzuki. Simple formulation of elasto-plastic embedment behavior of orthotropic wood considering densification. In *World Conference on Timber Engineering, Miyazaki, Japan*. Proceedings WCTE 2008, 2008.
- [TS12] H. Tanahashi and Y. Suzuki. Embedment mechanism and formulation of major types of traditional wooden joints in japan. In *World Conference on Earthquake Engineering, Lisbon, Portugal, 2012*.
- [TSH⁺08] H. Tanahashi, H. Shimizu, H. Horie, P. Yang, and Y. Suzuki. Elastic embedded displacements of orthotropic wood with a finite length based on pasternak model. *Journal of Structural and Construction Engineering (Transactions of AIJ)*, 73(625):417–424, 2008. (in Japanese).
- [TSS12] H. Tanahashi, H. Shimizu, and Y. Suzuki. Basic concept and general formulation of restoring force characteristics of traditional wooden joints. In *World Conference on Timber Engineering, Auckland, New Zealand*. Proceedings WCTE 2012, 2012.

6 Material characterization of spruce LVL in rotational partial compression

Abstract

A non-linear model is presented to characterize LVL Kerto-Q panels in rotational partial compression. It is built from typical stress-strain relationship including penalization of the elastic modulus in the plastic range. The elastic and plastic embedded volumes lead to the local forces and resisting moment calculation in single and double contact. Moment-rotation curves and decay coefficients are provided for different joint-to-grain and yield angles. The model's results confirmed the trend of Japanese assumptions on the embedment effect. In addition, the exponential profiles of the additional length were fitted on the captured surface deformations and compared with the analytical model.

Keywords Rotational partial compression, Triangular embedment, Decay coefficient, yield angle, LVL.

Objective ④

Characterize spruce LVL Kerto-Q in rotational partial compression

6.1 Introduction

6.1.1 Objectives

At WCTE 2016 in Vienna, Roche et al. [RGW16] (refer also to chapter 5) presented the improvement of the rotational stiffness of multiple tab-and-slot joints (MTSJ) by using closed slots and trough tenons (TT). The elementary deformed volumes that govern the stiffness of the joint were presented by their integrals. These volumes are part of an upcoming analytical model of the moment resisting behavior of MTSJ-TT. They allow the local forces calculation through the stresses in rotational partial compression. The Japanese theory was followed by Roche et al. [RGW16] (refer also to chapter 5) to present the rotational embedment effect on bending of MTSJ-TT (see Fig.6.1). The results of experimental tests primarily provided the decay coefficients and the yield rotation angles in single contact (SC) and double contact (DC) for the case-study of 90° edgewise connection of two 21mm-LVL Kerto Q spruce panels. The range of parameters was only limited to this specific case. The presented work proposes a methodology to characterize the material properties of LVL Kerto Q spruce panels in rotational embedment, typically decay coefficients which characterize the additional length of the indirectly loaded area and yield points which mark the transition from elasticity to plasticity. Both are essential for the elastic and plastic embedded volumes calculation. The properties are studied for different thicknesses and joint-to-grain angle α .

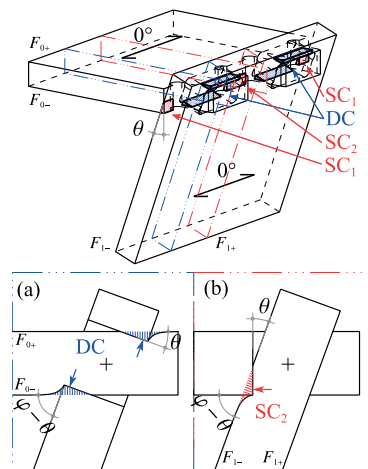


Figure 6.1 – Embedment effect in MTSJ-TT: (a) DC and (b) SC from [RGW16].

6.1.2 Additional length in partial compression

In the early Nineties, Inayama [Ina91, Ina93] proposed a formulation of the embedment in partial compression of wood, perpendicular to the grain. He both addressed translational (TPC) and rotational (RPC) partial compression. The deformation profile was defined by a directly loaded area and by an additional length representing the indirectly loaded part. This additional length is expressed by an exponential function ($f(x) = \delta \cdot e^{-a_e \cdot x}$) where a constant decay coefficient a_e is considered all along the deformation (elastic or plastic). a_e , γ and

b_i^* are all representing the decay coefficient in sense of Inayama, Tanahashi and the author, respectively. Based on the Madsen's work [MHH82] which determined a decay length (where stress and strain vanish to zero) of $1.5 \cdot H$, Inayama established the decay coefficients at $\frac{1.5}{H}$ and $\frac{1.5 \cdot n}{H}$ when the deformation is spread along or transverse to the grain, respectively. H is the height of the wood media, locally loaded in partial compression and n is a coefficient relevant of the grain orientation. In 2010, the Architectural Institute of Japan(AIJ) resumed this work in the fundamental theory of timber engineering [AIJ10]. Instead of $\frac{1.5}{H}$, Kimatori [KMKK09] experimentally proposed three differentiated decay coefficients: $\frac{2.5}{H}$, $\frac{3}{H}$ or $\frac{5.5}{H}$ for translational, rotational in single or double triangular embedment, respectively. Very recently, Ogawa [OSY15] derived the decay coefficient in the plastic range for an analytical model of crosspiece timber connection under bidirectional triangular embedment.

Almost ten years before Ogawa, Tanahashi applied the Pasternak model to formulate the elasto-plastic embedment displacement of an orthotropic wood with an infinite [TSS06a, TSS06b] and then a finite edge distance [TSH⁺08, TOS08]. He gave the exact hyperbolic solution of the governing equation and confirmed the Inayama's exponential expression with a simplified model. A combined experimental and numerical analysis supplied the decay coefficients which depends on the material properties in the plane (LR: $\frac{3}{H}$, LT: $\frac{2.7}{H}$, RT: $\frac{9}{H}$, LTR: $\frac{2.3}{H}$). The displacement profile along the beam height is also defined by an exponential shape function. His resulting stiffness model introduced both an increasing ratio (full compression to partial compression) and a decreasing factor by combination of yielding and hardening of wood due to densification. The embedment model was finally used for the analytical formulation of ductile Nuki joints, a beam penetrating through a column, present in many traditional timber constructions in Japan. The resisting moment is calculated by integration of the embedment stress from the expression of volume deformation.

In Western countries, the studies on local compression perpendicular to grain focused more on practical design method. Therefore, the limit value of the bearing strength is generally given at a certain value of the strain (e.g. 1% in EN408 [20112] and EN789 [20004]). The Madsen's research was also the starting point for the design rules of the Eurocode 5 [fSC08] but Blass [BG04] reduced the decay length at a threshold of 30 mm. This proposal still remains in the current version of the European timber code. Using the equilibrium method of the theory of plasticity, Van der Put [dP90, dP08, dP12] confirmed their empirical load spreading models. He outlined that they are not versatile enough and works only under specific geometrical constraints.

Leijten [LLdP10, LjdL12, Lei16] extended the validation of the physical Van der Put's model by comparison with large amount of data coming from different authors. He also conducted experimental and optical investigation to monitor the penetration depth of bearing stresses (experimental results similar in shape to the analytical Tanahashi's formulation). In a very recent publication, the theoretical stress dispersion model from Van der Put [dP08] was compared with the up-to-date semi-empirical model from Lathuilliere [LPB⁺15] and the empirical EC5's model [fSC08]. He again confirmed the reliability of the model for any beam size and load configurations. For softwood, the slope of the dispersing stresses is 1:1 for small

* b_i in this chapter is the improved definition of γ in chapter 5.

deformation (1% → 3%) and 1:1.5 for larger deformation ($\approx 10\%$). The latter value is typically the one introduced by Madsen and adopted by Inayama.

6.1.3 Yield point

Additionally to the embedment mechanism of wood in translation (or rotation), Inayama [Ina91, Ina93] and AIJ [AIJ10] gave formulas for the yield displacement (or rotation angle) which consider bearing strength, bearing length and distances to edges in longitudinal and transverse direction. As described by Tanahashi, the stress-strain curve of large strain embedment can be split as a linear elastic part at very low value of strain (1-2%), a strain hardening with a reduced positive stiffness after the yield point and an increasing slope due to densification beyond 50% strain level. Usually, the yield point of such curve is rather difficult to obtain with a good accuracy. Today, as mentioned by Munoz [nSMQ08], Blass [BS11], Jorissen [JF11], there is at least six methods to determine the yield point of such ductile curve. In most of the methods, the main data (the initial and plastic stiffnesses) are obtained through the ultimate load. Due to the behavior of wood in partial compression perpendicular to grain, the peak load is not really usable and the yield point is difficult to obtain accurately. Hereafter, simplified analytical model derived from Japanese works is used to provide the rotational embedment properties of LVL Kerto-Q.

6.2 Material characterization in rotational partial compression

It is worth noting that it is standardized to characterize engineering wood panels with mechanical properties as strengths, modulus of elasticity and shear modulus. These characteristics are given by range of thickness and layout of the layers [VESL16]. The following sections present the material characterization of LVL Kerto-Q spruce panels with 21, 27 and 39mm thickness in rotational partial compression, for SC and DC. In the context of the MTSJ-TT, the necessary properties are the yield rotation angles and the decay coefficients.

From an unique simplified analytical model described in section 6.4, the non-linear moment-rotation curves, the yield points and the decay coefficients are derived in single and double contact.

The decay coefficients (b_{SC} or b_{DC}) have also been investigated by a physical measurement according to the following fit function Eq.(6.1).

$$z = \delta_{\theta} \cdot e^{(-b \cdot x)} \quad (6.1)$$

6.3 Method

Two setups were designed to approach the actual kinematics of MTSJ-TT in bending and evaluate individually the two components of contact.

The material is a laminated veneer lumber Kerto-Q spruce panel (LVL-KQ) from Metsäwood. The layers are arranged as follows:

- 21mm = | - ||| - | (29% of cross-layer)
- 27mm = || - ||| - || (22% of cross-layer)

- o 39mm = || - ||| - ||| - || (23% of cross-layer)

Where (|) is the direction of the main layers parallel to grain and (-) is the direction of the cross-layers.

The tests are performed for each thickness and seven joint-to-grain angle α : 0°, 15°, 30°, 45°, 60°, 75° and 90°, knowing that 0° means the grain of main layers is parallel to the joint axis (see Fig.6.2). The specimens were loaded on the full width (45mm for SC, 110mm for DC). A room temperature of $20^\circ \pm 2^\circ$ with a relative humidity of 60% to 65% ensured a LVL moisture content stabilized between 11% and 12% during the experiments.

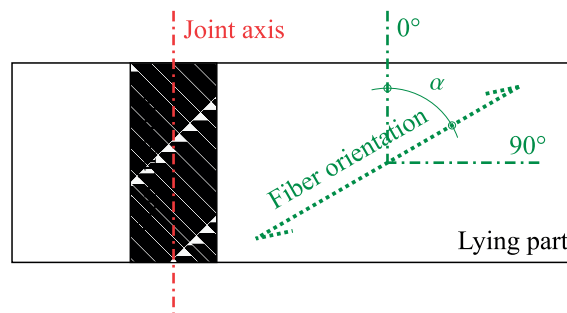


Figure 6.2 – Joint-to-grain angle

The actual embedment due to the MTSJ-TT in bending is bidirectional as shown in Fig.6.3. Fig.6.3a, b and c are for a joint-to-grain angle of 0°, 45° and 90°, respectively. The 3D profile was obtained by using a Faro scan. The Matlab treatment allowed to provide the deformation profile in the two directions (A-A' perpendicular to the joint axis and B-B' parallel to the joint axis). In this study, the deformation was analyzed in one direction at a time but with different joint-to-grain orientation.

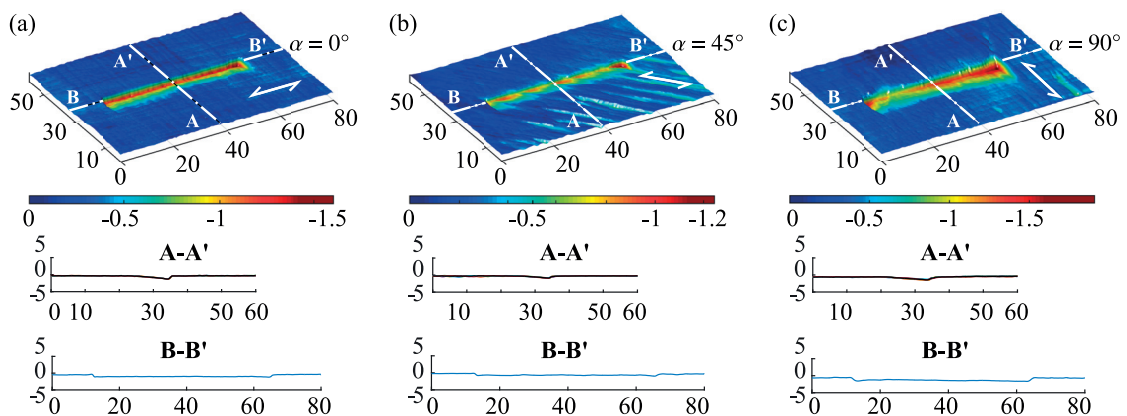


Figure 6.3 – Bidirectional deformation in mm

6.3.1 Single contact component

The SC component is characterized by a triangular embedment with an additional length only on one face of the panels. To suit with the actual kinematics of the MTSJ-TT, the rig has been improved since the publication at the World conference of Timber Engineering in Vienna

Chapter 6. Material characterization of spruce LVL in rotational partial compression

[RGW16]. The rotation axis is now settable in x by placing an adjusting shims depending on the sample thickness and still in z by endless-screw system (see Fig.6.4).

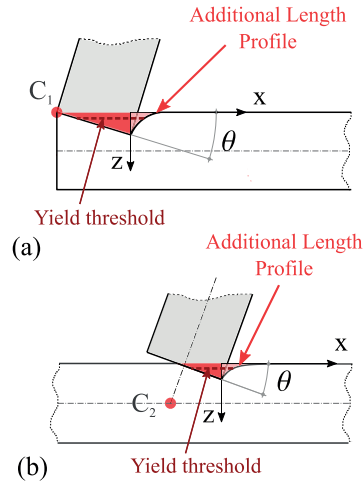


Figure 6.4 – Contact zone in SC – (a) old rotation axis C_1 at the of top surface [RGW16], (b) new rotation axis C_2 at the intersection of the panel mid planes like in the MTSJ-TT.

Description of the samples

The samples for SC are composed with a steel punch (SP) and a lying LVL-KQ die part (LP). The steel material allows to consider the bearing part infinitely rigid compared with the embedded part. It removes edge effect due to the local deformation at the corner if the punch was designed with wood. The angle between the two parts is 90° . The dimensions of the samples and the number of replicates are gathered in Fig.6.5 and Table 6.1. A total of 114 specimens were tested.

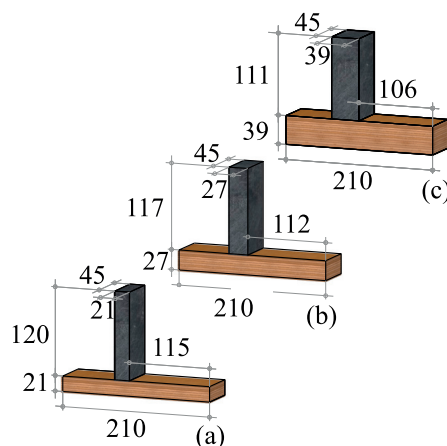


Figure 6.5 – Geometries of samples in rotational partial compression (SC) : (a) 21mm-thickness, (b) 27mm-thickness, (c) 39mm-thickness.

Thickness	Replicate at joint-to-grain angle						
	0°	15°	30°	45°	60°	75°	90°
21mm	5	5	5	10	5	5	6
27mm	5	5	5	6	5	5	6
39mm	5	5	5	5	5	5	6

LVL Kerto-Q spruce material, H% 11 ~ 12

Table 6.1 – Series of samples in rotational partial compression (SC).

Description of the test rig

The described samples were tested using a setup designed for rotational partial compression (see Fig.6.6). A steel lever arm ③ is actuated by a 20 kN cylinder ① to transmit rotation θ to the SP ④, which pressed the surface of the LP ⑤. Thanks to the 2-degree of freedom (2-DOF) head H, the load was kept perpendicular to the lever arm in any position (see details Fig.6.7). The LP was rigidly supported and fixed at each end by a steel clamp. Rotation and load were recorded by two inclinometers ⑦ and a cell load ② placed at the end of the cylinder.

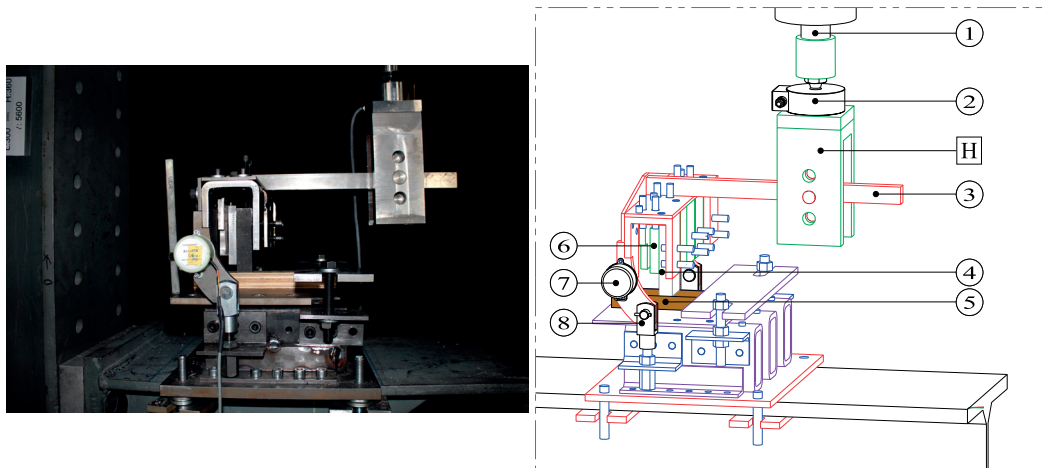


Figure 6.6 – Test rig for rotational partial compression in SC : ① Cylinder, ② Cell load 20kN, ③ Lever arm, ④ Steel punch (SP), ⑤ Sample (LP), ⑥ X-adjusting shim ⑦ Inclinometers (x2) ⑧ Z-settable rotation axis, H 2-DOF head.

The 200mm cylinder stroke limited the rotation angle to less than 30°. It corresponds to a strain of about 25%, quite far from the densification point. Nevertheless this angle is already much beyond the point where the connections are going to work.

6.3.2 Double contact component

The DC component has a similar behavior than the SC component but the embedment mechanism is simultaneously initiated on both sides of the through tab (see Fig.6.8). This series of tests is made to check the conclusion of Kimatori [KMKK09] on the decay coefficient. Is it confirmed or not that the double contact increases the value compared to the single contact ?

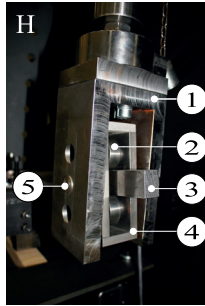


Figure 6.7 – The 2-DOF head accompanies the relative displacement of the lever arm with respect to the cylinder piston: ① Fixed part to cylinder, ② Roller on ball bearings ($\times 2$), ③ Lever arm, ④ support of rollers, ⑤ rotation axis of roller support.

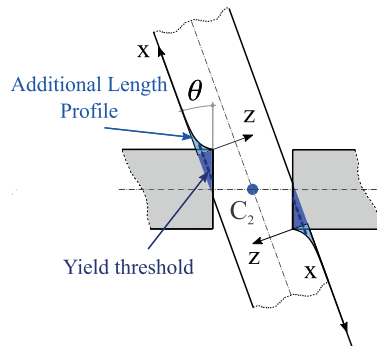


Figure 6.8 – Contact zones in Double Contact.

Description of the samples

In this case, the LVL-KQ die (LP) passed through two steel plate punches (SP) ④ & ⑥ on Fig.6.10. The thickness of the punches was chosen among 21mm, 27mm or 39 mm regarding the thickness of the embedded LVL-KQ panel. The distance between the punches was set by moving and screwing one of them ⑥, until tight contact with the LVL-KQ part. The steel material was still used to not skew the results. The angle between the parts is 90°. Fig.6.9 and Table 6.2 summarize the dimensions and the replicate numbers of the samples. A total of 45 specimens were tested.

Thickness	Replicate at joint-to-grain angle		
	0°	45°	90°
21mm	5	5	5
27mm	5	5	5
39mm	5	5	5

LVL Kerto-Q spruce material, H% 11 ~ 12

Table 6.2 – Series of samples in rotational partial compression (DC).

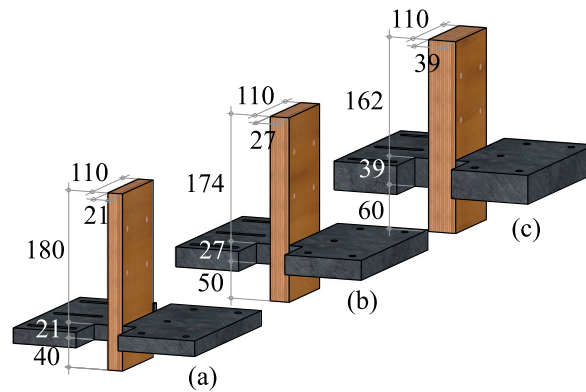


Figure 6.9 – Geometries of samples in rotational partial compression (DC) – (a) 21mm-thickness, (b) 27mm-thickness, (c) 39mm-thickness.

Description of the test rig

On the setup of Fig.6.10, a pure moment is applied to the LP ⑤ via two pairs of opposite forces. The forces are produced via the lever arm ③ and the 20kN cylinder ②. The transmitted moment M imposed the rotation θ to the LP which is play-free maintained between the two SP ④ & ⑥. The SP are rigidly fixed to the support frame. The loads are measured by two pairs of 10kN cell loads ② directly connected to the LP. The two inclinometers ⑦ which monitored the angle are screwed on both side of the LP.

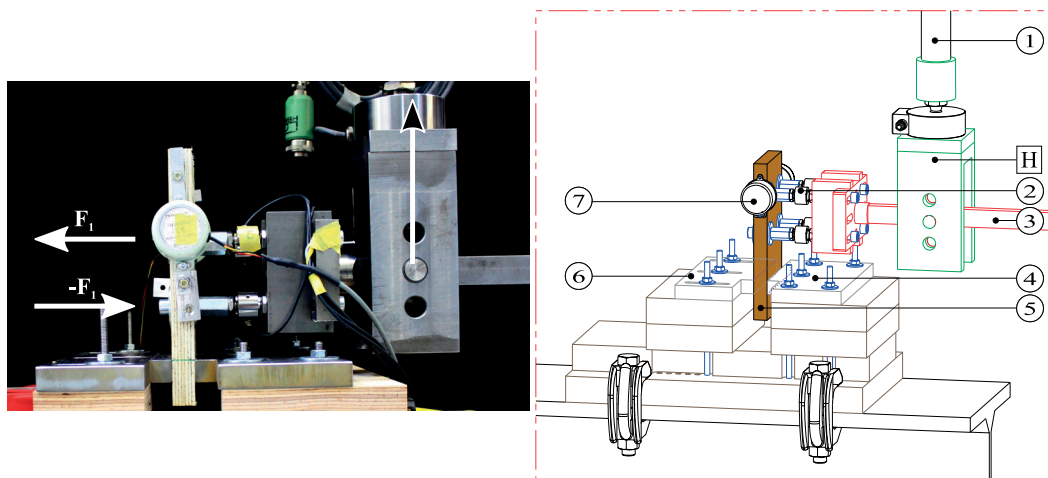


Figure 6.10 – Test rig for rotational partial compression in DC : ① 20kN Cylinder, ② 10kN Cell loads (x4), ③ Lever arm, ④ Fixed steel punch, ⑤ LVL-KQ die (LP), ⑥ X-adjusting steel punch ⑦ Inclinometers ($\times 2$), H 2-DOF head.

The rotation is limited this time for two main reasons :

- the stroke of the cylinder is 200 mm,
- with the embedment mechanism, the strength of the connection grown comparatively to the bending strength of the LP. In consequence, a significant bending rotation is added to rotation angle of the connection and should be filtered afterward.

6.3.3 Non-linear Measurements

As presented in section 6.2, the required experimental data are the applied moments, the resulting rotations and the profiles of the indirect loaded areas. These non-linear measurements are recorded in the same way for both cases (SC and DC).

Moment-rotation

The cylinder displacement was controlled by a manual hydraulic pump. The quasi-static test duration was between 240 and 300 seconds for 30° rotation. The data acquisition was done every 1s for SC and every 0.5s for DC. Every results (loads, rotation) are saved in TXT files and then numerically processed with Matlab R2015b. The rotation is finally obtained by averaging the two inclinometers. For SC, the moment is the product of the cylinder force by the corrected (sliding into the 2DF head) lever arm distance from the force line to the rotation center. For DC, the moment is calculated from the product of F_1 and 60 mm (distance between the upper and lower cell loads). Finally, experimental moment-rotation curves are plotted for every specimens.

Deformation profile

All along the tests, a high-resolution digital camera (18 MPixels) was placed perpendicularly to the specimen side to film continuously and take pictures of the deformation, every 6 seconds. The captured deformation profiles were sampled manually by points using the Rhinoceros 5.0 CAD software (with higher density at place of larger non linearity). This sampling method has been already qualified by Roche et al [RGW16]. The (x, z) points were exported via TXT files to Matlab R2015b for post-treatment described in section 6.5.2.

6.4 Simplified analytical model

Due to the RPC, the embedment deformation of the samples has a directly and indirectly loaded areas. The directly loaded area is characterized by a contact length L_θ and the indirectly loaded area is defined by the exponential function. The resulting profile is shown in Fig.6.11. For SC and DC, the length L_θ of the directly loaded surface is calculated as

$$L_\theta = \frac{T_1}{2} + \frac{T_0}{2} \tan \frac{\theta}{2} \quad (6.2)$$

T_0 and T_1 stand for the sample and the punch thicknesses, respectively.

The resulting deformed volume can be divided into two volumes (V_1 and V_4 , Figure 6.12). Each volume is described by Eqs.(6.3) and Eq.(6.4), which are expressed with the geometrical parameters of the directly and indirectly loaded area given in Figures 6.11,6.12 and Table 6.3.

In the following equations, i shall be replaced by SC for single contact and DC1 or DC2 for

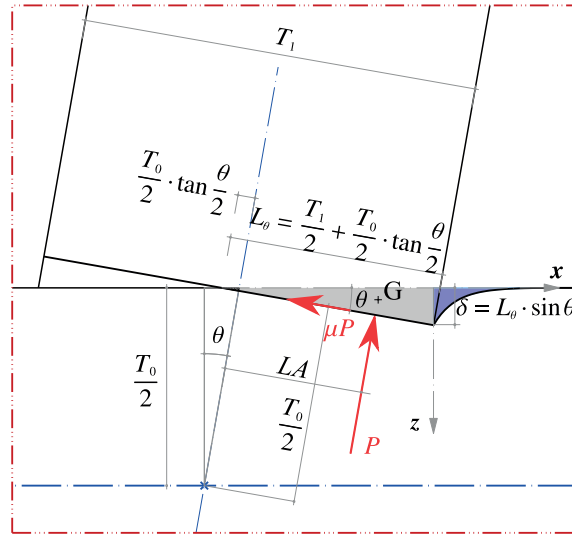


Figure 6.11 – Geometry of additional length profile.

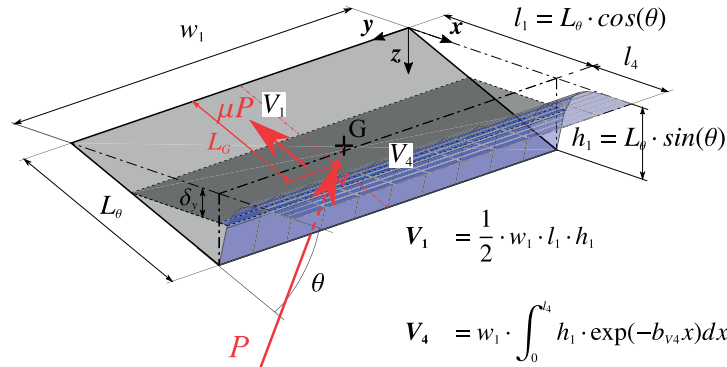


Figure 6.12 – Geometry of embedded volume for local forces P calculation.

Parameter	SC	DC1	DC2
T_0	21,27,39	21,27,39	21,27,39
T_1	21,27,39	21,27,39	21,27,39
w_1	45	110	110
l_1	$L_\theta \cos \theta$	$L_\theta \cos \theta$	$L_\theta \cos \theta$
l_4	115,112,106	40,50,60	180,174,162
h_1	$L_\theta \sin \theta$	$L_\theta \sin \theta$	$L_\theta \sin \theta$

Table 6.3 – Embedded volume parameter values (in mm)

double contact.

$$V_{1,i} = \frac{1}{2} \cdot w_{1,i} \cdot l_1 \cdot h_1 \tag{6.3}$$

$$V_{4,i} = w_{1,i} \cdot \int_0^{l_4} h_1 \cdot \exp(-b_{V4,i} \cdot x) dx \tag{6.4}$$

$$V_i = V_{1,i} + V_{4,i} \tag{6.5}$$

Chapter 6. Material characterization of spruce LVL in rotational partial compression

For Kerto-Q, the plastic limit is reached at an early stage during the deformation. Considering δ_y as the point where the plastic deformation starts, the plastic volumes are defined by Eqs.(6.6) and (6.7).

$$V_{p1,i} = \frac{1}{2} \cdot w_{1,i} \cdot l_{p1} \cdot (h_1 - \delta_y) \quad (6.6)$$

$$V_{p4,i} = w_{1,i} \cdot \int_0^{l_{p4,i}} (h_1 \cdot \exp(-b_{V4,i}x) - \delta_y) dx \quad (6.7)$$

$$V_{pi} = V_{p1,i} + V_{p4,i} \quad (6.8)$$

with

$$l_{p1} = l_1 - \frac{\delta_y}{\tan\theta} \quad (6.9)$$

$$l_{p4,i} = -\frac{1}{b_{V4,i}} \ln \frac{\delta_y}{h_1} \quad (6.10)$$

$$\delta_y = \left(\frac{T_1}{2} + \frac{T_0}{2} \tan \frac{\theta_y}{2} \right) \cdot \sin\theta_y \quad (6.11)$$

The elastic volumes are finally obtained as

$$V_{ei} = V_i - V_{pi} \quad (6.12)$$

The decay coefficients were differentiated between SC and DC but for each of the contact cases, the decay coefficient was considered the same in elastic and plastic range. The comparative analysis that lead to this assumption is developed in the coming section 6.5.2 within the SC results.

From the deformed volumes, the local elastic and plastic forces and resisting moments can be expressed by using typical stress-strain relationships.

Single contact

$$P_{e,\theta,SC} = \frac{V_{e,\theta,SC}}{T_0} \cdot E_\theta \quad (6.13)$$

$$P_{p,\theta,SC} = \frac{V_{p,\theta,SC}}{T_0} \cdot r_{p,SC} \cdot E_\theta \quad (6.14)$$

$$PF_{\theta,SC} = (P_{e,\theta,SC} + P_{p,\theta,SC}) \cdot \mu \quad (6.15)$$

$$M_{\theta,SC} = (P_{e,\theta,SC} + P_{p,\theta,SC}) \cdot LA_{\theta,SC} + PF_{\theta,i} \cdot T_0/2 \quad (6.16)$$

$$(6.17)$$

Double contact

$$P_{e,\theta,DCj} = \frac{V_{e,\theta,DCj}}{T_0} \cdot E_\theta \quad (6.18)$$

$$P_{p,\theta,DCj} = \frac{V_{p,\theta,DCj}}{T_0} \cdot r_{p,DCj} \cdot E_\theta \quad (6.19)$$

$$PF_{\theta,DCj} = (P_{e,\theta,DCj} + P_{p,\theta,DCj}) \cdot \mu \quad (6.20)$$

$$M_{\theta,DCj} = (P_{e,\theta,DCj} + P_{p,\theta,DCj}) \cdot LA_{\theta,DCj} + PF_{\theta,DCj} \cdot T_0/2 \quad (6.21)$$

$$M_{\theta,DC} = M_{\theta,DC1} + M_{\theta,DC2} \quad (6.22)$$

$$(6.23)$$

with

$$\frac{1}{E_\alpha} = \frac{\cos^4 \alpha}{E_{22}} + \frac{\sin^4 \alpha}{E_{11}} + \frac{\cos^2 \alpha \cdot \sin^2 \alpha}{A^{2 \cdot A} \cdot G_{12}} \quad (6.24)$$

$$E_\theta = \frac{E_\alpha \cdot E_{33}}{E_{33} \sin^c \theta + E_\alpha \cos^c \theta} \quad (6.25)$$

Here, $P_{e,\theta,i}$, $P_{p,\theta,i}$, $r_{p,i}$, μ , $M_{\theta,i}$ and $LA_{\theta,i}$ are the local elastic force, the plastic local force, the plastic reduction factor, the friction coefficient, the resisting moment and the lever arm from rotation center, respectively. Due to the rotational compression, the young modulus increases slightly with the angle of rotation θ combined to the joint-to-grain angle α . E_α is calculated with the Saliklis formula Eq.(6.24) [SF00] from the elastic modulus E_{11} (parallel to the grain along, $E_{0,mean}$), the elastic modulus E_{22} (perpendicular to grain edgewise, $E_{90,edge,mean}$) and the shear modulus G_{12} (edgewise, $G_{0,edge,mean}$). The coefficient A was established for Kerto-Q at 0.7 by fitting the values (pages 6 & 9) of the VTT certificate [VESL16]. E_θ is then calculated by using the Hankinson formula Eq.(6.25) where E_{33} is the elastic modulus perpendicular to grain flatwise ($E_{90,flat,mean}$) and θ is the rotation angle of the punch during the tests. The coefficient c is set to 1.8 for Kerto-Q by fitting.

For SC and DC, the lever arm $LA_{\theta,i}$ is defined as the distance from the rotation center to the action line of the local forces. The action line is perpendicular to the direct contact surface and pass by the gravity center of the embedded volume, see below the equations which govern the calculation.

$$x_{G,i} = \frac{1}{V_i} \iiint_{V_i} x \cdot dV_i \quad (6.26)$$

$$y_{G,i} = \frac{w_{1,i}}{2} \quad (6.27)$$

$$z_{G,i} = \frac{1}{V_i} \iiint_{V_i} z \cdot dV_i \quad (6.28)$$

$$L_{G,\theta,i} = x_{G,i} \cos \theta + z_{G,i} \sin \theta \quad (6.29)$$

$$LA_{\theta,i} = L_{G,i} - \frac{T_0}{2} \tan \frac{\theta}{2} \quad (6.30)$$

where $(x_{G,i}, y_{G,i}, z_{G,i})$ are the coordinates of the gravity center and $L_{G,\theta,i}$ is defined in Fig.6.12. The analytical formulas of the resisting moments were implemented in Matlab R2015b. They served to fit adequately the decay coefficients $b_{V4,SC}$, the plastic reduction factor $r_{p,\alpha,SC}$ and the yield angle $\theta_{y,\alpha,SC}$ for single contact and $b_{V4,DC}$, $r_{p,\alpha,DC}$, $\theta_{y,\alpha,DC}$ for double contact. $b_{V4,SC}$ and $b_{V4,DC}$ will be expressed as b_{SC} and b_{DC} in what follows.

6.5 Results for single contact

6.5.1 Adjustment of the analytical model

The coefficients b_{SC} , $r_{p,SC}$ and $\theta_{y,SC}$ of the analytical model have been determined by using the *lsqcurvefit* function of Matlab©R2015b and the 50 points *multistart* option to avoid stopping on a local minimum. Fig.6.13 shows an example of the results for $\alpha = 0^\circ$, a friction coefficient $\mu = 0.2$ and $\theta_y = 1.5^\circ$. All the models ($\alpha = 0, 15, 30, 45, 60, 75, 90^\circ$) with $\mu = 0.2$ and $\theta_y = 1.5^\circ$ can

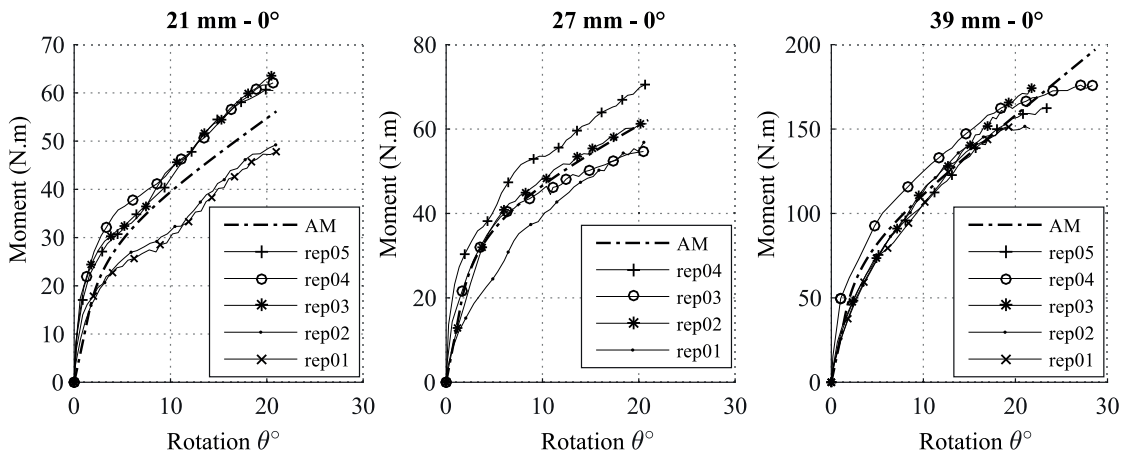


Figure 6.13 – Fit of analytical models parameters at 21,27 and 39mm - $\alpha = 0^\circ$ - $\mu = 0.2$ - $\theta_y = 1.5^\circ$ (SC).

be visualized on Fig.6.14. All the values for SC at different yield angle θ_y between 0.5° and 2.00° are summarized in Table 6.4. After $\theta_y = 2.00^\circ$, the adjusted Rsquare started to decrease significantly for certain joint-to-grain angles α .

6.5. Results for single contact

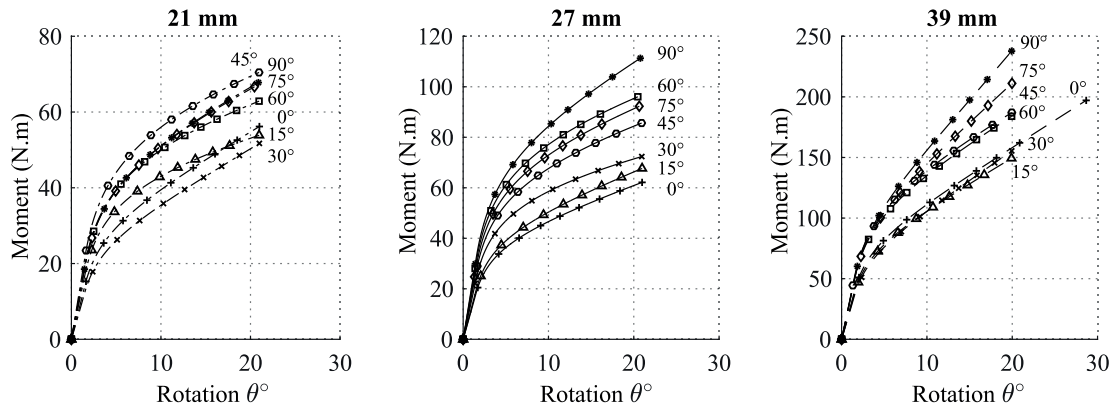


Figure 6.14 – Analytical models at 21,27 and 39mm - $\mu = 0.2$ - $\theta_y = 1.5^\circ$ (SC).

RPC - IVL Kerto-Q Single contact (SC)															
α	21 mm					27 mm					39 mm				
	b	$b \cdot T_0$	r_p	θ_y	adj. R^2	b	$b \cdot T_0$	r_p	θ_y	adj. R^2	b	$b \cdot T_0$	r_p	θ_y	adj. R^2
0°	0.11	2.2	0.05	0.50	0.84	0.10	2.8	0.03	0.50	0.88	0.07	2.7	0.05	0.50	0.96
	0.16	3.4	0.06	1.00	0.83	0.16	4.4	0.04	1.00	0.88	0.11	4.3	0.08	1.00	0.97
	0.21	4.4	0.07	1.50	0.82	0.22	6.0	0.04	1.50	0.88	0.15	5.7	0.09	1.50	0.97
	0.26	5.4	0.08	2.00	0.81	0.29	7.7	0.04	2.00	0.87	0.18	7.2	0.10	2.00	0.97
15°	0.09	1.8	0.01	0.50	0.89	0.10	2.6	0.03	0.50	0.98	0.07	2.9	0.06	0.50	0.98
	0.13	2.8	0.01	1.00	0.88	0.15	4.1	0.04	1.00	0.97	0.12	4.5	0.08	1.00	0.98
	0.17	3.6	0.01	1.50	0.86	0.21	5.6	0.05	1.50	0.96	0.16	6.1	0.09	1.50	0.97
	0.21	4.4	0.01	2.00	0.84	0.26	7.0	0.05	2.00	0.95	0.20	7.7	0.10	2.00	0.96
30°	0.12	2.5	0.06	0.50	0.97	0.08	2.1	0.01	0.50	0.95	0.08	3.0	0.07	0.50	0.98
	0.18	3.9	0.08	1.00	0.96	0.12	3.3	0.01	1.00	0.94	0.12	4.8	0.10	1.00	0.97
	0.24	5.1	0.09	1.50	0.96	0.16	4.4	0.01	1.50	0.92	0.17	6.5	0.12	1.50	0.97
	0.30	6.3	0.10	2.00	0.95	0.20	5.5	0.01	2.00	0.90	0.21	8.2	0.13	2.00	0.96
45°	0.07	1.5	0.01	0.50	0.90	0.07	2.0	0.02	0.50	0.91	0.06	2.2	0.04	0.50	0.93
	0.10	2.2	0.01	1.00	0.90	0.11	3.0	0.02	1.00	0.92	0.08	3.2	0.06	1.00	0.93
	0.13	2.8	0.01	1.50	0.89	0.14	3.8	0.02	1.50	0.92	0.11	4.2	0.06	1.50	0.93
	0.16	3.4	0.01	2.00	0.88	0.17	4.7	0.01	2.00	0.91	0.13	5.0	0.05	2.00	0.93
60°	0.08	1.6	0.01	0.50	0.79	0.07	1.8	0.02	0.50	0.98	0.06	2.2	0.04	0.50	0.93
	0.11	2.4	0.01	1.00	0.78	0.10	2.6	0.02	1.00	0.97	0.09	3.4	0.06	1.00	0.93
	0.15	3.1	0.01	1.50	0.77	0.12	3.3	0.01	1.50	0.96	0.11	4.4	0.06	1.50	0.94
	0.18	3.8	0.01	2.00	0.75	0.15	4.1	0.01	2.00	0.95	0.14	5.3	0.06	2.00	0.94
75°	0.08	1.7	0.03	0.50	0.89	0.07	1.9	0.02	0.50	0.92	0.06	2.3	0.07	0.50	0.97
	0.12	2.5	0.03	1.00	0.90	0.10	2.8	0.02	1.00	0.93	0.09	3.4	0.09	1.00	0.97
	0.15	3.2	0.03	1.50	0.89	0.13	3.5	0.01	1.50	0.94	0.11	4.4	0.10	1.50	0.98
	0.18	3.8	0.02	2.00	0.89	0.16	4.3	0.01	2.00	0.94	0.13	5.2	0.11	2.00	0.98
90°	0.08	1.7	0.03	0.50	0.88	0.06	1.7	0.03	0.50	0.95	0.06	2.3	0.09	0.50	0.94
	0.12	2.5	0.04	1.00	0.88	0.09	2.5	0.03	1.00	0.95	0.09	3.4	0.12	1.00	0.94
	0.15	3.2	0.03	1.50	0.88	0.12	3.2	0.03	1.50	0.94	0.11	4.3	0.14	1.50	0.95
	0.18	3.8	0.02	2.00	0.87	0.14	3.8	0.02	2.00	0.93	0.13	5.1	0.14	2.00	0.95

Table 6.4 – Fitted coefficients from the analytical model (SC).

6.5.2 Additional length profile

Deformation profile - fit functions

In addition, the decay coefficients b_{SC} which characterizes the indirectly loaded area was analyzed by a different way. A fit function based on the Inayama's exponential form [Ina91] was applied to the (x, z) points manually placed on the captured deformation profile as explained by Roche et al. [RGW16] and illustrated at Fig.6.15.

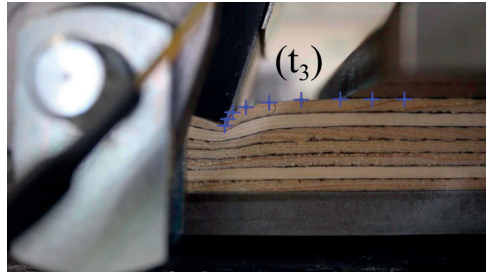


Figure 6.15 – Discretization in points of the captured deformation profile. Roche et al. [RGW16].

The **exponential function** is defined by :

$$z = \delta_{\theta} \cdot e^{-b_{sc} \cdot x} \quad (6.31)$$

where δ_{θ} stands for the amplitude of the deformation at a rotation angle θ and b_{sc} represents the decay coefficients, to be determined for the 3 different joint-thicknesses and 7 joint-to grain angles. The geometry of the additional length profile is illustrated in Fig.6.11. The amplitude of the deformation is calculated as follows :

$$\delta_{\theta} = h1 = L_{\theta} \cdot \sin \theta \quad (6.32)$$

The mean adjusted Rsquare of the exponential fits was 0.89.

Fig.6.16 shows the theoretical strains $\varepsilon = \delta_{\theta} / T_0$ with respect to the joint rotation θ . A strain of 26% at a 25° joint-rotation is observed, which is below the 50% strain where starts the densification of wood in perpendicular compression according to Tanahashi [TSS06a]. But in any case, the experimental deformations are already well beyond the point where the joint will work in an actual building.

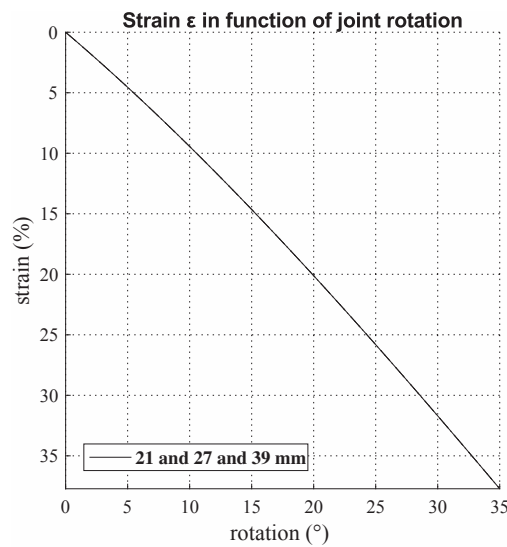


Figure 6.16 – Strain ε evolution with respect to joint-rotation θ (SC).

Comparative analysis

Exponential fit vs experimental results

A comparison was made between the exponential function and the experimental data points on the basis of the 2-dimensional total surface deformation. The total deformation is defined by the surface under the fitting curve (additional length profile, integrated from 0 to 46 mm on the horizontal axis*) in addition to the triangular deformation at the direct contact between SP and LP (See Fig.6.4). Finally, Fig.6.17 shows the error of the exponential function with respect to the experimental data. The error is calculated as follows.

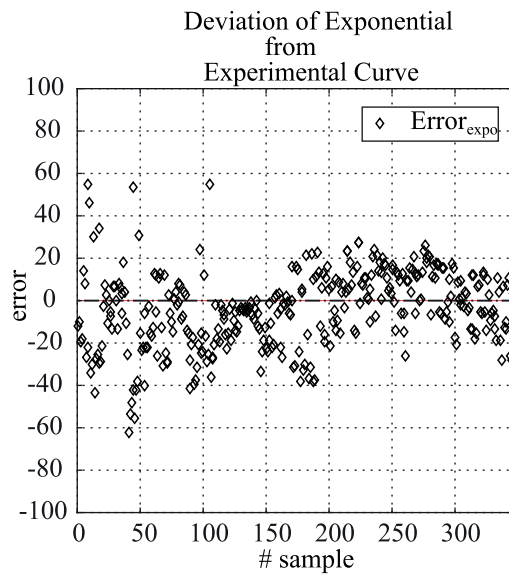


Figure 6.17 – Integral error of exponential curve with respect to experiments (SC).

$$Error_{expo} = \frac{I_{expo} - I_{exp}}{I_{exp}} \quad (6.33)$$

where I_{exp} was computed with the Matlab *trapz* function and the integration from the exponential function is

$$I_{expo} = 0.5 \cdot l_1 \cdot h_1 + \int_0^{46} \delta_\theta \cdot e^{-b_{sc} \cdot x} dx \quad (6.34)$$

Fig.6.18 gives the deviation of the errors and the associated quantiles. The fit tends to minimize the profile section of the embedded volume in most of the cases. Therefore the volume is estimated in a conservative way.

Evolution of decay coefficient during the angular deformation

The sampling method, by placing the points manually on the captured deformation profiles, was applied on each sample at four rotation angles : 8°, 12°, 20° and 25°. It is pointed out that for these four rotations, the plastic deformation is already reached. Below 8°, the deformation

*Data points have been drawn till 46 mm as no significant deformation are visible beyond.

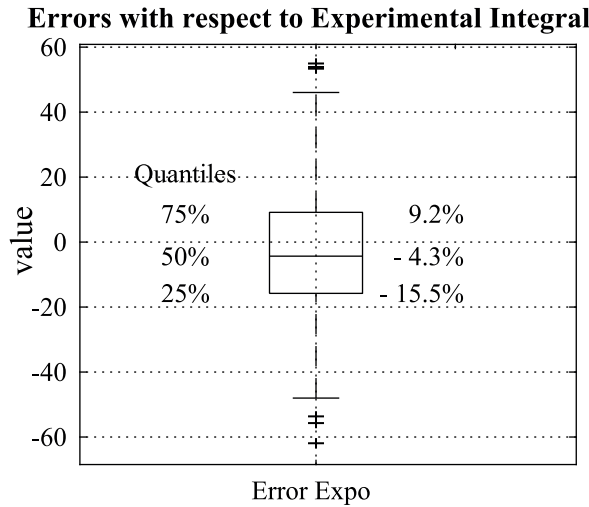


Figure 6.18 – Boxplot of integral error of exponential curve to experimental curve (SC).

is so small that the measurement of the profile can not be processed with accuracy. Moreover, the ratio of additional deformation to triangular deformation is so small that an error on the decay coefficient can be neglected. It is also shown later in the present work that an unique decay coefficient can be retained for any rotation angle $\theta = 8^\circ$ to 25° .

An analysis of the deformation profile was also made with a mean decay coefficient on the four rotation angles, for each joint-to-grain angle and thickness separately. The curves in Fig.6.19 have been drawn and calculated with 2 constant amplitudes δ_{8° at 8° and δ_{20° at 20° using alternately the decay coefficients $b_{SC,8^\circ}$, $b_{SC,12^\circ}$, $b_{SC,20^\circ}$ and $b_{SC,25^\circ}$ fitted at 8° , 12° , 20° and 25° , respectively.

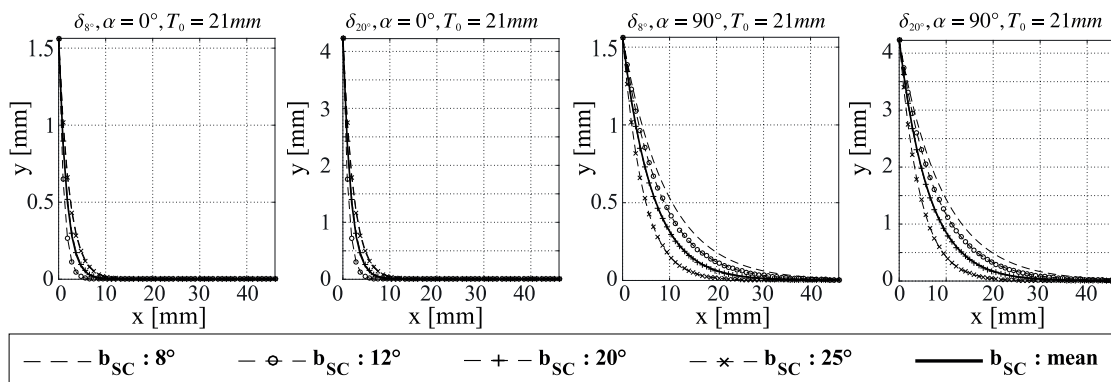


Figure 6.19 – Comparison of integrals for $b_{SC,8^\circ}$, $b_{SC,12^\circ}$, $b_{SC,20^\circ}$, $b_{SC,25^\circ}$ and $b_{SC,mean}$ for $\alpha=0^\circ, 90^\circ$, δ_{8° & δ_{20° and $T_0=21\text{mm}$.

In the mean time, the exponential integrals were recalculated with replacing $b_{SC,8^\circ}$, $b_{SC,12^\circ}$, $b_{SC,20^\circ}$ and $b_{SC,25^\circ}$ by $b_{SC,mean}$ and keeping the same amplitudes δ_{8° , δ_{12° , δ_{20° and δ_{25° . Fig.6.20 and Table 6.5 give the comparison of the initial integrals and those recalculated with $b_{SC,mean}$. Table 6.5 shows that by using an average coefficient $b_{SC,mean}$, the estimated embedded volume tends to be more conservative than using a range of decay coefficients

varying with the rotation angle. The surface under the exponential curve is smaller when the decay coefficient is higher for a same intercept δ_θ . Hence it results in a smaller volume, a smaller stiffness and a smaller stress. Nothing prohibits the use of a regression function to calculate a $b_{SC,\theta}$ as a function of θ but aside from the experimental error, this would not bring added value. So, one decay coefficient for each couple thickness- α angle was finally assumed for both elastic and plastic range.

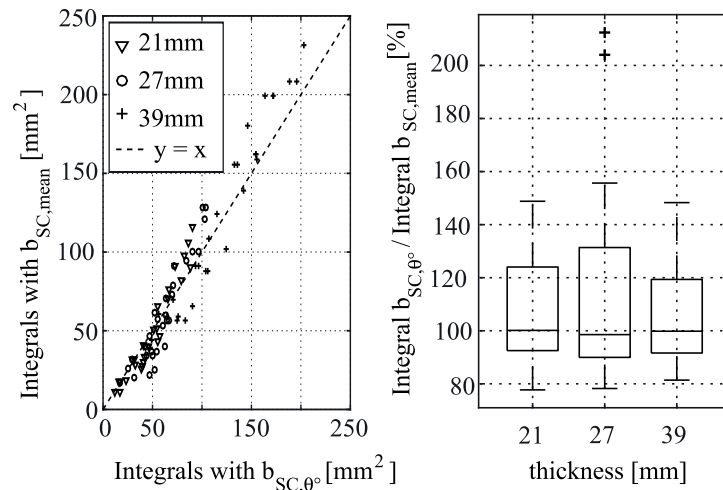


Figure 6.20 – Comparison of integrals for b_{SC,i° and $b_{SC,mean}$ for all samples.

Thickness	Integral dispersion [%] - quantiles		
	25%	50%	75%
21mm	93	100	124
27mm	90	99	131
39mm	92	100	119

Table 6.5 – Quantiles of boxplot in Fig.6.20.

Limitations of fitting the additional length profile

As shown in Table 6.6, the obtained decay coefficients obtained by a physical measurement differ from the ones of the analytical model. Different reasons could explain it. The additional length profile was measured on a top surface and it's worth noting as many authors mentioned it that the deformation propagates also through the depth of the samples. In our case, about half of the layers were impacted in the three different tested thicknesses (see Fig.6.21 where $\theta \approx 25^\circ$). At the same time, for certain α directions and in particular 0° and 45° , surface cracks developed very early at the beginning of deformation. This could significantly influence the stress distribution and how the volume of material ultimately deforms. Additionally, the layered arrangement of Kerto-Q beside solid wood seemed to impact on the irregularity of surface deformation. Obviously, like any other material characterization, the number

α	Decay Coefficients- Exponential		
	21 mm	27 mm	39 mm
0°	0.61	0.35	0.20
15°	0.07	0.09	0.11
30°	0.09	0.26	0.11
45°	0.58	0.90	0.33
60°	0.06	0.18	0.10
75°	0.08	0.09	0.08
90°	0.16	0.10	0.10

Table 6.6 – Exponential Decay Coefficients b_{SC} for all joint configurations.

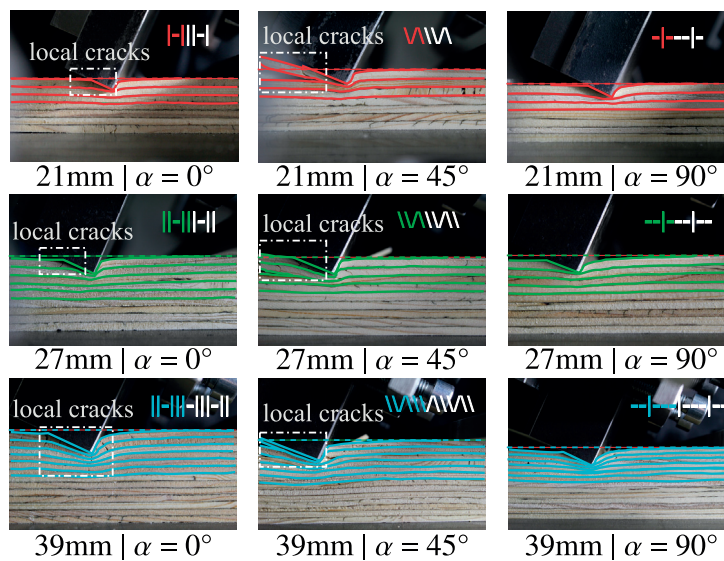


Figure 6.21 – The most stressed layers along the depth in SC, row : $T_0 = 21\text{ mm} \rightarrow 27\text{ mm} \rightarrow 39\text{ mm}$, column : $\alpha = 0^\circ \rightarrow 45^\circ \rightarrow 90^\circ$.

of replicates should be maximized. The model actually reflects a global behavior of the deformation whereas a fit of the contact surface rather reflects a local behavior. For the rest of the study in SC, the model results from Table 6.4 have been considered.

Influence of α , T_0 and θ_y on b_{SC}

Based on the results of the analytical model, the behavior of Kerto-Q panels in RPC was compared with previous Japanese works and their assumptions on the decay coefficients. Inayama [Ina91, Ina93] in 1991, Tanahashi [TSS06a, TSS06b, TSH⁺08, TOS08] in 2006-2008 and Kitamori [KMKK09] in 2009, proposed values for the product $b \cdot T_0$ of the decay coefficient b and the specimen thickness T_0 . In SC, their assumptions were as follows :

- (a) at 90° joint to grain orientation in TPC

$$b \cdot T_0 = 1.5 \text{ (Inayama),}$$

$$b \cdot T_0 = 3.0 \text{ (Tanahashi),}$$

$$b \cdot T_0 = 2.5 \text{ (Kitamori),}$$

(b) at 0° joint to grain orientation in TPC

$$b \cdot T_0 = 1.5n \text{ (Inayama),}$$

$$b \cdot T_0 = 9.0 \text{ (Tanahashi),}$$

(c) at 90° joint to grain orientation in RPC

$$b \cdot T_0 = 1.5 \text{ (Inayama),}$$

$$b \cdot T_0 = 3.0 \text{ (Kitamori),}$$

(d) at 0° joint to grain orientation in RPC

$$b \cdot T_0 = 1.5n \text{ (Inayama).}$$

In Table 6.4 are given the values $b \cdot T_0$ at different yield angles, for 7 joint-to-grain orientations. Like the mentioned authors did, we observe a larger value at $\alpha = 0^\circ$ than at $\alpha = 90^\circ$. The difference is less significant, as the evolution of the elastic modulus with α and θ was included in the proposed model. In Japan, they usually consider a elastic modulus perpendicular to the grain fixed at $E_{\perp} = E_{\parallel} / 20 \sim 50$. A simplified explanation is presented in Fig.6.22. As shown roughly, at joint-to-grain $\alpha = 0^\circ$, a landslide effect (the elastically connected “pipe rows” work more like being in series) caused a more pronounced slope break which lead to a higher decay coefficient of the resulting exponential profile. At joint-to-grain $\alpha = 90^\circ$, It is more a spreading effect diffused along “pipe rows” in parallel, which have larger shear and bending strength and stiffness. Hence the slope is gentler and the decay coefficient is smaller. At intermediate α angles, the behavior is in between both state.

Fig.6.14 and 6.4 show the evolution of the RPC behavior with α . The moment increases and the decay coefficient decreases slightly from 0°to 90°. For 27mm and 39 mm, three groups can be observed : (0°,15°,30°), (45°,60°,75°) and (90°). For 21mm where the percentage of cross-layer is the largest one (+32%), $\alpha = 45^\circ$ marked a particular behavior with a better strength than 90°.

For θ_y varying from 0.50°to 2.00°, b_{SC} is growing by a multiplier factor between 2.2 and 2.9. This factor is a little bit higher for the group (0°,15°,30°) than for the group (45°,60°,75°, 90°).

For the different thicknesses, the ratios $\frac{b_{39mm} \cdot 39}{b_{21mm} \cdot 21}$, $\frac{b_{39mm} \cdot 39}{b_{27mm} \cdot 27}$ and $\frac{b_{27mm} \cdot 27}{b_{21mm} \cdot 21}$ are never superior to the ratios between the different proposals of Inayama, Tanahashi and Kitamori. For instance, at $\alpha = 15^\circ$ and $\theta_y = 2.00^\circ$, the maximum $\frac{b_{39mm} \cdot 39}{b_{21mm} \cdot 21} = 1.75$ is inferior to $\frac{b \cdot T_0(\text{Kitamori})}{b \cdot T_0(\text{Inayama})} = 2$.

From the moment-rotation curves of Fig.6.14,obtained by applying the analytical model to SC, it can be observed that, for a same α joint-to-grain angle, the resisting moment increased with the thickness. It confirms the work from Van der Put [dP08] where bearing strength

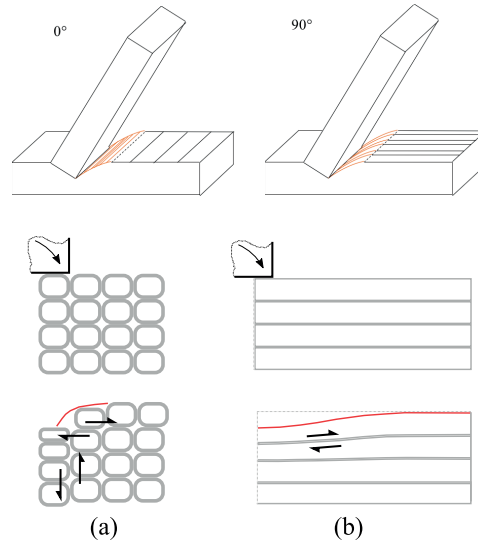


Figure 6.22 – Influence of α on the resisting moment : (a) $\alpha = 0^\circ$ and (b) $\alpha = 90^\circ$.

perpendicular to wood increased with the depth of the beam (or thickness of the panel in our case).

Globally, the behavior of Kerto-Q panel is similar in tendency to the previous Japanese works. Obviously, as the material is different in species and constitution (LVL Vs solid wood), the decay coefficients are different.

6.6 Results for double contact

The analysis described in previous sections was also done for rotational partial compression in double contact (DC).

6.6.1 Adjustment of the analytical model

Fig.6.23 shows the fit results of the analytical model for $\alpha = 0^\circ$ with a friction coefficient $\mu = 0.2$ and a yield angle $\theta_y = 1.5^\circ$. All the models (DC, $\alpha = 0, 15, 30, 45, 60, 75, 90^\circ$) with $\mu = 0.2$ and $\theta_y = 1.5^\circ$ can be seen on Fig.6.24. The RPC behavior for DC is gathered in Table 6.7. The range of θ_y was, this time, from 0.50 to 3.00° .

6.6.2 Additional length profile

The same method as in section 6.5.2 was applied to determine the decay coefficients for DC volume deformation. However, the deformation reached a smaller amplitude than in SC and the analysis was not precise enough to give accurate results. Further experiments should be done, with more replicates and an improved setup, to tend to converging values. The tests were only performed from $\alpha = 0^\circ, 45^\circ$ and 90° as tests in single contact shown a slight evolution at intermediate angles. The results are given for information in Table 6.8.

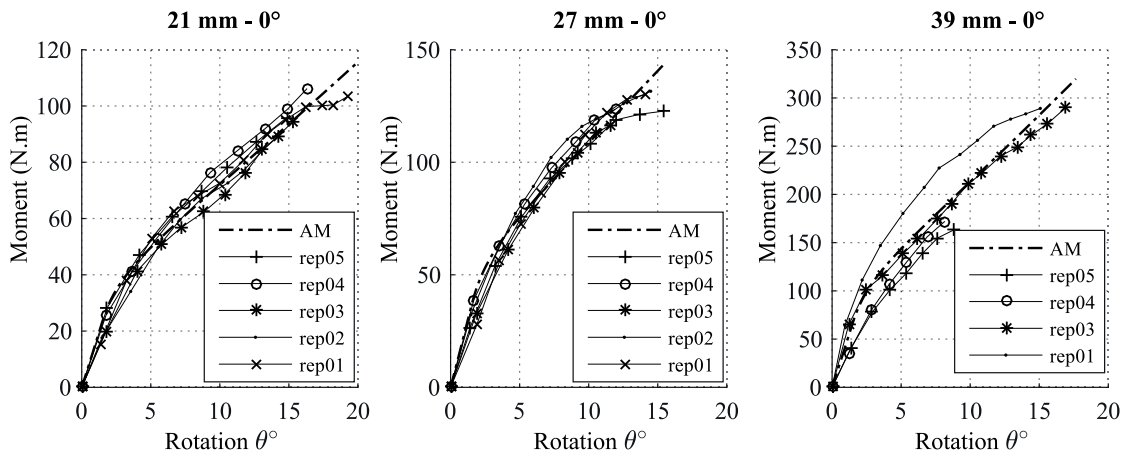


Figure 6.23 – Fit of analytical models parameters at 21,27 and 39mm - $\alpha = 0^\circ$ - $\mu = 0.2$ - $\theta_y = 1.5^\circ$ (DC).

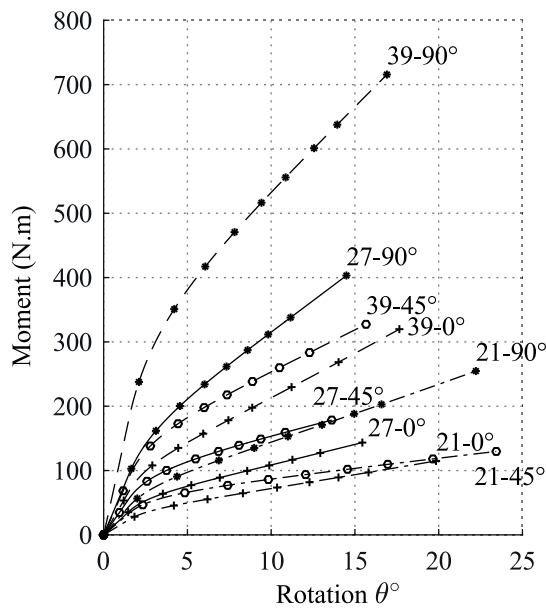


Figure 6.24 – Analytical models at 21,27 and 39mm - $\mu = 0.2$ - $\theta_y = 1.5^\circ$ (DC).

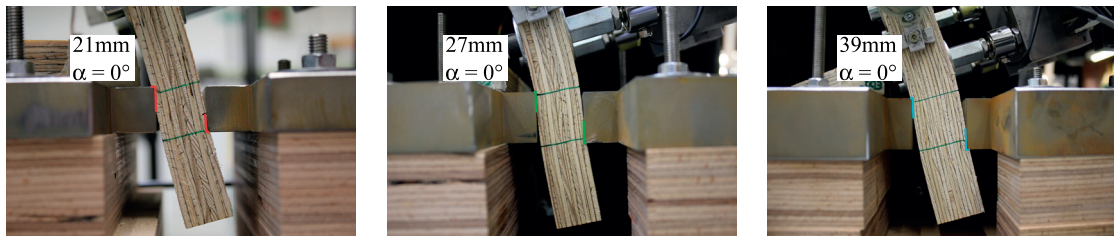


Figure 6.25 – Capture of local deformations at the contact zones in DC with $\theta = 15^\circ$.

Comparative analysis

Limitations of fitting the additional length profile

Chapter 6. Material characterization of spruce LVL in rotational partial compression

RPC - LVL Kerto-Q Double contact (DC)															
α	21 mm					27 mm					39 mm				
	b	$b \cdot T_0$	r_p	θ_y	adj. R^2	b	$b \cdot T_0$	r_p	θ_y	adj. R^2	b	$b \cdot T_0$	r_p	θ_y	adj. R^2
0°	0.37	7.8	0.11	0.50	0.97	0.34	9.1	0.11	0.50	0.95	0.31	11.9	0.14	0.50	0.92
	0.82	17.3	0.16	1.00	0.98	0.80	21.7	0.16	1.00	0.96	0.96	37.3	0.20	1.00	0.93
	1.72	36.1	0.19	1.50	0.98	1.93	52.2	0.19	1.50	0.97	4.00*	> 4T ₀	0.19	1.50	0.92
	4.00*	> 4T ₀	0.20	2.00	0.98	4.00*	> 4T ₀	0.16	2.00	0.98	4.00*	> 4T ₀	0.15	2.00	0.90
	4.00*	> 4T ₀	0.14	2.50	0.97	4.00*	> 4T ₀	0.07	2.50	0.95	4.00*	> 4T ₀	0.07	2.50	0.84
	4.00*	> 4T ₀	0.06	3.00	0.93	4.00*	> 4T ₀	0.01	3.00	0.88	4.00*	> 4T ₀	0.01	3.00	0.73
45°	0.22	4.6	0.05	0.50	0.87	0.19	5.0	0.08	0.50	0.96	0.18	6.9	0.09	0.50	0.90
	0.40	8.4	0.07	1.00	0.88	0.32	8.7	0.11	1.00	0.97	0.36	14.1	0.13	1.00	0.91
	0.63	13.1	0.08	1.50	0.89	0.47	12.8	0.11	1.50	0.97	0.66	25.6	0.15	1.50	0.91
	0.93	19.6	0.09	2.00	0.90	0.66	17.7	0.10	2.00	0.97	1.24	48.3	0.15	2.00	0.91
	1.39	29.3	0.09	2.50	0.91	0.88	23.8	0.07	2.50	0.97	3.00	116.9	0.15	2.50	0.90
	2.16	45.3	0.09	3.00	0.91	1.18	31.9	0.03	3.00	0.96	4.00*	> 4T ₀	0.07	3.00	0.89
90°	0.18	3.7	0.12	0.50	0.87	0.11	3.0	0.14	0.50	0.95	0.08	3.1	0.09	0.50	0.95
	0.28	6.0	0.17	1.00	0.87	0.16	4.4	0.18	1.00	0.96	0.12	4.8	0.11	1.00	0.95
	0.38	8.0	0.19	1.50	0.88	0.21	5.6	0.20	1.50	0.96	0.16	6.3	0.12	1.50	0.96
	0.48	10.0	0.21	2.00	0.88	0.24	6.6	0.19	2.00	0.97	0.20	7.7	0.12	2.00	0.96
	0.58	12.1	0.22	2.50	0.88	0.28	7.5	0.17	2.50	0.97	0.23	9.2	0.11	2.50	0.97
	0.68	14.2	0.21	3.00	0.89	0.31	8.3	0.14	3.00	0.97	0.27	10.6	0.10	3.00	0.97

* 4.00 means almost no additional length.

Table 6.7 – Fitted coefficients from the analytical model (DC).

α	Decay Coefficients - Exponential		
	21 mm	27 mm	39 mm
0°	0.70	2.06	2.72
45°	0.73	NA	1.6
90°	0.59	1.13	0.61

Table 6.8 – Decay Coefficients of exponential fit for all joint configurations (DC).

The results of additional length profile fits in DC were influenced by side effects when testing a through connection. The setup was designed this time to rotate the sample instead of moving the steel punch like in SC. The side effects are summarized hereafter.

SE1 In addition to the double embedment effect within the joint, the rotated LP is subjected to a significant bending during testing. Fig.6.26 shows the resulting additional rotation due to this bending. The experimental curves were corrected with subtracting the angle due to bending and then modeling as described in section 6.4. This theoretical correction of the bending effect could reduce the model accuracy of the actual behavior of the joint.

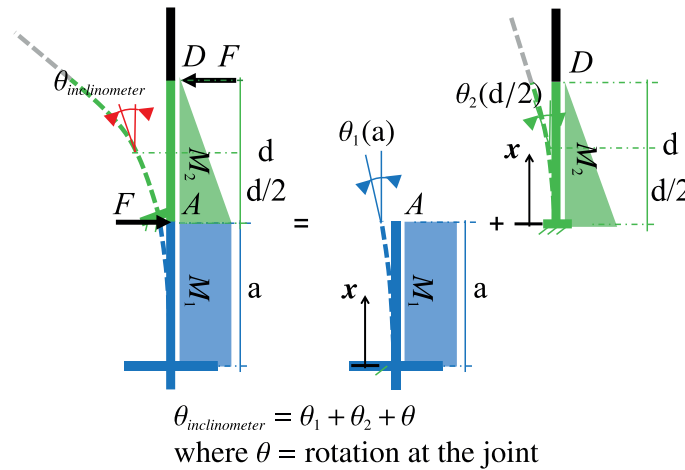


Figure 6.26 – Actual angle measured by inclinometers in DC.

The corrections was done with considering the moment diagrams of Fig.6.26. The rotation angle at the joint θ was calculated as $\theta = \theta_{inclinometer} - \theta_{bending}$, where :

$$\begin{aligned}
 \theta_{bending} &= \theta_1 + \theta_2 \\
 &= \frac{F \cdot d \cdot a}{E \cdot I} + \frac{3 \cdot F \cdot d^2}{8 \cdot E \cdot I}
 \end{aligned} \tag{6.35}$$

with E , the bending stiffness of the panel varying with the joint-to-grain angle, and $I = (W_0 \cdot T_0^3)/12$, the bending inertia of the panel. W_0 and T_0 are the width and the thickness of LP, respectively.

SE2 As soon as the embedment effect started at the double contact within the joint, the wood layers were compressed and locally densified increasingly as the local forces increased. The joint became rather rigid compare with the bending stiffness of the panel. Finally, the panel failed by bending before any failure occurred at the joint place (See Fig.6.27). The final deformation δ_θ is lower than for SC and the exponential-root profile reading is less precisely interpretable. The setup could be improved by for instance fixing LP and rotating SP like in single contact. But is quite challenging as the punch should be settable to the thickness of the sample and rigid at the same time. The Kert-Q sample should also be supported as close as possible of the contact zones without limiting the rotation. In any case, the skewing of the part between the two contact zones will stand.

SE3 Torsion appears on joint with $\alpha = 45^\circ$ as shown in Fig.6.27 (right). It caused the rotation and moment records to be slightly different to the reality. The error is reduced by taking an average value of the 2 inclinometers values.

Influence of α , T_0 and θ_y on b_{SC}

In DC, the Japanese researchers provided the following values for $b_{DC} \cdot T_0$:

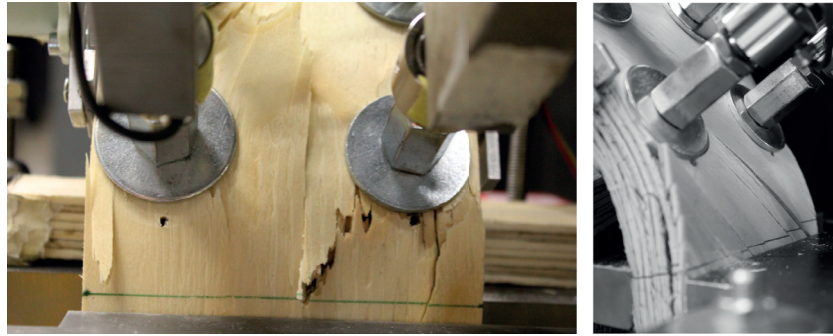


Figure 6.27 – Failure (left) and Torsion (right) in the panel.

at 90° joint to grain orientation in RPC

$$b \cdot T_0 = 4.0 \text{ (Tanahashi),}$$

$$b \cdot T_0 = 5.5 \text{ (Kitamori).}$$

As they concluded, the results of Table 6.7 show a higher value for the decay coefficients in DC than in SC. The additional length has much less effect in DC than in SC. Similarly, larger values are obtained at $\alpha = 0^\circ$ than at $\alpha = 90^\circ$.

The best compromise to maximize the overall adjusted Rsquares is found at $\theta_y = 1.50 \dots 2.00^\circ$. As the decay coefficients are much higher than in SC, the value of θ_y has a bigger influence on the values of b_{DC} . For θ_y varying from 0.50° to 2.00°, the multiplier factor of b_{DC} is up to 13 with limiting the decay coefficient to 4.00.

In DC, the moment is significantly higher at $\alpha = 90^\circ$ for all thicknesses. For $\alpha = 0^\circ$ and 45° , the curves are quite close. Even if the bending effect was theoretically removed, It could still partially noise the results and overestimate the data.

6.7 Conclusion

In the context of multiple-tab-and-slot joint submitted to bending, the embedment effect of LVL Kerto-Q in rotational partial compression (RPC) is the key point to define the rotational stiffness of through tenon variant. This work gave a model to obtain the decay coefficient in a range of yield angles for LVL-spruce panels in RPC. Different values were provided both in single contact and double contact for 21, 27, 39mm thicknesses and 0°, 15°, 30°, 45°, 60°, 75°, 90° joint-to-grain angles. The decay coefficients is larger at 0° than at 90° like Japanese researchers mentioned in their study. These decay coefficients are also increasing drastically from single contact to double contact conditions. Higher is the decay coefficient, lower is the influence of the additional length on the total deformed volume. Like any other material properties, the presented values should be refined with testing more replicates. Especially for the double contact, the setup should be improved to remove or at least reduce the bending effect in the LVL panel. However, the results are very encouraging and can now be used in an analytical model of the moment-rotation relationship of the trough-tenon variant of the multiple tab-and-slot joint.

Outcomes ④

From the experiments in rotational partial compression perpendicular to the panel plane in single and double contact, with three different thicknesses and up to seven joint-to-grain angles of LVL Kerto-Q, the most important outcomes are the following :

The decay coefficients in single (b_{SC}) and double (b_{DC}) contact were provided as a range depending on the yield angles θ_y .

b_{SC} was smaller than b_{DC} meaning that the additional length effect increases in SC.

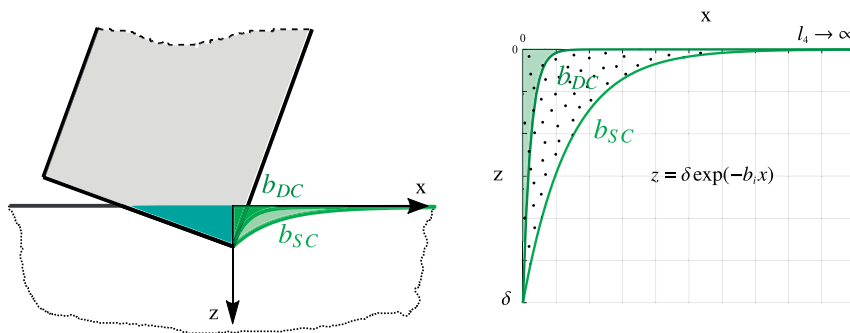


Figure 6.28 – Increase of the additional length effect from double contact to single contact.

b_{90° was smaller than b_{0° meaning that the additional length effect increases when $\alpha \rightarrow 90^\circ$.

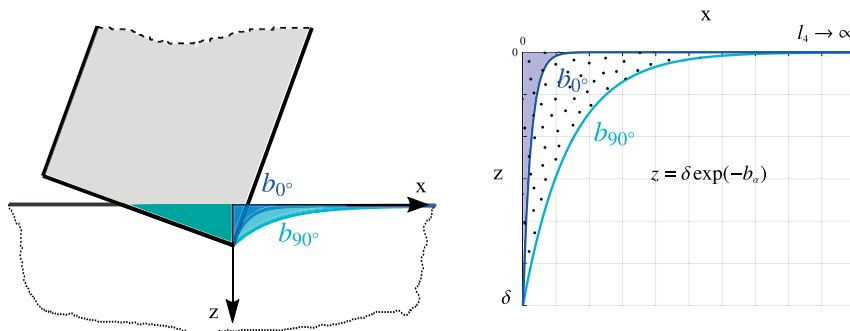


Figure 6.29 – Increase of the additional length effect ffrom $\alpha = 0^\circ$ to $\alpha = 90^\circ$.

For 27mm & 39mm thick panels, one $b_{SC} = f(\alpha)$ for each of the 3 following groups could be considered : $(0^\circ, 15^\circ, 30^\circ)$, $(45^\circ, 60^\circ, 75^\circ)$, (90°) .

21mm thick panel at $\alpha = 45^\circ$ shown highest strength than for other angles α .

The number of replicates (5) of each sample could be increased for more accurate material characterization.

Chapter 6. Material characterization of spruce LVL in rotational partial compression

The simplified analytical model used to obtain the decay coefficients and the yield angles has to be developed in a generalized form for the whole joint.

→ **Objective ⑤** (see chapter 7)

References

- [20004] CEN-EN789:2004 *Timber Structures, Test Methods, Determination of Mechanical Properties of Wood Based Panels*. European Committee for Standardization (CEN), Brussels, 2004.
- [20112] CEN-EN408:2010+A1:2012 *Timber Structures, Structural Timber and Glued Laminated Timber, Determination of Some Physical and Mechanical Properties*. European Committee for Standardization (CEN), Brussels, 2012.
- [AIJ10] AIJ. *Fundamental Theory of Timber Engineering, 1st edn*. Architectural Institute of Japan (AIJ), Maruzen, Tokyo, Japan, 2010. (in Japanese).
- [BG04] H. J. Blass and R. Gortlacher. Compression perpendicular to the grain. In *8th World Conference of Timber Engineering, Helsinki, Finland*. Proceedings WCTE 2004, 2004.
- [BS11] H. J. Blass and Patrick Schädle. Ductility aspects of reinforced and non-reinforced timber joints. *Engineering Structures*, 33(11):3018–3026, 2011.
- [dP90] T. A. C. M. Van der Put. Tension perpendicular at notches and joints. In *CIB-W18 paper 23-10-1, Lisboa*, 1990.
- [dP08] T. A. C. M. Van der Put. Derivation of the bearing strength perpendicular to the grain of locally loaded timber blocks. *Holz als Roh und Werkstoff*, 66(6):409–417, 2008.
- [dP12] T. A. C. M. Van der Put. Restoration of exact design for partial compression perpendicular to the grain. *Wood Material Science & Engineering*, 7(4):225–236, 2012.
- [fSC08] European Committee for Standardization (CEN). *CEN-EN1995-1-1:2005+A1 - Eurocode 5: Design of timber structures - Part 1-1: General - Common rules and rules for buildings*. (CEN), Brussels, 2008.
- [Ina91] M. Inayama. *Wooden Embedment Theory and its Application*. PhD thesis, The University of Tokyo, Tokyo, Japan, 1991. (in Japanese).
- [Ina93] M. Inayama. Study on compression perpendicular to the grain in wood, part 4: analytic functions for the relation between compression load and elastic deformation perpendicular to the grain in wood. In *Proceedings of AIJ, Tokyo, Japan*, pages 907–908, 1993. (in Japanese).
- [JF11] André Jorissen and Massimo Fragiocomo. General notes on ductility in timber structures. *Engineering Structures*, 33(11):2987–2997, 2011.
- [KMKK09] A. Kitamori, T. Mori, Y. Kataoka, and K. KOMATSU. Effect of additional length on partial compression perpendicular to the grain of wood. *Journal of Structural and Construction Engineering (Transactions of AIJ)*, 74(642):1477–1485, 2009.

Chapter 6. Material characterization of spruce LVL in rotational partial compression

- [Lei16] A. J. M. Leijten. The bearing strength capacity perpendicular to grain of norway spruce – evaluation of three structural timber design models. *Construction and Building Materials*, 105:528 – 535, 2016.
- [LJdL12] A.J.M. Leijten, A.J.M. Jorissen, and B.J.C. de Leijer. The local bearing capacity perpendicular to grain of structural timber elements. *Construction and Building Materials*, 27(1):54–59, 2012.
- [LLdP10] A.J.M. Leijten, H.J. Larsen, and T.A.C.M. Van der Put. Structural design for compression strength perpendicular to the grain of timber beams. *Construction and Building Materials*, 24(3):252–257, 2010.
- [LPB⁺15] D. Lathuilliere, O. Pop, L. Bléron, F. Dubois, F.Fouchal, and J. F. Bocquet. Spreading of transverse compressive stresses in glued laminated timber. *European Journal of Wood and Wood Products*, 73(4):475–484, 2015.
- [MHH82] B. Madsen, R. F. Hooley, and C. P. Hall. A design method for bearing stresses in wood. *Canadian Journal of Civil Engineering*, 9(2):338–349, 1982.
- [nSMQ08] W. Mu noz, A. Salenikovich, M. Mohammad, and P. Quenneville. Determination of yield point and ductility of timber assemblies: in search for a harmonised approach. In *World Conference on Timber Engineering, Miyazaki, Japan*. Proceedings WCTE 2008, 2008.
- [OSY15] K. Ogawa, Y. Sasaki, and M. Yamasaki. Theoretical modeling and experimental study of japanese “watari-ago” joints. *Journal of Wood Science*, 61(5):481–491, 2015.
- [RGW16] S. Roche, J. Gamarro, and Yves Weinand. Multiple tab-and-slot joint : Improvement of the rotational stiffness for the connection of thin structural wood panels. In *World Conference on Timber Engineering, Vienna, Austria*. Proceedings WCTE 2016, 2016.
- [SF00] E. P. Saliklis and R. H. Falk. Correlating off-axis tension tests to shear modulus of wood-based panels. *Journal of Structural Engineering*, 126(5):621–625, 2000.
- [TOS08] H. Tanahashi, M. Okamura, and Y. Suzuki. Performances of wooden ladder-type frames for seismic reinforcement of traditional timber structures. In *14th World Conference on Earthquake Engineering, Beijing, China*, 2008.
- [TSH⁺08] H. Tanahashi, H. Shimizu, H. Horie, P. Yang, and Y. Suzuki. Elastic embedded displacements of orthotropic wood with a finite length based on pasternak model. *Journal of Structural and Construction Engineering (Transactions of AIJ)*, 73(625):417–424, 2008. (in Japanese).
- [TSS06a] H. Tanahashi, H. Shimizu, and Y. Suzuki. Elastic surface displacements of orthotropic wood due to partial compression based on pasternak model. *Journal of*

- Structural and Construction Engineering (Transactions of AIJ)*, (609):129–136, 2006. (in Japanese).
- [TSS06b] H. Tanahashi, H. Shimizu, and Y. Suzuki. Formulation of elasto-plastic moment-resisting performance of timber connections using pasternak model. In *World Conference on Timber Engineering, Portland, USA*. Proceedings WCTE 2006, 2006.
- [VESL16] Finland VTT Expert Services Ltd. *Kerto-VTT-C-184-03-Certificate:2016 Kerto-S and Kerto-Q Structural Laminated Veneer Lumber, Certificate NO.184/03*. 2004, Updated 17.5.2016.

7 Semi-rigid Moment-resisting Model of the Through Tenon variant of Multiple Tab-and-Slot Joint for LVL panels

Abstract

The mechanical behavior of the through tenon variant of multiple tab-and-slot joints (MTSJ-TT), a wood-to-wood angular connection for thin LVL panels, demonstrated its ability to transfer efficiently bending with a semi-rigid behavior. A total of seventeen different geometries were theoretically modeled and tested with a “pure bending setup”. The nonlinear model was based on the embedment theory from Japan. Local forces, which counterbalance the moment about the joint axis, were obtained from the Hook’s law, the expression of the embedded volumes and a plastic reduction factor. The study highlighted the influence of certain geometric parameters on the stiffness of the MTSJ. This simplified model fitted rather well the experimental data and it is promising for further work.

Keywords Embedment, Semi-rigidity, LVL, Through tenon, Multiple tab-and-slot joint, Analytical model.

Objective ⑤

Provide a non linear moment-resisting model of the MTSJ TT-variant

Chapter 7. Semi-rigid Moment-resisting Model of the Through Tenon variant of Multiple Tab-and-Slot Joint for LVL panels

7.1 Introduction

Zoetemeijer [Zoe83] introduced the component method (CM) principles in the 80s. Ten years later the method was part of the annex J of European Prestandard Eurocode 3 for the beam-to-column connections in design of steel structures [fSC92]. In 2005, it was finally accepted to the European standard Eurocode 3 [fSC05]. The whole joint is split into individual basic components as in finite elements analysis for a structure. Every different components are described by a load-slip responses which deliver strength and stiffness. Then, the components are assembled as a set of serial and/or parallel springs and the external loads are distributed within joint with respect of the relative stiffness and the strength capacity of each component. The CM was applied to traditional timber joint at the very end of the 1990s. Drdácý et al. [DWM99] considered a model employed for soil-foundation interaction, the deformation of a rigid plate resting on a linear elastic half-plane, to express the component stiffness of wood in compression. They simplified a halved joint into an equivalent spring model and introduced the response in the structural analysis of a historical timber frame. Descamps et al. [DG09, DL09, DN09] refined the same component model to overcome the limit of the assumption of an infinite half-space with addition of cut factors on the Young's modulus.

Even if the term of CM is not used by the Asiatic researchers, the way they mechanically analyze their traditional Nuki joint is very similar. Suggested by the work from Inayama [Ina91, Ina93], The architectural institute of Japan (AIJ) published in 2010, the fundamental theory of timber engineering. Written in Japanese, it included the principle of wood embedment which characterize the elastic deformation of wood under partial compression. The surface displacement of wood under a rigid plate uniformly loaded comprises a vertical component beneath the plate and an additional part which spreads beyond. The profile of this additional part is an exponential function with a decay coefficient set at 1.5 divided by the initial depth of the compressed beam. In the Nuki joint, when external loads cause a moment, the rotation of a beam, which penetrates through a column mortise, is counterbalanced by two components diagonally opposed. The induced reaction forces are governed by the wood embedment theory. Design formulas for stiffness and yield points of crosspiece joints are provided as well. Many researchers from Japan and Taiwan highlighted the performance of a such joint in the ductile behavior of ancestral structures submitted to typhoons and earthquakes. The moment-rotation relationship and the rotational stiffness were addressed with more or less complexity. Chang et al. [CHK06, CH07] just defined the embeded volume with a triangular distribution of stresses without additional length. Using the Hankinson' formula [Han21], they correct the young modulus of wood perpendicular to grain with respect to the rotation angle. Sakata et al. [SYO12] added a indirectly deformed part which linearly vanish to 0 at half the contact length. Komatsu et al. [KKJM09] extended the AIJ model to the plastic range with considering the ratio of rotation angle to yield angle. Again with the same base model, Ogawa et al. [OSY15] proposed for the Watari-ago joint a practical decomposition of the three dimensional rotational embeded volume into elastic and plastic part. The non linear expression of the resisting moment included a reduction factor to penalize the young modulus after the yield point. Like European researchers, Tanahashi et al. took inspiration

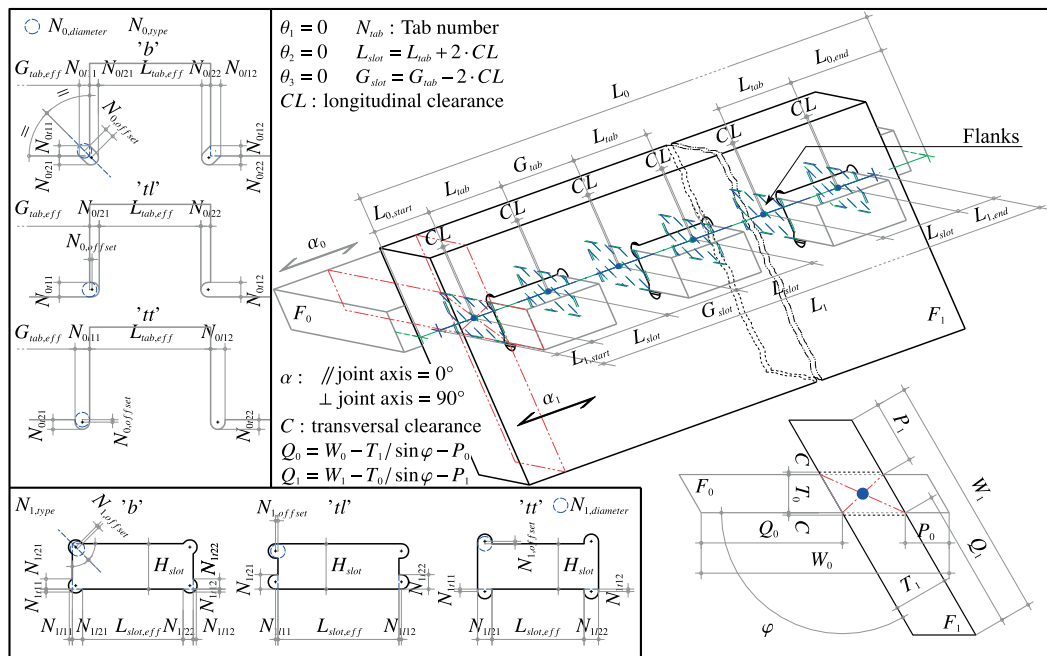
7.2. Geometry of the multiple tab-and-slot joint with through tenon

from soil mechanics and adapted their elasto-plastic Pasternak model to the moment-rotation formulation of several traditional timber joints [TS11, TSS12, TS15].

The model presented hereafter adapts the different Japanese developments of the embedment theory to the behavior of the multiple tab-and-slot joint (MTSJ). MTSJ is also a wood-to-wood crosspiece joint for which the preliminary experiments has shown that it behaves similarly to Nuki joints.

7.2 Geometry of the multiple tab-and-slot joint with through tenon

The general geometry of the through tenon variant of a multiple tab-and-slot joint is shown in Fig.7.1.



<p>Repl. : Number of tested replicates</p> <p>$\theta_1, \theta_2, \theta_3$: The Bryant's angles ($^\circ$)</p> <p>φ : Dihedral angle (angle between panels, $^\circ$)</p> <p>L_{tab} : Tab length (mm)</p> <p>G_{tab} : Gap between tabs in F_0-panel (mm)</p> <p>N_{tab} : Number of tabs</p> <p>CL : Longitudinal clearance (mm)</p> <p>C : Transverse clearance (mm)</p> <p>L_{slot} : Slot length (mm)</p> <p>G_{slot} : Gap between slots in F_1-panel (mm)</p> <p>H_{slot} : Slot height (mm)</p>	<p>$L_{j,start}$: Start length to the 1st tab/slot of F_j-panel (mm)</p> <p>$L_{j,end}$: End length from the last tab/slot of F_j-panel (mm)</p> <p>L_j : Total length of F_j-panel (mm)</p> <p>W_j : Total width of F_j-panel (mm)</p> <p>T_j : Thickness of F_j-panel (mm)</p> <p>P_j : Tab/Slot protrusion(end length) of F_j-panel (mm)</p> <p>Q_j : Panel side end length of F_j-panel (mm)</p> <p>α_j : joint-to-grain angle of F_j-panel ($^\circ$)</p> <p>$N_{j,diameter}$: Notch diameter of F_j-panel (mm)</p> <p>$N_{j,offset}$: Notch offset of F_j-panel (mm)</p> <p>$N_{j,type}$: Notch type of F_j-panel, "b" bisector, "tl" tangent offset along, "tt" tangent offset across</p>
--------------------------------------------------------------------------------------------------------------------------------------------------------------------------------------------------------------------------------------------------------------------------------------------------------------------------------------------------------------------------------------------------------------------------------------------------------------------------------------------------------------------------------------------------------------------------------------------------------------------------------------------------------------------------------------------------	----------------------------------------------------------------------------------------------------------------------------------------------------------------------------------------------------------------------------------------------------------------------------------------------------------------------------------------------------------------------------------------------------------------------------------------------------------------------------------------------------------------------------------------------------------------------------------------------------------------------------------------------------------------------------------------------------------------------------------------------------------------------------------------------------------------------------------------------------------------------------------------------------------------------------------------------------------------------------------------------------------------------

Figure 7.1 – MTSJ-TT geometry and parameters.

Tables 7.1, 7.2 and 7.3 summarizes the parameters values of $17 \times 3 \sim 6$ replicates of different geometries which serve later to compare the proposed model with experimental results.

Chapter 7. Semi-rigid Moment-resisting Model of the Through Tenon variant of Multiple Tab-and-Slot Joint for LVL panels

Label	Repl.	θ_1	θ_2	θ_3	φ	N_{tab}	CL	C	C_{mean}
21-01	3	0	0	0	90	2	0	0	0.26
21-02	3	0	0	0	90	2	0	0	0.12
21-03	3	0	0	25	90	2	0	0	0.18
21-04	5	90	0	25	90	2	0	0	0.11
21-05	3	0	0	0	90	1	0	0	0.02
21-06	6	0	0	0	90	6	0	0	0.15
21-07	5	0	0	0	90	6	0	0	0.13
21-08	3	0	0	0	90	6	0	0	0.20
21-09	3	0	0	0	90	2	0	0	0.05
27-01	3	0	0	0	60	4	0	0	0.40
27-02	3	0	0	0	90	4	0	0	0.40
27-03	3	0	0	0	120	4	0	0	0.33
27-04	3	0	0	0	90	4	0	0	0.19
27-05	3	0	0	0	90	6	0	1	1.11
39-01	3	0	0	0	90	4	0	0	0.31
39-02	3	0	0	0	90	4	2	0	0.35
39-03	3	0	0	0	90	4	0	0	0.31

Table 7.1 – Common parameters of the samples

Label	$L_{0,start}$	L_{tab}	G_{tab}	$L_{0,end}$	L_0	W_0	$T_{0,mean}$	P_0	α_0	$N_{0,diameter}$	$N_{0,type}$	$N_{0,offset}$
21-01-F0	25	50	50	25	200	200	21.2	10.5	0	8	'b'	0
21-02-F0	25	50	50	25	200	200	21.2	21	0	12	'b'	0
21-03-F0	25	50	50	25	200	200	21.2	21	0	12	'b'	0
21-04-F0	25	50	50	25	200	200	21.2	21	0	12	'b'	0
21-05-F0	25	50	0	25	100	200	21.2	21	0	12	'b'	0
21-06-F0	25	50	50	25	600	200	21.2	21	0	12	'b'	0
21-07-F0	25	50	50	25	600	200	21.2	21	45	12	'b'	0
21-08-F0	25	50	50	25	600	200	21.2	21	90	12	'b'	0
21-09-F0	25	50	50	25	200	200	21.2	10.5	0	12	'b'	0
27-01-F0	50	100	100	50	800	220	27.2	27	0	12	'b'	0
27-02-F0	50	100	100	50	800	220	27.2	27	0	12	'b'	0
27-03-F0	50	100	100	50	800	220	27.2	27	0	12	'b'	0
27-04-F0	75	150	75	75	975	220	27.2	27	0	12	'b'	0
27-05-F0	50	100	100	50	1200	220	27.2	27	0	12	'b'	0
39-01-F0	75	150	150	75	1200	240	39.2	39	0	12	'b'	0
39-02-F0	75	150	150	75	1200	240	38.2	39	0	12	'b'	0
39-03-F0	75	150	150	50	1175	240	39.2	39	0	12	'tt'	0

Table 7.2 – F_0 panel parameters of the samples

Label	$L_{1,start}$	L_{slot}	G_{slot}	$L_{1,end}$	L_1	W_1	T_1	P_1	α_1	$N_{1,diameter}$	$N_{1,type}$	$N_{1,offset}$
21-01-F1	25	50	50	25	200	200	21.2	10.5	0	8	'b'	0
21-02-F1	25	50	50	25	200	200	21.2	21	0	12	'b'	0
21-03-F1	25	50	50	25	200	200	21.2	21	0	12	'b'	0
21-04-F1	25	50	50	25	200	200	21.2	21	0	12	'b'	0
21-05-F1	25	50	0	25	100	200	21.2	21	0	12	'b'	0
21-06-F1	25	50	50	25	600	200	21.2	21	0	12	'b'	0
21-07-F1	25	50	50	25	600	200	21.2	21	45	12	'b'	0
21-08-F1	25	50	50	25	600	200	21.2	21	90	12	'b'	0
21-09-F1	25	50	50	25	200	200	21.2	10.5	0	12	'b'	0
27-01-F1	50	100	100	50	800	200	27.2	27	0	12	'b'	0
27-02-F1	50	100	100	50	800	200	27.2	27	0	12	'b'	0
27-03-F1	50	100	100	50	800	200	27.2	27	0	12	'b'	0
27-04-F1	50	150	75	50	925	200	27.2	27	0	12	'b'	0
27-05-F1	50	100	100	50	1200	200	27.2	27	0	12	'b'	0
39-01-F1	75	150	150	75	1200	240	39.2	39	0	12	'b'	0
39-02-F1	73	154	146	73	1200	240	39.2	39	0	12	'b'	0
39-03-F1	100	150	150	75	1225	240	39.2	39	0	12	'tl'	0

Table 7.3 – F_1 panel parameters of the samples

7.3 Analytical moment-resisting model

7.3.1 Assumptions

1. When a moment is applied to the connection, the latter responds by embedment perpendicular to the grain at the contact zones.
2. The bearing part is considered rigid with respect to the embedded part : $E_{11} \approx 80 \times E_{33}$ and $E_{22} \approx 20 \times E_{33}$.
3. The embedment components act in parallel both in SC and DC as experiments shown that they do not interfere with each other.
4. The profile of the additional length is an exponential function defined by $z = \delta \cdot e^{-bx}$.
5. The decay coefficient b is function of the joint-to-grain angle α and different in SC and DC.
6. The rotation axis remains at the intersection of the mid plane of panels F_0 and F_1 .
7. The panels F_0 and F_1 are made of the same material, LVL Kerto-Q from Metsäwood. Hence, same mechanical properties are taken from [VESL16], with respect to the stiffness (e.g. $E_{F0,33} = E_{F1,33} = E_{90,flat,mean}$).
8. The friction is considered at the embedment places with a value of $\mu = 0.2$, frequently found in literature.
9. The reaction forces are calculated on the Hooke's law in the elastic stage.
10. When the angle of rotation θ reaches the yield angle θ_y , the total embedded volume starts having a plastic part.
11. When the plasticity increases, the part of plastic volume increases relatively to the already embedded elastic volume.
12. The plastic reduction factor r_p which penalizes the elastic modulus is set equal both in SC and DC.

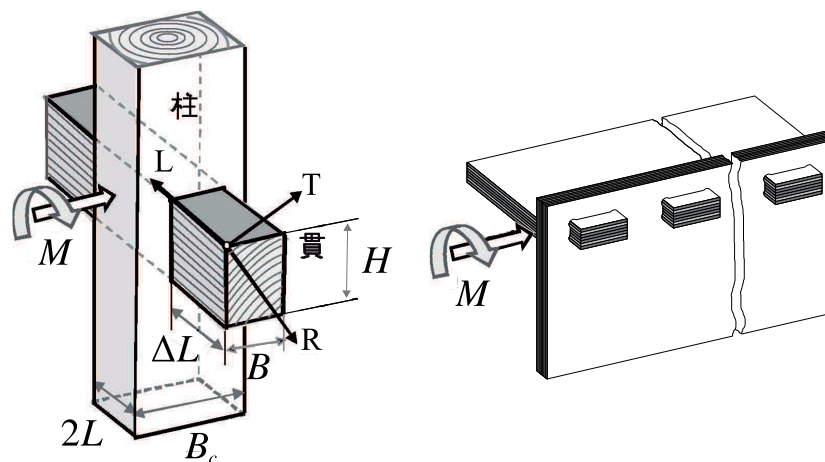


Figure 7.2 – Crosspiece timber joints : Nuki(right) and MTSJ-TT(left)

Chapter 7. Semi-rigid Moment-resisting Model of the Through Tenon variant of Multiple Tab-and-Slot Joint for LVL panels

7.3.2 Flowchart

Main steps

The general procedure that was followed to obtain the Moment-rotation relationship of MTSJ-TT is presented by a flow chart in Fig.7.3.

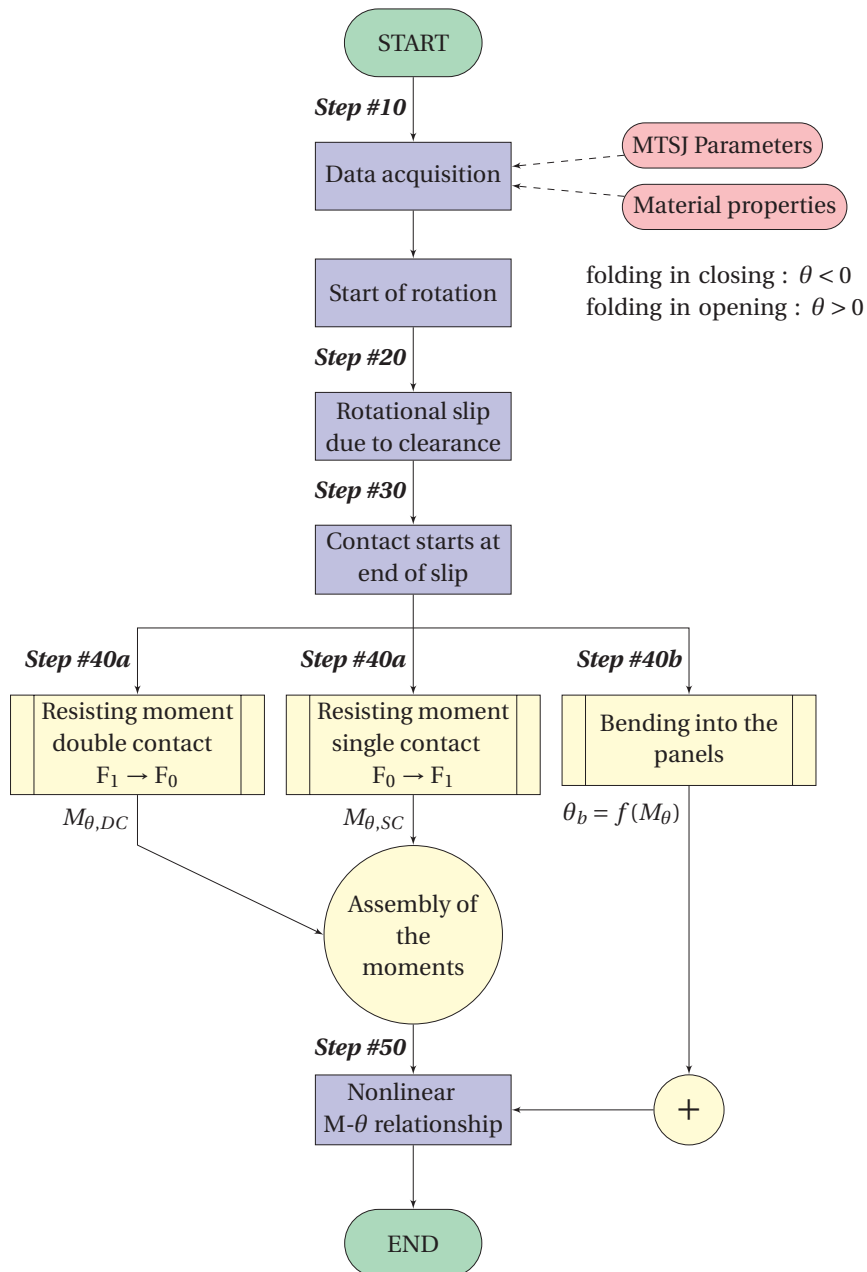


Figure 7.3 – Main approach of the model

The “subroutines” to calculate and assembly the components, typically the calculation of the local forces and resisting moment from the embedded volume formulations are developed in Fig.7.4.

Subroutines - calculation and assembly of components

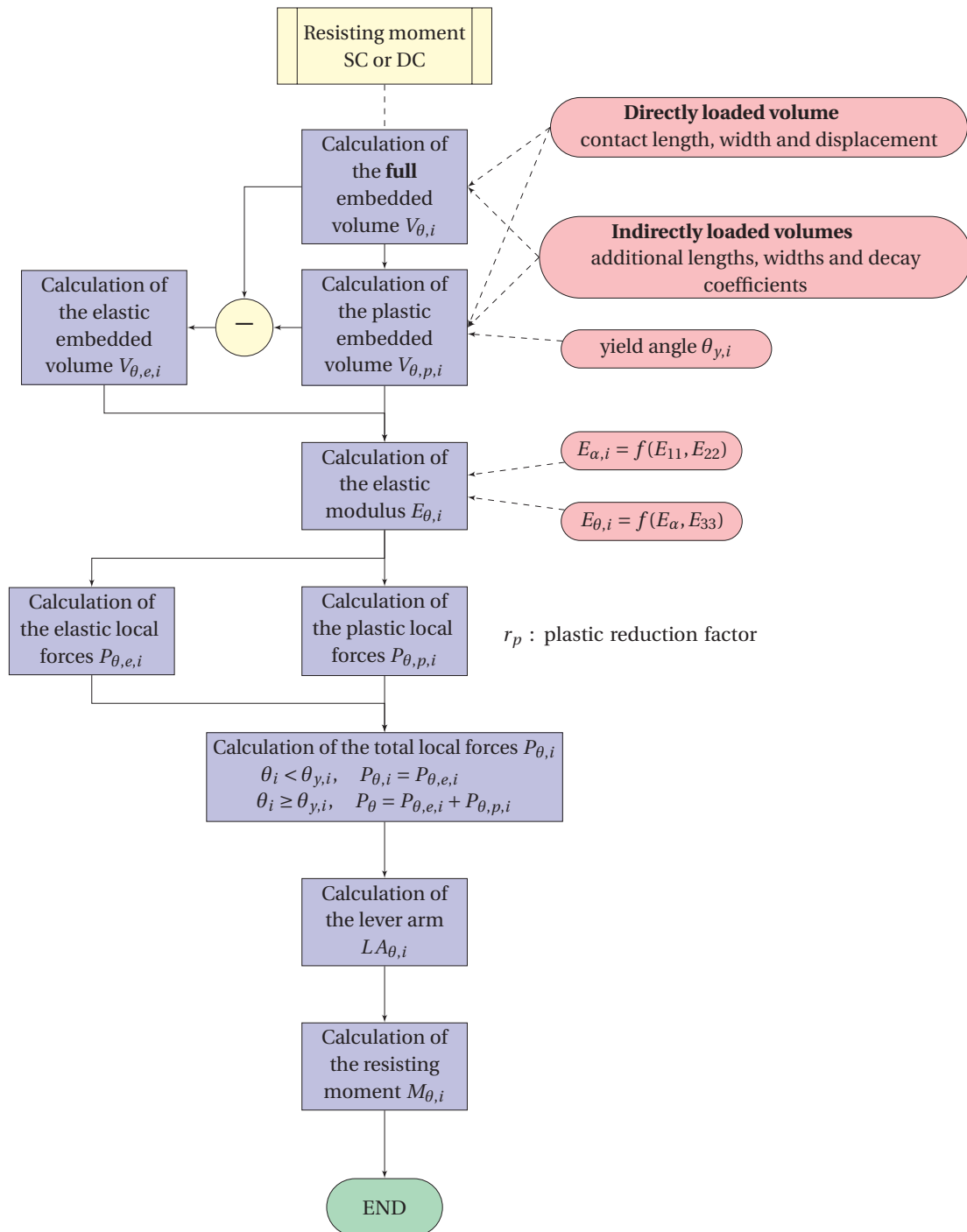


Figure 7.4 – Calculation and assembly of the components

Before developing the analytical model of a joint, it is important to understand physically the kinematics when a load is applied. This observation was preliminary done in chapter 5 and completed during the present campaign of tests.

Chapter 7. Semi-rigid Moment-resisting Model of the Through Tenon variant of Multiple Tab-and-Slot Joint for LVL panels

7.3.3 Kinematics of the MTSJ-TT in bending

Step #10 - Assembly of two panels

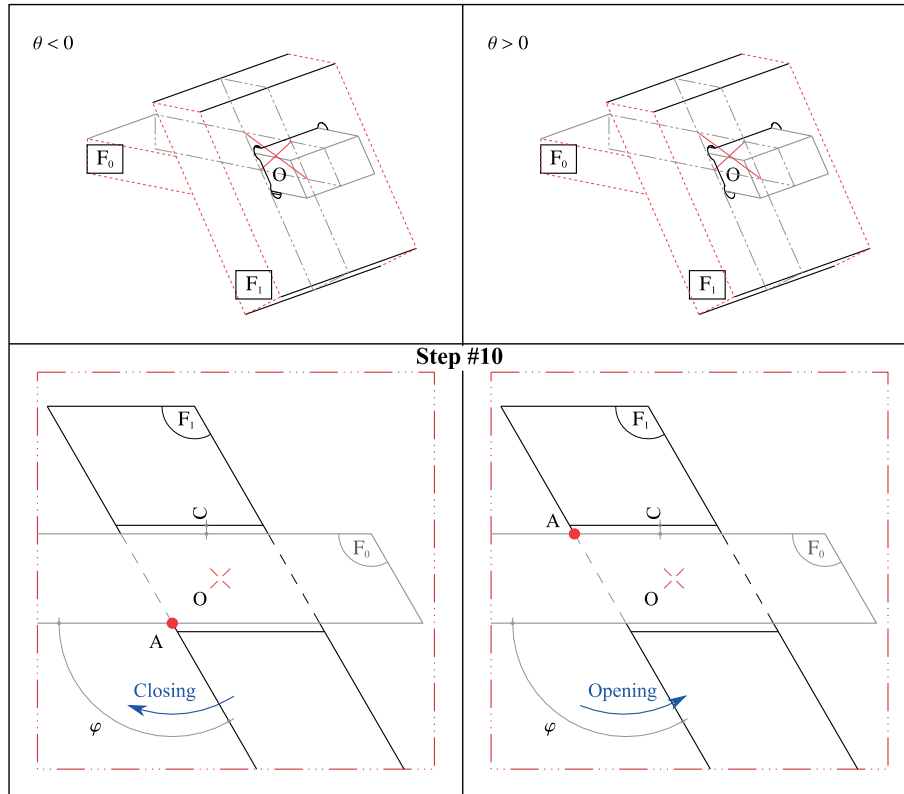


Figure 7.5 – Step #10 - Assembly of the two panels with transversal clearance

Let consider step#10/Fig.7.5 as the initial step where the geometry of the MTSJ-TT is defined. It can pointed out that the translational clearance C is included in the model. This clearance is usually the result of either a desire to set a gap for assembly or a fabrication tolerance. It has a significant influence : it imposes an initial rotational slip and reduces the contact length at the beginning of the embedment with respect to a tight joint. The kinematics is described in closing ($\theta < 0$) and opening ($\theta > 0$) since the contact lengths are not identical for MTSJ-TT joints with dihedral angles varying from 90° .

7.3. Analytical moment-resisting model

Step #20 - Rotational slip due to assembly clearance

Step #30 - Contact of the two panels

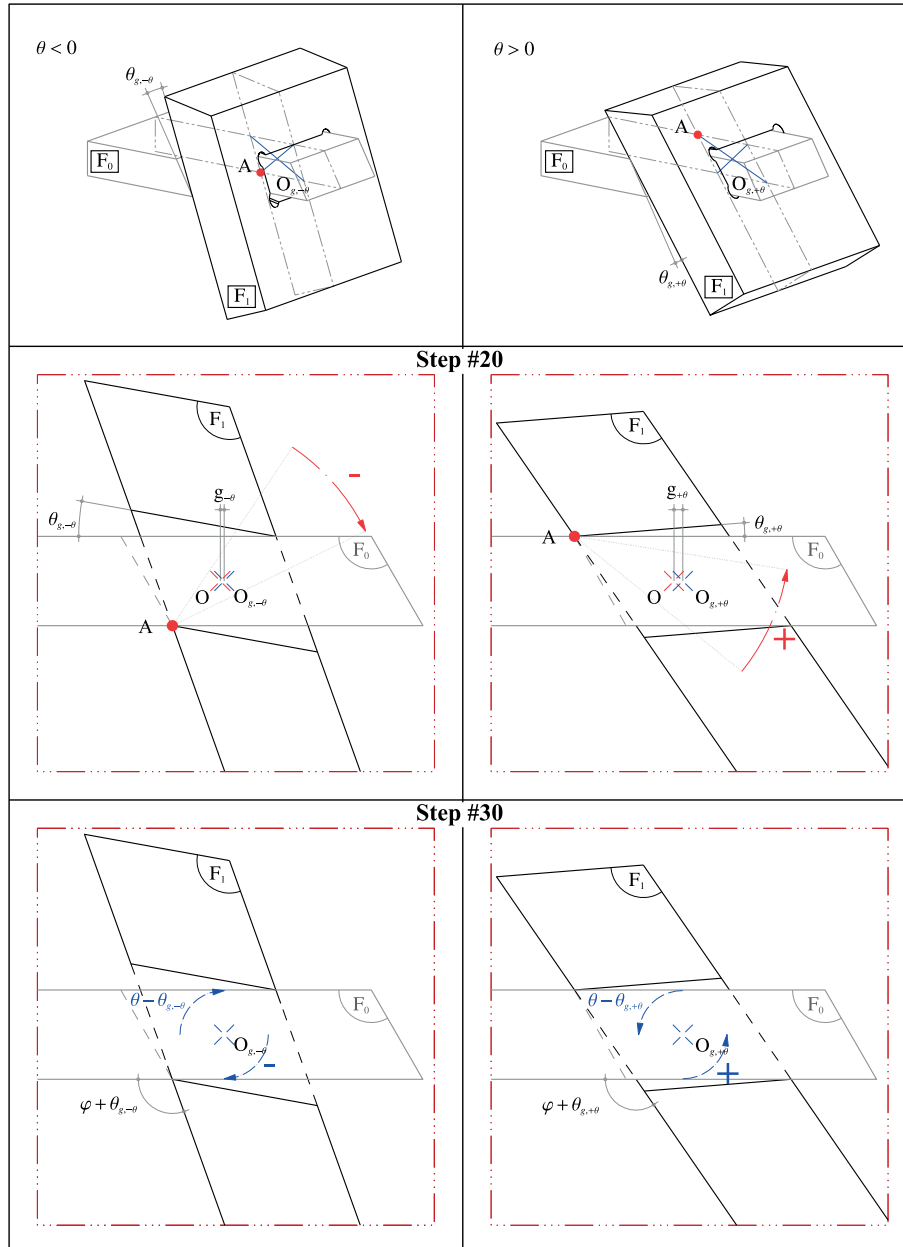


Figure 7.6 – Step #20 - Rotational slip, then Step #30 - contacts start

The initial slip angle induces a first rotation without any transfer of forces (Step #20//Fig.7.6). Then, the two panels come into contact and the mechanical resistance of the joint to the applied moment can start (Step #30//Fig.7.6).

Chapter 7. Semi-rigid Moment-resisting Model of the Through Tenon variant of Multiple Tab-and-Slot Joint for LVL panels

Step #40a - Resisting moment due to normal reaction forces

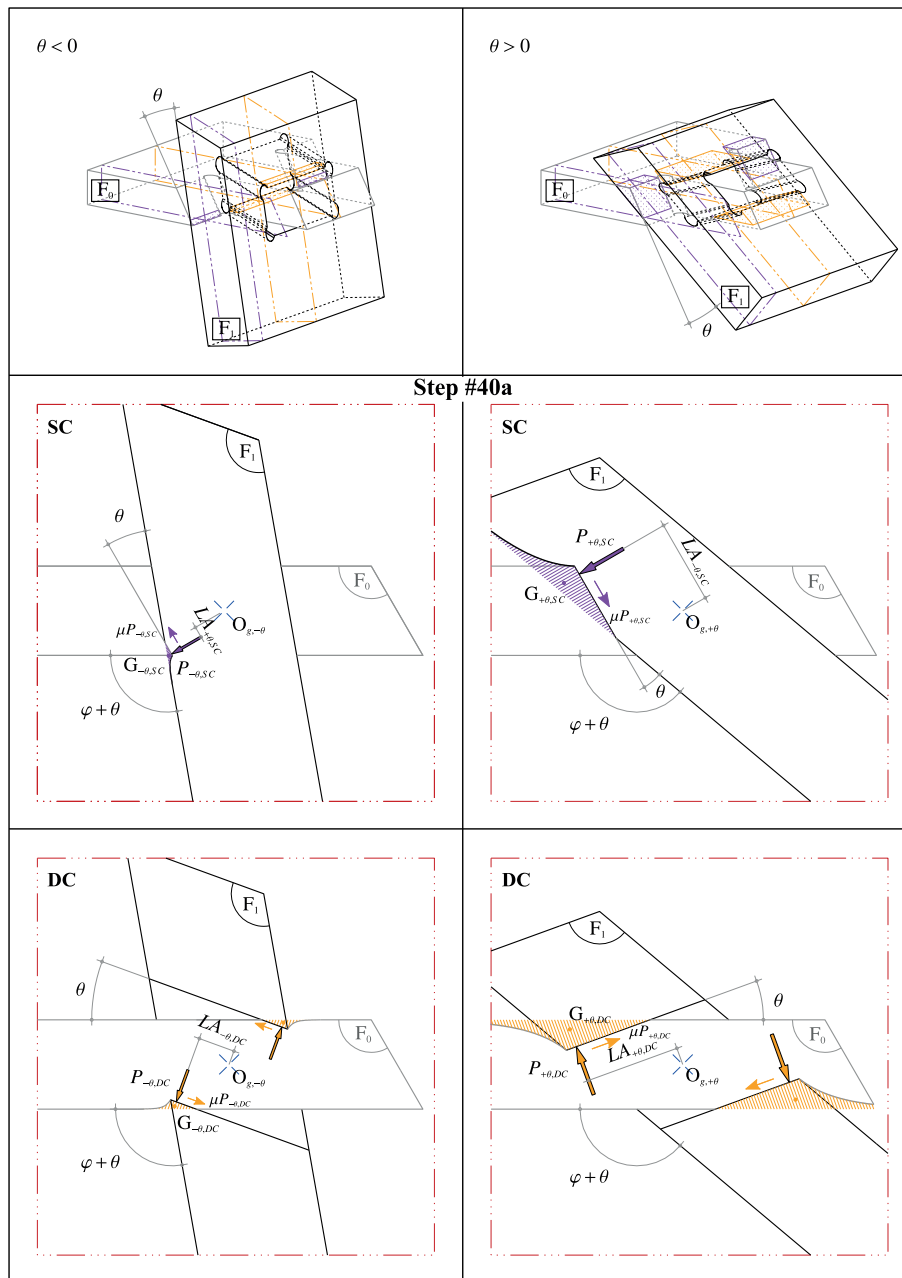


Figure 7.7 – Step #40a - Resisting moment due to normal reaction forces

Step #40a/Fig.7.7 is the most important one where the MTSJ-TT resists to an external moment by the normal reaction forces due to SC (purple in Fig.7.7) and DC (orange in Fig.7.7). Here the formulation of the force components follow the embedment theory proposed by the Japanese scientific community. The choice of the embedment theory with two kinds of contact was made from the conclusions of chapter 6.

Step #40b - Bending in the two panels

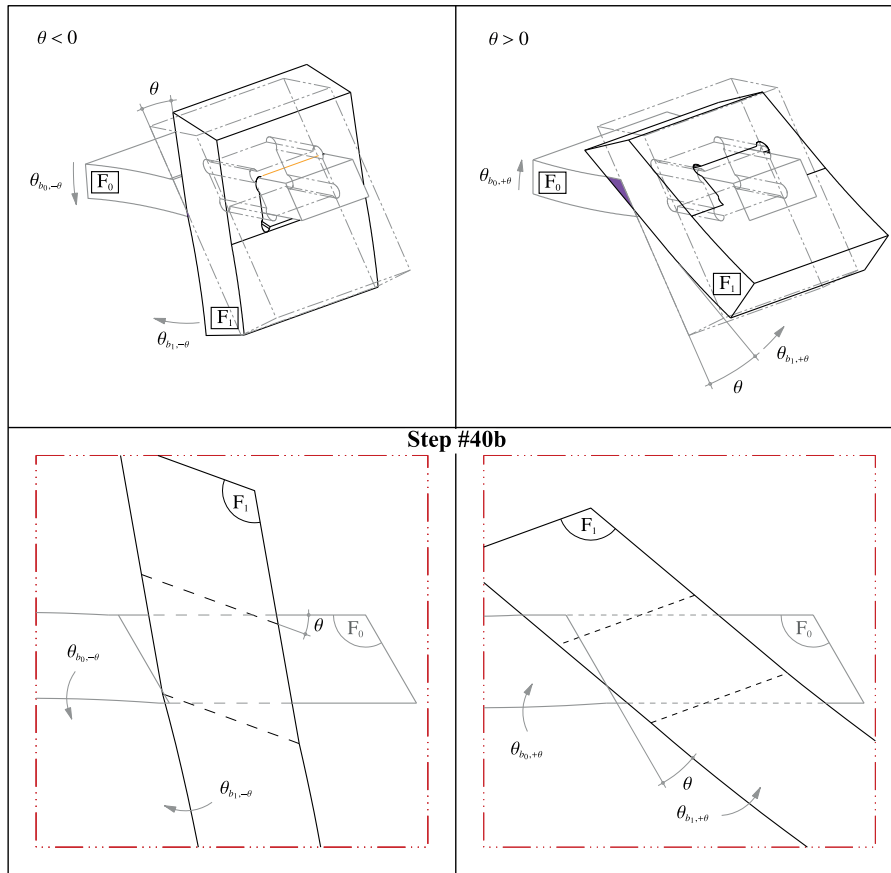


Figure 7.8 – Step #40b - Bending in the two panels

Once normal reaction forces exist, the panels start to bend as the semi-rigid joint partially fixes them. The joint rigidity is influenced both by the rotational stiffness of the connection and the flexural stiffness of the panels. Stiff panels will appear less restrained in rotation than flexible panels for the same level of partial rigidity at the joint [McG95, LHFC00]. In our case, the joint tends to increase its stiffness as the wood, loaded perpendicular to the grain, goes “in the direction” of densification. Note nonetheless that the latter will never be reached within the joint as it usually begins around 50% strain [TOS08, TOIS11]. Therefore the bending angular deformations of the panels has to be deducted to get the real behavior of the joint. How the bending effect is removed is detailed later. Finally, the panels failed by bending.

7.3.4 Characteristic lengths

The first substep of the Step#40a subroutine (Fig.7.4) is the calculation of the embedded volumes ($V_{\theta,i}$, $V_{\theta,p,i}$, $V_{\theta,e,i}$). To express them, we need $L_{\pm\theta,i}$, the contact length of the triangular part of the embedment. $LA_{\pm\theta,i}$, the lever arm from the rotation axis to the line support of the reaction forces, calculated at the second last step is also necessary to figure out the resisting moment. The different characteristic lengths are expressed from the set of equations of Fig.7.9 to Fig.7.10 and that of Fig.7.11 for SC and DC, respectively.

Chapter 7. Semi-rigid Moment-resisting Model of the Through Tenon variant of Multiple Tab-and-Slot Joint for LVL panels

Single contact (SC)

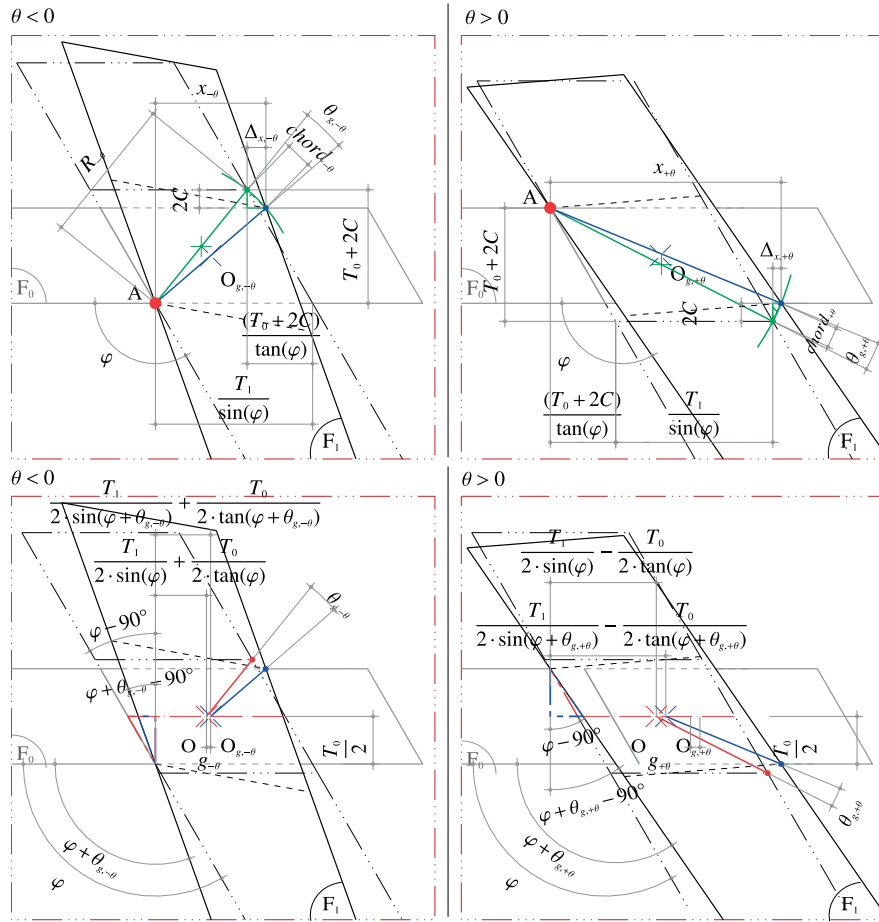


Figure 7.9 – Initial slip angle due to transversal clearance

$\theta < 0$

$$R_{-\theta} = [(T_1 / \sin \varphi + (T_0 + 2C) / \tan \varphi)^2 + (T_0 + 2C)^2]^{1/2} \quad (7.1)$$

$$x_{-\theta} = \sqrt{(R_{-\theta}^2 - T_0^2)} \quad (7.2)$$

$$\Delta_{x,-\theta} = x_{-\theta} - (T_1 / \sin \varphi + (T_0 + 2C) / \tan \varphi) \quad (7.3)$$

$$chord_{-\theta} = \sqrt{(\Delta_{x,-\theta}^2 + (2C)^2)} \quad (7.4)$$

$$\theta_{g,-\theta} = -2 \cdot \arcsin(chord_{-\theta} / (2 \cdot R_{-\theta})) \quad (7.5)$$

$$g_{-\theta} = (T_1 / 2) \cdot (1 / \sin(\varphi + \theta_{g,-\theta}) - 1 / \sin \varphi) + (T_0 / 2) \cdot (1 / \tan(\varphi + \theta_{g,-\theta}) - 1 / \tan \varphi) \quad (7.6)$$

$\theta > 0$

$$R_{+\theta} = [(T_1 / \sin \varphi - (T_0 + 2C) / \tan \varphi)^2 + (T_0 + 2C)^2]^{1/2} \quad (7.7)$$

$$x_{+\theta} = \sqrt{(R_{+\theta}^2 - T_0^2)} \quad (7.8)$$

$$\Delta_{x,+\theta} = x_{+\theta} - (T_1 / \sin \varphi - (T_0 + 2C) / \tan \varphi) \quad (7.9)$$

$$chord_{+\theta} = \sqrt{(\Delta_{x,+\theta}^2 + (2C)^2)} \quad (7.10)$$

$$\theta_{g,+\theta} = 2 \cdot \arcsin(chord_{+\theta} / (2 \cdot R_{+\theta})) \quad (7.11)$$

$$g_{+\theta} = (T_1 / 2) \cdot (1 / \sin(\varphi + \theta_{g,+\theta}) - 1 / \sin \varphi) - (T_0 / 2) \cdot (1 / \tan(\varphi + \theta_{g,+\theta}) - 1 / \tan \varphi) \quad (7.12)$$

In Eq.(7.5), (7.6), (7.11) & (7.12), $\theta_{g,\pm\theta,SC}$ and $g_{\pm\theta,SC}$ are the slip angle and the transverse slip of the rotation axis, respectively. They denotes the initial slip due to transversal clearance C .

7.3. Analytical moment-resisting model

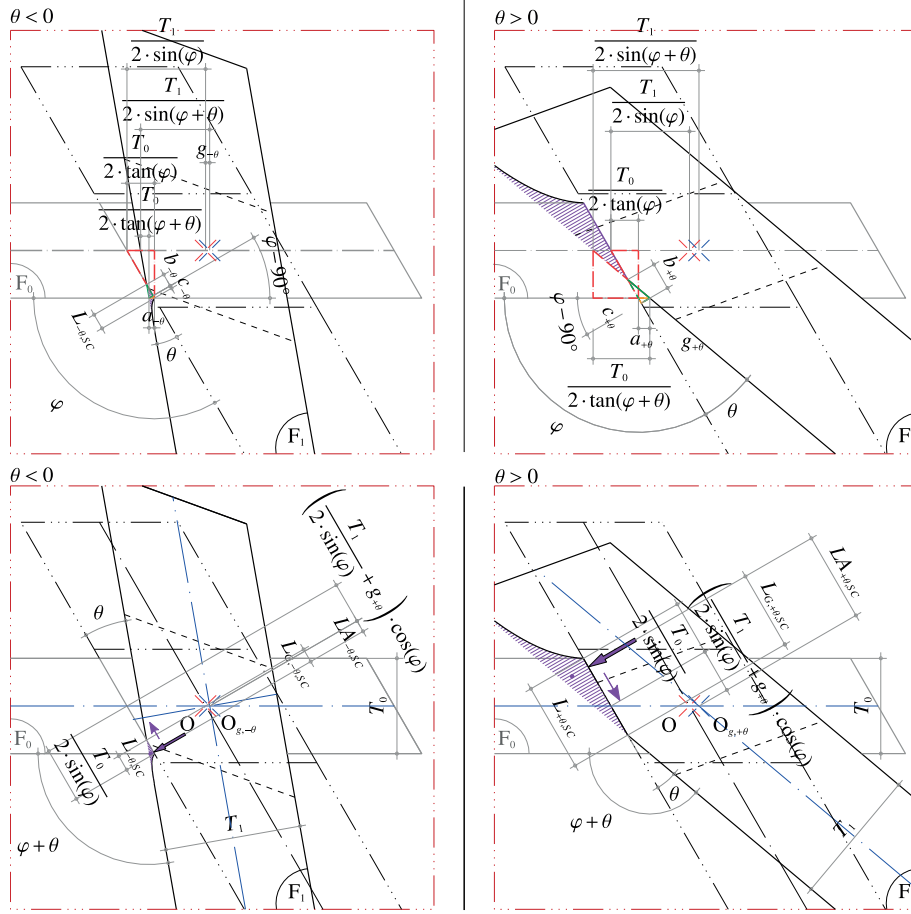


Figure 7.10 – Characteristic lengths in SC

$\theta < 0$

$$a_{-\theta} = -T_0 / (2 \tan \varphi) - T_1 / (2 \sin \varphi) - g_{-\theta} + T_1 / (2 \sin(\varphi + \theta)) + T_0 / (2 \tan(\varphi + \theta)) \quad (7.13)$$

$$b_{-\theta} = a_{-\theta} \sin \varphi / \tan \theta \quad (7.14)$$

$$c_{-\theta} = a_{-\theta} \cos \varphi \quad (7.15)$$

$$L_{-\theta, SC} = -b_{-\theta} - c_{-\theta} \quad (7.16)$$

$$LA_{-\theta, SC} = T_0 / (2 \sin \varphi) - L_{-\theta, SC} + L_{G_{-\theta, SC}} - (T_1 / (2 \sin \varphi) + g_{-\theta}) \cos \varphi \quad (7.17)$$

$$L_{G_{-\theta, SC}} = x_{G_{-\theta, SC}} \cos \theta + z_{G_{-\theta, SC}} \sin \theta \quad (7.18)$$

$$\text{with } x_{G_{-\theta, SC}} = \frac{1}{V_{-\theta, SC}} \iiint_{V_{-\theta, SC}} x \cdot dV_{-\theta, SC}$$

$$\text{and } z_{G_{-\theta, SC}} = \frac{1}{V_{-\theta, SC}} \iiint_{V_{-\theta, SC}} z \cdot dV_{-\theta, SC}$$

$\theta > 0$

$$a_{+\theta} = T_0 / (2 \tan \varphi) + T_1 / (2 \sin \varphi) + g_{+\theta} - T_1 / (2 \sin(\varphi + \theta)) - T_0 / (2 \tan(\varphi + \theta)) \quad (7.19)$$

$$b_{+\theta} = a_{+\theta} \sin \varphi / \tan \theta \quad (7.20)$$

$$c_{+\theta} = a_{+\theta} \cos \varphi \quad (7.21)$$

$$L_{+\theta, SC} = T_0 / \sin \varphi - b_{+\theta} - c_{+\theta} \quad (7.22)$$

$$LA_{+\theta, SC} = T_0 / (2 \sin \varphi) - L_{+\theta, SC} + L_{G_{+\theta, SC}} + (T_1 / (2 \sin \varphi) + g_{+\theta}) \cos \varphi \quad (7.23)$$

$$L_{G_{+\theta, SC}} = x_{G_{+\theta, SC}} \cos \theta + z_{G_{+\theta, SC}} \sin \theta \quad (7.24)$$

$$\text{with } x_{G_{+\theta, SC}} = \frac{1}{V_{+\theta, SC}} \iiint_{V_{+\theta, SC}} x \cdot dV_{+\theta, SC}$$

$$\text{and } z_{G_{+\theta, SC}} = \frac{1}{V_{+\theta, SC}} \iiint_{V_{+\theta, SC}} z \cdot dV_{+\theta, SC}$$

In addition to the geometrical parameters of the joint as usual, $g_{\pm\theta, SC}$ and $L_{G_{\pm\theta, SC}}$ allow to finally obtained $L_{\pm\theta, SC}$ and $LA_{\pm\theta, SC}$.

Chapter 7. Semi-rigid Moment-resisting Model of the Through Tenon variant of Multiple Tab-and-Slot Joint for LVL panels

Ogawa [OSY15] explained that the simplification he did, with taking the lever arm distance at 2/3 of the triangular embedment without considering the indirectly loaded deformed part, was certainly part of the shortcomings of its model. In our case, we decided to define $L_{G,\pm\theta,SC}$, the orthogonal projected distance of the center of gravity on the contact surface, from the exact formulation of the embedded volume.

Double contact (DC)

Similar calculations are made for the characteristic lengths in DC.

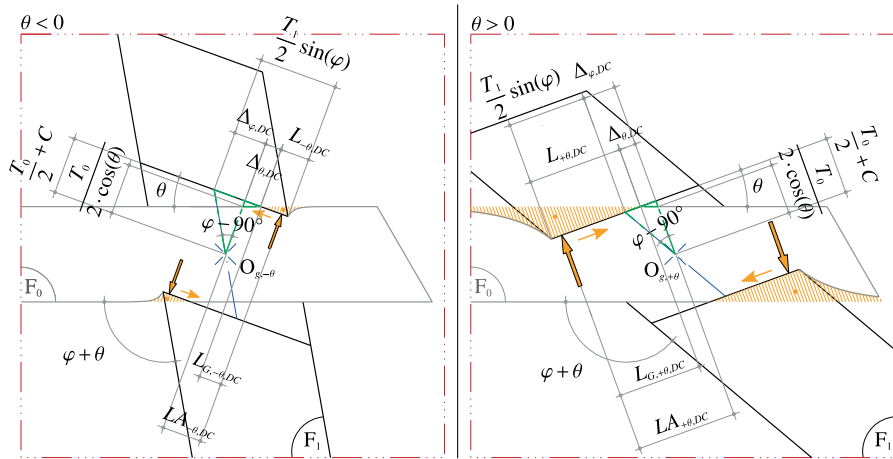


Figure 7.11 – Characteristic lengths in DC

$\theta < 0$

$$\Delta_{\theta,DC} = C / \tan \theta - (T_0/2) \tan(\theta/2) \quad (7.25)$$

$$\Delta_{\phi,DC} = (T_0/2 + C) / \tan \phi \quad (7.26)$$

$$L_{-\theta,DC} = (T_1/2) / \sin \phi + \Delta_{\phi,DC} + \Delta_{\theta,DC} \quad (7.27)$$

$$L_{A,-\theta,DC} = \Delta_{\theta,DC} + L_{G,-\theta,DC} \quad (7.28)$$

$$L_{G,-\theta,DC} = x_{G,-\theta,DC} \cos \theta + z_{G,-\theta,DC} \sin \theta \quad (7.29)$$

$$\text{with } x_{G,-\theta,DC} = \frac{1}{V_{-\theta,DC}} \iiint_{V_{-\theta,DC}} x \cdot dV_{-\theta,DC}$$

$$\text{and } z_{G,-\theta,DC} = \frac{1}{V_{-\theta,DC}} \iiint_{V_{-\theta,DC}} z \cdot dV_{-\theta,DC}$$

$\theta > 0$

$$\Delta_{\theta,DC} = C / \tan \theta - (T_0/2) \tan(\theta/2) \quad (7.30)$$

$$\Delta_{\phi,DC} = (T_0/2 + C) / \tan \phi \quad (7.31)$$

$$L_{+\theta,DC} = (T_1/2) / \sin \phi - \Delta_{\phi,DC} - \Delta_{\theta,DC} \quad (7.32)$$

$$L_{A,+\theta,DC} = \Delta_{\theta,DC} + L_{G,+\theta,DC} \quad (7.33)$$

$$L_{G,+\theta,DC} = x_{G,+\theta,DC} \cos \theta + z_{G,+\theta,DC} \sin \theta \quad (7.34)$$

$$\text{with } x_{G,+\theta,DC} = \frac{1}{V_{+\theta,DC}} \iiint_{V_{+\theta,DC}} x \cdot dV_{+\theta,DC}$$

$$\text{and } z_{G,+\theta,DC} = \frac{1}{V_{+\theta,DC}} \iiint_{V_{+\theta,DC}} z \cdot dV_{+\theta,DC}$$

Since the differentiation in the calculation of the characteristic lengths is done, $\pm\theta$ is omitted as subscript in the next equations, to clarify the rest of the discussion.

7.3.5 Embedded volumes

In traditional Japanese timber joints like Nuki, the width of the beam is fully loaded and the additional part spreads only along the beam. The Watari-ago joint analyzed by Ogawa [OSY15] produced an embedded volume which also spreads unilaterally across when resisting to shear forces.

In the case of the MTSJ-TT, the total deformed volume V_i due to the rotational partial compression is divided into elementary volumes ($V_{k,i}$, Fig.7.12). Each volume is calculated by integration (Equations (7.35) to (7.40)). The integrals are expressed with the geometrical parameters of the directly and indirectly embedded area. These parameters are gathered in Fig.7.12, Table 7.4 for SC and Table 7.5 for DC. The notch (see Fig. 7.1 left top and bottom) due to cutting constraint make the widths of the volumes shorter than both theoretical tab & slot lengths and gaps.

$V_{1,i}$ is the triangular embedment at the directly loaded area. In addition, the additional deformed volumes $V_{2,i}, V_{3,i}, V_{4,i}$ in Fig.7.1 expand along x and y axes. At the intersection of these volumes, $V_{5,i}$ and $V_{6,i}$ are defined by Eq.(7.39) and Eq.(7.40), respectively. The volumes thus created theoretically are really close to those observed experimentally. The three-dimensional representation of the full embedded volume is depicted in Fig.7.1a and the plastic volume when $\theta > \theta_y$ in Fig.7.1b.

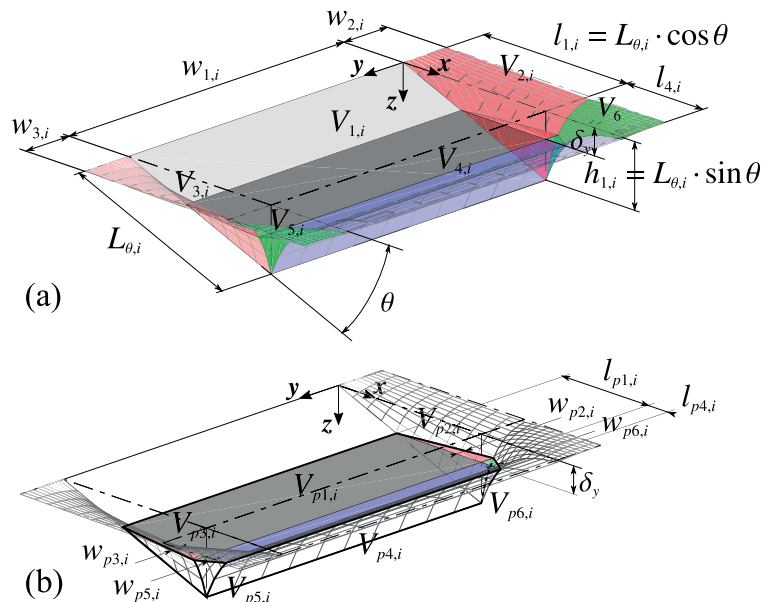


Figure 7.12 – (a) Elasto-plastic deformed volumes. (b) Details after yield point.

Chapter 7. Semi-rigid Moment-resisting Model of the Through Tenon variant of Multiple Tab-and-Slot Joint for LVL panels

Label	$w_{1,start}$	$w_{2,start}$	$w_{3,start}$	$l_{4,start}$	$w_{1,int}$	$w_{2,int}$	$w_{3,int}$	$l_{4,int}$	$w_{1,end}$	$w_{2,end}$	$w_{3,end}$	$l_{4,end}$
21-01	19.34	0	4.49	168.50	38.69	4.49	4.49	168.50	19.34	4.49	0	168.50
21-02	16.51	0	6.73	158	33.03	6.73	6.73	158	16.51	6.73	0	158
21-03	10.65	0	8.42	158	21.30	9.36	9.36	158	10.65	8.42	0	158
21-04	13.66	0	4.51	158	27.31	4.51	4.51	158	13.66	4.51	0	158
21-05	16.51	0	6.73	158	0	0	0	0	16.51	6.73	0	158
21-06	16.51	0	6.73	158	33.03	6.73	6.73	158	16.51	6.73	0	158
21-07	16.51	0	6.73	158	33.03	6.73	6.73	158	16.51	6.73	0	158
21-08	16.51	0	6.73	158	33.03	6.73	6.73	158	16.51	6.73	0	158
21-09	16.51	0	6.73	168.50	33.03	6.73	6.73	168.50	16.51	6.73	0	168.50
27-01	41.51	0	6.73	141.82	83.03	6.73	6.73	141.82	41.51	6.73	0	141.82
27-02	41.51	0	6.73	146	83.03	6.73	6.73	146	41.51	6.73	0	146
27-03	41.51	0	6.73	141.82	83.03	6.73	6.73	141.82	41.51	6.73	0	141.82
27-04	41.51	0	6.73	146	58.03	6.73	6.73	146	41.51	6.73	0	146
27-05	41.51	0	6.73	146	83.03	6.73	6.73	146	41.51	6.73	0	146
39-01	66.51	0	6.73	162	133.03	6.73	6.73	162	66.51	6.73	0	162
39-02	66.51	0	4.73	162	133.03	4.73	4.73	162	66.51	4.73	0	162
39-03	63	25	6	162	126	6	6	162	63	6	25	162

Table 7.4 – Volume parameters in mm of the samples in SC

Label	$w_{1,DC1}$	$w_{2,DC1}$	$w_{3,DC1}$	$l_{4,DC1}$	$w_{1,DC2}$	$w_{2,DC2}$	$w_{3,DC2}$	$l_{4,DC2}$
21-01	38.69	5.66	5.66	10.5	38.69	4.49	4.49	168.1
21-02	33.03	8.49	8.49	21	33.03	6.73	6.73	157.5
21-03	27.13	6.45	6.45	21	39.74	7.94	7.94	157.6
21-04	21.48	9.36	9.36	21	41.07	6.59	6.59	157.4
21-05	33.03	8.49	8.49	21	33.03	6.73	6.73	157.2
21-06	33.03	8.49	8.49	21	33.03	6.73	6.73	158
21-07	33.03	8.49	8.49	21	33.03	6.73	6.73	158
21-08	33.03	8.49	8.49	21	33.03	6.73	6.73	158
21-09	33.03	8.49	8.49	10.5	33.03	6.73	6.73	168.1
27-01	83.03	8.49	8.49	27	83.03	6.73	6.73	161.82
27-02	83.03	8.49	8.49	27	83.03	6.73	6.73	166
27-03	83.03	8.49	8.49	27	83.03	6.73	6.73	161.82
27-04	133.03	8.49	8.49	27	133.03	6.73	6.73	166
27-05	83.03	8.49	8.49	27	83.03	6.73	6.73	166
39-01	133.03	8.49	8.49	39	133.03	6.73	6.73	132
39-02	137.03	6.49	6.49	39	137.03	4.73	4.73	162
39-03	150	0	0	39	150	0	0	162

Table 7.5 – Volume parameters in mm of the samples in DC

$$V_{1,i} = \frac{1}{2} \cdot w_{1,i} \cdot l_{1,i} \cdot h_{1,i} \quad (7.35)$$

$$V_{2,i} = \int_0^{l_{1,i}} \int_0^{w_{2,i}} x \cdot \tan \theta \cdot \exp(-b_{V_{2,i}} y) dy dx \quad (7.36)$$

$$V_{3,i} = \int_0^{l_{1,i}} \int_0^{w_{3,i}} x \cdot \tan \theta \cdot \exp(-b_{V_{3,i}} y) dy dx \quad (7.37)$$

$$V_{4,i} = w_{1,i} \cdot \int_0^{l_{4,i}} h_{1,i} \cdot \exp(-b_{V_{4,i}} x) dx \quad (7.38)$$

$$V_{5,i} = \int_0^{l_{4,i}} \int_0^{w_{3,i}} h_{1,i} \cdot \exp(-b_{V_{4,i}} x) \cdot \exp(-b_{V_{3,i}} y) dy dx \quad (7.39)$$

$$V_{6,i} = \int_0^{l_{4,i}} \int_0^{w_{2,i}} h_{1,i} \cdot \exp(-b_{V_{4,i}} x) \cdot \exp(-b_{V_{2,i}} y) dy dx \quad (7.40)$$

$$V_i = V_{\theta,i} = \sum_{k=1}^6 V_{k,i} \quad (7.41)$$

7.3. Analytical moment-resisting model

where $l_{1,i} = L_{\theta,i} \cos \theta$ and $h_{1,i} = L_{\theta,i} \sin \theta$.

The plastic range is reached at low rotation angle (less than 3°) during the deformation. If we consider that $\delta_y = L_{\theta_y} \cdot \sin \theta_y$ is the point where the plastic deformation starts, then the elementary plastic volumes are defined by Equations (7.42) to (7.47).

$$V_{p_1,i} = \frac{1}{2} \cdot w_{1,i} \cdot l_{p_1,i} \cdot (h_{1,i} - \delta_y) \quad (7.42)$$

$$V_{p_2,i} = \int_{l_{1,i}-l_{p_1,i}}^{l_{1,i}} \int_0^{w_{p_2,i}} (x \cdot \tan \theta \cdot \exp(-b_{V_{2,i}} y) - \delta y) dy dx \quad (7.43)$$

$$V_{p_3,i} = \int_{l_{1,i}-l_{p_1,i}}^{l_{1,i}} \int_0^{w_{p_3}} (x \cdot \tan \theta \cdot \exp(-b_{V_{3,i}} y) - \delta y) dy dx \quad (7.44)$$

$$V_{p_4,i} = w_{1,i} \cdot \int_0^{l_{p_4,i}} (h_{1,i} \cdot \exp(-bx) - \delta y) dx \quad (7.45)$$

$$V_{p_5,i} = \int_0^{l_{p_4,i}} \int_0^{w_{p_5,i}} (h_{1,i} \cdot \exp(-bx) \cdot \exp(-b_{V_{3,i}} y) - \delta y) dy dx \quad (7.46)$$

$$V_{p_6,i} = \int_0^{l_{p_4,i}} \int_0^{w_{p_6,i}} (h_{1,i} \cdot \exp(-bx) \cdot \exp(-b_{V_{2,i}} y) - \delta y) dy dx \quad (7.47)$$

$$V_{p,i} = V_{\theta,p,i} = \sum_{k=1}^6 V_{p_k,i} \quad (7.48)$$

with

$$l_{p_1,i} = l_{1,i} - \frac{\delta y}{\tan \theta} \quad (7.49)$$

$$w_{p_2,i} = -\frac{1}{b_{V_{2,i}}} \ln \frac{\delta y}{x \tan \theta} \quad \text{with } l_{1,i} - l_{p_1,i} \leq x \leq l_{1,i} \quad (7.50)$$

$$w_{p_3,i} = -\frac{1}{b_{V_{3,i}}} \ln \frac{\delta y}{x \tan \theta} \quad \text{with } l_{1,i} - l_{p_1,i} \leq x \leq l_{1,i} \quad (7.51)$$

$$l_{p_4,i} = -\frac{1}{b_{V_{4,i}}} \ln \frac{\delta y}{h_{1,i}} \quad (7.52)$$

$$w_{p_5,i} = -\frac{1}{b_{V_{3,i}}} \ln \frac{\delta y}{h_{1,i} \cdot \exp(-b_{V_{4,i}} x)} \quad \text{with } l_{1,i} - l_{p_1,i} \leq x \leq l_{1,i} \quad (7.53)$$

$$w_{p_6,i} = -\frac{1}{b_{V_{2,i}}} \ln \frac{\delta y}{h_{1,i} \cdot \exp(-b_{V_{4,i}} x)} \quad \text{with } l_{1,i} - l_{p_1,i} \leq x \leq l_{1,i} \quad (7.54)$$

The elastic embedded volumes are obtained by

$$V_{e_k,i} = V_{k,i} - V_{p_k,i} \quad \text{for } k = 1 \dots 6 \quad (7.55)$$

and

$$V_{e,i} = V_{\theta,e,i} = \sum_{k=1}^6 V_{e_k,i} \quad (7.56)$$

Chapter 7. Semi-rigid Moment-resisting Model of the Through Tenon variant of Multiple Tab-and-Slot Joint for LVL panels

7.3.6 Elasto-plastic moment-rotation relationship

From the deformed volume formulations, the normal reaction forces in elastic stage and plastic stage, respectively $P_{e,i}$ and $P_{p,i}$, are obtained by using typical stress-strain relationships:

SC

$$P_{e,i} = \frac{V_{e,i}}{T_1} \cdot E_\theta \quad \text{for } i = SC_{start}, SC_{int}, SC_{end} \quad (7.57a)$$

$$P_{p,i} = \frac{V_{p,i}}{T_1} \cdot r_p E_\theta \quad \text{for } i = SC_{start}, SC_{int}, SC_{end}, \text{ if } \theta > \theta_y \quad (7.57b)$$

Subscripts *start*, *int* and *end* means F_0 -panel embeds into F_1 -panel at the start of the joint, at the inter-slots and at the end of the joint, respectively.

DC

$$P_{e,i} = \frac{V_{e,i}}{T_0} \cdot E_\theta \quad \text{for } i = DC_1, DC_2 \quad (7.58a)$$

$$P_{p,i} = \frac{V_{p,i}}{T_0} \cdot r_p E_\theta \quad \text{for } i = DC_1, DC_2, \text{ if } \theta > \theta_y \quad (7.58b)$$

Subscripts 1 and 2 means F_1 -panel embeds into F_0 -panel at the tab protrusion side and at the panel side, respectively.

r_p is the plastic reduction factor which penalize the Young's modulus E_θ in the plastic part of the moment-rotation relationship of the whole joint.

In Eq.(7.57) and (7.58), the Young's modulus E_θ is expressed from the joint-to-grain angle α in plane 1-2 and the angle of rotation θ (see chapter 6). It is worth noting that $\alpha = \text{rotates of } 90^\circ$ from the fiber direction.

$$E_\theta = \frac{E_\alpha \cdot E_{33}}{E_{33} \sin^{1.8} \theta + E_\alpha \cos^{1.8} \theta} \quad (7.59)$$

with

$$\frac{1}{E_\alpha} = \frac{\cos^4 \alpha}{E_{22}} + \frac{\sin^4 \alpha}{E_{11}} + \frac{\cos^2 \alpha \cdot \sin^2 \alpha}{0.7^{2 \times 0.7} \cdot G_{12}} \quad (7.60)$$

Only because of rotational compression, this young modulus increases slightly with the angle of rotation and the joint-to-grain angle. We recall that the modulus of elasticity perpendicular to grain, edgewise (when the joint-to-grain angle is equal to 0°) is 2400 N/mm^2 and the modulus of elasticity parallel to grain (when the joint-to-grain angle is equal to 90°) are 10000 and 10500 N/mm^2 up to 24mm and beyond 24mm , respectively. Using the Saliklis's formula [SF00], the modulus of elasticity at the considered joint-to-grain angle is estimated. For instance, It is 1228 N/mm^2 for 27mm -thick Kerto-Q panel at $\alpha = 45^\circ$. Then using the Hankinson'formula [Han21], the initial modulus of elasticity perpendicular to grain, flatwise

7.3. Analytical moment-resisting model

Property	Symbol	orthotropic	21mm [*]	27-39mm	Unit
Elastic modulus					
// to grain, along	$E_{0,mean}$	E_{11}	10000	10500	Mpa
// to grain, across	$E_{90,mean}$	E_{90}^{**}	3300	2000	Mpa
⊥ to grain, edgewise	$E_{90,edge,mean}$	E_{22}	2400	2400	Mpa
⊥ to grain, flatwise	$E_{90,flat,mean}$	E_{33}	130	130	Mpa
Shear modulus					
Edgewise	$G_{0,edge,mean}$	G_{12}	600	600	Mpa

^{*}To be use for bending of the panels when joint-to-grain angle $\alpha = 0^\circ$

^{**}21mm with | - || - | arrangement layer

Table 7.6 – Elastic properties of LVL Kerto-Q (mean values)

of 130 N/mm² is corrected to 130.7 N/mm² for $\theta = 5^\circ$.

Then, using the lever arm lengths $LA_{\theta,i}$ from Eq.(7.17) & (7.28) or (7.23) & (7.33), the resisting moments $M_{e,j}$ and $M_{p,j}$ are calculated by the following expression :

SC

Elastic stage

$$M_{e,SC} = P_{e,SC_{start}} \cdot LA_{\theta,SC_{start}} + P_{e,SC_{int}} \cdot LA_{\theta,SC_{int}} \cdot (N_{tab} - 1) + P_{e,SC_{end}} \cdot LA_{\theta,SC_{end}} \quad (7.61a)$$

$$MF_{e,SC} = [P_{e,SC_{start}} \cdot T_1/2 + P_{e,SC_{int}} \cdot T_1/2 \cdot (N_{tab} - 1) + P_{e,SC_{end}} \cdot T_1/2] \cdot \mu \quad (\text{if friction}) \quad (7.61b)$$

Plastic stage

$$M_{p,SC} = P_{p,SC_{start}} \cdot LA_{\theta,SC_{start}} + P_{p,SC_{int}} \cdot LA_{\theta,SC_{int}} \cdot (N_{tab} - 1) + P_{p,SC_{end}} \cdot LA_{\theta,SC_{end}} \quad (7.61c)$$

$$MF_{p,SC} = [P_{p,SC_{start}} \cdot T_1/2 + P_{p,SC_{int}} \cdot T_1/2 \cdot (N_{tab} - 1) + P_{p,SC_{end}} \cdot T_1/2] \cdot \mu \quad (\text{if friction}) \quad (7.61d)$$

DC

Elastic stage

$$M_{e,DC} = [P_{e,DC_1} \cdot LA_{\theta,DC_1} + P_{e,DC_2} \cdot LA_{DC_2}] \cdot N_{tab} \quad (7.62a)$$

$$MF_{e,DC} = [P_{e,DC_1} \cdot (T_0/2 + C) + P_{e,DC_2} \cdot (T_0/2 + C)] \cdot N_{tab} \cdot \mu \quad (\text{if friction}) \quad (7.62b)$$

Plastic stage

$$M_{p,SC} = [P_{p,DC_1} \cdot LA_{\theta,DC_1} + P_{p,DC_2} \cdot LA_{DC_2}] \cdot N_{tab} \quad (7.62c)$$

$$MF_{p,SC} = [P_{p,DC_1} \cdot (T_0/2 + C) + P_{p,DC_2} \cdot (T_0/2 + C)] \cdot N_{tab} \cdot \mu \quad (\text{if friction}) \quad (7.62d)$$

Finally, the resisting moment due to embedment effect in rotational partial compression, perpendicular to the grain, flatwise is obtained as a function of the rotation angle θ in Eq.(7.63):

Chapter 7. Semi-rigid Moment-resisting Model of the Through Tenon variant of Multiple Tab-and-Slot Joint for LVL panels

$$M_{\theta} = M_{e,DC} + M_{e,SC} + M_{p,DC} + M_{p,SC} + MF_{e,DC} + MF_{e,SC} + MF_{p,DC} + MF_{p,SC} \quad (7.63)$$

Closed forms* of V_i , $V_{p,i}$, $V_{e,i}$, $P_{e,i}$, $P_{p,i}$ and LA_i were provide and allowed to implement the models in Matlab ©R2015b . Providing a range of θ , we get the moment rotation simulation for any geometry of joint defined by the parameters of section 7.2.

7.4 Experimental study

7.4.1 Series of samples

A total of 43 samples were tested. The geometries of the sample is gathered in Fig.7.1 and Tables 7.1, 7.2 and 7.3. As the transversal clearance has a large influence on the initial contact length, certain dimensions of the samples were checked after milling on a five axis CNC machine Maka MM7s. The tab height H_{tab} , typically the thickness of F0-panel measured at the tab location, and the slot height H_{slot} were measured for each tab and slot of each sample and then averaged sample by sample. From them, the mean value of the actual transversal clearance is obtained as $C_{mean} = (H_{slot} - H_{tab})/2$. It is available in Tables 7.1 and 7.2. For the panel thickness, the average values of $21^{+1.43}_{-1.03}$, $27^{+1.61}_{-1.21}$, $39^{+1.97}_{-1.57}$ have been considered (values in mm, provided by [VESL16]). All these values were also entered into the model.

7.4.2 Description of the bending test

In chapters 4 & 5, the experimental tests were performed with a so-called folding machine. However this rig had some shortcomings. First, it was designed only for rather short samples (450 mm) without protrusion. Second, it did not apply a pure moment as it was like loading a cantilever beam with a punctual load at the end. The shear force was neglected at this occasion. Regarding research work on wood furniture connections, an improvement track appeared. In 2005, Sydor designed a pure-bending test machine for small angular connections for furniture. The details of this pulley-loaded rig can be seen in his PhD thesis [Syd05]. Based on the same principle, a new rig for MTSJ was built to test larger and stronger structural joint than furniture connections. It is presented in Fig.7.13. The F_1 -panel was attached to a series of pairs of tensile/compression cell loads ⑤, mounted on a rigid support ⑥. Forces were applied to the F_0 -panel via a series of pairs of tensile/compression cell loads ⑤. The forces are produced into the cell loads via the lever arm ② and the 20kN cylinder ①. In a pair, the forces are opposed, one working in compression, the other one in tension. Each pair of cell loads of F_0 -panel are in the same “plane” than F_1 -panel. The number of pairs is adapted to the joint length. The shortest samples require one pair for each panel, while the longest ones require four. The loads which causes the closing of the edge-to-edge connected panels were recorded every 0.5 s via the cell loads ③ & ⑤, connected to a data acquisition system. Two inclinometers ⑦ which monitored the closing angle are placed at the end of F_0 -panel. The total rotation $\theta_{inclinometer} = \theta + \theta_{b0} + \theta_{b1}$ is obtained by averaging the two inclinometers. θ_{b0} and θ_{b1} are the

*The full expressions are unfortunately too long to be written in the present dissertation

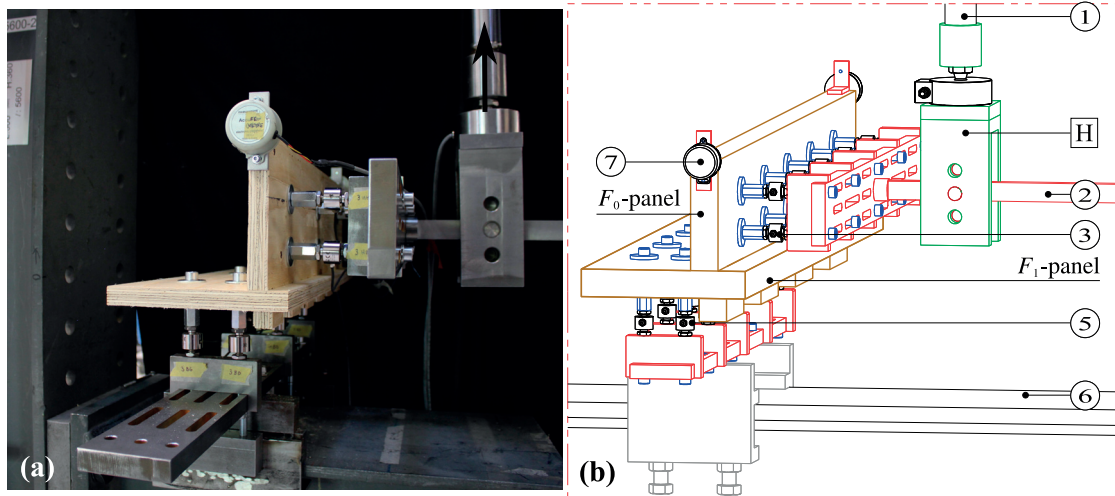


Figure 7.13 – Bending test for MTSJ-TT : (a) Applied loads, (b) ① Cylinder, ② Lever arm, ③ Cell loads 20kN, ④ Sample, ⑤ Rigid support, ⑥ Inclinometers (x2), H 2DF head.

bending angles into F_0 -panel and F_1 -panel, respectively. The cylinder displacement (200mm max) is manually operated by a hydraulic pump. The duration to test one sample was between 240 and 300 seconds for about 30° rotation. Every results (loads,rotation) are saved in TXT files and then numerically processed with Matlab©R2015b.

The resulting moment and shear force diagrams are shown in Fig.7.14. Using this new setup, the shear forces were virtually eliminated. Only an side effect remained as the generating force $F_{cylinder}$ was offset on the right : a residual shear forces into F_1 -panel. The MTSJ-TT received bending moment from both panels as would the common fixed support of two beams. The difference here was that the semi-rigidity of the MTSJ-TT provided a complementary rotation. The moments at the joint were obtained from the measured forces at the bottom panel F_1 , $M_B = (a + d) \cdot F_{BL} - a \cdot F_{BR}$ and at the top panel F_0 , $M_T = (a + d) \cdot F_{TT} - a \cdot F_{TB}$. It is worth noting that $F_{TT} \approx F_{TB}$ but $F_{BR} > F_{BL} > F_{TT}$.

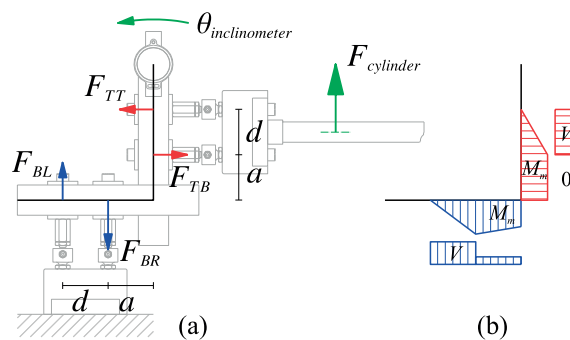


Figure 7.14 – (a) Quasi-static equilibrium (b) Moment M_s and shear force V diagrams.

In addition, the bending angle θ_{b0} and θ_{b1} were obtained by the classical elastic formulas of beams as $\theta_{b0} = 1/(2EI_{F_0,r}) \cdot [F_{BL} \cdot (a+d)^2 - a^2 \cdot F_{BR}]$ and $\theta_{b1} = 1/(2EI_{F_1,r}) \cdot [F_{TT} \cdot (a+d)^2 - a^2 \cdot F_{TB}]$. They must be subtracted from $\theta_{inclinometer}$ to obtain the contribution of the joint to the whole

Chapter 7. Semi-rigid Moment-resisting Model of the Through Tenon variant of Multiple Tab-and-Slot Joint for LVL panels

rotation. $I_{F_0,r}$ and $I_{F_1,r}$ are the effective moments of inertia when the cut in the panels are deduce from the total lengths L_0 and L_1 , respectively. By simplification, the plasticity in bending was not considered in the correction of the rotation angle. Obviously it has some drawbacks like giving too much plastic stiffness to the experimental moment-rotation curves of the MTSJ-TT. Normally in the plastic range, the bending angles should be larger than the one estimated.

7.4.3 Embedment parameters for the model

As already seen in chapter 6, the values of the decay coefficients may vary according mainly to the yield angle. Yield angles are difficult to determine with accuracy in wood. So we decide to adjust the models with ranges of parameters $b_{V_2,DC}$, $b_{V_4,DC}$, $b_{V_2,SC}$, $b_{V_4,SC}$, $\theta_{y,DC}$ and $\theta_{y,SC}$ for each thickness and each joint-to-grain angles α . In the presented samples, α is limited to 0° , 45° and 90° for 21mm-thickness and 0° , for 27 and 39mm-thickness. $b_{V_{k,i}}$ are the decay coefficients of the exponential shape function of the additional embedded parts and $\theta_{y,i}$ are the yield angles. The parameter values are collected Tables 7.7 to 7.11. The simulations were run with an unique plastic reduction factor r_p of 0.4 by using the *lsqcurvefit* from Matlab©R2015b.

21 – 0°	$b_{V_2,DC}$	$b_{V_4,DC}$	$b_{V_2,SC}$	$b_{V_4,SC}$	$\theta_{y,DC}$	$\theta_{y,SC}$
start	0.38	1.72	0.12	0.16	1.50	1.00
low	0.18	0.37	0.08	0.11	0.50	0.50
up	0.68	4.00	0.18	0.26	3.00	2.00

Table 7.7 – Embedment parameters for 21mm- $\alpha_i = 0^\circ$

21 – 45°	$b_{V_2,DC}$	$b_{V_4,DC}$	$b_{V_2,SC}$	$b_{V_4,SC}$	$\theta_{y,DC}$	$\theta_{y,SC}$
start	0.63	0.63	0.10	0.10	1.50	1.00
low	0.22	0.22	0.07	0.07	0.50	0.50
up	2.16	2.16	0.16	0.16	3.00	2.00

Table 7.8 – Embedment parameters for 21mm- $\alpha_i = 45^\circ$

21 – 90°	$b_{V_2,DC}$	$b_{V_4,DC}$	$b_{V_2,SC}$	$b_{V_4,SC}$	$\theta_{y,DC}$	$\theta_{y,SC}$
start	1.72	0.38	0.16	0.12	1.50	1.00
low	0.37	0.18	0.11	0.08	0.50	0.50
up	4.00	0.68	0.26	0.18	3.00	2.00

Table 7.9 – Embedment parameters for 21mm- $\alpha_i = 90^\circ$

27 – 0°	$b_{V2,DC}$	$b_{V4,DC}$	$b_{V2,SC}$	$b_{V4,SC}$	$\theta_{y,DC}$	$\theta_{y,SC}$
start	0.21	1.93	0.09	0.16	1.50	1.00
low	0.11	0.34	0.06	0.10	0.50	0.50
up	0.31	4.00	0.14	0.29	3.00	2.00

Table 7.10 – Embedment parameters for 27mm- $\alpha_i = 0^\circ$

39 – 0°	$b_{V2,DC}$	$b_{V4,DC}$	$b_{V2,SC}$	$b_{V4,SC}$	$\theta_{y,DC}$	$\theta_{y,SC}$
start	0.16	0.96	0.09	0.11	1.50	1.00
low	0.08	0.31	0.06	0.07	0.50	0.50
up	0.27	4.00	0.13	0.18	3.00	2.00

Table 7.11 – Embedment parameters for 39mm- $\alpha_i = 0^\circ$

7.5 Results and discussion

7.5.1 Moment-rotation curves of MTSJ-TT

The results of the simulations versus the experimental corrected curves are presented in Fig.7.16 to Fig.7.18. The characteristic values are summarized in Table 7.12 where $M_{exp,max}$ is the ultimate moment, K_{exp} the experimental stiffness, L_{MTSJ} the MTSJ length, $K_{\theta,exp}$ the experimental stiffness when the bending angles are removed and $K_{\theta,model}$ the stiffness from the model. Hereafter are the comments which refer both to table and curves. Most of the parameters were similar in a series of same thickness, “→” mentions those which differed from a reference sample.

Label	$M_{exp,max}$ N·m	K_{exp} N·m/°	N_{tab} N_{tab}	K_{exp}/N_{tab} N·m/°	L_{MTSJ} m	K_{exp}/L_{MTSJ} N·m/°/m	$K_{\theta,exp}$ N·m/°	$K_{\theta,model}$ N·m/°
21-01	170	16	2	8	0.200	79	27	22
21-02	215	19	2	10	0.200	96	37	27
21-03	183	16	2	8	0.200	81	27	23
21-04	180	16	2	8	0.200	80	27	15
21-05	114	10	1	10	0.100	103	21	12
21-06	592	53	6	9	0.600	88	93	55
21-07	741	65	6	11	0.600	108	90	52
21-08	758	81	6	13	0.600	134	103	55
21-09	172	18	2	9	0.200	92	38	27
27-01	960	97	4	24	0.800	121	156	194
27-02	920	79	4	20	0.800	99	118	114
27-03	965	36	4	9	0.800	45	42	33
27-04	741	87	4	22	0.950	92	133	181
27-05	1288	99	6	17	1.200	83	136	91
39-01	2342	183	4	46	1.200	153	227	175
39-02	1974	174	4	43	1.200	145	213	152
39-03	2385	209	4	52	1.200	174	265	201

Table 7.12 – Characteristic values of moment-rotation curves

In general, the model underestimated the stiffnesses which places the simulation on the conservative side. As explained above, considering the plasticity in the calculation of the bending angles after the yield point could substantially reduce the difference.

Chapter 7. Semi-rigid Moment-resisting Model of the Through Tenon variant of Multiple Tab-and-Slot Joint for LVL panels

21-02 - reference

→ 2 tabs

It is the reference geometry for a thickness of 21mm.

21-01

→ $N_{j,diameter} = 8\text{mm}$, $P_j = 0.5 \times T_j$

It was the MTSJ-TT sample tested in chapter 5. Smaller notch diameter do not impact the stiffness at all. Compared with 12mm-diameter notch, the increase of the embedded volume is so small that it is lost in the experimental error. The failure came from the F_1 -Panel where a smaller protrusion had more influence for the slot than for the tab. The ultimate moment was therefore lower as tearing appeared at the slot. The rotational stiffness K_{exp} and the ultimate moment $M_{exp,max}$ with the new setup (“pure bending”) were higher than those determined experimentally in chapter 5. It confirmed the work from Sydor [Syd05]: “the connections in a pure bending state of stress are significantly more rigid than those in a combined stress state (bending + shear)”. He also concluded that “only the results of tests of samples loaded with pure bending moment can be used for theoretical analysis. Samples in a complex state of stress would be extremely difficult or impossible to describe analytically”.

Samples 21-03 and 21-04 were made for comparison to the TT variant ($\theta_0 = \theta_2 = \theta_3 = 0^\circ$) on which was based the model.

21-03

→ $\theta_3 = 25^\circ$, see Fig.7.15a

The dovetail shape of the connection did not bring any significant effect in bending. As the model was written for TT variant, the possible additional compression between the tab flanks and the slot flanks was not considered. It seems not being so important, the behavior is rather similar with the sample of reference.

21-04

→ $\theta_1 = 90^\circ$ and $\theta_3 = 25^\circ$, see Fig.7.15b

Same statement for these geometry than for 21-03 but the connection appeared less stable. Indeed The shape of the tabs tends to facilitate the disassembly of the two panels when rotating.

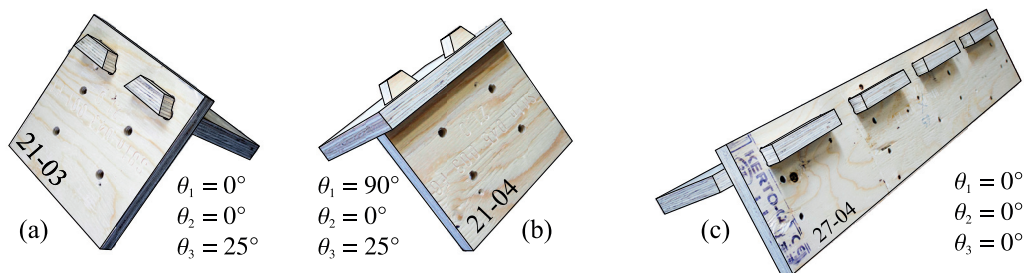


Figure 7.15

21-05

→ 1 tab

if the stiffness K_{exp}/N_{tab} is compared with the reference sample and with 6 tabs samples, it is obvious that the assumption of component assembled in parallel is confirmed. This connection also supported half of the efforts received by the reference sample and about 6 times less than those with 6 tabs. Its length is also in the same proportion.

For the three next samples, the influence of the joint-to-grain angle α is compared. As a reminder, the joint-to-grain angle is the direction of the joint axis with respect to the grain. They were designed with 6 tabs. Hence, the applied bending moment reached higher values and the angular correction error in plastic zone was more sensitive.

21-06

→ 6 tabs

It is the reference panel for 21mm-thickness with six tabs and $\alpha = 0^\circ$, the weakest direction of bending ($E_{90,mean} = 2900 \text{ Mpa} < E_{0,mean} = 10000 \text{ Mpa}$). Note that here, 90 and 0 means the grain orientation from [VESL16]). Its ultimate moment lost almost 25% compared with samples 21-07 and 21-08.

21-07

→ 6 tabs, $\alpha_j = 45^\circ$

It shown a similar behavior to 21-06 but reached a larger ultimate moment. The plates are rotated of 45° from sample 21-06 and the modulus of elasticity in bending flatwise was assumed half way between $E_{90,mean}$ and $E_{0,mean}$.

21-08

→ 6 tabs, $\alpha_j = 90^\circ$

The joint is solicited in the strongest direction of panel bending. The ultimate moment is also higher than 21-06 and it is not very different from 21-07. By cons if we compare its stiffness with the other two, the increase is around 25% if we consider the bending while it is only 10% otherwise.

21-09

→ $P_j = 0.5 \times T_j$

Close curves and characteristic values, the conclusions are the same than sample 21-01.

27-02 - reference

→ 4 tabs

It is the reference geometry for a thickness of 27mm. When the resisting moment is still increasing, the preponderant role of the initial slip is more visible. For the simulations, C_{mean} was used instead of the theoretical transversal clearance C . In that case, there was a big gap between one replicate and the two others. As the resulting mean slip angle was quite small compare to the actual one, the slope at the beginning of the curve was steeper. It implied a

Chapter 7. Semi-rigid Moment-resisting Model of the Through Tenon variant of Multiple Tab-and-Slot Joint for LVL panels

model stiffness larger than the experimental one.

The two following samples demonstrated the influence of the dihedral angle φ on the kinematics of the MTSJ.

27-01

→ $\varphi = 60^\circ$

In Figs.7.10 & 7.11 are presented the contact lengths both in closing(left) and opening(right). For the figures, φ was set to 120° . In the case of sample 27-01, φ was equal to 60° and the loads were applied to close the joint. Kinematically, for the calculation of the contact length, it corresponds to a joint with $\varphi = 60^\circ$ in opening. So, as show in Figs.7.11 & 7.10 (left sides), the contact length is much longer in this configuration. It is directly demonstrated experimentally and theoretically with a joint stiffness more than 30% larger than the reference square connected sample 27-02.

27-03

→ $\varphi = 120^\circ$

Here, the sample with $\varphi = 120^\circ$ is exactly in the configuration of Figs.7.10 & 7.11 (left sides), the contact length is really shorter and the stiffness is lower as well. The latter represents less than 46% of the reference sample 27-02 and less than 37% of the sample 27-01 with $\varphi = 60^\circ$. In an other hand, they experimented the same ultimate moment.

27-04

→ $L_{0,start} = L_{0,end} = 75\text{mm}$, $L_{tab} = 150\text{mm}$, $G_{tab} = 75\text{mm}$, $L_{1,start} = L_{1,end} = 50\text{mm}$, $L_{slot} = 150\text{mm}$, $G_{slot} = 75\text{mm}$

The sample 27-04 is shown before in Fig.7.15c. It is worth noting that, in that case, sample 27-04 has an offset of 25mm between F_0 -panel start and F_0 1-panel start because $L_{0,start} > L_{1,start}$. This joint is longer than the reference sample (950 to 800mm) but its ultimate moment was smaller (741 to 920 N·m). It is explained by the amount of material which transferred the loads. In sample 27-04, the rest of material after the slot cuts represented 325mm while in sample 27-02, it represented 400mm. The ratio $325/400 = 81.2\%$ was very close to the moment ratio $741/920 = 80.5\%$. As the total length $N_{tab} \times L_{tab}$ of the components in DC was also higher than in sample 27-02 (600mm to 400mm), the stiffness is a little higher. The model overestimated the stiffness, certainly due to a slip angle underestimated.

27-05

→ 6 tabs, $C = 1\text{mm}$

This sample was cut with a large transversal clearance (1mm) and the results of tests were quite unstable with respect to the slip angle. The difference of slip was clearly marked compare with the others samples. The stiffness due to a reduced contact length at the beginning was slightly lower than sample 27-02.

The shape of the curves for 39mm-thick panels was more linear. The panels were much more rigid in bending than for 21mm and 27mm-thick panels recalling that the loads were applied substantially with the same lever arms. The error due to the bending angle correction was less marked. Thereby, the model fits rather well the curves and the stiffnesses were quite close to the experimental ones.

39-01 - reference

→ 4 tabs

It is the reference geometry for a thickness of 39mm.

39-02

→ $CL = 2\text{mm}$

A longitudinal clearance was added to suppress the friction effect at the contact between the flanks of tab and slots. From the stiffness value in Table 7.12, it seemed that the lateral friction had a little effect.

39-03

→ $N_{0,type} = "tt"$, $N_{1,type} = "tl"$, $L_{0,start} = 75\text{mm}$, $L_{0,end} = 50\text{mm}$, $L_{1,start} = 100\text{mm}$, $L_{1,end} = 75\text{mm}$

By using the tangential cuts instead of bisector cuts, sample 39-03 offered a full compressed width in DC. The effect was marked by an increase in rigidity of 17% with respect to sample 39-01.

Chapter 7. Semi-rigid Moment-resisting Model of the Through Tenon variant of Multiple Tab-and-Slot Joint for LVL panels

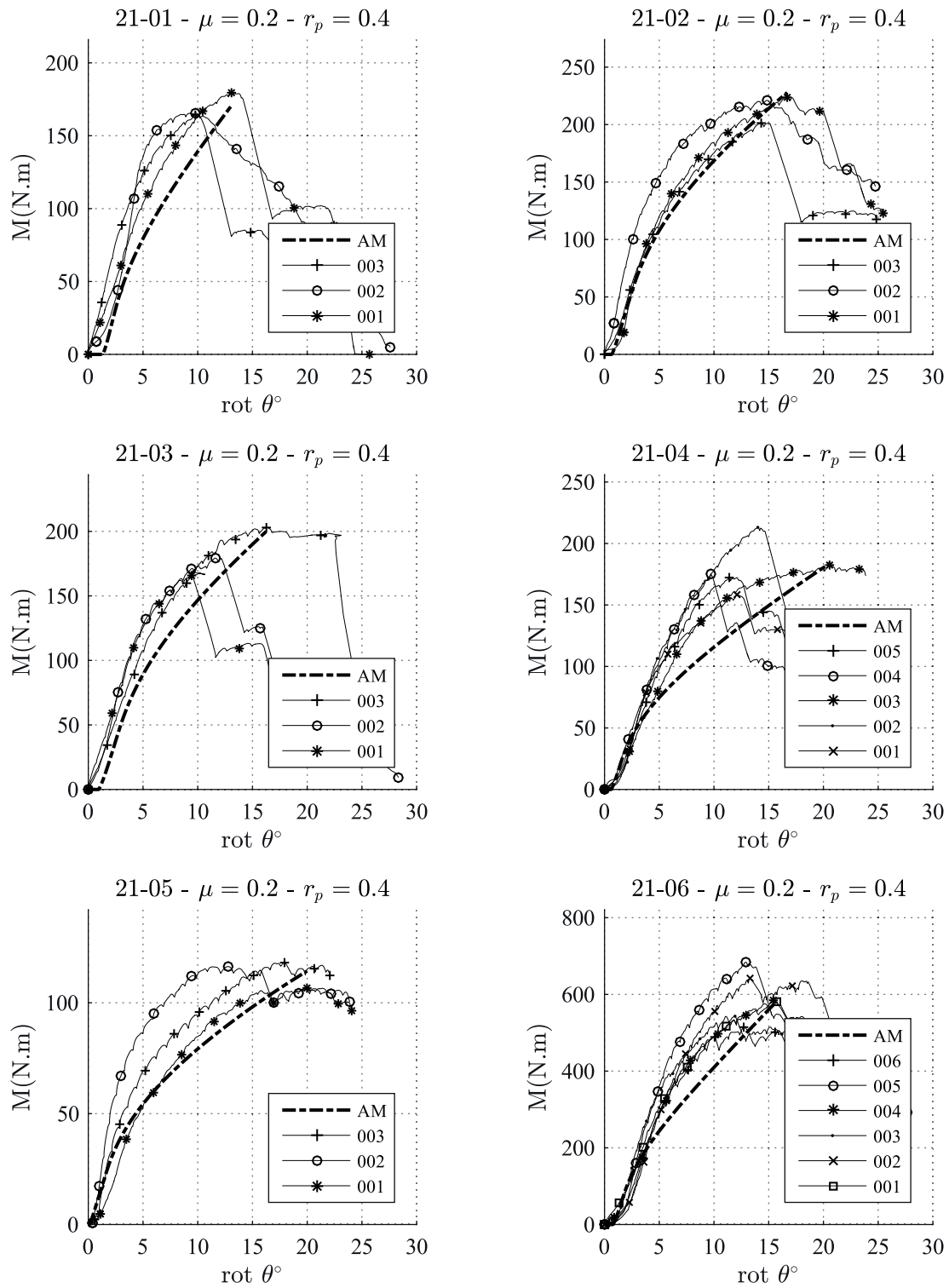


Figure 7.16 – Analytical model Vs Experimental curves - 1/3

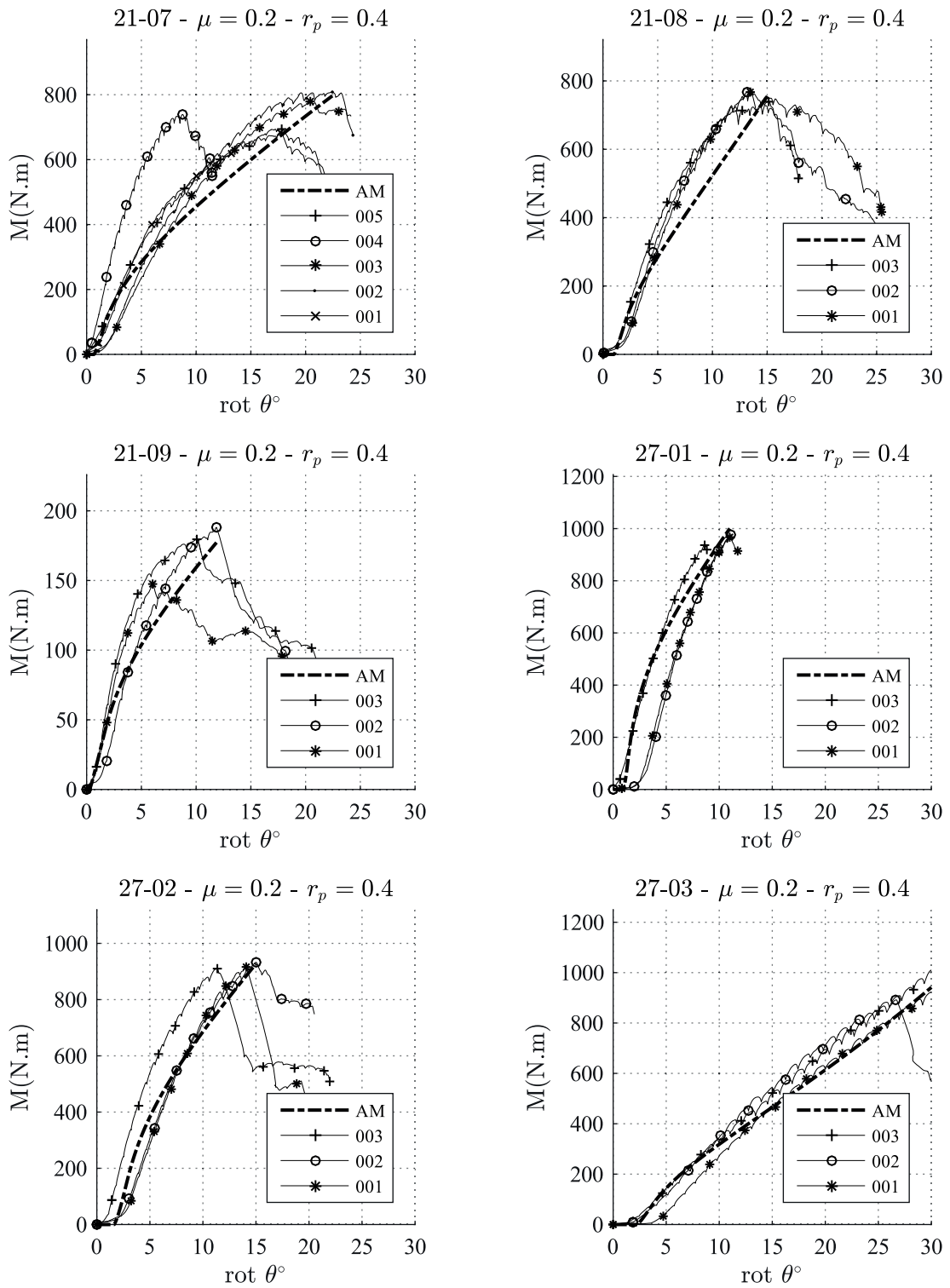


Figure 7.17 – Analytical model Vs Experimental curves - 2/3

Chapter 7. Semi-rigid Moment-resisting Model of the Through Tenon variant of Multiple Tab-and-Slot Joint for LVL panels

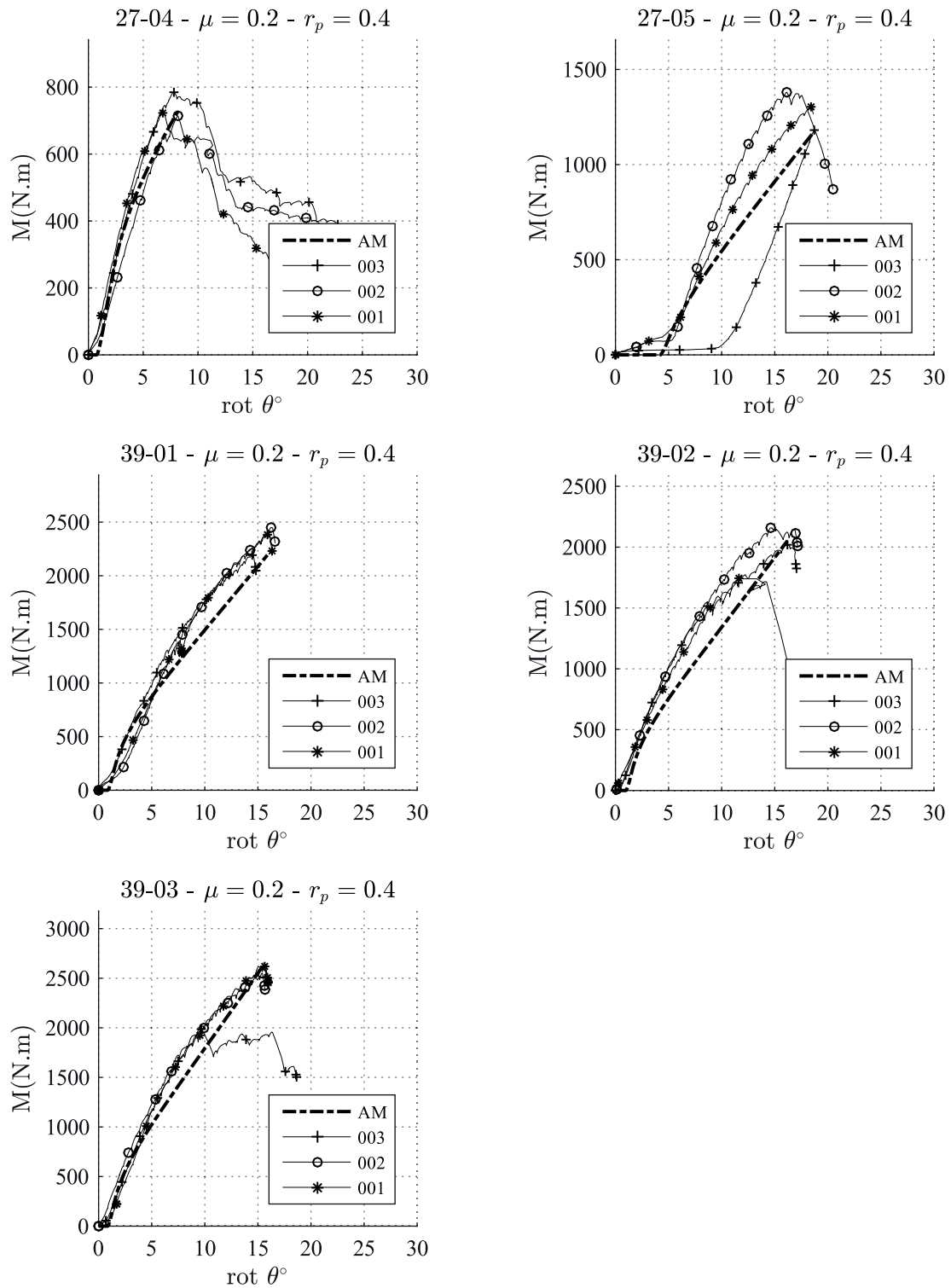


Figure 7.18 – Analytical model Vs Experimental curves - 3/3

7.5.2 Failure modes

From the different experimental results, it appeared that the failure came by bending into the panels at the joint. At this location, the cross section and the inertia of the joint were reduced compared to the rest of the panel. Indeed, the cutting of tabs and slots weakened especially this area. Obviously, it never failed because of the RPC (“densification”). It is worth noting that RPC effect influences the deflection within a whole structure but provides also a certain ductility.

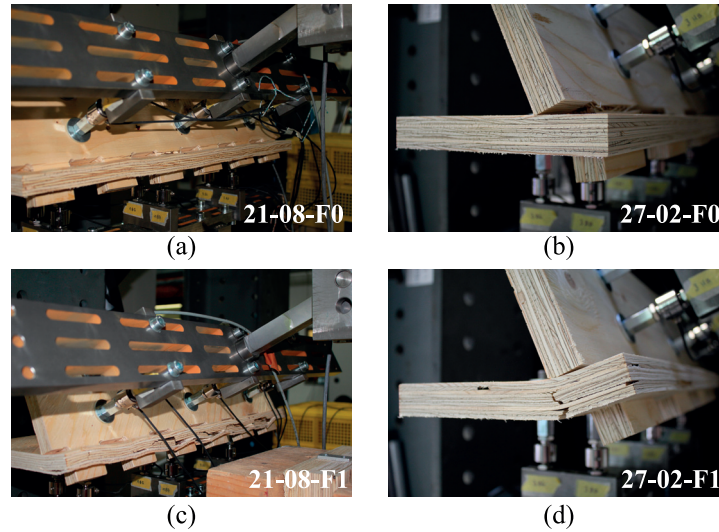


Figure 7.19 – Failure modes by bending : Geometry 27-02 (a) Failure of F_0 -Panel, (b) Failure of F_1 -Panel, Geometry 21-08 (c) Failure of F_0 -Panel, (d) Failure of F_1 -Panel

Fig.7.19 shows the three mode of failures that was found for all the samples. Fig.7.19a&b is the failure due to bending in F_0 -panel (mode A) while Fig.7.19d is the failure due to bending in F_1 -panel (mode B). On the other hand, Fig.7.19c is a failure by delamination of the veneers (mode C). As already explained, for sample 27-04, only F_1 -panel failed for all replicates but for the other cases, the failure came indifferently in both panels for one of the other of the replicates.

Label	21-01	21-02	21-03	21-04	21-05	21-06	21-07	21-08	21-09	27-01	27-02	27-03	27-04	27-05	39-01	39-02	39-03
σ_{b,F_0}	13.0	17.8	15.2	14.9	17.7	16.2	20.2	20.6	13.9	10.3	10.0	10.4	5.0	9.2	7.7	6.6	8.1
σ_{b,F_1}	14.0	20.1	16.9	16.8	22.2	18.5	23.1	23.8	16.3	11.8	11.2	11.8	11.8	10.5	8.9	7.6	8.4
$f_{m,90,edge,k}$	14	14	14	14	14	14	14	-	14	8	8	8	8	8	8	8	8
$f_{m,0,edge,k}$	-	-	-	-	-	-	32	32	-	-	-	-	-	-	-	-	-
mode	A&B	A&B	A&B	A&B	A&B	A&B	A&B	A&B	A&B	A&B	A&B	A&B	B	A&B	A&B	A&B	A&B

Table 7.13 – Average bending stress into the panels (in MPa)

Table 7.13 confirms quantitatively the conclusions coming from the visual inspection of the failure modes. The stresses were calculated at the reduced area at the joint place. For instance, the value of the bending stresses in the F_1 -panel which broke first for all the replicates is much greater than that of the F_0 -panel. For the others, the stresses were closer for both panels and reached the characteristic strength provided by the VTT certificate [VESL16].

7.6 Conclusions

The moment-resisting behavior of multiple tab-and-slot joints was investigated in previous publication for different variants : dovetail (DJ), finger(FJ), Japanese(JJ) or through tenon(TT). The through tenon variant which is the only one with closed slots was selected here for its efficiency to transfer bending between two LVL thin panels connected at various dihedral angles. A model was developed for geometries having the Bryant's angles all set to zero but was also applied with success to connection where the Bryant's angles were symmetrically turned on both tab flanks. The geometrical parameters of the joint were clarified and the kinematics of the joint was detailed. The latter begins with an initial slip angle due to transversal clearance and then the embedment effect starts to be activated. The characteristic lengths which allow the calculation of the embedded volumes and the lever arm were provided both in single contact(SC) and double contact(DC). The embedment parameters, the decay coefficients and the yield angles came from previous study on the additional length effect in the rotational partial compression of LVL perpendicular to the orthotropic panel plane. The normal reaction forces were obtained by integration of the embeded volumes and then nested in the Hook's law. The elastic modulus in compression perpendicular to grain was corrected according to the fiber orientation in the panel plane and the rotation angle of the joint. Both elastic and plastic ranges were addressed. A reduction factor served to penalize the modulus of elasticity perpendicular to grain after the yield point. 17 Simulations by the model was run with considering a range of embedment parameters for single contact(SC) and double contact(DC). The model and the comparative experiments highlighted the influence of the dihedral angle, the transversal clearance and the total slot length ratio to joint length on the stiffness of the MTSJ. The predicted stiffnesses seemed conservative with the corrected experimental joint stiffness. The latter was obtained by removing the angle due to bending into the panels from the total measured rotation. The plasticity in bending was not addressed in this correction and it can explain a certain gap between modeled and tested stiffnesses. Three modes of failures were identified : bending in one or the other of the panels or delamination in the panel with slots. The stress calculations at the ultimate moments confirmed the observed failures. The model shown promising results with a range of embedment parameters. Further work will have to be undertaken to refine the embedment characteristic of LVL in rotational partial compression.

Outcomes ⑤

Comparing the analytical model and the experimental results, the general outcomes are provided as follows :

In general, the stiffness is slightly underestimated in the analytical model.

Larger is the transversal clearance C , smaller is the initial stiffness (see Fig.7.20). The contact length, when the embedment starts, is reduced and thus the deformed volume at the directly loaded area is also reduced.

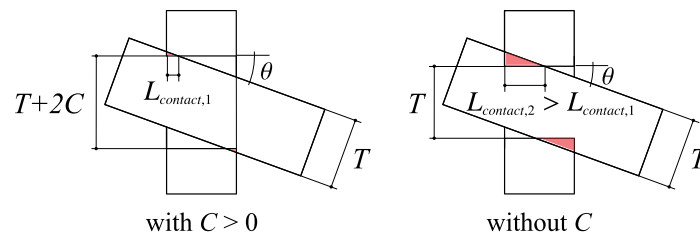


Figure 7.20 – Influence of the transversal clearance C on the contact length.

The dihedral angle coupled to the sense of rotation influences notably the initial stiffness. Similarly to the transversal clearance, they impact the contact length and deformed volumes as presented in Fig.7.21.

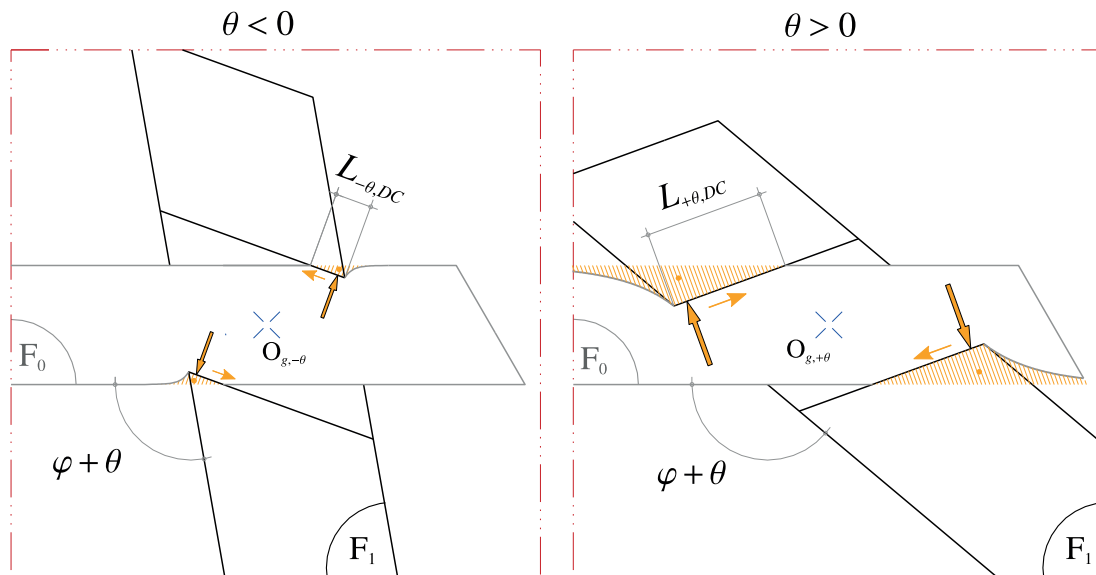


Figure 7.21 – Influence of the dihedral angle φ on the contact length in opening and closing.

The assumption of parallel assembly of the components was experimentally confirmed by

Chapter 7. Semi-rigid Moment-resisting Model of the Through Tenon variant of Multiple Tab-and-Slot Joint for LVL panels

showing proportional stiffnesses with respect to 1,2 or 6 tabs.

The friction between tab and slot flanks (locking faces) can be neglected.

Even if the model was built for the MTSJ TT-variant with $\theta_1, \theta_2, \theta_3 = 0$, MTSJ-TT with $\theta_3 \neq 0$ can be evaluated with good accuracy by considering different widths w_1 of the deformed volumes for the components in double contact *DC1* and *DC2*.

The size and position of the notches also modify the net widths of the deformed volumes.

The limit strength of MTSJ-TT was shown coming from bending into the panels at the places of reduced moment of inertia due to the cuts for tabs and slots.

The moment-rotation relationship provided by the model was computed (in our case with Matlab) as the different integrations of the volumes and calculation of the lever arms were too long and complex to be written as a simple expression. In order to transfer the generalized analytical model to a practical use, a simplified calculation sheet is given for information in appendix A.

References

- [CH07] W.-S. Chang and M.-F. Hsu. Rotational performance of traditional nuki joints with gap ii : the behavior of butted nuki joint and its comparison with continuous nuki joint. *Journal of Wood Science*, 53(5):401–407, 2007.
- [CHK06] W.-S. Chang, M.-F. Hsu, and K. Komatsu. Rotational performance of traditional nuki joints with gap i : Theory and verification. *Journal of Wood Science*, 52(1):58–62, 2006.
- [DG09] T. Descamps and G. Guerlement. Component method for the assessment of the axial, shear and rotational stiffness of connections in old timber frames. In *9ième Congrès de Mécanique, Marrakech*. FS Semlalia, 2009.
- [DL09] T. Descamps and P. Lemlyn. Effects of the rotational, axial and transversal stiffness of the joints on the static response of old timber framings. In Federico Mazzolani, editor, *Protection of Historical Buildings*, volume 1, pages 281–286. PROHITECH 09, 2009.
- [DN09] T. Descamps and J. Noël. Semi-rigid analysis of old timber frames : Definition of equivalent springs for joints modeling, enhancement of the method, numerical and experimental validation. *International Review of Mechanical Engineering*, 3(issue 2):230 – 239, 2009.
- [DWM99] M. Drdácký, F. Wald, and J. Mareš. Modelling of real historic timber joints. *WIT Transactions on the Built Environment*, 39:169–178, 1999.
- [fSC92] European Committee for Standardization (CEN). *ENV 1993-1-1:1992 - Eurocode 3: Design of steel structures - Part 1-1: General rules and rules for buildings, European Prestandard*. (CEN), Brussels, 1992.
- [fSC05] European Committee for Standardization (CEN). *CEN-EN1993-1-1:2005 - Eurocode 3: Design of steel structures - Part 1-1: General rules and rules for buildings*. (CEN), Brussels, 2005.
- [Han21] R. L. Hankinson. Investigation of crushing strength of spruce at varying angles of grain. *Air Force Information Circular No. 259*, 1921.
- [Ina91] M. Inayama. *Wooden Embedment Theory and its Application*. PhD thesis, The University of Tokyo, Tokyo, Japan, 1991. (in Japanese).
- [Ina93] M. Inayama. Study on compression perpendicular to the grain in wood, part 4: analytic functions for the relation between compression load and elastic deformation perpendicular to the grain in wood. In *Proceedings of AIJ, Tokyo, Japan*, pages 907–908, 1993. (in Japanese).
- [KKJM09] K. Komatsu, A. Kitamori, K. Jung, and T. Mori. Estimation of the mechanical properties of mud shear walls subjecting to lateral shear force. In *Proceedings of*

Chapter 7. Semi-rigid Moment-resisting Model of the Through Tenon variant of Multiple Tab-and-Slot Joint for LVL panels

the 11th International Conference on Non-conventional Materials and Technologies (NOCMAT 2009), Bath, UK, 6-9 September 2009.

- [LHFC00] R. J. Leichti, R. A. Hyde, M. L. French, and S. G. Camillos. The continuum of connection rigidity in timber structures. *Wood and Fiber Science*, (1):11–19, 2000.
- [McG95] J. McGuire. Notes on semi-rigid connections. <https://femci.gsfc.nasa.gov/semirigid/>, 1995.
- [OSY15] K. Ogawa, Y. Sasaki, and M. Yamasaki. Theoretical modeling and experimental study of japanese “watari-ago” joints. *Journal of Wood Science*, 61(5):481–491, 2015.
- [SF00] E. P. Saliklis and R. H. Falk. Correlating off-axis tension tests to shear modulus of wood-based panels. *Journal of Structural Engineering*, 126(5):621–625, 2000.
- [Syd05] M. Sydor. *Właściwości konstrukcyjne półsztywnych kątowych połączeń płyt drewnopochodnych ze złączami (eng. Construction properties of semi-rigid joints of wood-based boards with fasteners. PhD dissertation)*. PhD thesis, Faculty of Machines and Transport, Poznań University of Technology, Poland, 2005.
- [SYO12] H. Sakata, Y. Yamazaki, and Y. Ohashi. A study on moment resisting behavior of mortise-tenon joint with dowel or split wedge. In *15th World Conference on Earthquake Engineering, Lisbon, Portugal, 24-28 September 2012*.
- [TOIS11] H. Tanahashi, Y. Ooka, K. Izuno, and Y. Suzuki. Yielding mechanism of embedment of wood and formulation of elasto-plastic embedded displacements. *Journal of Structural and Construction Engineering (Transactions of AIJ)*, 76(662):811–819, 2011. (in Japanese).
- [TOS08] H. Tanahashi, M. Okamura, and Y. Suzuki. Simple formulation of elasto-plastic embedment behavior of orthotropic wood considering densification. In *World Conference on Timber Engineering, Miyazaki, Japan*. Proceedings WCTE 2008, 2008.
- [TS11] H. Tanahashi and Y. Suzuki. Characteristics of elasto-plastic rotational embedment of traditional wooden joints and formulation of crosspiece joints. *Journal of Structural and Construction Engineering (Transactions of AIJ)*, 76(667):1675–1684, 2011. (in Japanese).
- [TS15] H. Tanahashi and Y. Suzuki. Three effects of mechanisms in traditional timber structures. In *IABSE Conference Elegance of Structures, Nara, Japan, May 13-15, 2015*.
- [TSS12] H. Tanahashi, H. Shimizu, and Y. Suzuki. Basic concept and general formulation of restoring force characteristics of traditional wooden joints. In *World Conference on Timber Engineering, Auckland, New Zealand*. Proceedings WCTE 2012, 2012.

- [VESL16] Finland VTT Expert Services Ltd. *Kerto-VTT-C-184-03-Certificate:2016 Kerto-S and Kerto-Q Structural Laminated Veneer Lumber, Certificate NO.184/03*. 2004, Updated 17.5.2016.
- [Zoe83] P. Zoetemeijer. Summary of the research on bolted beam-to-column connections (period 1978 - 1983). Technical report, University of Technology Delft, 1983. Report No. 6-85-M, Steven Laboratory.

Conclusion



8 Conclusion

Design and construction of freeform structures is a pretty hot topic. Various research teams are working on optimization, discretization, planarization, form-finding and so on. The derivation of such work recently appeared in wood construction. The first unconventional timber buildings were designed with bars and nodes and require a big effort of design and computing. The exotic forms proposed by the architects were somewhat rationalized but nevertheless the complexity of the forms led to production of doubly-curved wood members and high machine times. In addition, the cost of water and air tightness when covering such building is also an obstacle to their development.

To overcome these limitations, it is advantageous to combine envelope and structure so that, in a single operation, the following steps of erection can be facilitated. It is the challenge raised by the timber plate structures. Ease of fabrication and build at a reasonable price leads to prefabricate upstream to the workshop to minimize the time spent on site. Reflexion is moved to the design level. At the same time, the algorithms of tessellation and planarization allow to build irregular geometries with only polygonal flat panels. As Robeller explained in his thesis, the passage from a complex surface to the panel cutting, even on a 5-axis machine, is directly linked and straight forward.

Despite all these advantages, there were not any emblematic freeform timber plate at the beginning of the present thesis, except relatively constrained folded plate structures and a spherical dome. For this reason, a preliminary survey was conducted in chapter 2 to get the best practices at least from research projects. This analysis revealed the lack of practical solutions and corresponding model for edge-to-edge angular connections with a certain amount of rigidity. There was even no solution of a moment-resisting wood-to-wood connection except the work initiated at IBOIS but mainly oriented towards geometry and manufacturing. Thus this thesis conducted investigations to confirm an adequate solution and a model proposal.

Investigations

The first investigation (chapter 3) was really a discovery of the IMA developed at IBOIS. The first application which emerged before the beginning of this thesis was the assembly of straight or curved boxed beams. It was the time of the first improvement and development to design and fabricate efficiently such joint. The collaboration with C.Robeller started at this point where the architect needed to accompany his work with a feedback on the mechanical behavior of the

proposed solutions. The geometric complexity of the assembly was understood and explained mathematically with the Bryant's angles. The name of multiple tab-and-slot joint (MTSJ) also came in view of the typology of the connection. However, experimental works began first with the simplest configurations of this one-degree-of-freedom (1DOF) connection: the finger and dovetail type (MTSJ-FJ and MTSJ-DJ, respectively) for assembly of 3-layered boxed beams. The 3-point bending tests on such beam demonstrated that the 1DOF connection is a good alternative in shear to traditional screwed connections with reasonable spacing. It offered a large increase of rigidity with a much lower time of assembly. Moreover, screwed assembly do not comply with standard for such thin panel. The 1DF IMA was confirmed as a semi-rigid connection and numerically modeled accordingly. It was really an important phase to deepen and understand the complexity of the joint, to set up the first tests and to fabricate samples using the five-axis cutting machine. The wood material was also selected at this step among solid wood, solid wood panels (SWP) and laminated veneer lumber with cross-layer (LVL). With a better knowledge of the different constraints, it was also the time to join from a mechanical point of view the new works coming at IBOIS in the field of complex geometries. A teamwork started to design more advanced timber plate structures connected with MTSJ joint, using the fold or not. The exploration of other load cases than shear was decided (e.g. moment about edges of plate elements) and modeling the local semi-rigid behavior was one of the challenge to finely perform global structural analyzes.

During these exploratory works, the IBOIS projects moved to more complex applications such as surface-active structures (SAS). Attention was focused on the prefabrication of discrete plates or sub-modules in the workshop, which are then erected and arranged on site. This division for reasons of transportation and manufacturing introduced points of weakness in these SAS. Reconstituting sufficient rigidity is therefore essential for the overall performance of such structures. It guided the work of this thesis on the rotational stiffness as a first priority. Among SAS, the folded plate structures (FPS) are solutions to provide higher static height to thin panels, by the fold. Doubly-curved prototype of such FPS was built at IBOIS. It needed the in-space multi-edge interlocking connection of discrete panels. The MTSJ was adapted in its Japanese variant (MTSJ-JJ, Nejiri Arigata design) that allows the insertion of plates with multi-edges connected at a time. It overcame the issue of screws which not comply with the required edge distance recommended by the standards. The geometry of the joints is much more complex. Hence, parametric design and five-axis cutting are essential. As before, the joint is milled during cutting at the outline of the plates. Then the plates were assembled in space without assembly template or falsework. The geometry, the fabrication and the assembly was solved by C. Robeller but what about the mechanical behavior of this solution. The second investigation (chapter 4) was carried out on the bending stiffness at the ridges to clarify this question mark. MTSJ-JJ with two tabs were tested on a dedicated folding machine, considering different combination of the Bryant's angle. The combinations were theoretically determined with respect to the tool inclination limit and the dihedral angle, as well as the angle between consecutive edges on the contour of a plate. The experimental results generally showed a ductile behavior but with a relatively low stiffness. A numerical model based on continuum damage mechanisms was implemented and announced good

opportunities to numerically simulated bending and certainly also later complementary loading cases. The model was finally transferred to A.C.Nguyen for further works. Both experimentally and numerically, the rotational stiffness was too low with open slots. The results of this investigation were presented at the IABSE conference in Nara(Japan).

An evolution with through tenon and closed slots (MTSJ-TT) was used at the same time to build a double-layer curved shell with a Miura-Ori pattern. The geometry of the SAS started to move from folded plates to more freeform design with double layers. The bi-layered system have two main advantages, the increase of the static height and a cavity for blown-in thermal insulation. It keeps also advantages of prefabrication in a more rigid and compact way. Bending tests on MTSJ-TT demonstrated a rotational stiffness equivalent or higher to that of a screwed joint without the drawbacks of edge distance constraints. From the literature review came the first tracks to analytically study the mechanisms that make MTSJ-TT stiffer in bending than others variants. The embedment effect was pointed out after a detailed examination of the areas deformed by rotational partial compression (RPC) perpendicular to the panel plane. Searching for embedment effect was inspired by the work of the Japanese researchers, which used it to simulate the moment-resiting behavior of the Nuki joint, a beam penetrating through a column, in ancestral shrines. During the IABSE conference, I met Prof. H.Tanahashi and discussed with him about publications on the topic.

Thus, Chapter 5 was the transcript of this preliminary investigation on MTSJ-TT and its triangular embedment effect. The bending tests on the MTSJ-TT were summarized comparatively to the stiffer joint of the 2nd investigation, screwed solutions and example of snap-fit variants. The snap-fit variant was not developed in this thesis. It is a solution that provides an additional function to lock the last degree of freedom (the one in the insertion direction), unfortunately at the price of a smaller effective embedded surface when subjected to bending. The comparison confirmed that MTSJ-TT performs the best as a moment-resisting angular connection for thin LVL panels. The triangular embedment effect for a such joint was described for the components both in single contact(SC) and double contact(DC). Each components were based on the same analytical expression of the elastic and plastic deformed volumes but with different values of the parameters. An experimental method was provided to analyze the additional part of the volumes whose profile is approximated by an exponential function where the deformation spread beyond the directly loaded area. First estimations of the decay coefficients of the exponential function and the yield angles were given for the RPC of 21mm-thick LVL Kerto-Q panels perpendicularly loaded to their plane, with a joint-to-grain angle set to 0°. The joint-to-grain angle is typically the usual angle-to-grain turned of 90°. The identified embedment mechanism explained the semi-ductile behavior that was identified from the moment-rotation curves of the tests.

As embedment effect of LVL Kerto-Q in RPC is one of the key points of this thesis, the previous estimation of the additional length characteristics were completed by new investigations (Chapter 6) with a larger range of joint-to-grain angles (0° to 90° with increments of 15°) and various thicknesses (21, 27, 39mm). The previous methods of analysis were reproduced with an improvement of the SC setup and a new setup for DC. The image-based method used to fit the additional deformed part profile showed limitations for certain joint-to-grain angle. To

overcome the limitations, the analyses were performed, this time, through simplified analytical models. A range of decay coefficients with respect to yield angles between 0.5° and 3° were supplied, both in SC and DC. Most of the conclusions of Japanese research were confirmed, the main ones being that the decay coefficients are larger at 0° than at 90° and increase from SC to DC. With high decay coefficients, it could be assumed that there is not any additional effect. The new approach with an analytical model was applied to more than 150 specimens, with at least 5 replicates for each configuration. The number of replicates is tight to characterize a material properties but the moment-rotation curves were close. It is worth noting that the RPC topic could be a complete object of study. The first collected data gave a basis of work to develop and feed a upgraded moment-resisting model extended to the behavior of the whole MTSJ-TT.

This global model of MTSJ-TT was finally presented in details in Chapter 7. It was limited to geometries having the Bryant's angles all set to zero. From the kinematics of the joint under moment about its axis, the local forces and corresponding lever arms which resist to the induced rotation were expressed from the embedded volumes and the Hook's law. The plastic range was also addressed by the calculation of the plastic volume after the yield angle and its proportion on the full deformed volume. A reduction factor was employed to penalize the elastic modulus of LVL perpendicular to grain at the plastic state. The influence on the stiffness of the initial slip angle due to transversal clearance, the dihedral angle and the total slot length ratio to joint length were highlighted. Generally speaking, the predicted stiffnesses of the 17 different geometries seemed conservative compared with the experimental results. It placed the model on the safe side of limit state analyzes. The failures came by bending or by delamination into the panels at the place where the cut tabs and slots weaken the panels. The model shown promising results and a simplified method for "manual" calculation was provided in appendix A.

Strong potential in timber plate structures

MTSJ was first used on prototype of laboratories and derived in different variants. The simplest one, MTSJ-FJ and MTSJ-DJ are very similar to connections used in the furniture market. Their easy-to-achieve geometry demonstrated a real potential to transfer shear in very basic component like beams. It can be imagined to derive such connection for timber wall or elements of floor. The more complex MTSJ-JJ is also more versatile, with providing possibility to set the insertion direction for simultaneous multi-edge assembly in space. If, in addition, the rotational stiffness at edges needs to be improved, MTSJ-TT offers with through tenon and closed clots a very efficient alternative to usual metal connectors. Without adhesive bonding or metal fasteners, it can transfer significant bending moment between discrete elements in a surface-active structures even with an irregular freeform.

Appendices



A Simplified methodology for the calculation of MTSJ-TT in pure bending

Hereafter is proposed a simplified approach which allows to calculate “manually” the rotational behavior of the joint under certain assumptions.

Appendix A. Simplified methodology for the calculation of MTSJ-TT in pure bending

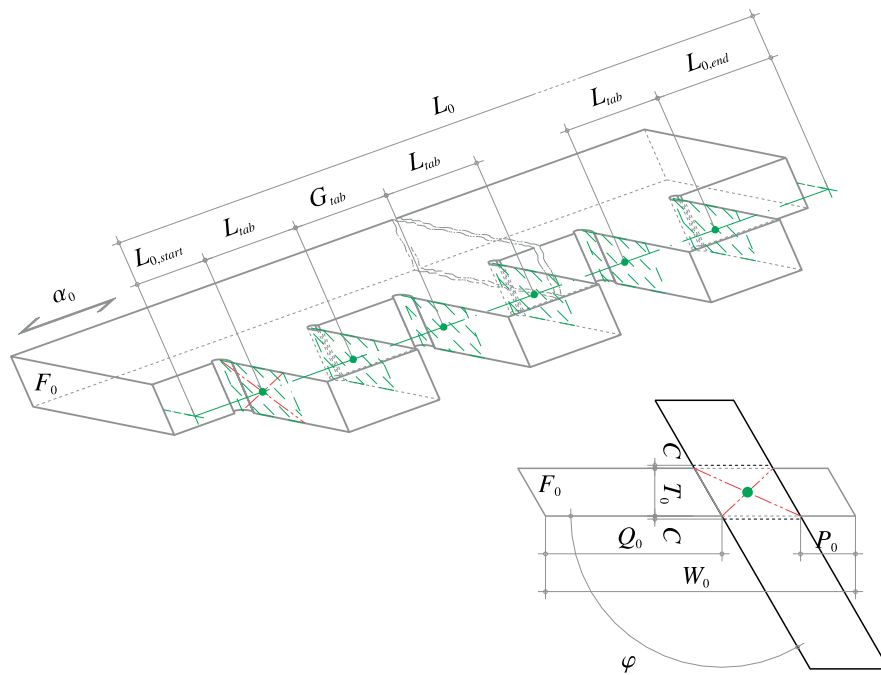
A.1 Parameters

A.1.1 Geometry

The geometrical parameters of the MTSJ-TT are defined for :

- panel F_0 in Fig.A.1,
- panel F_1 in Fig.A.2,
- the assembly of panels F_0 & F_1 and the notch reductions due of the tool path, in Fig.A.3.

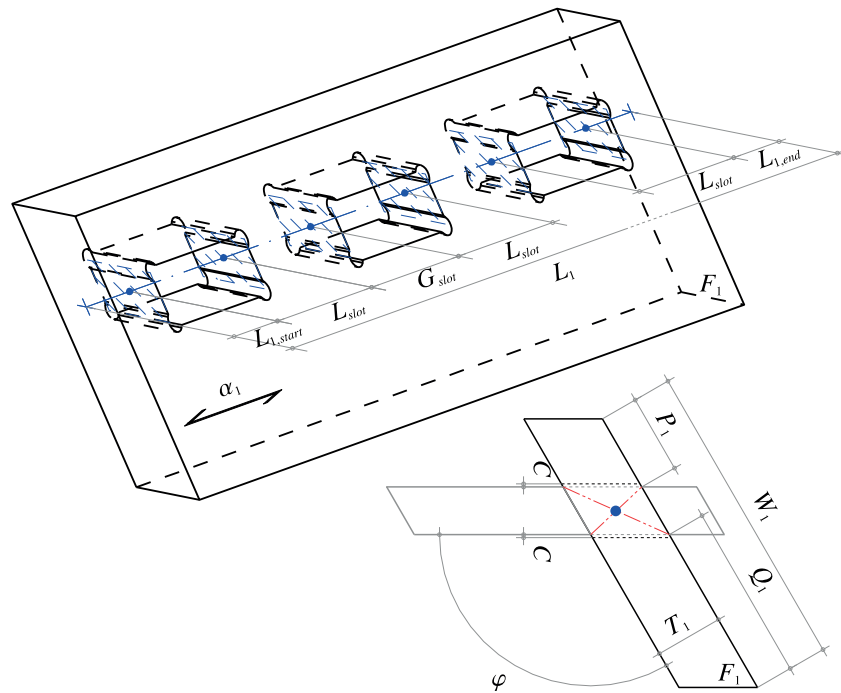
Panel F_0



$L_{0,start}$: Start length to the 1 st tab (mm)	$L_{0,end}$: End length from the last tab (mm)
L_0	: Total length (mm)	W_0	: Total width (mm)
L_{tab}	: Tab length (mm)	G_{tab}	: Gap between tabs (mm)
T_0	: Thickness (mm)	α_0	: joint-to-grain angle (°)
P_0	: Tab protrusion (end length) (mm)	Q_0	: Panel side end length (mm)
$N_{0,diameter}$: Notch diameter (mm)	$N_{0,offset}$: Notch offset (mm)
N_{tab}	: Number of tabs	$N_{0,type}$: Notch type, “b” bisector, “tl” tangent offset along, “tt” tangent offset across

Figure A.1 – MTSJ-TT geometric parameters of panel F_0

Panel F_1



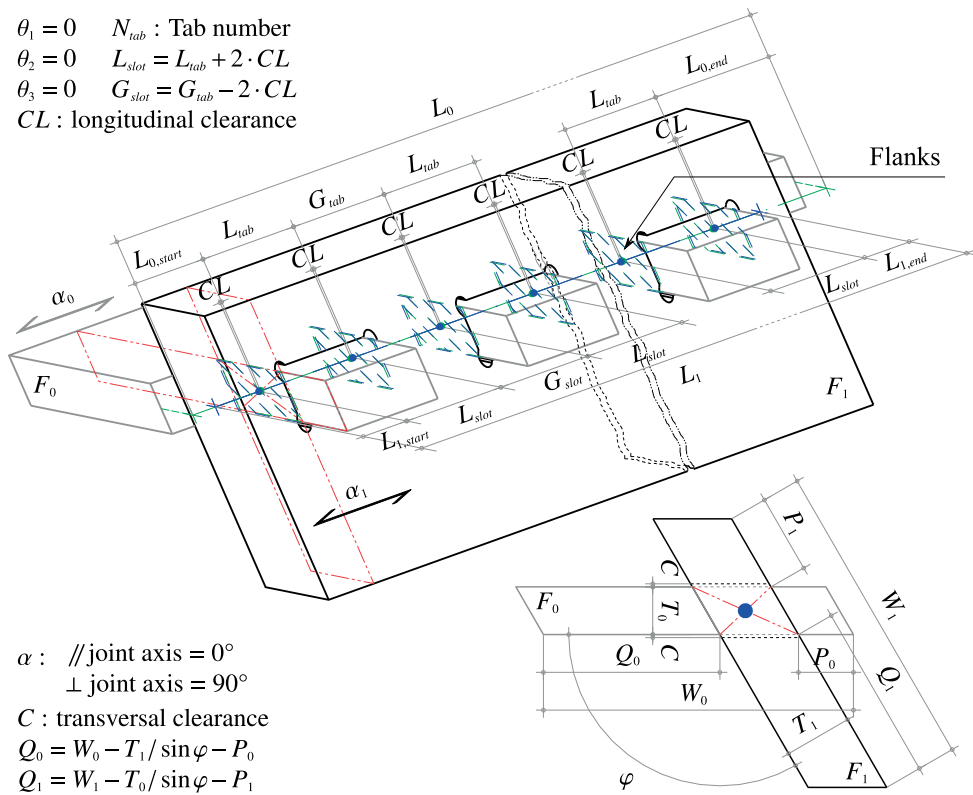
$L_{1,start}$: Start length to the 1 st slot (mm)	$L_{1,end}$: End length from the last slot (mm)
L_1	: Total length (mm)	W_1	: Total width (mm)
T_1	: Thickness (mm)	α_1	: joint-to-grain angle (°)
P_1	: Slot protrusion (end length) (mm)	Q_1	: Panel side end length (mm)
L_{slot}	: Slot length (mm)	G_{slot}	: Gap between slots (mm)
$N_{1,diameter}$: Notch diameter (mm)	$N_{1,offset}$: Notch offset (mm)
H_{slot}	: Slot height (mm)	$N_{1,type}$: Notch type , “b” bisector, “tl” tangent offset along, “tt” tangent offset across

Figure A.2 – MTSJ-TT geometric parameters of panel F_1

Appendix A. Simplified methodology for the calculation of MTSJ-TT in pure bending

Assembly of panels F_0 and F_1

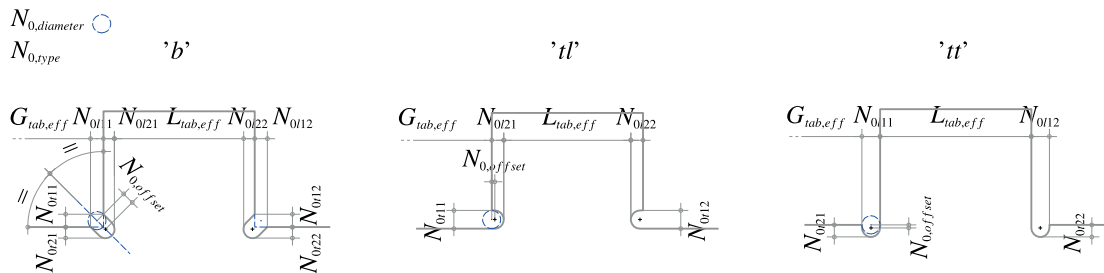
$$\begin{aligned} \theta_1 = 0 & \quad N_{tab} : \text{Tab number} \\ \theta_2 = 0 & \quad L_{slot} = L_{tab} + 2 \cdot CL \\ \theta_3 = 0 & \quad G_{slot} = G_{tab} - 2 \cdot CL \\ CL & : \text{longitudinal clearance} \end{aligned}$$



$$\begin{aligned} \alpha & : \text{// joint axis} = 0^\circ \\ & \quad \perp \text{ joint axis} = 90^\circ \\ C & : \text{transversal clearance} \\ Q_0 & = W_0 - T_1 / \sin \varphi - P_0 \\ Q_1 & = W_1 - T_0 / \sin \varphi - P_1 \end{aligned}$$

$$\theta_1, \theta_2, \theta_3 : \text{The Bryant's angles } (^\circ) \quad \varphi : \text{Dihedral angle } (^\circ)$$

Notch reduction - Tab Panel F_0



Notch reduction - Slot Panel F_1

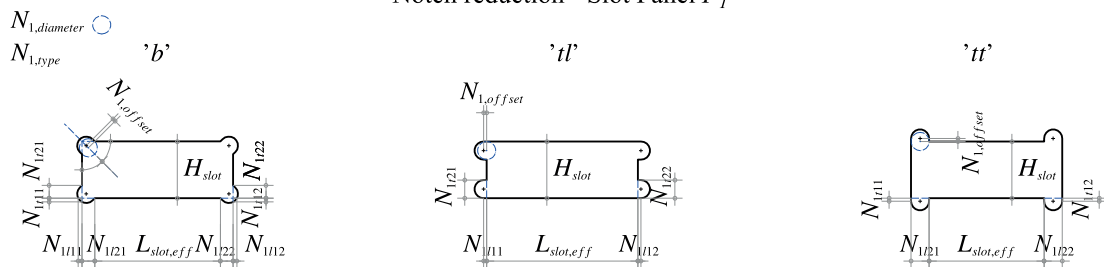


Figure A.3 – MTSJ-TT geometric parameters of F_0 – F_1 assembly and notches

A.1.2 Material properties

The material properties of engineered wood products are usually provided by datasheet of manufacturers or obtained by specific tests.

Elastic properties of the material

e.g. LVL Kerto-Q (mean values)

Property	Symbol	orthotropic	21mm*	27-39mm	Unit
Bending strength					
// to grain, flatwise	$f_{m,0,flat,mean}$ **		40	45	Mpa
⊥ to grain, flatwise	$f_{m,90,flat,mean}$ **		16.8	9.6	Mpa
Elastic modulus					
// to grain, along	$E_{0,mean}$	E_{11}	10000	10500	Mpa
⊥ to grain, edgewise	$E_{90,edge,mean}$	E_{22}	2400	2400	Mpa
⊥ to grain, flatwise	$E_{90,flat,mean}$	E_{33}	130	130	Mpa
Shear modulus					
Edgewise	$G_{0,edge,mean}$	G_{12}	600	600	Mpa

Note that the angle to grain is equal to $90^\circ - \alpha$

* 21mm with | - || - | arrangement layer

** The mean value is obtained from the characteristic value by multiplying by 1.20

Table A.1 – Elastic properties of LVL Kerto-Q (mean values)

Elastic modulus E_θ with respect to the rotation angle θ

The Hankinson's formula is used to correct the elastic modulus perpendicular to the panel plane with respect to the rotation angle θ .

$$E_\theta = \frac{E_\alpha \cdot E_{33}}{E_{33} \sin^c \theta + E_\alpha \cos^c \theta} \quad (\text{A.1})$$

e.g. c is equal to 1.8 for LVL Kerto-Q.

Elastic modulus E_α with respect to the joint-to-grain angle α

The Saliklis' formula is used to calculate the in-plane elastic modulus according to the angle α between the joint rotation axis and the grain.

$$\frac{1}{E_\alpha} = \frac{\cos^4 \alpha}{E_{22}} + \frac{\sin^4 \alpha}{E_{11}} + \frac{\cos^2 \alpha \cdot \sin^2 \alpha}{A^{2 \cdot A} \cdot G_{12}} \quad (\text{A.2})$$

e.g. A is equal to 0.7 for LVL Kerto-Q

A.2 Semi-rigid moment-resisting behavior of MTSJ-TT

A.2.1 Kinematics in pure bending

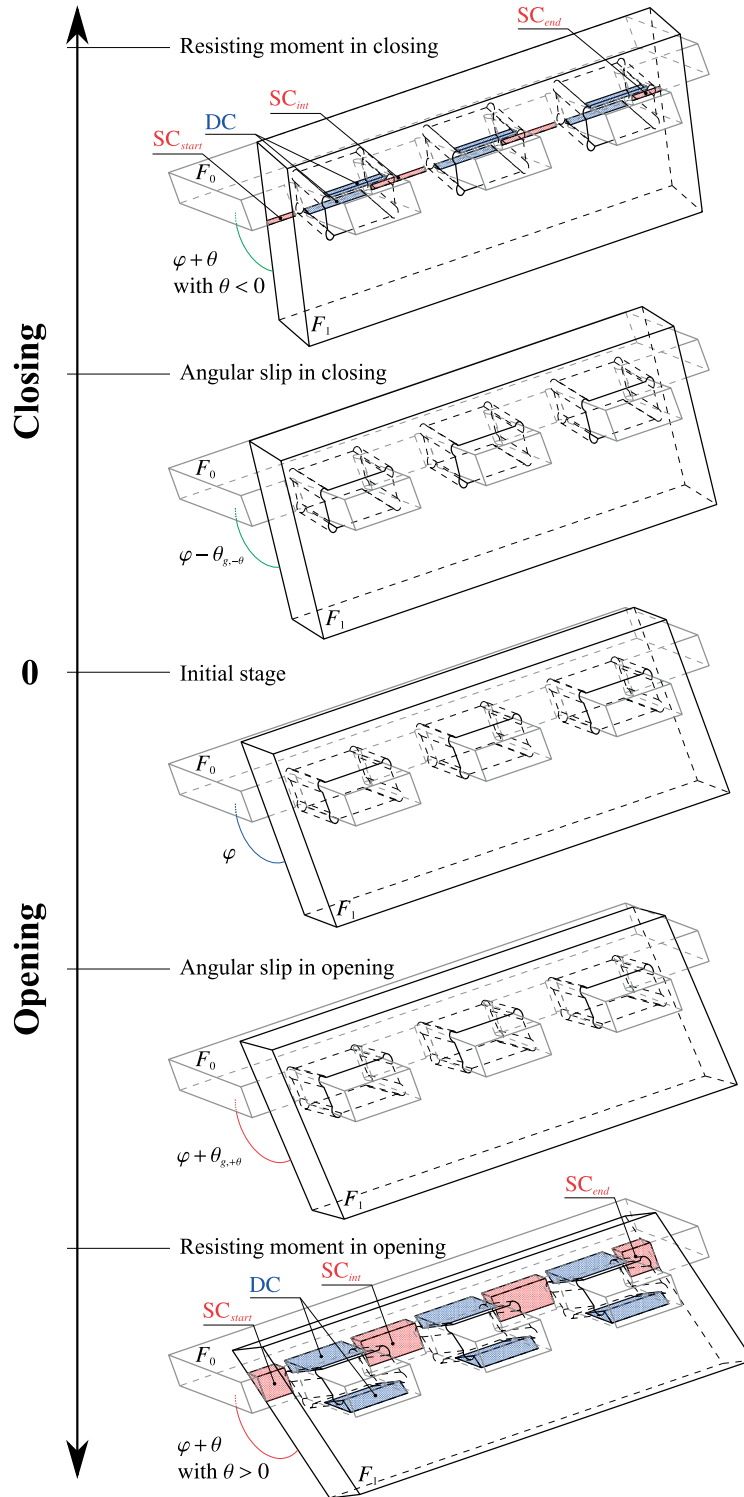


Figure A.4 – MTSJ-TT under bending : Closing ($\theta < 0$) and Opening ($\theta > 0$).

A.2.2 Assumptions for simplification

1. If the transversal clearance C is less than 0.05 (normally possible with CNC machine), it can be neglected in the exact equations presented in chapter 7. Under this condition, the angular slips are neglected both in closing and opening (see Fig.A.4).

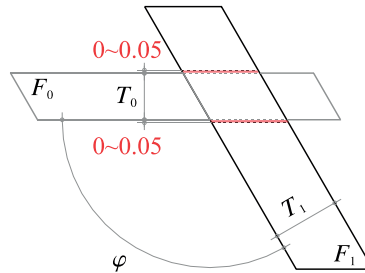


Figure A.5 – Tolerances for transversal clearance C .

2. The thicknesses T_0 and T_1 of the panels F_0 and F_1 are both set equal to T as it is usually the case in timber plate structures.
3. The simplified formulas are just proposed in the elastic stage with a rotation angle $\theta < 10^\circ$:
 - (a) the rotational stiffness is k_θ as shown in Fig.A.6
 - (b) $\tan \theta \approx \theta$ in rad
 - (c) $\sin \theta \approx \theta$ in rad
 - (d) $\cos \theta \approx \left(1 - \frac{\theta^2}{2}\right)$ in rad
4. The material and the joint-to-grain angle α are the same for both panels : $E_{\theta, F_0} = E_{\theta, F_1} = E_\theta$,
 $b_{V_4, F_0, SC} = b_{V_4, F_1, SC} = b_{V_4, SC}$ and $b_{V_4, F_0, DC} = b_{V_4, F_1, DC} = b_{V_4, DC}$.

A.2.3 Characteristic moment-rotation curve

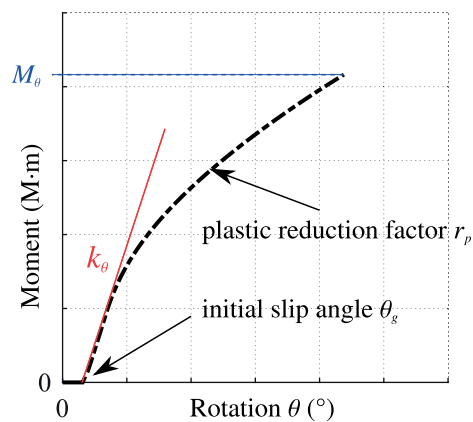


Figure A.6 – Semi-rigid moment-resisting behavior of MTSJ-TT.

Appendix A. Simplified methodology for the calculation of MTSJ-TT in pure bending

The simplified methodology allows to determine the ultimate moment M_θ from the bending strength and the initial stiffness k_θ when $\theta < 10^\circ$. Both are depicted in Fig.A.6.

A.2.4 Simplified formulas

By rotational partial compression perpendicular to the plane of the panels (embedment effect), the components, in single contact, “*SC, start*” at the start of the joint, “*SC, end*” at the end of the joint, “*SC, int*” at each gap between slots and, in double contact, “*DC1*” and “*DC2*” at each tab can be described by Fig.A.7(b) in a simplified form.

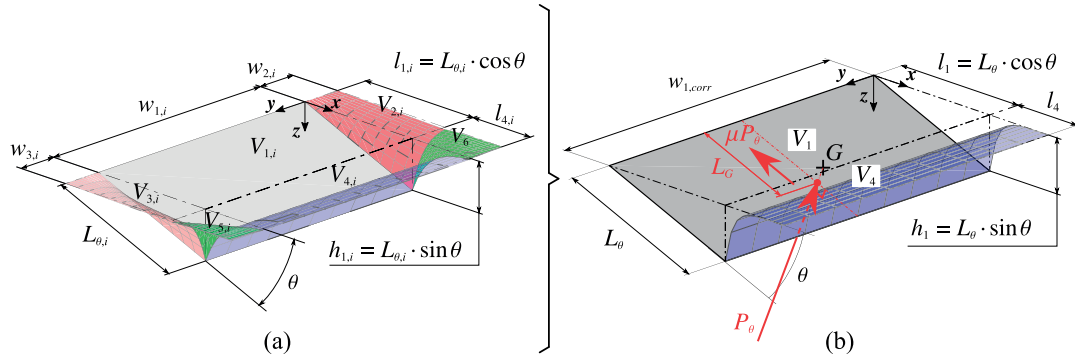


Figure A.7 – Simplified embedded volumes for stiffness formula.

Under the assumptions of section A.2.2, the following formulas apply indifferently to the different components *SC, start*, *SC, int*, *SC, end*, *DC1* and *DC2*, substituting in each the relevant values for T , φ , θ , L_θ , l_1 , h_1 , $w_{1,corr}$, l_4 , b_{V_4} and E_θ .

Contact lengths in single and double contact (in mm)

If the dihedral angle φ is not equal to 90° , the contact lengths in closing Eq.(A.3a) and opening Eq.(A.3b) are different.

$$L_{-\theta} = \frac{1}{2}T \left(\frac{1}{\tan \frac{\varphi}{2}} - \frac{\theta}{2} \right) \quad \text{if closing } \theta < 0 \quad (\text{A.3a})$$

$$L_{+\theta} = \frac{1}{2}T \left(\tan \frac{\varphi}{2} + \frac{\theta}{2} \right) \quad \text{if opening } \theta > 0 \quad (\text{A.3b})$$

After calculation, L_θ will be set to $L_{-\theta}$ or $L_{+\theta}$, according to the direction of folding. Then, L_θ applies in the following formulas. For the calculation of the embedded volumes, it is worth noting that

$$l_1 = L_\theta \cos \theta \approx L_\theta \left(1 - \frac{\theta^2}{2} \right) \quad \text{if } \theta < 10^\circ \quad (\text{A.4a})$$

$$h_1 = L_\theta \sin \theta \approx L_\theta \theta \quad \text{if } \theta < 10^\circ \quad (\text{A.4b})$$

Embedded volumes in elastic range (in mm³)

From Fig.A.7(b), the deformed volume V of each component can be expressed from (A.5c) which is the sum of the elementary volumes V_1 and V_4 calculated from (A.5a) and (A.5b), respectively.

$$V_1 = \frac{1}{2}\theta w_{1,corr} l_1^2 \quad (A.5a)$$

$$V_4 = w_{1,corr} h_1 \frac{(1 - e^{-b_{V_4} l_4})}{b_{V_4}} \quad (A.5b)$$

$$V = V_1 + V_4 = w_{1,corr} \frac{\left(\frac{1}{2}\theta l_1^2 b_{V_4} - h_1 e^{-b_{V_4} l_4} + h_1 \right)}{b_{V_4}} \quad (A.5c)$$

Reaction force (in N)

The reaction force P of each component is obtained from the Hook's law written as

$$P = \frac{V}{T} \cdot E_\theta = \frac{E_\theta w_{1,corr}}{b_{V_4} T} \left(\frac{1}{2} b_{V_4} \theta l_1^2 + h_1 (1 - e^{-b_{V_4} l_4}) \right) \quad (A.6)$$

Lever arm (in mm)

$$L_G = x_G \left(1 - \frac{\theta^2}{2} \right) + z_G \theta$$

$$= \frac{-6h_1 (\theta^2 - 2) (e^{-b_{V_4} l_4} (b_{V_4} l_1 + b_{V_4} l_4 + 1) - b_{V_4} l_1 - 1) + 3b_{V_4} h_1^2 \theta (e^{-2b_{V_4} l_4} - 1) - 4\theta l_1^3 b_{V_4}^2}{12b_{V_4} \left(-\frac{1}{2} b_{V_4} \theta l_1^2 + h_1 (e^{-b_{V_4} l_4} - 1) \right)} \quad (A.7)$$

L_G , in Eq.(A.7), is the length of the orthogonal projection onto the contact area (in gray Fig.A.7b) of the vector between the points $(0, y_G, 0)$ and (x_G, y_G, z_G) . (x_G, y_G, z_G) are the coordinates of the exact center of gravity G of the volume V .

$$LA = L_G - \frac{T}{4}\theta \quad (A.8)$$

LA is the lever arm between the support line of the reaction force, perpendicular to the contact area and the rotation axis of the joint.

Appendix A. Simplified methodology for the calculation of MTSJ-TT in pure bending

Elementary resisting moments (in N.m)

The resisting moment of each component is defined as

$$\begin{aligned}
 M &= P \cdot \frac{LA}{1000} \\
 &= \frac{E_{\theta} w_{1,corr}}{4000 b_{V_4}^2 T} \left(\left((2l_1 + 2l_4) \theta^2 + T\theta - 4l_1 - 4l_4 \right) b_{V_4} + 2\theta^2 - 4 \right) h_1 e^{-b_{V_4} l_4} \\
 &\quad - e^{-2b_{V_4} l_4} b_{V_4} h_1^2 \theta + b_{V_4} h_1^2 \theta + \left(-2l_1 \theta^2 - T\theta + 4l_1 \right) b_{V_4} - 2\theta^2 + 4 \Big) h_1 \\
 &\quad - \frac{1}{2} \theta l_1^2 \left(T\theta - \frac{8}{3} l_1 \right) b_{V_4}^2 \Big)
 \end{aligned} \tag{A.9}$$

The additional resisting moment of each component due to friction is

$$\begin{aligned}
 MF &= P \cdot \frac{T}{2 \cdot 1000} \cdot \mu \\
 &= \frac{E_{\theta} w_{1,corr}}{2000 b_{V_4}} \left(\frac{1}{2} b_{V_4} \theta l_1^2 + h_1 (1 - e^{-b_{V_4} l_4}) \right) \cdot \mu
 \end{aligned} \tag{A.10}$$

Total resisting moment (in N.m)

Then the total resisting moment of the whole joint is obtained by the assembly in parallel of all the active components. This assembly in the elastic stage can be written by the following equations :

Elastic stage

SC

$$M_{SC} = M_{SC_{start}} + M_{SC_{int}} \cdot (N_{tab} - 1) + M_{SC_{end}} \tag{A.11a}$$

$$MF_{SC} = MF_{SC_{start}} + MF_{SC_{int}} \cdot (N_{tab} - 1) + MF_{SC_{end}} \quad (\text{if friction}) \tag{A.11b}$$

DC

$$M_{DC} = (M_{DC_1} + M_{DC_2}) \cdot N_{tab} \tag{A.11c}$$

$$MF_{DC} = (MF_{DC_1} + MF_{DC_2}) \cdot N_{tab} \quad (\text{if friction}) \tag{A.11d}$$

Total

$$M_{\theta} = M_{DC} + M_{SC} + MF_{DC} + MF_{SC} \tag{A.11e}$$

A.3 Serviceability Limit States (SLS)

A.3.1 Limitation of the rotation angle

According to the assumptions already mentioned,

$$0^\circ < \theta < 10^\circ \quad (\text{A.12})$$

A.3.2 Elementary rotational stiffnesses (in N·m/°)

The initial stiffness of each component is defined as

$$k = \frac{E_\theta w_{1,corr} \pi}{720000 b_{V_4}^2 T \theta} \left(\left((2l_1 + 2l_4) \theta^2 + T \theta - 4l_1 - 4l_4 \right) b_{V_4} + 2\theta^2 - 4 \right) h_1 e^{-b_{V_4} l_4} - e^{-2b_{V_4} l_4} b_{V_4} h_1^2 \theta + b_{V_4} h_1^2 \theta + \left(-2l_1 \theta^2 - T \theta + 4l_1 \right) b_{V_4} - 2\theta^2 + 4 \right) h_1 - \frac{1}{2} \theta l_1^2 \left(T \theta - \frac{8}{3} l_1 \right) b_{V_4}^2 \quad (\text{A.13})$$

The additional initial stiffness of each component due to friction is

$$kF = \frac{E_\theta w_{1,corr}}{2000 b_{V_4} \theta} \left(\frac{1}{2} b_{V_4} \theta l_1^2 + h_1 (1 - e^{-b_{V_4} l_4}) \right) \cdot \mu \quad (\text{A.14})$$

Total rotational stiffness (in N·m/°)

Then the total rotational stiffness of the whole joint is obtained by the assembly in parallel of all the active components. This assembly in the elastic stage can be written by the following equations :

Elastic stage

SC

$$k_{SC} = k_{SC_{start}} + k_{SC_{int}} \cdot (N_{tab} - 1) + k_{SC_{end}} \quad (\text{A.15a})$$

$$kF_{SC} = kF_{SC_{start}} + kF_{SC_{int}} \cdot (N_{tab} - 1) + kF_{SC_{end}} \quad (\text{if friction}) \quad (\text{A.15b})$$

DC

$$k_{DC} = (k_{DC_1} + k_{DC_2}) \cdot N_{tab} \quad (\text{A.15c})$$

$$kF_{DC} = (kF_{DC_1} + kF_{DC_2}) \cdot N_{tab} \quad (\text{if friction}) \quad (\text{A.15d})$$

Total

$$k_\theta = k_{DC} + k_{SC} + kF_{DC} + kF_{SC} \quad (\text{A.15e})$$

Appendix A. Simplified methodology for the calculation of MTSJ-TT in pure bending

A.4 Ultimate Limit States (ULS)

With protrusions $P_0, P_1 \geq T$, the ultimate moment is due to bending into the panels with the smallest effective moment of inertia.

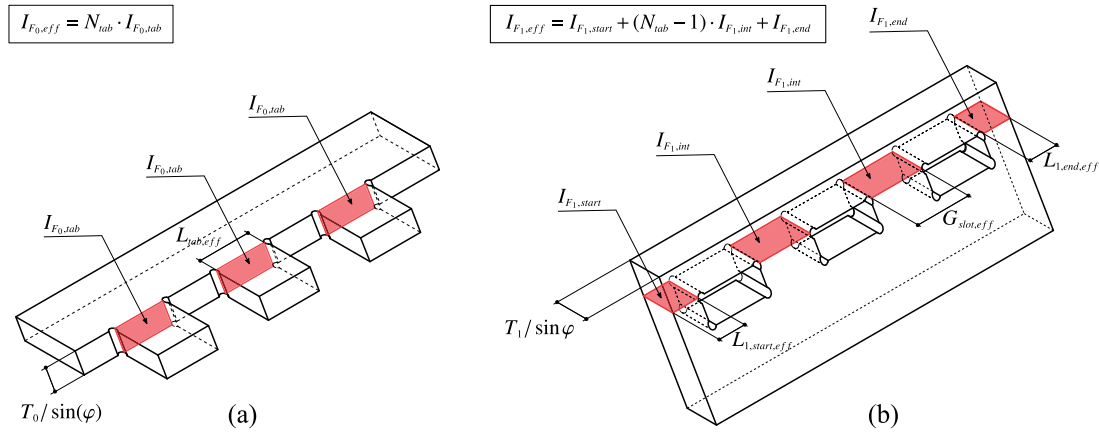


Figure A.8 – Effective moment of inertia for MTSJ-TT bending strength.

$$M_{b,F_0} = \frac{f_{m,90-a,flat,mean} \cdot N_{tab} \cdot L_{tab,eff} \cdot T^2}{6 \cdot \sin^2 \varphi \cdot 1000} \quad (A.16a)$$

$$M_{b,F_1} = \frac{f_{m,90-a,flat,mean} \cdot (L_{1,start,eff} + (N_{tab} - 1) \cdot G_{slot,eff} + L_{1,end,eff}) \cdot T^2}{6 \cdot \sin^2 \varphi \cdot 1000} \quad (A.16b)$$

$$M_{\theta} \leq (M_{b,F_0} + M_{b,F_1}) \quad (A.17)$$

A.5 Examples

The sample 21-02 of chapter 7 was evaluated in closing with a simplification of the initial parameters.

A.5.1 Geometrical parameters

θ_1	θ_2	θ_3	φ	T	N_{tab}	CL	C
0	0	0	90	21	2	0	0

$L_{0,start}$	L_{tab}	G_{tab}	$L_{0,end}$	L_0	W_0	P_0	α_0	$N_{0,diameter}$	$N_{0,type}$	$N_{0,offset}$
25	50	50	25	200	200	21	0	12	'b'	0

$L_{1,start}$	L_{slot}	G_{slot}	$L_{1,end}$	L_1	W_1	P_1	α_1	$N_{1,diameter}$	$N_{1,type}$	$N_{1,offset}$
25	50	50	25	200	200	21	0	12	'b'	0

Table A.2 – Geometrical parameters of the example case (in mm)

A.5.2 Material properties

LVL Kerto-Q 21 mm with $\alpha = 0^\circ$ and $\theta = 8^\circ$:

- Bending strength $f_{m,90-\alpha,flat,mean} = f_{m,90,flat,mean} = 16.8$ Mpa
- Elastic modulus $E_\alpha = E_{22} = 2400$ Mpa
- Elastic modulus $E_\theta = 132.10$ Mpa for $\theta = 8^\circ$

A.5.3 Simplified formulas

Contact lengths in single and double contact (in mm)

$$L_\theta = 11.23 \text{ mm}$$

Calculation of embedded volumes

	SC_{start}	SC_{int}	SC_{end}	$DC1$	$DC2$
$w_{1,corr}$ (mm)	19	38	19	38	38
l_4 (mm)	158	158	158	21	157.5
b_{V_4} (mm)	0.26	0.26	0.26	1.72	1.72
V_1 (mm ³)	164	328	164	328	328
V_4 (mm ³)	114	229	114	35	35
V (mm ³)	278	557	278	363	363

Calculation of reaction forces (in N)

	SC_{start}	SC_{int}	SC_{end}	$DC1$	$DC2$
P	1753	3506	1753	2283	2283

Calculation of the lever arms (in mm)

	SC_{start}	SC_{int}	SC_{end}	$DC1$	$DC2$
LA	9.75	9.75	9.75	7.09	7.09

Calculation of the elementary resisting moments (in N.m)

	SC_{start}	SC_{int}	SC_{end}	$DC1$	$DC2$
M	17.1	34.2	17.1	16.2	16.2
MF	3.7	7.4	3.7	4.8	4.8

Calculation of the total resisting moment (in N.m)

$$M_{SC} = 68.4 \text{ N} \cdot \text{m}$$

$$MF_{SC} = 14.8 \text{ N} \cdot \text{m}$$

$$M_{DC} = 64.8 \text{ N} \cdot \text{m}$$

$$MF_{DC} = 19.2 \text{ N} \cdot \text{m}$$

$$M_\theta = 167.2 \text{ N} \cdot \text{m}$$

Appendix A. Simplified methodology for the calculation of MTSJ-TT in pure bending

Calculation of elementary rotational stiffnesses (in N·m/°)

	SC_{start}	SC_{int}	SC_{end}	$DC1$	$DC2$
k	2.13	4.27	2.13	2.02	2.02
kF	0.46	0.92	0.46	0.60	0.60

Calculation of the total rotational stiffness (in N·m/°)

$$k_{SC} = 8.53\text{N} \cdot \text{m}/^\circ$$

$$kF_{SC} = 1.84\text{N} \cdot \text{m}/^\circ$$

$$k_{DC} = 8.08\text{N} \cdot \text{m}/^\circ$$

$$kF_{DC} = 2.40\text{N} \cdot \text{m}/^\circ$$

$$k_\theta = 20.9\text{N} \cdot \text{m}$$

Calculation of the maximal bending moments in N·m/°

$$N_{0,type} = N_{1,type} = "b" \quad \longrightarrow \quad L_{tab,eff} = L_{tab}, L_{1,start,eff} = L_{1,start}, L_{1,end,eff} = L_{1,end}, G_{slot,eff} = G_{slot}$$

$$M_{b,F_0} = 123.5\text{N} \cdot \text{m} \quad \text{for panel } F_0$$

$$M_{b,F_1} = 123.5\text{N} \cdot \text{m} \quad \text{for panel } F_1$$

$$M_\theta (= 167.2) \leq 247\text{N} \cdot \text{m} \quad \text{for the MTSJ-TT}$$

B MTSJ Geometry Script

Since the number of samples to be prepared was huge, A Python script have been developed under Rhinoceros©5.0 during the present thesis. The algorithm is described below :

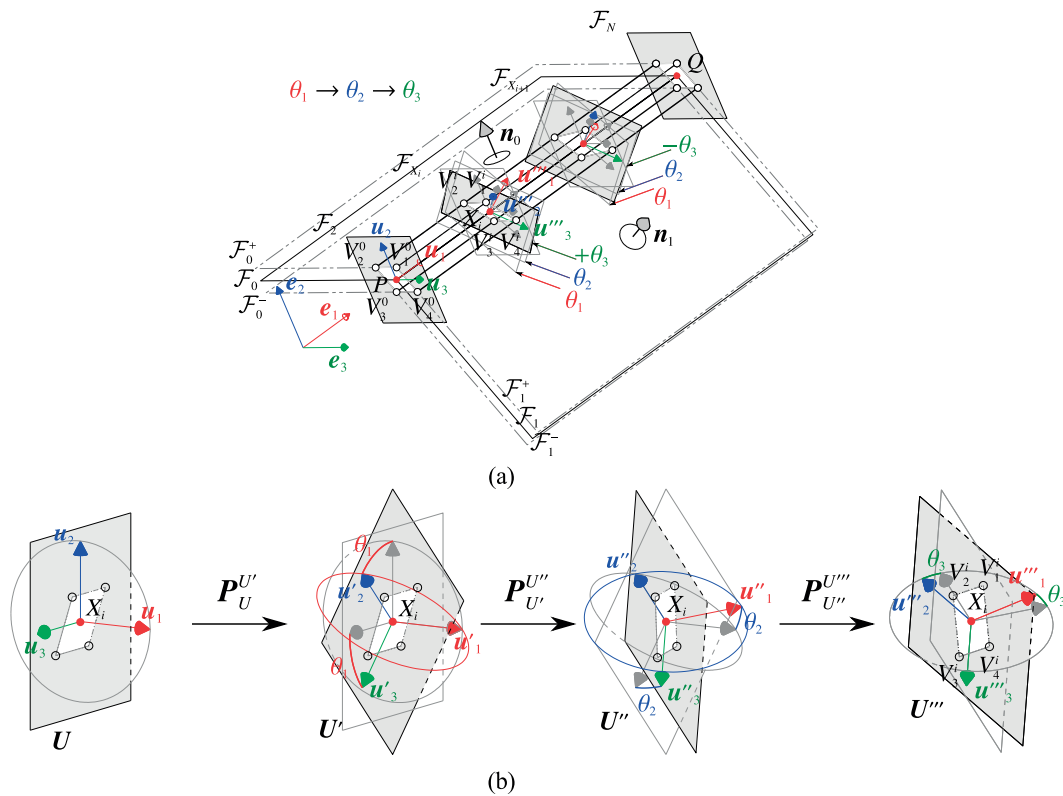


Figure B.1 – General geometrical description for multiple tab-and-slot joints

Let \mathbb{E}^3 be the usual three-dimensional Euclidean space with the associated vector space \mathbb{R}^3 . Geometric points of \mathbb{E}^3 will be denoted by Capital *italic* letters as A, B, C, \dots . The frame of \mathbb{E}^3 is the pair $(O, (\mathbf{e}_1, \mathbf{e}_2, \mathbf{e}_3))$, consisting of the origin O together with three unit base vectors $\{\mathbf{e}_1, \mathbf{e}_2, \mathbf{e}_3\}$ of \mathbb{R}^3 . The position of point Q relative to point P is recorded by a unique vector \mathbf{r}_{PQ} of \mathbb{E}^3 , also denoted \overrightarrow{PQ} , that is referred to as a position vector when P is taken as the origin O . From the parallelogram rule, the position vector \overrightarrow{OM} of any point M is expressed by $\mathbf{r}_{OM} = \mathbf{r}_M - \mathbf{r}_O = \mathbf{r}_M$, where \mathbf{r}_O stands for the zero vector $\mathbf{o} = (0, 0, 0)$.

Appendix B. MTSJ Geometry Script

As depicted in Fig.B.1, the two reference planes $\mathcal{F}_i = \{\mathbf{x} \in \mathbb{R}^3 | \mathbf{x} \cdot \mathbf{n}_i = f_i, f_i = \mathbf{r}_P \cdot \mathbf{n}_i\}$ $i = 0, 1$ of respective normal \mathbf{n}_0 and \mathbf{n}_1 intersect along the line $\mathcal{L}_{PQ} = \{(1-\lambda)\mathbf{r}_P + \lambda\mathbf{r}_Q, \lambda \in \mathbb{R}\}$ that passes through the points P and Q . Physically, \mathcal{F}_0 and \mathcal{F}_1 are the mid-planes of the two constitutive timber panels (0) and (1) of respective thicknesses t_0 and t_1 . The line segment $[P, Q]$ between P and Q is obtained by taking $0 \leq \lambda \leq 1$ (convex subset). Another useful notation for the line is $\mathcal{L}(P, \mathbf{n}_2)$ by taking the director $\mathbf{n}_2 = \mathbf{r}_Q - \mathbf{r}_P$. Note that $\mathbf{n}_2 \cdot \mathbf{n}_0 = \mathbf{n}_2 \cdot \mathbf{n}_1 = 0$. The norm $|\mathbf{n}_2|$ gives the associated beam length.

Let us further introduce the upper and lower surfaces $\mathcal{F}_0^\pm = \{\mathbf{x} \in \mathbb{R}^3 | \mathbf{x} \cdot \mathbf{n}_0 = f_0^\pm, f_0^\pm = \mathbf{r}_{P_0^\pm} \cdot \mathbf{n}_0\}$ of panel (0) passing through the points P_0^+, P_0^- such that $\mathbf{r}_{P_0^\pm} = \mathbf{r}_P \pm \frac{t_0}{2} \frac{\mathbf{n}_0}{|\mathbf{n}_0|}$. Similarly for panel (1),

$$\mathcal{F}_1^\pm = \{\mathbf{x} \in \mathbb{R}^3 | \mathbf{x} \cdot \mathbf{n}_1 = f_1^\pm, f_1^\pm = \mathbf{r}_{P_1^\pm} \cdot \mathbf{n}_1\} \text{ such that } \mathbf{r}_{P_1^\pm} = \mathbf{r}_P \pm \frac{t_1}{2} \frac{\mathbf{n}_1}{|\mathbf{n}_1|}.$$

All the points $P, P_0^+, P_0^-, P_1^+, P_1^-$ belong to a common plane \mathcal{F}_2 of normal \mathbf{u}_1 such that $\mathcal{F}_2 = \{\mathbf{x} \in \mathbb{R}^3 | \mathbf{x} \cdot \mathbf{n}_2 = f_2, f_2 = \mathbf{r}_P \cdot \mathbf{n}_2\}$. Four generating lines $\mathcal{L}(V_k^0, \mathbf{u}_1)$ through four points $\{V_1^0, V_2^0, V_3^0, V_4^0\}$ of \mathcal{F}_2 and parallel to the edge \mathcal{L}_{PQ} are required to define the vertices of the tab elements. They are defined as intersections of the upper and lower surfaces \mathcal{F}_0^\pm and \mathcal{F}_1^\pm with a plane \mathcal{F}_2 of normal \mathbf{u}_1 defined by $\mathcal{F}_2 = \{\mathbf{x} \in \mathbb{R}^3 | \mathbf{x} \cdot \mathbf{n}_2 = f_2, f_2 = \mathbf{r}_P \cdot \mathbf{n}_2\}$.

Their position vectors are evaluated through

$$\mathbf{r}_{A_k^0} = \frac{f_0^k(\mathbf{n}_1 \times \mathbf{n}_2) + f_1^k(\mathbf{n}_2 \times \mathbf{n}_0) + f_2(\mathbf{n}_0 \times \mathbf{n}_1)}{[\mathbf{n}_0, \mathbf{n}_1, \mathbf{n}_2]} \quad (\text{B.1})$$

where the scalar triple product $[\mathbf{n}_0, \mathbf{n}_1, \mathbf{n}_2] = (\mathbf{n}_0 \times \mathbf{n}_1) \cdot \mathbf{n}_2$, using the following tables

$$\begin{array}{|c|} \hline f_0^1 \\ \hline f_0^2 \\ \hline f_0^3 \\ \hline f_0^4 \\ \hline \end{array} \leftrightarrow \begin{array}{|c|} \hline f_0^+ \\ \hline f_0^+ \\ \hline f_0^- \\ \hline f_0^- \\ \hline \end{array} \quad \text{and} \quad \begin{array}{|c|} \hline f_1^1 \\ \hline f_1^2 \\ \hline f_1^3 \\ \hline f_1^4 \\ \hline \end{array} \leftrightarrow \begin{array}{|c|} \hline f_1^+ \\ \hline f_1^- \\ \hline f_1^- \\ \hline f_1^+ \\ \hline \end{array}$$

The tab surfaces cut the segment $[PQ]$ through the set of N equally spaced points X_i whose position vectors are given by

$$\mathbf{r}_{X_i} = (1-\lambda_i)\mathbf{r}_P + \lambda_i\mathbf{r}_Q, \quad \lambda_i = \frac{i}{N}, \quad i = 0..N \quad (\text{B.2})$$

In particular, $\mathbf{r}_{X_0} = \mathbf{r}_P$ and $\mathbf{r}_{X_N} = \mathbf{r}_Q$. Points X_0 and X_N belong to plane \mathcal{F}_2 and the translated plane $\mathcal{F}_N = \mathcal{F}_2 + \{\mathbf{n}_2\}$, respectively. They correspond to the ‘‘end sections’’ of the associated beam.

Considering the local orthonormal frame $(\mathbf{u}_1, \mathbf{u}_2, \mathbf{u}_3)$ along the segment $[PQ]$ such as $\mathbf{u}_1 = \mathbf{n}_2/|\mathbf{n}_2|$, $\mathbf{u}_2 = \mathbf{n}_0/|\mathbf{n}_0|$, $\mathbf{u}_3 = \mathbf{u}_1 \times \mathbf{u}_2$, the direction of insertion, \mathbf{u}''_3 is given by two successive rotations, first about \mathbf{u}_1 by an angle θ_1 ; then about \mathbf{u}'_2 by an angle θ_2 .

Finally the normal vector $\mathbf{n}_{X_i} = \tilde{n}_1^{X_i} \mathbf{u}_1 + \tilde{n}_2^{X_i} \mathbf{u}_2 + \tilde{n}_3^{X_i} \mathbf{u}_3$ that orientates the (lateral) tab surface through the point X_i is obtained by an additional frame rotation about \mathbf{u}''_3 by an angle $\pm\theta_3$. Thus, the transformation matrix $\mathbf{P}_{U''}^{U''''}$ is found by considering three planar transformation matrices, $\mathbf{P}_{U'}^{U''}$, $\mathbf{P}_{U''}^{U''''}$ and $\mathbf{P}_{U''}^{U''''}$ as $\mathbf{P}_{U''}^{U''''} = \mathbf{P}_{U''}^{U''''}(\theta_3, \mathbf{u}''_3) \mathbf{P}_{U'}^{U''}(\theta_2, \mathbf{u}'_2) \mathbf{P}_{U'}^{U''}(\theta_1, \mathbf{u}_1)$ with

$$[\mathbf{P}_{U'}^{U''}] = \begin{bmatrix} 1 & 0 & 0 \\ 0 & c_1 & s_1 \\ 0 & -s_1 & c_1 \end{bmatrix} \quad [\mathbf{P}_{U''}^{U''''}] = \begin{bmatrix} c_2 & 0 & -s_2 \\ 0 & 1 & 0 \\ s_2 & 0 & c_2 \end{bmatrix}$$

$$[\mathbf{P}_U^{U''''}] = \begin{bmatrix} c_3 & s_3 & 0 \\ -s_3 & c_3 & 0 \\ 0 & 0 & 1 \end{bmatrix} \quad [\mathbf{P}_U^{U''''}] = \begin{bmatrix} c_2 c_3 & c_1 s_3 + s_1 s_2 c_3 & s_1 s_3 - c_1 s_2 c_3 \\ -c_2 s_3 & c_1 c_3 - s_1 s_2 s_3 & s_1 c_3 + c_1 s_2 s_3 \\ s_2 & -s_1 c_2 & c_1 c_2 \end{bmatrix}$$

where $s_i = \sin \theta_i$, $c_i = \cos \theta_i$.

Explicitly in $\{\mathbf{u}_1, \mathbf{u}_2, \mathbf{u}_3\}$

$$\mathbf{n}_{X_i} = [\mathbf{P}_U^{U''''}]^T \mathbf{u}_1$$

$$\begin{pmatrix} \bar{n}_1^{X_i} \\ \bar{n}_2^{X_i} \\ \bar{n}_3^{X_i} \end{pmatrix} = \begin{bmatrix} c_2 c_3 & -c_2 s_3 & s_2 \\ c_1 s_3 + s_1 s_2 c_3 & c_1 c_3 - s_1 s_2 s_3 & -s_1 c_2 \\ s_1 s_3 - c_1 s_2 c_3 & s_1 c_3 + c_1 s_2 s_3 & c_1 c_2 \end{bmatrix} \begin{pmatrix} 1 \\ 0 \\ 0 \end{pmatrix}$$

Note that \mathbf{u}''''_1 and $\mathbf{u}''''_3 = \mathbf{u}''_3$ are the normal vector and the insertion vector in the local frame $\{\mathbf{u}''''_1, \mathbf{u}''''_2, \mathbf{u}''''_3\}$, respectively.

To proceed further, the normal vector is expressed in the global frame $\{\mathbf{e}_1, \mathbf{e}_2, \mathbf{e}_3\}$ as

$\mathbf{n}_{X_i} = n_1^{X_i} \mathbf{e}_1 + n_2^{X_i} \mathbf{e}_2 + n_3^{X_i} \mathbf{e}_3$, using a classical change of basis. One has

$$\begin{pmatrix} n_1^{X_i} \\ n_2^{X_i} \\ n_3^{X_i} \end{pmatrix} = [\mathbf{Q}] \begin{pmatrix} \bar{n}_1^{X_i} \\ \bar{n}_2^{X_i} \\ \bar{n}_3^{X_i} \end{pmatrix} \quad \text{or} \quad \begin{pmatrix} \bar{n}_1^{X_i} \\ \bar{n}_2^{X_i} \\ \bar{n}_3^{X_i} \end{pmatrix} = [\mathbf{Q}]^T \begin{pmatrix} n_1^{X_i} \\ n_2^{X_i} \\ n_3^{X_i} \end{pmatrix}$$

where the orthogonal tensor is given by

$$[\mathbf{Q}] = \begin{bmatrix} \mathbf{e}_1 \cdot \mathbf{u}_1 & \mathbf{e}_1 \cdot \mathbf{u}_2 & \mathbf{e}_1 \cdot \mathbf{u}_3 \\ \mathbf{e}_2 \cdot \mathbf{u}_1 & \mathbf{e}_2 \cdot \mathbf{u}_2 & \mathbf{e}_2 \cdot \mathbf{u}_3 \\ \mathbf{e}_3 \cdot \mathbf{u}_1 & \mathbf{e}_3 \cdot \mathbf{u}_2 & \mathbf{e}_3 \cdot \mathbf{u}_3 \end{bmatrix}$$

Note that, with a single edge $[PQ]$, it is always possible to place $[PQ]$ along the \mathbf{e}_1 axis and to take \mathbf{n}_0 in the direction of \mathbf{e}_2 such that $\mathbf{Q} = \mathbf{I}$ and $(\mathbf{e}_1, \mathbf{e}_2, \mathbf{e}_3) = (\mathbf{u}_1, \mathbf{u}_2, \mathbf{u}_3)$ without losing the generality. Finally, the generating lines are parametrized as $\mathcal{L}(V_k^0, \mathbf{u}_1) = \{\mathbf{r}_{V_k^0} + \lambda \mathbf{u}_1, \lambda \in \mathbb{R}\}$

$k = 1, 4$

At a cutting point X_i along the edge $[PQ]$, the plane equation is given by

$$\mathcal{F}_{X_i} = \{\mathbf{x} \in \mathbb{R}^3 | \mathbf{x} \cdot \mathbf{n}_{X_i} = f_{X_i}, f_{X_i} = \mathbf{r}_{X_i} \cdot \mathbf{n}_{X_i}\}.$$

The four tab vertices $\{V_1^i, V_2^i, V_3^i, V_4^i\}$ are obtained as the intersection of the four lines $\mathcal{L}(V_k^0, \mathbf{u}_1)$ and the plane \mathcal{F}_{X_i} as

$$\mathbf{r}_{V_k^i} = \left(\mathbf{I} - \frac{\mathbf{u}_1 \otimes \mathbf{n}_{X_i}}{\mathbf{u}_1 \cdot \mathbf{n}_{X_i}} \right) \mathbf{r}_{V_k^0} + \frac{f_{X_i}}{\mathbf{u}_1 \cdot \mathbf{n}_{X_i}} \mathbf{u}_1 \quad k = 1..4 \quad (\text{B.3})$$

where the identity $(\mathbf{a} \otimes \mathbf{b})\mathbf{c} = (\mathbf{b} \cdot \mathbf{c})\mathbf{a} \quad \forall \mathbf{a}, \mathbf{b}, \mathbf{c} \in \mathbb{R}^3$ is understood.

The main function which are finally provided are listed as follows.

Fig.B.2a Generation of the geometry of the joint (outlines, characteristic surfaces and frames) in 3D,

Fig.B.2b Identification of the vertices which limit the characteristic surfaces,

Fig.B.2c Orientation of the flanks of the tabs/slots (e.g. $\theta_1 = 0^\circ, \theta_2 = 0^\circ, \theta_3 = 25^\circ$),

Appendix B. MTSJ Geometry Script

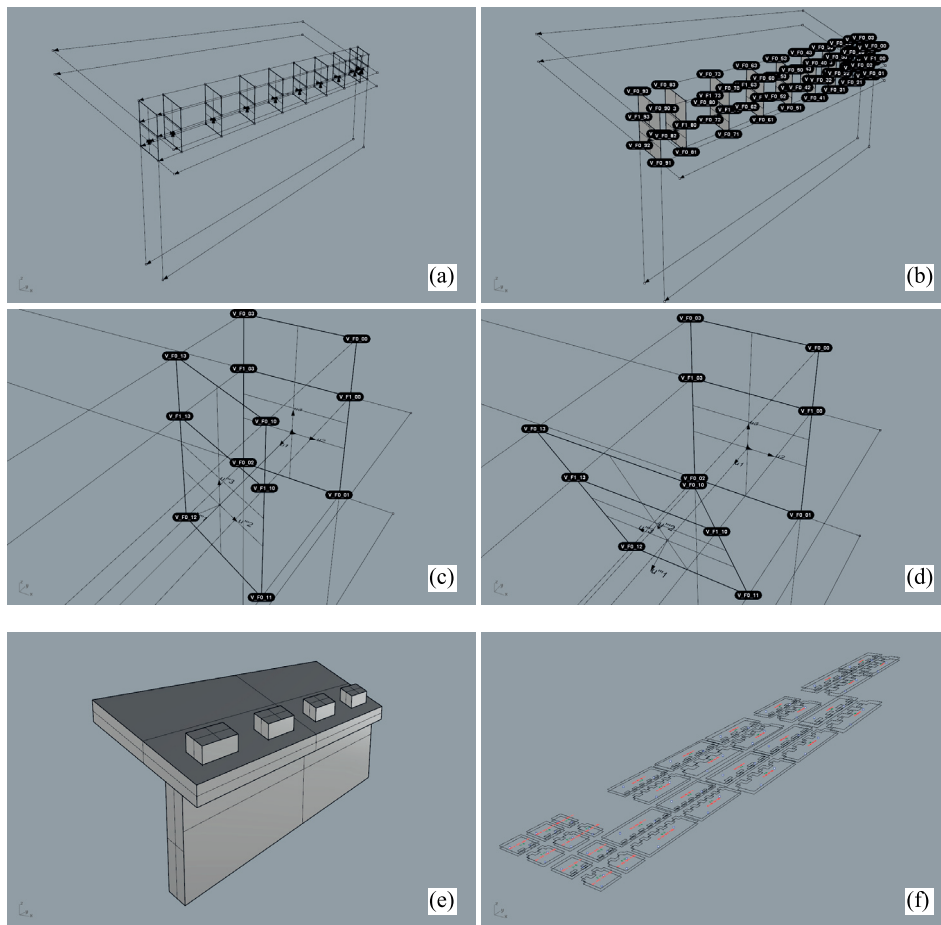


Figure B.2 – Screenshots of MTSJ Geometry Script

Fig.B.2d Orientation of the flanks of the tabs/slots (e.g. $\theta_1 = 0^\circ$, $\theta_2 = 90^\circ$, $\theta_3 = 25^\circ$),

Fig.B.2e Solid model ($\theta_1 = 0^\circ$, $\theta_2 = 0^\circ$, $\theta_3 = 0^\circ$, 4 tabs),

Fig.B.2f Contour lines ready to be computed with the Grasshopper® plug-in, developed by C.Robeller to automatically generate the G-code for 5-axis cutting on CNC machine.

MTSJ-FJ, MTSJ-DJ, MTSJ-JJ can obviously be parametrized with the same script by setting, for instance, the protrusions to zero.

List of Figures

Introduction and State-of-the-Art	1
1 Introduction	3
1.1 Planar subdivision mesh	5
1.2 Gaussian curvatures	6
1.3 Stable faceted structures	6
2 State-of-the-Art	11
2.1 Angular connections for CLT,LVL and Glulam panels	12
2.2 Angular connections for CLT	13
2.3 Textile junction	14
2.4 Bending tests on textile junction	15
2.5 Example design of rigid origami structure	16
2.6 Plywood Prototype 01	17
2.7 2013 - Curved-folded thin shell structure	18
2.8 2014 - Interlocking shell prototype	19
2.9 IBOIS FPS evolution	20
2.10 2014 - Snap-fit joint and double layer	21
2.11 2016 - Doubly-curved shell with two layers and Miura-Ori pattern	21
2.12 Thannhausen Rehearsal Room	23
2.13 Saint Loup Chapel	24
2.14 Vidy theater	24
2.15 Vidy theater prefab	25
2.16 Vidy theater erection	25
2.17 Vidy theater joint tests	26
2.18 2010–2012 - Kobra structure	26
2.19 Falsework for the Kobra structure	28
2.20 2011 - The ICD/ITKE Research Pavilion	29
2.21 2013 - A timber plate funicular shell	30
2.22 2016 - A double-layered timber plate shell 1/2	31
2.23 2016 - A double-layered timber plate shell 2/2	32

List of Figures

2.24 2014 - The Landesgartenschau Exhibition Hall	33
2.25 Cross-screwed finger joint	34
2.26 3-way vertices structure	37
2.27 2015 - The Solar Energy House	38
2.28 Joint behavior in portal frames	39
2.29 Rotational response of joint	40
2.30 Level of rigidity for timber beams	41
2.31 Component method	43
2.32 Assembly of the components	44
2.33 Nuki joint in shrine	47
2.34 Details of Nuki joint	47
2.35 Nuki joint in Taiwan by Chang	48
2.36 Tenon-mortise with dowel in Japan by Sakata	48
2.37 Penetrating joints in Japan by Komatsu	48
2.38 Nuki joint in Japan by Tanahashi	48
2.39 Watari-ago in Japan by Ogawa	49
2.40 Kumimono joint in Japan by Kitamori	56
2.41 Dieh-dou joint in Taiwan by Yeo	56
2.42 Elastostatics of a half space in soil mechanics	58
2.43 Triangular embedment with simplified additional length	65
2.44 Additional length effect	66
2.45 Triangular embedment in penetrating joint	72
2.46 Translational partial compression AIJ	73
2.47 Translational partial compression Kitamori	73
2.48 Rotational partial compression - single contact	73
2.49 Rotational partial compression - double contact	73
2.50 Rotational partial compression at the end - double contact	73
2.51 Translational partial compression LR plane	73
2.52 Translational partial compression LT plane	74
2.53 Translational partial compression LR plane	74
2.54 Translational partial compression LTR plane	74
2.55 Two parameter soil models	75
2.56 Pasternak model for embedment of wood	76
2.57 Shape function for Pasternak model	82
2.58 Yielding mechanism for PM	83
2.59 MTSJ with open slots	88
2.60 MTSJ with closed slots and protrusion	89
Investigations and Publications	103
3 On the semi-rigidity of dovetail joint for the joinery of LVL panels	105

3.1	Box beam cross section with semi-rigid interfaces	107
3.2	Description of the sequence of rotation by Bryant's angles	111
3.3	Sample connection specifications	112
3.4	Three-point bending tests with LVDT locations	114
3.5	Deflection curves of the tested beams for F=3000 N	115
3.6	Individual rigidity modulus vs tab length or screw spacing	116
3.7	Deflection curves of the tested beams for F=3000 N	117
3.8	MTSJ joints applied to more complex assemblies	118
3.9	MTSJ Japanese joint variant (JJ)	119
3.10	MTSJ Finger joint variant (FJ)	119
3.11	MTSJ Dovetail joint variant (DJ)	120
4	Rotational Stiffness at Ridges of Timber Folded-plate Structures	123
4.1	Single-fold plate roof as V-section beams	125
4.2	Moments and Forces in MTSJ	126
4.3	Description of the sequence of rotation by Bryant's angles	128
4.4	Assembly constraints	129
4.5	Combination of Bryant angles	129
4.6	Bending tests, closing and opening mode, samples	130
4.7	Reduced contact on the locking faces	131
4.8	Material frame and orientation	131
4.9	Brittle behaviour	133
4.10	Ductile behaviour	134
4.11	Algorithm of the USDFLD subroutine	135
4.12	S01–Moment max and Stiffness	136
4.13	S02–Moment max and stiffness.	136
4.14	S01 - Moment-rotation average non-linear curves for bending in closing	137
4.15	S02 - Moment-rotation average non-linear curves for bending in opening	137
4.16	S01 - Moment-rotation average linear curves for bending in closing	137
4.17	S02 - Moment-rotation average linear curves for bending in opening	137
4.18	High-stiffness effect on glued and screwed joints	138
4.19	S01 - Numerical curves versus experimental results	141
4.20	S02 - Numerical curves versus experimental results	141
4.21	MTSJ: open slot (left), closed slot (right)	142
4.22	MTSJ-JJ - Average stiffness : closing and opening	143
4.23	MTSJ-JJ - Best stiffness : closing and opening	143
4.24	MTSJ-JJ - Best stiffness : closing and opening	144
4.25	MTSJ-JJ - Dissymetry in stiffness : closing and opening	144
4.26	MTSJ-JJ : sample (c), sample (a), sample (d)	144
4.27	Closing - Moment-rotation linear range from 10% to 40% M_{max}	145
4.28	Opening - Moment-rotation linear range from 10% to 40% M_{max}	145

5	Improvement of the Rotational Stiffness for the Connection of Thin Structural Wood Panels	149
5.1	Yoshimura and Double-layer Miura-ori pattern	151
5.2	MTSJ sample design	152
5.3	Geometry of MTSJ with TTs	152
5.4	Folding machine : closing and opening	153
5.5	Moment–rotation curves up to the maximum point, in closing	154
5.6	Moment–rotation curves up to the maximum point, in opening	155
5.7	Symmetrical behavior of TT	156
5.8	Scan of F_{0+} embedment area with a FaroArm	157
5.9	Embedment effect in MTSJ-TT	158
5.10	Sample geometries for in rotational partial compression	158
5.11	Rotational partial compression setup	159
5.12	Mechanical behavior in rotational partial compression	160
5.13	Corresponding stiffness with steel or Kerto Q punch	160
5.14	SC moment–rotation curves	161
5.15	Double contact moment–rotation curves	162
5.16	Selected times on the moment–rotation curve	163
5.17	Time-lapse photographs of the displacement profile	164
5.18	γ , decay coefficients	165
5.19	Elasto-plastic deformed volumes	165
5.20	Comparison between TT-variant and screws	168
5.21	Analogy MTSJ-TT to Nuki joint by component method.	169
5.22	Embedment in single and double contact: Kerto-Q 21mm, $\alpha = 0^\circ$	170
6	Material characterization of spruce LVL in rotational partial compression	173
6.1	Embedment effect in MTSJ-TT	174
6.2	Joint-to-grain angle	177
6.3	Bidirectional deformation in mm	177
6.4	Contact zone in SC	178
6.5	Geometries of samples in rotational partial compression (SC)	178
6.6	Test rig for rotational partial compression in SC	179
6.7	2DF head for RPC	180
6.8	Contact zones in Double Contact	180
6.9	Geometries of samples in rotational partial compression (DC)	181
6.10	Test rig for rotational partial compression in DC	181
6.11	Geometry of additional length profile	183
6.12	Geometry of embedded volume for local forces P calculation	183
6.13	Fit of analytical models parameters (SC)	186
6.14	Analytical models at 21,27 and 39mm (SC)	187
6.15	Discretization in points of the captured deformation profile	188
6.16	Strain ε evolution with respect to θ (SC)	188

6.17 Integral error exponential curve / experiments (SC)	189
6.18 Boxplot of integral error exponential curve / experiments (SC)	190
6.19 Comparison of integrals relative to decay coefficients (SC)	190
6.20 Comparison of integrals for b_{SC,i° and $b_{SC,mean}$ for all samples	191
6.21 The most stressed layers along the depth in SC	192
6.22 Influence of α on the resisting moment	194
6.23 Fit of analytical models parameters at 21,27 and 39mm (DC)	195
6.24 Analytical models at 21,27 and 39mm	195
6.25 Capture of local deformations in DC with $\theta = 15^\circ$	195
6.26 Actual angle measured by inclinometers in DC	197
6.27 Failure (left) and Torsion (right) in the panel	198
6.28 Increase of the additional length effect from double contact to single contact	199
6.29 Increase of the additional length effect from $\alpha = 0^\circ$ to $\alpha = 90^\circ$	199
7 Semi-rigid Moment-resisting Model of the Through Tenon variant of Multiple Tab-and-Slot Joint for LVL panels	205
7.1 MTSJ-TT geometry and parameters	207
7.2 Crosspiece timber joints : Nuki and MTSJ-TT joints	209
7.3 Flowchart - main approach of the model	210
7.4 Subroutines : Calculation and assembly of the components	211
7.5 Step #10 - Assembly of the two panels	212
7.6 Step #20 - Rotational slip, then Step #30 - contacts start	213
7.7 Step #40a - Resisting moment due to normal reaction forces	214
7.8 Step #40b - Bending in the two panels	215
7.9 Initial slip angle due to transversal clearance	216
7.10 Characteristic lengths in SC	217
7.11 Characteristic lengths of double contact	218
7.12 (a) Elasto-plastic deformed volumes. (b) Details after yield point.	219
7.13 Bending test for MTSJ-TT	225
7.14 (a) Quasi-static equilibrium (b) Moment M_s and shear force V diagrams.	225
7.16 Analytical model Vs Experimental curves - 1/3	232
7.17 Analytical model Vs Experimental curves - 2/3	233
7.18 Analytical model Vs Experimental curves - 3/3	234
7.19 Failure modes by bending	235
7.20 Influence of the transversal clearance C on the contact length	237
7.21 Influence of the dihedral angle φ on the contact length	237
Conclusion	242
8 Conclusion	245
	273

Appendices	249
A.1 MTSJ-TT geometric parameters of panel F_0	252
A.2 MTSJ-TT geometric parameters of panel F_1	253
A.3 MTSJ-TT geometric parameters of F_0 - F_1 assembly	254
A.4 MTSJ-TT under bending : Closing ($\theta < 0$) and Opening ($\theta > 0$)	256
A.5 Tolerances for transversal clearance C	257
A.6 Semi-rigid moment-resisting behavior of MTSJ-TT	257
A.7 Simplified embedded volumes for stiffness formula	258
A.8 Effective moment of inertia for MTSJ-TT bending strength	262
B.1 General geometrical description for multiple tab-and-slot joints	265
B.2 Screenshots of MTSJ Geometry Script	268

List of Tables

Introduction and State-of-the-Art	1
2 State-of-the-Art	11
2.1 Types of joint models	42
2.2 Component method for timber	46
2.3 Models for traditional Asiatic penetrating joints	49
2.4 Models for traditional Asiatic interlocking brackets joints	56
2.5 Influence factor for the settlement of rectangular flexible area	62
2.6 Influence factor for the settlement of rectangular rigid plate	63
2.7 Decay coefficients in partial compression	74
2.8 Increasing stiffness ratio in partial compression	82
2.9 Increasing stiffness ratio in partial compression	82
Investigations and Publications	103
3 On the semi-rigidity of dovetail joint for the joinery of LVL panels	105
3.1 Geometrical and mechanical properties for the 3-layered boxed beams	113
3.2 Deflection of beam samples at $1/200^{th}$ of span	116
4 Rotational Stiffness at Ridges of Timber Folded-plate Structures	123
4.1 Sample parameters	129
4.2 Elastic properties of spruce	132
4.3 Mechanical properties of spruce	135
4.4 S01 - Mean and SD	136
4.5 S02 - Mean and SD	136
4.6 Comparative analysis of the combination of Bryant angles	140
4.7 S01 - Model stiffness vs Experimental stiffness	142
5 Improvement of the Rotational Stiffness for the Connection of Thin Structural Wood Panels	149

List of Tables

5.1	Average stiffness and ultimate moment for S01	154
5.2	Average stiffness and ultimate moment for S02	155
5.3	Sample parameters for partial compression	158
5.4	Elasto-plastic values for rotational partial compression	161
5.5	Comparison of SC and DC	162
5.6	Comparative fit of γ coefficient - Scan vs camera	162
5.7	γ coefficient at 25° of rotation	163
5.8	γ coefficients for SC or DC	164
5.9	Evolution of γ with rotation steps	165
5.10	Embedded volume parameter values	166
6	Material characterization of spruce LVL in rotational partial compression	173
6.1	Series of samples in rotational partial compression (SC)	179
6.2	Series of samples in rotational partial compression (DC)	180
6.3	Embedded volume parameter values	183
6.4	Fitted coefficients from the analytical model (SC)	187
6.5	Quantiles of boxplot in Fig.6.20	191
6.6	Exponential Decay Coefficients b_{SC} for all configurations of joint	192
6.7	Fitted coefficients from the analytical model (DC)	196
6.8	Decay Coefficients of exponential fit for all joint configurations (DC)	196
7	Semi-rigid Moment-resisting Model of the Through Tenon variant of Multiple Tab-and-Slot Joint for LVL panels	205
7.1	Common parameters of the samples	208
7.2	F_0 panel parameters of the samples	208
7.3	F_1 panel parameters of the samples	208
7.4	Volume parameters of the samples in SC	220
7.5	Volume parameters of the samples in DC	220
7.6	Elastic properties of LVL Kerto-Q (mean values)	223
7.7	Embedment parameters for 21mm- $\alpha_i = 0^\circ$	226
7.8	Embedment parameters for 21mm- $\alpha_i = 45^\circ$	226
7.9	Embedment parameters for 21mm- $\alpha_i = 90^\circ$	226
7.10	Embedment parameters for 27mm- $\alpha_i = 0^\circ$	227
7.11	Embedment parameters for 39mm- $\alpha_i = 0^\circ$	227
7.12	Characteristic values of moment-rotation curves	227
7.13	Average bending stress into the panels	235
A.1	Elastic properties of LVL Kerto-Q (mean values)	255
A.2	Geometrical parameters of the example case	262

Stéphane Roche

6 rue de la Source – 74 500 Champanges – France

☎ +33 (0)6 85 45 74 40 • 📞 +33 (0)4 50 26 82 24 • ✉ steph.roche@wanadoo.fr
French, Married, 47 years

Work experience

Wood construction.....

École Polytechnique Fédérale de Lausanne, Laboratory of Wood Construction **Lausanne, Switzerland**
Research assistant 2013–2017

Farizon, Wood Construction Company **Thonon-les-Bains, France**
Project manager 2009–2013

Eribois, Design Office in Wood Construction **Paris, France**
Technical director 2009

Gaujard Technologie, Design Office in Wood Construction & Biosourced Materials **Avignon, France**
Master internship 2008

Industry.....

Saint-Gobain Glass, Glass Manufacturing **International**
Project manager, Float glass facility construction, Cutting lines 2004–2008

Saint-Gobain Crystals, Synthetic Crystals Factory **Saint-Pierre-lès-Nemours, France**
Maintenance / new works manager 2001–2004

Abac, Building Energy Management System **Villebéon, France**
Technical sales engineer 1996–2001

Education

École Polytechnique Fédérale de Lausanne, Laboratory of Wood Construction **Lausanne, Switzerland**
Doctoral Student 2013–2017

Association Ouvrière des Compagnons du Devoir du Tour de France **Tours, France**
Art of Carpentry 2009

École Nationale Supérieure des Techniques et Industries du Bois **Épinal, France**
Master II, Wood Materials and Applications in Construction, with honors 2007–2008

Institut National des Sciences et Techniques Nucléaires **Saclay, France**
Post-grade, Industrial Automation and Robotics 1994–1995

École Nationale d'Ingénieurs de Tarbes **Tarbes, France**
Master II, Mechanical Computer-Aided Design 1990–1993

Languages

French: Mother tongue
English: C1

